SLAC-PUB-1526
January 1975

DIFFRACTIVE PROCESSES*

David W.G.S. Leith

Stanford Linear Accelerator Center,
Stanford University, Stanford, California 94305

Lecture notes for the 1974 SLAC Summer Institute
in Particle Physics

(Extracted from SLAC Summer Institute, SLAC Report 179, Volume I)

*Work supported by the U. S. Atomic Energy Commission.

OUTLINE

I. INTRODUCTION
   1. General
   2. Models
      A. The t-channel View
      B. The s-channel View
      C. s-channel Unitarity and the Overlap Function
   3. The Data
   4. The Rules

II. TOTAL CROSS-SECTION AND ELASTIC SCATTERING
   1. Total Cross-Sections
   2. Elastic Cross-Sections
   3. Elastic Differential Cross-Sections
      A. Baryon-baryon scattering
      B. Meson-baryon scattering
      C. Meson-meson scattering
      D. The cross-over phenomena
      E. Real part of the forward scattering amplitude
      F. Some theoretical comments
   4. Summary

III. PHOTOPRODUCTION OF VECTOR MESONS
   1. Cross-Sections
   2. Differential Cross-Sections

IV. DIFFRACTION DISSOCIATION (EXCLUSIVE INELASTIC DIFFRACTION)
   1. Introduction
   2. Baryon Dissociation
      A. $N \to N\pi$ dissociation
      B. $N \to N\pi\pi$ dissociation
      C. Nucleon dissociation at high energies
      D. Hyperon dissociation
   3. Meson Dissociation
      A. Cross-sections
      B. Differential cross sections
   4. Summary
   5. Final Comments

V. RULES OF DIFFRACTION
   1. Introduction
   2. Quantum Numbers in Pomeron Exchange
      A. $I = 0$ exchange
      B. $C = +1$ exchange
      C. Spin-parity charge
      D. G-parity exchange
   3. Spin structure in Diffractive Processes
   4. Factorization

VI. INCLUSIVE INELASTIC DIFFRACTION
   1. High Energy Inclusive pp Scattering
      A. Missing mass distribution
      B. Energy dependence, or scaling
      C. Momentum transfer dependence
      D. Aside on missing mass effects
      E. Back to t dependence
   2. Pion Diffraction Scattering
   3. Multiplicity in Inclusive Collisions
   4. Single Particle Inclusive Studies at Low Energy
   5. Conclusion

VII. TRIPLE REGGE PHENOMENOLOGY
   1. Which Terms are Unimportant?
   2. Decoupling of the Triple Pomeron Term as $t \to 0$

VIII. IMPACT PARAMETER ANALYSIS OF HIGH ENERGY SCATTERING
   1. Summary of Data
   2. Elastic Scattering Analysis
   3. Inelastic Diffractive Scattering Analysis
   4. Slope-Mass Correlation
   5. Rise of Total Cross-section
   6. Conclusion

IX. CONCLUSION

I. INTRODUCTION

1. General

These lectures are intended to review what we know of diffractive processes--to summarize the available data and what it teaches us about the structure of the proton and the dynamics of high energy scattering.

Despite the large volume of data presented in these notes, there are some topics which I know (and probably many more that I am not so aware of), that have not been discussed--I apologize for the omissions.

Finally, I list a set of review papers[1-20] that I have found invaluable in preparing my lectures--I recommend them to you for further study.

Diffraction is an important phenomenon in high energy physics, accounting for ~ 30% of the total cross-section. Our motivations for studying these processes range through the following viewpoints:

- That the diffractive processes are not the most fundamental or interesting processes in themselves, but that they cover up,[†] or conceal, the remaining two-thirds of the cross-section which is accounted for by a variety of processes which exhibit a great deal of exciting structure, and from which one is going to learn about the dynamics of two body scattering, particle production and perhaps, the internal structure of the nucleon. In other words, one has to understand the one before proceeding to the other;
- That diffraction is simply related to geometry, optics and absorption, and also represents the single largest cross-section we deal with in particle physics--therefore we should try to understand it before moving on to the more complex, smaller cross-section processes;
- or perhaps we feel that because diffraction is basically the reflection of all the absorptive processes, that through its study we might find other insights into the regularities of the inelastic scattering, or into the structure of the proton itself;

[†]Apologies to R.M.N., Rodino, Ervin et al.

Whatever our motivation, we are going to spend the next four lectures thinking about these diffractive processes.

2. Models

Diffraction scattering can be discussed in terms of two pictures--the t-channel or the s-channel pictures. In the t-channel, or exchange picture the scattering is thought to proceed through the exchange of a singularity called the Pomeron. The language of this picture is that of Regge exchange models, and we will discuss below the properties of the Pomeron trajectory and how we use this picture to learn more of the Pomeron. The s-channel picture or direct channel, is seen in geometric or optical terms--here diffraction is generated by the absorption due to the competition among the many inelastic channels. The target proton is talked of in terms of an absorbing disc of a given size and with a given opacity, and sometimes with some edge structure.

The experience has been that both the s-, and t-channel points of view seem to be important for the description of the various systematic features of elastic and inelastic amplitudes. In general, the t-channel picture has been more successful in explaining the energy dependence of hadronic amplitudes, while the s-channel picture has been very useful in understanding the structure of amplitudes as a function of momentum transfer. In discussing the Pomeron, or the diffractive mechanism, we will be using both points of view.

A. The t-channel view

In Regge theory the scattering amplitude is given by

$$F(s,t) = \beta(t)\,\frac{[1 + \tau\, e^{-i\pi\alpha(t)}]}{\sin \pi\alpha(t)} \cdot \left(\frac{s}{s_0}\right)^{\alpha(t)} ,$$

where $\tau = \pm 1$ for even or odd signature trajectories, and where the trajectory of the exchange system is

$$\alpha(t) = \alpha_0 + \alpha' \cdot t \ .$$

In general, the physical interpretation of this amplitude is that the crossed channel Regge pole represents the collective amplitude due to single exchanges of all the particles that lie on the trajectory.

Within this model, the energy dependence of the cross-section is controlled by the trajectory properties of the exchanged particle--

$$\sigma(s) \propto s^{\alpha(0)-1}$$

Also the behaviour of the differential cross-section is given by

$$\frac{d\sigma}{dt}(s,t) \propto s^{2\alpha(t)-2}$$

So, studies of the s-, and t-dependence of the cross-sections of diffractive processes will teach us about the Pomeron trajectory.

The assumption that the asymptotic behavicur of total cross-sections would be a constant required that the leading trajectory have $\alpha(0) = 1$ and $\tau = +1$.

In fact Khuri[21] has shown that in any unitary theory satisfying the two conditions--

- that an exclusive cross-section for producing n particles does not outgrow the total elastic cross-section by a power of the energy,
- that the multiplicity of secondaries must grow slower than a power of the energy

then $\alpha(0) = 1$. The data from high energy interactions suggest that these conditions are easily fulfilled.

The Pomeron has quite an unusual role in particle physics, in that--

- no other pole has a trajectory with $\alpha(0) = 1.0$;
- there is no known particle to be associated with this trajectory--i.e. unusual behaviour of the trajectory in $t > 0$ region
- the behaviour of the trajectory for $t < 0$, as seen in the shrinkage of the differential cross-section, is quite different from other trajectories. The Pomeron trajectory is observed to have a rather flat t-dependence, with

$$\alpha_P(t) = 1 + \alpha' \cdot t \quad \text{and} \quad 0 < \alpha' < 0.3 \ ,$$

while most Regge trajectories for meson exchanges behave like

$$\alpha_R(t) = 0.5 + 1.0 \cdot t \quad \text{i.e.} \quad \alpha' \sim 1.0 \ .$$

- the Pomeron behaves in scattering processes as though it carried the quantum numbers of the vacuum, whereas it behaves with respect to the energy dependence of cross-sections, as though it carries spin 1.

In all of these properties the Pomeron is quite different from the other known Regge trajectories. Further, we have no idea about the physical origin of this singularity.

B. <u>The s-channel view</u>

The geometrical model describes scattering in terms of the size and opacity of the object from which scattering.

$$\frac{d\sigma}{dt} = \pi |F(s,t)|^2$$

where

$$F(s,t) = \frac{1}{\pi} \int d^2b \ e^{iq \cdot b} \ f(s,b)$$

and

$$q = \sqrt{-t}$$

$$b = \text{impact parameter}$$

and $f(s,b)$ is the partial wave amplitude corresponding to angular momentum $\ell \sim bk$.

In the eikonal form,

$$f(s,b) = \frac{i}{2}\,[1 - e^{2i\delta(s,b)}]$$

where $\delta(s,b) = \delta_R(s,b) + i\delta_I(s,b)$.

For diffraction scattering, we assume the scattering is due to the absorption of the incoming wave caused by the many open inelastic channels. For this case $\delta_R \sim 0$.

$$\mathrm{Im}\, f(s,b) = \frac{1}{2}\left(1 - e^{-2\delta_I(s,b)}\right)$$

If we define $\Omega(b) = 2\delta_I$ as the opaqueness of the target, we have

$$\sigma_T = 4\pi \int_0^\infty (1 - e^{-\Omega(b)})b\, db$$

$$\sigma_{el} = 2\pi \int (1 - e^{-\Omega(b)})^2 b\, db$$

$$\sigma_{in} = 2\pi \int (1 - e^{-2\Omega(b)})b\, db\ .$$

The differential cross-section is a measure of the size of the scattering object, and of its opacity. The determination of $\Omega(b)$ allows a mapping of the blackness, and size, of the scatterer.

The transformation from t-space to impact parameter space is given by (for given s),

$$F(t) \sim \int_0^\infty b\, db\, J_0(b\sqrt{-t})\cdot f(b)$$

For a peripheral collision, the t-dependence is then a J_0 Bessel function giving a peak at small t; a central collision will result in either a J_1 Bessel function, or an exponential, t-dependence depending on how sharp the edge is in $f(b)$. Various examples are given in Fig. 1. It is interesting to see how deformations of $f(b)$ from a gaussian distribution in b affect the distribution of $f(t)$ and hence the elastic differential cross-section. If one adds some large partial wave contributions to $f(b)$, they result in an increase of the slope of $F(t)$ near $t = 0$. (See Fig. 2.) If one absorbs out some low partial waves from $f(b)$, then this produces large t structure in the exponential $F(t)$, producing a dip followed by a secondary maximum. (Again see Fig. 2.)

It is therefore of interest to study the s-, and t-dependence of the diffractive cross-sections to determine $f(s,b)$ or $\Omega(s,b)$, within the direct channel picture and through them learn of the proton's structure.

C. <u>s-channel unitarity and the overlap function</u>

One can extend these simple geometrical ideas by formally applying the idea that diffraction scattering is the shadow of absorption, which in turn is due to the many open inelastic channels.

One may write (following Van Hove[22] and others),

$$\mathrm{Im}\, T_{fi} = \sum_{el} T^*_{el,f}\cdot T_{el,i} + \sum_{in} T^*_{in,f}\cdot T_{in,i}$$

where the T's represent the initial and final states in inelastic (in) and elastic scattering (el). This may be illustrated as shown in Fig. 3. Usually the two terms on the left-hand side above are written as $G_{el} + G_{in}$, the elastic and inelastic overlap functions.

So we see that the imaginary part of the elastic amplitude is built up by two parts--the shadow of the inelastic channels and the elastic scattering itself. The strong lesson from these studies is that not only are the magnitudes of the inelastic amplitudes important in making up G_{in}, but also the phases of all the open channels.

It is interesting to transform this relationship into impact parameter space--there the s-channel unitarity relation becomes

$$\mathrm{Im}\, a(s,b) = |a(s,b)|^2 + a_{in}(s,b)$$

where a_{in} is the inelastic overlap function. Notice that this equation connects the inelastic and total overlap functions at the <u>same</u> impact parameter! This makes the impact parameter representation very convenient to study unitarity effects.

For a purely imaginary high energy amplitude we have the above relation rewritten

$$a_{tot}(s,b) = a_{el}(s,b) + a_{in}(s,b)$$

and

$$a_T^2 = a_{el}$$

therefore

$$a_{tot} = \frac{1}{2}\left[1 - \sqrt{1 - 4a_{in}}\right] .$$

The relationship of the various overlap functions, as a function of the inelasticity are shown in Fig. 4. Notice that $[0 \leq a_{in} \leq 1/4]$.

Here we see the rapid variation of the elastic amplitude with inelasticity; for full absorption, $a_{in} = 1/4$ and $\sigma_{el}/\sigma_{tot} = 1/2$. But as the scatterer becomes just slightly less than black, the elastic contributions fall quickly and σ_{el}/σ_{tot} falls rapidly from 1/2. For $a_{in} \sim 75\%$, the ratio is about 25%.

So, once more, for small inelasticity the imaginary part of the elastic amplitude is given by the inelastic contribution--as the inelastic cross-section grows, the elastic part increases.

This picture of the impact structure of high energy collisions is very useful, and we will return to it in trying to interpret the structure of the proton from high energy proton-proton scattering and diffraction inelastic scattering.

3. The Data

Now, having discussed the viewpoints from which we may analyze the diffraction scattering, let us consider the processes that we may study.

- $A + B \to A + B$

  Elastic scattering, and through the optical theorem, the total cross-section, allows study of the Pomeron, or the absorption profile. These data are reviewed in Chapter II.

- $A + B \to A^* + B$

  $A + B^*$.

  Inelastic exclusive diffraction scattering. This process was discussed by Good and Walker[23] in analogy to optical diffraction by an opaque disc. They predicted that such processes would occur, that they would proceed coherently in nuclei, and that the scattering properties would be very similar to those of elastic reaction. This data is reviewed in Chapters III and IV.

  $A + B \to A + X$

  $\to X + B$.

  Leading particle inclusive scattering. This process becomes of considerable interest at high energies. These data are reviewed in Chapters VI and VII.

4. The Rules

Unfortunately beyond the two pictures discussed above, we have no good theoretical description of the dynamics of diffractive processes, or no basic understanding of what the Pomeron singularity is--we rather have a set of phenomenological rules which allow us to identify what we mean by diffraction--

These rules are listed below.[12]

--energy independent cross sections (to factors of $\log s$)

--sharp forward peak in $d\sigma/dt$

--particle cross sections equal to antiparticle cross sections

--factorization

--mainly imaginary amplitude

--exchange processes characterized by the quantum numbers of the vacuum in the t-channel (i.e. $I = 0$, $C = +1$). Also, the change in parity in the scattering process follows the natural spin-parity series $(-1)^J$ or $P_f = P_i \cdot (-1)^{\Delta J}$, where ΔJ is spin change.

--the spin structure in the scattering is s-channel helicity conserving (SCHC).

These rules and how well the diffractive processes obey them, are discussed in Chapter V.

II. TOTAL CROSS-SECTIONS AND THE ELASTIC SCATTERING REACTION

1. Total Cross-Sections

The most classical of particle experiments is the measurement of the total cross-section. Interest in these measurements stems from the insight into the behaviour of the elastic scattering amplitude obtained through the optical theorem:

$$\sigma_T(s) \propto \mathrm{Im}\, f_{el} \qquad (s,\ t = 0)$$

where f_{el} is the forward spin-averaged elastic scattering amplitude. The linear relationship between σ_T and $\mathrm{Im}\, f_{el}$ allows a study of the different contributions to the elastic amplitude and their separate energy dependence, without the difficulty of unscrambling the information from expressions involvin the absolute squares of amplitudes, as determined in studies of the elastic scattering reaction itself.

From the optical theorem, the s-dependence of σ_T is fixed when the behaviour of the elastic scattering amplitude is defined. This is usually done through Regge pole fits, since this theory has done a fair job of describin two-body peripheral processes. In these fits two components are postulated--

- an energy independent term due to the exchange of the Pomeron, with trajectory $\alpha(t) = 1$,
- an energy dependent term due to the exchange of ρ, ω, f, A_2 trajectories, which are usually assumed to have the same form--

$$\alpha(t) = \frac{1}{2} + t$$

This formalism leads to the simple parametrization--

$$\sigma_T(AB) = a(AB) + b(AB)\, p^{-1/2}$$

$$\sigma_T(\bar{A}B) = a(\bar{A}B) + b(\bar{A}B)\, p^{-1/2}$$

The terms $a(AB)$, $b(AB)$ represent the two terms described above, and p is the laboratory momentum of the particles.[24]

The Pomeranchuck theorem which states that at infinite energy, particle cross-sections will be equal to antiparticle cross-sections, is taken care of in this model with $a(AB) = a(\bar{A}B)$.

The data up to 30 GeV (i.e. in pre-Serpukov days) for all hadron and photon cross-sections were well fit by this description--that is, the data fell on straight lines when plotted against $p^{-1/2}$, and particle and antiparticle data converged to a common asymptotic limit (or at least everything was consistent with such a picture).

Representative fits are shown in Figs. 5 and 6, and the parameters for these fits given in Table I.[25]

Data from the Serpukov accelerator, extending these measurements up to 65 GeV/c dispelled this simple picture of the elastic amplitude. Data for $\pi^{\pm}p$, $K^{\pm}p$, $p^{\pm}p$ total cross-sections are shown in Fig. 7, and may be summarized as follows--

- $\pi^{\pm}p$, $K^{-}p$, $K^{-}n$, pp, pn total cross-sections seem to have reached a plateau with little or no energy dependence;
- $\bar{p}p$, $\bar{p}n$ total cross-sections are decreasing;
- $K^{+}p$, $K^{+}n$ total cross-sections are increasing with energy through the region (20-60) GeV/c;
- the difference between particle and antiparticle cross-sections, $\Delta\sigma = \sigma(\bar{x}p) - \sigma(xp)$ is decreasing with energy, and fits $\Delta\sigma \propto Ap^{-n}$.

The values of the exponent for π, K, p are given in Table II.[26]

This data indicated that probably at just slightly higher energies, the Okun-Pomeranchuck theorem (which states that the cross-sections for particles belonging to the same isospin multiplet should become equal asymptotically), and the Pomeranchuck theorem would be satisfied.

Other measurements became available around this time, which generally confirmed the above trends.

a) The Λp and Λn total cross sections were measured at CERN[27] with a wire chamber spectrometer set up to study K^0 decays. The results are shown in Fig. 8, together with the cross-section for $\Sigma^{-}p$ measured at 19 GeV/c in the hyperon beam at CERN.[28]

The additive quark model gives relationships between ΛN, pN, KN, πN cross sections--

$$\sigma_T(\Lambda p) = \sigma_T(pp) + \sigma_T(K^{-}n) - \sigma_T(\pi^{+}p)$$

which seem to be reasonably satisfied (see Fig. 8).

b) The total cross-section for γp and γn have been measured up to 30 GeV at Serpukov (extending the old SLAC, DESY and DARESBURY measurements).[29] The data is shown in Fig. 9. The s-dependence of these data is fit to

$$\sigma_T(\gamma p) = A + Bp^{-1/2}$$
$$= (97.4 \pm 1.9) + (55 \pm 5)^{I=0}\, E^{-1/2} + (12 \pm 2.5)^{I=1}\, E^{-1/2} .$$

The photon data up through 30 GeV behave very much like the $\pi^{\pm}N$ cross-sections (only 1/200 smaller).

When the ISR--the proton-proton storage rings at CERN--started doing experiments, there were almost immediately rumors of large p-p absorption cross-sections. Last year these preliminary reports settled down, and the picture of the elastic amplitude has again been shattered--the pp total cross-section rises ~ 4mb through the ISR energy region (~ 200 - 1500 GeV/c equivalent momentum range). It is now clear that statements on σ_T becoming constant must be modified--it may become constant asymptotically or it may not. The simple picture in which there are just two contributions--an energy independent one, due to Pomeron exchange, and a decreasing contribution as energy increases due to Regge exchange, is not a good model. It is now clear that the region which gave credibility to the idea of constant asymptotic cross-section is actually only a local minimum, where the s-dependence of the various contributions cancel. Whether eventually σ_T does approach a constant (this time from below), or continues to rise indefinitely, remains for some experimenters of the future. (See Fig. 10.)

Let us now review these exciting new measurements in more detail. The data (when finally the ISR was running reliably enough to make precision cross-section measurements) came from two groups using two quite different methods--

1.) CERN-Rome:[30] They measure the forward scattering angular distribution $d\sigma/dt$, with a scintillation counter telescope and extrapolate to find the the forward cross-section, $d\sigma/dt\big|_{t=0}$. They also measure the real part of the forward scattering amplitude in this energy range and find it small and essentially negligible. From the optical theorem, they can then determine the total cross-section

$$\sigma_T^2 = 16\pi \left.\frac{d\sigma}{dt}\right|_{t=0} .$$

This experiment normalizes their total cross-section measurement two ways--(a) internally, by measuring the elastic scattering into small enough angles to observe the Coulomb scattering, which can be absolutely calculated, and (b) externally, by using the Van der Meer luminosity measurement of the circulating proton beams. Both methods agree well.

2) Pisa-Stony Brook.[31] They measure the reaction rate in pp collisions with an almost 4π counter hodoscope. This experiment is normalized using two external methods--the Van der Meer beam displacement measurement, and actual measurement of the individual beam profiles by scattering in gas. Again, both these methods of normalizing agree well. This group has made the highest energy measurement, when the stored 25 GeV/c proton beams were accelerated in the storage ring to 31.4 GeV/c in each beam.

The results of these experiments are shown in Fig. 11, and summarized in Table III.

Good agreement is obtained between these two groups in the cross-section rise. It is interesting to note that they depend quite differently on the luminosity measurement--

CERN-Rome $\qquad \sigma_T \propto \sqrt{\left.\frac{d\sigma}{dt}\right|_{t=0} \cdot \frac{1}{L}}$

Pisa-Stony Brook $\qquad \sigma_T \propto \frac{\text{Rate}}{L}$

So if there were systematic problems with the measurement of the ISR luminosity, it would affect the total cross-sections of these two experiments in a markedly different way. The agreement is evidence that they indeed do measure L reliably.

A further interesting comment should be made on the independence of the rise in $\sigma_T(pp)$ on the luminosity measurement. It is clear from the above discussion that the ratio of the measured quantity in these two experiments is a measure of the total cross-section, completely independently of measurements of L

$$\left[\left.\frac{d\sigma}{dt}\right|_{t=0} \Big/ \text{Rate}\right] \propto \frac{\sigma_T^2 \cdot L}{\sigma_T \cdot L} = \sigma_T$$

If the proton beam phase space and luminosity does not vary around the ring, then the data from the two groups taken simultaneously (a small fraction of their total running) could be used to perform this check. It is interesting that the results confirm the measured rise in $\sigma_T(pp)$, but with poorer error since one has to add the errors of the two measurements and only a small fraction of the data satisfied conditions of simultaneous running, and well steered beams. The cross-sections are given in Table IV.[2]

To summarize, the luminosity measurements seem to be well understood and in good agreement, and the 4 mb rise in the pp total cross-section through the ISR energy range, an established fact.

This rise in $\sigma_T(pp)$ was also indicated in an analysis of very high energy proton flux at an atmospheric depth of 550 gm/cm^2 on a mountain top in Bolivia, compared to the flux at the top of the atmosphere. This analysis (by Yodh, Pal and Trefil)[32] indicated that the nucleon-nucleon cross-section increased with energy significantly at laboratory energies about 500 GeV. The lower bound for the energy dependence, from their analysis, agrees well with the measured increase through the ISR--and is indicated in Fig. 12 by the dashed line.

One amusing thought, while still considering this rising cross-section: for many years we have been concerned about how fast the $\bar{p}p$ cross-section is falling as the energy increased, and wondering when it would finally fall sufficiently to reach the pp cross-section to fulfill the Pomeranchuck theorem. Now the pp cross-section has risen so high that we now have the situation that the $\bar{p}p$ total cross-section will have to turn around and <u>increase</u> with energy to catch up with the pp cross-section.

Kycia[33] will report on the new precision measurements for $\pi^{\pm}N$, $K^{\pm}N$, $p^{\pm}N$ at NAL at the Topical Conference.

The energy dependence of the $\sigma_T(pp)$ have been shown to be compatible with both a $\ln s$ and $\ln^2 s$ growth with energy.

2. <u>Elastic Cross-Section</u>

We first review the p-p scattering data through the ISR energy region, and then follow other particle scattering up through Serpukov energies.

At the ISR the CERN-Rome[34] and ACGHT[36] groups measured the elastic scattering distribution (described in the next section), and by integration obtain the elastic cross-section. This data, together with measurements from the NAL bubble chambers[36] is summarized in Fig. 13, and Table V. The elastic cross-section increases by ~ 10% through the ISR region--the same fraction as σ_T.

The 205 GeV/c NAL-LBL-Berkeley HBC π^-p experiment[37] has measured the π^-p elastic cross-section as (3.03 ± 0.3)mb. This result is plotted with other π^-p data in Fig. 14. Also shown are the energy dependencies for K^-p and $\bar{p}p$ elastic scattering. The π^-p data shows evidence of flattening out, similar to the p-p data. (The extrapolated value of the 205 GeV/c cross-section if the lower energy s-dependence had continued would have given $\sigma_{el} \sim 2.3$ mb.)

New measurements of the high energy elastic cross-section are summarized in Table VI, and the fitted energy dependencies of the cross-sections given in Table VII. (Remember that this slow falling of the cross-section eventually flattens out as shown for π^-p and pp in Figs. 13 and 14--and that the σ_{el} at sufficiently high energy starts to rise with σ_T, as shown in Fig. 13 for pp.)

The new elastic scattering experiments at NAL will be reviewed by Ritson at the Topical Conference.[38]

Before finishing our examination of the elastic scattering data, I would like to consider two interesting ratios: a) (σ_{el}/σ_T), and b) $[\sigma(AB \to AB)/\sigma(\bar{A}B \to \bar{A}B)]$.

a) In asymptotic geometrical models, where the proton is seen as a completely absorbing black disc of radius R, the ratio of the elastic to the total cross-section is 0.5. However, for a gaussian distributed absorption, 100% at $R = 0$ the ratio is ~ 0.15-0.20, being 0.185 for $R = 1f$. The ratio is plotted in Figs. 15 and 16 for p-p and π^-p interactions, respectively. The rather sparse data for other processes is given in Table VIII. Clearly, the ratio is

far from 0.5, and, moreover, for the $\pi^- p$ and p-p reactions (where there is data at high energy), has reached a plateau value which is independent of energy.

b) Martin[39] has proved (for quite general assumptions on the analyticity of the elastic scattering amplitude) that one should expect the elastic (diffractive) cross-section for particle processes to equal the antiparticle elastic cross-section at asymptotic energies. This work has been generalized to include inelastic quasi-two-body cross-sections too.[40] Table IX summarizes some data on the ratios of particle to antiparticle elastic cross-sections. It is surprising the extent to which the equality seems to be preserved, even at energies where one knows that Regge exchange processes contribute substantially, and therefore, the scattering cannot be all due to Pomeron exchange.

3. Elastic Differential Cross-Sections.

In this section we review the data on $d\sigma/dt$ for elastic processes, first the p-p scattering at ISR and NAL and then working down in energy, for both baryon-baryon and baryon-meson scattering.

A. Baryon-baryon scattering

The forward angular distribution in pp elastic scattering is sharply peaked, as expected in a diffractive process. However, recently, very accurate measurements at the ISR have shown the presence of some interesting structure around $t \sim 0.15\ \mathrm{GeV}^2$. (This possibility had been pointed out many years earlier by Carrigan,[41] who noted that at (10-30) GeV energies the value of the slope in pp scattering differed experiment to experiment. He suggested the changes were due to the different t ranges being studied. However, no sufficiently systematic and accurate experiments had been done before the ISR studies brought the feature to clear light.)

The small t-region ($t < .15\ \mathrm{GeV}^2$) has been studied by CERN-Rome[42] and ACGHT[43] at the ISR, and by US-USSR group[44] at NAL. Lower energy measurements are also available from Serpukov.

The large t-region of the forward scattering ($.2 < t < .5\ \mathrm{GeV}^2$) has been studied by the ACGHT group at ISR.[43] The same group has also measured large t-scattering out to t values of $\sim 5\ \mathrm{GeV}^2$.[45]

We first consider the systematics of the forward region. The general conclusion is that the region with $t < .15\ \mathrm{GeV}^2$ has a steep slope ($\approx 12\ \mathrm{GeV}^{-2}$), which shrinks as energy increases. The region with ($.2 < t < .5\ \mathrm{GeV}^2$) has a somewhat flatter angular distribution (about 2 units smaller slope value), and exhibits essentially no energy dependence.

Typical data is shown in Fig. 17, where (a) shows data from the highest energy ISR studies of the ACGHT group--the two regions of the scattering distribution are clearly visible; (b) shows data from the US-USSR collaboration at one of the energies in this NAL experiment--this experiment measures entirely in the "small t-region" discussed above. Notice in the very forward direction the observation of p-p Coulomb scattering.

There has been much discussion as to whether there really are two distinct regions or whether the slope smoothly decreases as the scattering angle increases. New data from CERN-Rome[42] at $\sqrt{s} = 53$ GeV show that the slope is not continuously changing through the "small t region," but that one value of the slope parameter describes all of the data. If the cross-section within this "small t" interval is fit with $\frac{d\sigma}{dt} = \left.\frac{d\sigma}{dt}\right)_0 \cdot e^{-bt}$, then for

$$0.01 < t < 0.06\ \mathrm{GeV}^2 \quad \text{they find} \quad b = 13.1 \pm 0.3\ \mathrm{GeV}^{-2}$$
$$0.04 < t < 0.16\ \mathrm{GeV}^2 \quad \text{they find} \quad b = 13.0 \pm 0.3\ \mathrm{GeV}^{-2}$$

Further confirmation of this effect can be seen in Table X, where all of the ISR forward slope measurements are gathered.[3]

The slope of the larger t region is also quite stable with t interval used. The results of the fitting in this region are also given in Table X.[3]

The situation on the s-dependence of the slope prior to the NAL experiment is shown in Fig. 18. The data were fit to an exponential in the two ranges, $t < 0.1$ GeV^2 and $0.15 < t < 0.5$ GeV^2, from 1 GeV/c beam momentum through the ISR energy (~ 2000 GeV/c equivalent momentum). The Serpukov data were lowered by $\Delta b \sim 0.4$ GeV^{-2}, which is within their quoted systematic error. The data show b increasing with increasing energy, but the rate of change becoming relatively constant above 30 GeV/c. The data above 30 GeV/c were fit to

$$b(s,t) = b_0(t) + 2\alpha'(t) \ln \frac{s}{s_0} .$$

The fits are quite good and result in the following parameters

$$\text{(low } t \text{ region):} \qquad b_0 = (7.0 \pm 1.2), \qquad \alpha' = (0.37 \pm 0.08)$$

$$\text{(larger } t \text{ region):} \qquad b_0 = (9.2 \pm 0.94), \qquad \alpha' = (0.10 \pm 0.06)$$

In other words, the cross-section is made up of a forward region which exhibits substantial shrinkage, and a larger t region which is essentially constant in t.

The US-USSR group[44] at NAL have studied small t pp elastic scattering, detecting the recoil proton from 'beam-hydrogen gas jet' collisions in an array of solid state counters. A typical $d\sigma/dt$ was shown in Fig. 17. This group found their data consistent with a logarithmic growth of the slope with energy, and fitting their data above $s \sim 100$ GeV^2 to

$$b(s) = b_0 + 2\alpha' \ln s$$

yielded

$$\left.\begin{aligned} b_0 &= 8.23 \pm 0.27 \text{ GeV}^{-2} \\ \alpha' &= 0.278 \pm 0.024 \text{ GeV}^{-2} \end{aligned}\right\} \quad \text{for } t < 0.15 \text{ GeV}^2$$

The most complete analysis of all of the data is shown in Fig. 19 (from Amaldi '73), where the dashed line corresponds to the parameters

$$\left.\begin{aligned} b_0 &= 8.32 \text{ GeV}^{-2} \\ \alpha' &= 0.275 \pm 0.02 \text{ GeV}^{-2} \end{aligned}\right\} \quad \text{for } t < 0.12 \text{ GeV}^2$$

The ACGHT group[45] have extended their studies of elastic pp scattering out to larger momentum transfers by using a double arm wire chamber spectrometer with momentum analysis in both arms. This set-up provides enough discrimination against the inelastic background that they can follow the cross-section down seven orders of magnitude. The scattering distributions are shown in Fig. 20 for four energies at the ISR. The break in the pp scattering cross-section for $t \sim 1.2$ GeV^2 observed at lower energies now becomes a sharp dip, with a secondary peak. The position of the dip, and the height of the secondary peak are essentially independent of energy.

[At London, apparently the CHVO group reported preliminary results on a second generation study of large angle pp elastic scattering. This new data is claimed to show the position of the dip moving in (i.e. to smaller t-values) as the energy increased, and the height of the secondary maximum also increasing.]

The break in the pp scattering distribution at low energies is shown in Fig. 21 and again in Fig. 22 where the measured cross-section has been divided by $G^4(t)$, where $G(t)$ is the electromagnetic form factor $G(t) = [(1 + t/\mu^2)^2]^{-1}$, and $\mu^2 = 0.71$ GeV^2. (This is the optical model of Chou-Yang, where the matter density is assumed to have the same distribution as the charge density. The shape of this curve is shown in Fig. 21.) Not too much energy dependence is apparent.

The ACGHT group report the t-value of the dip, as a function of energy:

$\sqrt{s}$ (GeV)	t_{dip} (GeV^2)
23.5	--
30.7	1.45 ± .1
44.9	1.38 ± .04
53.0	1.37 ± .04

The $G(t)$[4] description clearly does not fit the data, but the model has been extended by Durand and Lipes (and others) to give a good representation of the scattering of ISR energies. These fits will be discussed later.

The data on np elastic scattering shows very much the same structure as the pp data discussed above. Two experiments--one at CERN studying $np \to np$ up to 24 GeV/c[46] and the other at Serpukov[47] measuring up to 65 GeV/c --are reviewed. The $d\sigma/dt$ of the CERN experiment are presented in Fig. 23 and clearly show the development of the large t-dip. Figure 24 compares the n-p scattering distribution with the data of Allaby et al. at 19.2 GeV/c--the agreement is very good.

The shape of the angular distribution has been analyzed in terms of the exponential slope, b. The results below 30 GeV/c are shown in Fig. 25, where the p-p and n-p data have been fit for $t < 0.3$ GeV^2. The higher energy data has been obtained in a gas jet target experiment at Serpukov, and measures only the small t-region. The value of the slope for $t < 0.05$ GeV^2, for np scattering data between (10-65) GeV/c is given in Fig. 26, where it is compared to the dashed line--which represents the fit to the small t pp data discussed above. For both experiments the agreement between the np and p-p data is good.

It is interesting to notice that the small t slope for np is 1-2 units in b larger than the slope measured for data with $.07 < t < .3$ GeV^2, in keeping with the effect observed for pp scattering (i.e. 2 region in $d\sigma/dt$).

As a final comment on baryon-baryon scattering, the hyperon beam group at BNL (the Yale-NAL group)[48] have studied the slope of $\pi^- p$ and $\Sigma^- p$ elastic scattering at 23.3 GeV/c, while setting up to study the Σ-decays. Figure 27 shows the two differential cross-sections. The data are well represented by $d\sigma/dt = Ae^{-bt}$; with

$$\left.\begin{aligned} b_\pi &= 7.99 \pm 0.22 \text{ GeV}^{-2} \\ b_\Sigma &= 8.97 \pm 0.26 \text{ GeV}^{-2} \end{aligned}\right\} \quad (0.07 < t < 0.21 \text{ GeV}^2)$$

The slope parameter for Σp is, not surprisingly, very similar to the slope in p-p scattering at the same energy. (The p-p data in Fig. 25 are taken over a similar t-range, and indicate a value of the slope ~ 8.8 GeV^{-2}.)

B. Meson-baryon scattering

We now move on to consider meson-baryon scattering data.

Some recent data on $\pi^- p$ elastic scattering is summarized in Table XI. Three experiments, covering similar t ranges analyzed the cross-section in terms of $d\sigma/dt = Ae^{-bt}$, and the slope values are given in the top part of the table. Weak evidence of shrinkage is observed. However, it is clear from the high statistics studies at 14,[49] 25, 40[50] GeV/c that there is curvature in the cross-section, and that if one attempts to fit the data out to large t, a quadratic term is required--see Figs. 28 and 29. The slope b from this analysis is given in the bottom part of Table XI, and displayed in Fig. 30. Very clear evidence of shrinkage is observed.

Figure 29 also shows the differential cross-section for $K^- p$ and $\bar{p}p$ elastic scattering at 25, 40 GeV/c from Serpukov.[50] The slope parameters are summarized in Table XII.

The CERN-Serpukov group[50] studied the shrinkage of the forward peak by fitting all the available data for $10 < s < 70$ GeV^2, at $t = 0.2$ GeV^2 with the slope parametrized as

$$b = b_0 + 2\alpha' \ln s \ .$$

They found quite small shrinkage for the $\pi^- p$, $K^- p$ scattering, and very substantial antishrinkage for $\bar{p}p$.

$$\left.\begin{aligned} \alpha'(\pi^-) &= 0.18 \pm .04 \\ \alpha'(K^-) &= 0.19 \pm .04 \\ \alpha'(\bar{p}) &= -0.5 \pm .05 \end{aligned}\right\} \quad \text{at} \quad t \sim 0.2 \ \text{GeV}^2$$

However, they also observed a rather strong t-dependence to the shrinkage. This effect is shown in Table XIII where $2\alpha'$ is listed as a function of the t-value at which it was evaluated. The $\pi^- p$ and $K^- p$ scattering is seen to have very substantial shrinkage for $t \lesssim 0.1$ GeV^2 with $\alpha \sim (0.26\text{-}0.36)$ GeV^{-2}, while for t larger then 0.2 GeV^2 the shrinkage is quite small with $\alpha' \sim 0.1$ GeV^{-2}.

<u>This is very reminiscent of what we have learned of the pp system above</u>.

Another experiment commenting on the curvature of the differential cross-section is reported by 10 GeV/c $K^- p$ CERN-HBC collaboration.[51] They report a slope of 9.8 ± 0.5 GeV^{-2} for the elastic $K^- p$ peak for $t < 0.1$ GeV^2, and a slope of $7.1 \pm .2$ GeV^{-2} when $.12 < t < .4$ GeV^2.

A word of caution is in order here. The curvature of the differential cross-section in processes like $\pi^{\pm} p$, $K^- p$ and $\bar{p}p$ elastic scattering at low (or even moderate) energies should not be taken as indicative of diffractive behavior. It <u>may</u> be associated with the behavior of p-p scattering at the ISR (and hence the "Pomeron"), but it may very well not--since we do have an alternative explanation.

We know that there is substantial Regge exchange contribution to the $\pi^{\pm} p$, $K^- p$ elastic amplitudes in the (5-40) GeV/c range--if from nothing else, the $\pi^- p \to \pi^0 n$, $K^- p \to \bar{K}^0 n$ cross-sections or from the energy dependence of the difference in total cross-sections discussed in II.1 above. We believe these Regge components to be peripheral, and so contribute a term like $J_0(R\sqrt{-t})$ to the differential cross-section. The diffractive contribution we believe is central in impact parameter space, and behaves like an exponential, e^{-bt}. Therefore, the $d\sigma/dt$ for these processes is the sum of the Bessel function and the exponential, which certainly shows curavture or may even look like two exponentials. (See Fig. 31.) A good example of such behaviour is shown in Fig. 32 where $K^+ p$ and $K^- p$ elastic $d\sigma/dt$ at 5 GeV/c is shown. The $K^+ p$ process is believed to be mainly diffractive (with very little Regge), while the $K^- p$ is believed to have quite substantial peripheral Regge amplitude in addition to the diffractive contribution. The $K^- p$ cross-section is seen to start higher than the $K^+ p$ forward cross-section, fall faster and then oscillate about the essentially exponential $K^+ p$ data. This is just the behavior one would expect from the above model.

We should therefore be skeptical of assuming the $d\sigma/dt$ behaviour of the $\pi^{\pm} p$, $K^- p$ is the same phenomenon observed in p-p. It will be interesting to see the results of high statistics studies of $K^+ p$ scattering in the (5-20) GeV/c region, and the behaviour of all of these processes at NAL. If the NAL experiments find the small t steepening of the cross section, and it proves to be s-independent, then we will be forced to associate this behaviour with that observed in pp scattering at ISR, and of course, with the Pomeron. It will be especially interesting to see the results of the NAL $K^+ p$ experiments and the very high statistics $K^+ p$ scattering at SLAC--here the Regge contributions are known to be small.

If the experimental evidence supports that indeed the small t steepening is due to the Pomeron, the same two component mechanism discussed above may be at work (i.e. a $J_0(R\sqrt{-t})$ term adding to a central, e^{-bt}, term)--where now the peripheral contribution may be associated with the Pomeron, an additional piece coming from the grey ring around the edge of the proton. We discuss such a model[52] for the Pomeron later.

C. Meson-meson scattering

There is very little systematic data on π-π, K-π scattering in the diffraction-dominated region, although there are several good experiments studying the resonance region. The difficulties in these studies are 1) having high energy so that the diffraction region is accessible in the meson-meson scattering, 2) the event rate is small since the meson cloud presents a low luminosity target for the scattering, and 3) finding a reliable analysis technique to separate meson diffraction from resonance production at the other vertex. Below we report briefly on some π-π, K-π scattering data to give a flavor of what is known.

Walker et al.[54] have studied

$$\pi^- p \to \pi^+\pi^- n \qquad \text{at } 25 \text{ GeV/c}$$

$$\pi^- p \to \pi^-\pi^-\Delta \qquad \text{for } (5\text{-}25) \text{ GeV/c}$$

The production angular distributions are shown in Fig. 35. They find the forward peak is well fit to

$$\frac{d\sigma}{dt} \propto e^{-bt}$$

$$b(\pi^+\pi^-) = 5.9 \pm 0.54 \text{ GeV}^{-2}$$

$$b(\pi^-\pi^-) = 6.1 \pm 0.51 \text{ GeV}^{-2}$$

The integrated data yields $\sigma_{el}(\pi^+\pi^-) \sim \sigma_{el}(\pi^-\pi^-) \sim 1.5$ mb and the total cross-sections are $\sigma_T(\pi^+\pi^-) \sim \sigma_T(\pi^-\pi^-) \sim 15$ mb. (See Fig. 36.) This analysis compared all data[54,55] to isolate the 3 isospin cross-section in π-π scattering and found (as expected for diffractive processes) that they were all equal

$$\sigma_0 \sim \sigma_1 \sim \sigma_2 = (15\text{-}20) \text{ mb} .$$

(Again, there is rumor from the London Conference that the Carnegie-Mellon-BNL group presented an analysis of 8, 16 GeV/c $\pi^- p$, $K^- p$ elastic scattering data and report a break in the $d\sigma/dt$ at $t \sim 0.2$ GeV^2. I do not know if the data demands a break or is merely consistent with curvature as in the data discussed above.)

A summary of the s-dependence of the slope for elastic scattering as measured at $t \sim 0.2$ GeV^2, is shown in Fig. 33. The slopes for particle and for antiparticle scattering seem to become equal at high energies, with asymptotic slopes of ~ 8 GeV^{-2} for πN, ~ 7.5 GeV^{-2} for KN and ~ 11 GeV^{-2} for NN. The $\pi^- p$ and $K^- p$ data show almost no shrinkage (i.e. no s-dependence of the slope), while the $\bar{p}p$ data shows considerable antishrinkage up through the Serpukov energy region. The $K^+ p$ and pp data show considerable shrinkage, while the $\pi^+ p$ data also shows shrinkage, but much less. Ritson will present the preliminary results on the NAL elastic scattering slopes at the Topical Conference.[38]

Why do the $\pi^\pm p$ angular distributions show so little energy dependence compared to $K^+ p$ and pp, if they are all diffraction dominated? This question was answered in a very nice analysis by Davier,[53] applying the Dual Absorption Model to the combination of the $\pi^+ p$ and $\pi^- p$ that isolates isoscalar exchange, and assuming only the Pomeron and f-meson contribute to the exchange amplitude. The Pomeron was parametrized as a central collision process while the f^0 was given a Regge energy dependence and assumed to be peripheral. The data were well fit with this composite amplitude and the resulting Pomeron contribution showed substantial shrinkage, in good agreement with the $K^+ p$ data. Figure 34 shows the $K^+ p$ slope as a function of energy as the shaded band, and the data points are the Pomeron contribution to the $\pi^\pm p$ scattering from Davier's analysis. The agreement is good. It is interesting to see that small admixtures of a non-diffractive amplitude may markedly change the energy dependence of the differential cross-section, and, further, that the Pomeron derived from this analysis agrees so well with the classic "$K^+ p$ Pomero

In addition, some data is available from 8 GeV/c π^+p and 12 GeV/c K^+p experiments at LBL.[56] The diffractive scattering is isolated by choosing small t for the meson-scattering, selecting $M(p\pi^+) > 1400$ MeV to remove the strong pion exchange reaction, and requiring $M(\pi\pi)$ or $M(K\pi)$ to be greater than 1600 MeV to isolate the diffractive scattering from the "s-channel" resonance formation processes.

For $t < 0.3$ GeV^2 they find

$$b(\pi\pi) = 4.14 \pm .22 \text{ GeV}^{-2}$$

$$b(K\pi) = 4.10 \pm .25 \text{ GeV}^{-2}$$

D. *Cross-over phenomenon*

The differential cross-section for the elastic scattering reaction $\bar{X}p \to \bar{X}p$ is known to have a steeper slope and a larger forward intercept than the reaction $Xp \to Xp$. This leads to the well-known cross-over effect in which the differential cross-sections cross at a t-value of ~ 0.2 GeV^2. The difference in these cross-sections is due to the imaginary part of the non-flip odd C amplitude in the t-channel. This phenomenon is understood in terms of the Dual Absorption Model in which the K^+p and pp reactions (being exotic in the s-channel) have dominant contribution from the Pomeron, while $\pi^\pm p$, K^-p and $\bar{p}p$ all have a mixture of Pomeron and Regge terms. The KN and NN data show clear cross-overs (since the Regge contribution appears only in one term), while the $\pi^\pm p$ differential cross-sections have very similar slopes and magnitudes, since both terms (Regge and Pomeron) contribute to both cross-sections.

A beautiful experiment[57] at Argonne has studied these phenomena in the (3-6) GeV/c region--the data is displayed in Figs. 37-40 and summarized in Table XIV. The cross-over in particle antiparticle cross-section were found to be quite energy independent

$$\pi : t_c = 0.14 \pm .03 \text{ GeV}^2$$

$$K : t_c = 0.19 \pm .006 \text{ GeV}^2$$

$$p : t_c = 0.16 \pm .004 \text{ GeV}^2$$

At SLAC a high statistics wire chamber experiment[58] is in progress studying $K^\pm p$ scattering at 6, 10, 14 GeV/c, and $\pi^\pm p$ and $p^\pm p$ scattering at 10 GeV/c. A preliminary measurement was performed at 13 GeV/c for $K^\pm p$ (see Fig. 41), and indicated $t_c = 0.21 \pm .03$ GeV^2. Final results on the SLAC systematic study should be available shortly. (Representative cross-sections are shown in Fig. 42.)

The s-independence of t_c indicates that the effective radius of the peripheral amplitude (the odd C Regge exchange term) is constant and not expanding as the energy increases.

E. Real parts of forward scattering amplitude

Typical differential cross-sections are shown in Figs. 43 and 44 for the NAL experiment[59] and the CERN-Rome ISR epxeriment,[60] respectively.

This quantity is becoming very interesting, given the observation of rising total cross-sections. Dispersion relations provide a connection between the behavior of the ratio of the real to imaginary parts of the forward scattering amplitude, ρ, and the energy dependence of the pp and $\bar{p}p$ total cross-sections. This integral relation is such that ρ measured at energy E is sensitive to the behavior of $\sigma_T(pp)$ and $\sigma_T(\bar{p}p)$ for energies larger than E.

Khuri and Kinoshita[61] have shown that total cross-sections, rising indefinitely as a power of the logarithm of the energy, imply ρ approaching zero from above. The argument goes as follows:

An amplitude that corresponds to $\sigma_T \propto (\ln s)^\nu$ *at high energies is* $F^+(s) = i|\gamma^+|s\,(\log s)^{\nu^+}$.

However, this amplitude does not satisfy the requirements of analyticity and crossing in the complex energy plane. Such an amplitude can, instead, be written as

$$F^+(s) = i|\gamma^+|s\,(\log s - i\,\tfrac{\pi}{2})^{\nu^+}$$
$$\sim i|\gamma^+|s\,(\log s)^{\nu^+} + \frac{\pi\nu^+}{2}\,\gamma^+ s\,(\log s)^{\nu-1^+}$$

Thus

$$\rho = \frac{\mathrm{Re}\,F^+(s)}{\mathrm{Im}\,F^+(s)} = +\frac{\pi\nu}{2}\cdot\frac{1}{\log s}$$

The derivation is for the sum of the pp and $\bar{p}p$ amplitudes (i.e. the even signature amplitude), but for no pathological behaviour of $\bar{p}p$ it may be assumed to apply to the pp data alone.

Then, for the total cross-section approach a constant from above, the ρ goes to zero from below, but for a rising cross-section, the ρ must be positive (and if the $d(\sigma_T)/ds$ stops, ρ approaches zero from above).

Therefore, one may use careful measurements of ρ to try to gain insight on the s-dependence of σ_T at still higher energies. How sensitive is it? Bartels and Diddens[62] have investigated this sensitivity by calculating $\rho(s)$ for σ_T becoming constant at various energies. The results are shown in Fig. 45. Clearly, precision measurements through the ISR region would allow useful limits to be placed on the high energy behavior of $\sigma_T(pp)$.

The measurements for pp are shown in Fig. 46 up through 400 GeV/c,[59] while new data on the real part for np scattering at Serpukov[47] is shown in Fig. 47. It is interesting to see the agreement between this data and the p-p data discussed above.

Finally, Fig. 48 shows the real part measured in π^-p scattering through Serpukov energies.[63] It will be interesting to see what is measured at NAL, both in terms of the $\sigma_T(\pi^+p)$ and their real parts.

F. Some theoretical comments

I. Asymptotic Bounds

At asymptotic energies, the bound of Lugunov and Van Hieu (Topical Conference on H.E. Collisions, Vol. II, p. 74, 1968) may be written

$$\sigma_{el} \gtrsim \frac{\sigma_T^2}{(\ln s)^2}$$

but we know

$$\sigma_{el} \leq \sigma_T$$

Then, if $\sigma_T \propto (\ln s)^{\alpha}$,

for $\alpha = 1$, $\quad$ constant $\leq \sigma_{el} \leq \ln s$

and $\alpha = 2$, $\quad \sigma_{el} \propto \ln^2 s$

Further, if $d\sigma/dt = \sigma_T^2 \cdot e^{-bt}$, then

$$b = \frac{\sigma_T^2}{\sigma_{el}}$$

and

for $\alpha = 1$, $\quad \ln^2 s \geq b \geq \ln s$

and $\alpha = 2$, $\quad b \propto \ln^2 s$

One interesting point of these bounds is that if the σ_T ever saturat the Froissart bound and increases like $\ln^2 s$, then the energy dependence of b must change from the present $\ln s$ behaviour.

II. Fits to High Energy p-p Scattering

There are two main types of models for the Pomeron in pp elastic scattering:

(a) the two component models typical of the work of Cheng-Walker-Wu, Kane,[8,9,10] Barger-Geer-Phillips,[65] Allcock-Cottingham-Michael,[66] which are summarized in Fig. 49.

The main contribution to the Pomeron is from the central collisions giving rise to the exponential,(or $e^{at} J_1(R\sqrt{-t})$, t-dependence arising from absorption from a disc of radius of about 0.6 f. The e^{at} modifier accounts for the smoothing of the edge of the disc. The dip at $t \sim 1.4$ GeV^2 is the diffraction zero from the disc.

In addition to this central piece there is a peripheral contribution from the edge of the proton. Constructive interference between these two terms produces the upward curvature in $d\sigma/dt$ for small t.

There are differences in the details of the models, but the essential two components are as described.

Allcock et al.[66] make the point that the edge component may be due to 2π exchange. Their calculation indicates that in shape and in magnitude the 2π exchange term fits the extra high partial wave tail that is the characteristic of the second component.

Henyey et al.[10] describe this component as due to dissociation of the incoming particle; Cheng-Walker-Wu[64] ascribe Diffraction Dissociation to the ring component.

(b) The pole and cut models, typical of the work of Durand-Lipes,[67] Chou-Yang,[68] Frautschi-Margolis,[69] etc. These models are described in Fig. 50. The dip at large t is generated by the destructive interference of a structureless pole term, with a cut of opposite sign.

The small t structure has to be explained by introducing modifications to the pole term (e.g. the 2π contribution discussed in the above models could be used to modify the pole term).

A typical fit to the scattering data at the ISR is shown in Fig. 51. The height of the secondary maximum is related to the total cross-section used in the optical model calculation (40 mb in this case), so a more realistic σ_T would allow for better fit in this t range.

4. Summary

- $\sigma_T(pp)$ increases for (200-1500) GeV/c by $(10 \pm 2)\%$,
  $\sigma_{el}(pp)$ increases for (200-1500) GeV/c by $(12 \pm 4)\%$,
  $\rho \sim 0$ for 300 GeV/c
  slope, b, increases for (200-1500) GeV/c by $(11 \pm 3)\%$
  $\sigma_{inel}(pp)$ increases for (200-1500) GeV/c by $(10 \pm 2)\%$.

This data is consistent with an optical model picture of a gray absorbing disc of constant opacity, (σ_{el}/σ_T flat), and with the radius increasing with energy.

Since, in this picture σ_T, b, σ_{el}, σ_{inel} are all proportional to R^2 --the radius of the proton--then R should have increased by ~ 5%. If we interpret the deep dip in pp scattering as a diffraction minimum, then this is a measure of the radius of the scatterer: the dip should move in t-value--it seems that it probably does.

If one looks at the rate of change of R with energy--the σ_T, b are consistent with (ln s) growth in R^2, while the diffraction minimum seems consistent with moving to smaller t-values like $\sqrt{\ln s}$--again things make a consistent picture.

If one looks more carefully, this picture requires more fine structure. The small t p-p scattering implies that the proton has an outer edge or "ring," and that this is expanding quite rapidly with energy, ~ ln s. The large t scattering gives us information on the "core" of the proton, which even at ISR energies is not black but ~ 92% of its unitary value, and quite constant with energy.

- The real part crossing zero and going positive for momentum ~ 300 GeV/c is consistent with the measured rise in σ_T up through 2000 GeV/c. Careful measurements of the real part in pp scattering up through 2000 GeV/c would give useful constraints on the behaviour of $\sigma_T(pp)$ up to $(10^4 - 10^5)$ GeV.

The elastic scattering data shows that diffractive scattering is sharply peaked and well parametrized as $as(d\sigma/dt) \sim Ae^{-bt}$ for small t. Good indications for steepening of the $d\sigma/dt$ as a function of t are observed for $\pi^{\pm}p$ and K^-p in the (5-40) GeV/c energy region, which is parametrized as two exponentials or one exponential with quadratic t dependence. A straightforward explanation for the steepening of $d\sigma/dt$ for these processes is found in a peripheral Regge exchange contribution to the t-channel amplitude. However, similar behaviour is observed in p-p scattering at 2000 GeV/c where Regge is not expected to play a great role. This may imply a peripheral piece to the Pomeron.

The slope parameter, b, is steeper in $\bar{X}p$ scattering than for Xp scattering. This fact, together with the observed equality of the integrated cross-sections (i.e. $\sigma_{el}(\bar{X}p) = \sigma_{el}(Xp)$), implies a cross-over of the differential cross-sections. This cross-over phenomena has been studied for $p <$ 15 GeV/c and no s-dependence found. It will be interesting to follow these studies at NAL.

The slopes of the scattering distribution are observed to change with energy--the K^+p and pp systems exhibiting strong shrinkage, the $\pi^{\pm}p$ and K^-p slopes being essentially flat, and the $\bar{p}p$ scattering showing an anti-shrinkage behaviour. This shrinkage phenomena observed in K^+p and pp scattering, is normally understood as being due to the slope of the Pomeron trajectory--the effect is masked by Regge effects in the other elastic reactions.

- Pomeranchuck theorem predicts asymptotically $\sigma_T(AB) = \sigma_T(\bar{A}B)$, while Martin has shown that $\sigma_{el}(AB)$ should equal $\sigma_{el}(\bar{A}B)$, and the slope, $b(AB)=b(\bar{A}B)$.

The data is consistent with these predictions; the differences in particle and antiparticle total cross-section are falling like $s^{-0.5}$, while elastic cross-sections are equal even at low energy. The slopes of the differential cross-section seem consistent with an asymptotic common value for particle and antiparticle scattering.

III. PHOTOPRODUCTION OF VECTOR MESONS

In this section we review data on the photoproduction of vector mesons, (ρ, ω, ϕ).[19] Within the spirit of the Vector Dominance Model, (VDM), these processes should be more properly considered with the elastic scattering reactions (see Fig. 52), than considered together with the other exclusive inelastic diffraction processes. The early experimental results on rho production with polarized photons strongly supported that picture.[70] (See Fig. 53 where the $\rho \to 2\pi$ decay distributions show that the ρ has fully taken over the polarization of the photon, and that no longitudinal ρ decays are observed.) We shall summarize the data on cross-sections and angular distributions.

1. Cross-Sections

The cross-section for $\gamma p \to \rho^0 p$ is shown in Fig. 54, for photon energies between (1-15) GeV/c. The cross-section falls rapidly as the energy increases up to ~ 5 GeV, above which it has a rather slow energy dependence. For comparison the energy dependence of the πN elastic cross-section is shown; it exhibits an s-dependence very similar to $\gamma p \to \rho p$.

The ω photoproduction cross-section is shown in Fig. 55 from threshold to 9 GeV. Again one sees a very rapid fall-off of the cross-section at low energies, flattening out around 5 GeV. The SLAC-Berkeley-Tufts experiment[71] using a polarized photon beam (obtained by backscattering a laser beam on the primary SLAC electron beam) is able to separate the cross-section into the natural parity and unnatural parity t-channel contributions at 2.8, 4.7 and 9.3 GeV.† The unnatural parity cross-section falls very rapidly, in good agreement with the one-pion exchange model, and is essentially zero by 9 GeV. The natural parity exchange cross-section, which one would hope to be diffraction dominated, falls off like the ρ photoproduction data shown above, and hence like the πN elastic data.

†For natural parity exchange the pions from ρ decay, emerge preferentially in the plane of the photon polarization, while for unnatural parity exchange they emerge perpendicular to it.

The ϕ photoproduction cross-section is plotted in Fig. 56. The energy dependence for this process is either flat or rising very slowly--however, it is a small cross-section reaction and not very well measured.

2. Differential Cross-Sections

The differential cross-section for $\gamma p \to \rho^0 p$ is shown in Figs. 57 and 58, for two representative experiments. In Fig. 57, the $d\sigma/dt$ is displayed for a hydrogen bubble chamber experiment at 9.3 GeV,[71] while Fig. 58 shows the cross-section from (9-16) GeV from a wire spark chamber experiment.[72]

The differential cross-section have been fit to the form

$$\frac{d\sigma}{dt} = \left.\frac{d\sigma}{dt}\right|_{t=0} \cdot e^{-bt}$$

and the resulting slopes plotted as a function of photon energy, in Fig. 59 (from an analysis by Moffeit[19] of all the $\gamma p \to \rho^0 p$ data that could be analyzed in a standard way). Note the different t-ranges used in obtaining these slopes--especially remembering what we learned of the t-dependent shrinkage behaviour in elastic scattering in Chapter II. Figure 60 shows $d\sigma/dt$ (from the SBT bubble chamber, and from the SLAC wire chamber) for the small t region, where the two experiments overlap--the agreement is good. However, the slopes obtained from the two experiments are different by ~ 2.5 units when the full t-range of the HBC data is used--perhaps an indication of the same steepening of the $d\sigma/dt$ slope as t becomes smaller, that we observed for πN scattering in the (5-40) GeV/c energy region. The slopes show very little energy variation (at most 1 - 1/2 units for 3-16 GeV), and are consistent with the s-dependence of the average of the $\pi^{\pm} p$ elastic scattering slopes in the region $0.1 < t < .4$ GeV^2, shown as a dashed line in Fig. 59.

We might ask again, why a diffractive process should show so little shrinkage. Chadwick et al.[73] have performed an analysis on the energy dependence of the slope for $\gamma p \to \rho^0 p$, similar to that of Davier[53] described in the πN elastic section in Chapter II. They assume a central Pomeron and a peripheral f^0-meson exchange dominate the reaction, à la Davier, and hence uncover shrinkage in the Pomeron contribution to $\gamma p \to \rho^0 p$, which behaves just like the "K^+p Pomeron" and the "Davier πN Pomeron." Their fits to the data, and the results of the Pomeron and f^0 slopes as a function of energy are shown in Fig. 61.

The ω differential cross-sections, from the S-B-T collaboration,[71] are given in Fig. 62. The slope of the cross-section is reported as ~ 7 GeV^{-2} and quite independent of energy. (An analysis of the natural parity contribution results in the same conclusion, but with somewhat larger errors.)

The study of the photoproduction of the ϕ meson has been an interesting area. Since the ϕ meson decouples from other mesons we do not expect any strong t-channel amplitudes other than the Pomeron. Thus, the study of ϕ photoproduction should be an ideal laboratory to learn of the Pomeron's properties--much better in principle than the study of K^+p or pp where the Pomeron dominance depends on cancellations of Regge amplitudes through exchange degeneracy.

The ϕ is observed to be strongly produced coherently from complex nuclear targets, and the t-channel amplitude in $\gamma p \to \phi p$ is essentially purely natural parity (from asymmetry studies with polarized photons). These observations support the Pomeron exchange dominance hypothesis.[74]

The data on the differential cross-section is rather sparse and quite inconclusive as to whether there is any shrinkage of the forward slope, never mind any quantitative measure of how much it shrinks! Figure 63 shows the S-B-T bubble chamber data for (2.8 + 4.7) GeV and 9.3 GeV, respectively, and compared to neighboring energy data from other groups, there is clearly very little energy dependence at large t, and unfortunately, essentially no data

in the small t region, where we have seen from elastic scattering the strongest s-dependence may be expected. Figure 64 shows another summary of the data on $d\sigma/dt$ ($\gamma p \to \phi p$), displaying new data from a Bonn group measuring at 2 GeV. A summary[12,19] of the slopes from these experiments is given in Fig. 65.

A recent SLAC experiment[75] measures the s-dependence of the ϕ cross-section at a fixed $t = 0.6$ GeV^2. Their data, together with the 2 GeV Bonn point[76] are shown in Fig. 66. Clearly the data support the "no shrinkage" conclusion, and more quantitatively, when fit to a slope with the usual energy dependence

$$b = b_0 + 2\alpha' \ln s$$

find $\alpha' = 0.14 \pm 0.09$ GeV^{-2}. This is in strong contrast to the strong energy dependence found in p-p scattering at the same energies--see Fig. 67.

It is interesting to note that the analysis of $\pi^- p$ and $K^- p$ elastic scattering reported in Chapter II and summarized in Table XIII, gave $\alpha'_\pi = 0.04 \pm 0.03$ GeV^{-2} and $\alpha'_K = 0.00 \pm 0.04$ GeV^{-2} for t-values around 0.4 GeV^2. Further, at high energies the pp scattering distributions for approximately the same t-values show no energy dependence. The fits to the ISR p-p scattering data in this t range yield $\alpha' = 0.10 \pm 0.06$. These results are remarkably in agreement with the ϕ photoproduction data. This prompts the question of whether the s-dependence observed in p-p scattering in the (5-20) GeV/c region (see Fig. 67) is due to Regge, or other non-diffractive effects and that the bare Pomeron properties are seen in the very high energy scattering. Then $\gamma \to \phi$ may indeed be exhibiting Pomeron like behaviour at low energies, as expected.

An interesting explanation of the lack of shrinkage is offered in the two component model of the Pomeron described by Kane. He introduces a central contribution (the conventional Pomeron) and an additional peripheral piece which accounts for the small t shrinkage observed in high energy p-p scattering. These two contributions would then lead to the picture shown in Fig. 68. The central contribution has a slow (or zero) energy dependence while the peripheral contribution shrinks quite rapidly (like $\ln s$). The peripheral contribution behaves in t-space like a Bessel function and has its first zero around $t \sim 0.2$ GeV^2. As s increases there is a region in t around ~ 0.5 GeV^2 where the peripheral contributions cross for different s values, and which therefore displays no (or very weak) energy dependence. This model allows an explanation of the small t shrinkage, and the lack of it in the large (~ 0.4-0.8 GeV^2) region.

It would be nice to have some good data at small t, to see if the $\gamma \to \phi$ cross-section does indeed shrink for small t.

IV. DIFFRACTION DISSOCIATION (EXCLUSIVE INELASTIC DIFFRACTION)

1. Introduction

By Diffraction Dissociation we mean the non-elastic processes in which either the incident particle or the target particle is excited to a low mass system. These excitations seems to be strongest near to quasi-two-body thresholds and it is far from clear whether they are due to resonant behavior or to some kinematic effect which enhances the scattering cross-section. There is a growing amount of evidence that at least the dominant effect is due to kinematices. For the moment we will not try to answer the question of whether these inelastic processes are kinematic in origin or are caused by resonance production, but merely observe that production of "the A region" by π's, or "the Q region" by K's, or "excited N^*'s" by N's are well defined, clearly indentifiable reactions characterized by natural parity exchange in the t-channel and dominated by a single well defined spin-parity state in the meson decay system. The cross-sections for these processes are slowly varying in energy, and the differential cross-sections are sharply forward peaked. The general trends of these data are very similar to the elastic scattering and photoproduction of vector meson processes reviewed in Chapters II and III.

2. Baryons

A. $N \to N\pi$ Dissociation

We first examine the process $N \to N\pi$, from studies of

$$\pi N \to \pi\pi N \qquad \text{(IV.1)}$$

$$NN \to NN\pi \qquad \text{(IV.2)}$$

The cross-section for reaction (IV.1) is shown in Fig. 69. The data are consistent with a fall-off of $p^{-1.6}$, which is typical of meson exchange processes. A CERN bubble chamber collaboration[77] studied the charge related reactions

$$\pi^+ p \to \pi^+ p \pi^0$$
$$\pi^+ \pi^+ n$$

at 4, 5, 8, and 16 GeV/c, and were able to isolate the isospin of the $(N\pi)$ system. The cross-sections for the separate isospin states are shown in Fig. 70, where the $I = 1/2$ cross-section falls slowly like $p^{-.6}$ while the $I = 3/2$ part falls like meson exchange, $p^{-1.6}$. The mass spectra for the separate I-spin states are shown in Fig. 71, for the 8 and 16 GeV/c data. The $I = 3/2$ plots show strong production of Δ, and the relative cross-section at the two energies reflects the steep energy dependence of this amplitude. The $I = 1/2$ mass spectrum shows a smooth low mass enhancement, extending from below 1300 MeV to about 1700 MeV, but exhibiting no structure at the masses of known nuclear isobars. The cross-section for this low mass bump changes very little between 8 and 16 GeV/c (at 16 GeV/c it is ~ 1/2 of the $\pi\pi N$ cross-section).

The same group[77] studied both $\pi^+ p \to \pi\pi N$ and $\pi^- p \to \pi\pi N$ at 16 GeV/c and were able to isolate the isospin exchanged in the scattering process (i.e. find I_t). The various matrix elements are shown in Fig. 72--where all moments are seen to be small except the $M_1^{3/2}$ and $M_0^{1/2}$ (i.e. isovector production of the $I = 3/2$ πN system, and isoscalar exchange leading to the $I = 1/2$ πN system).

A similar analysis has been performed in the reaction (IV.2) by another bubble chamber collaboration (Bonn-Hamburg-Munich),[78] working at 12 and 24 GeV/c. The two cross-sections are shown in Fig. 73, and the $M_{0,1}^{1/2}$ and $M_1^{3/2}$ mass spectra are shown in Fig. 74 and 75 respectively. The same features of smooth, energy independent, low mass enhancement for the diffraction process, and the fast falling Δ production for the exchange process.

This feature of low mass enhancement is confirmed in studies of $n \to p\pi^-$; Fig. 76 shows the results of an experiment using a deuteron beam at 25 GeV/c to study "stripped" neutron interactions in a hydrogen bubble chamber,[74] especially the reaction--

$$np \to p\pi^- p \quad \text{at} \quad 12.5 \text{ GeV/c};$$

Fig. 77 shows the $p\pi^-$ mass plot for the reaction

$$K^+d \to K^+p\pi^-(p_s) \quad \text{at} \quad 12 \text{ GeV/c}.^{80}$$

The differential cross-section for $n \to p\pi^-$ in this latter experiment is shown in Fig. 78 for three mass cuts. The cross-section has a very steep slope for the lowest masses, flattening out as the mass of $(p\pi^-)$ increases. The values of the slopes found are :--

$$1.1 < M(p\pi) < 1.3 , \qquad b = 14 \quad \text{GeV}^{-2}$$
$$1.3 < M(p\pi) < 1.5 , \qquad b = 8 \quad \text{GeV}^{-2}$$
$$1.5 < M(p\pi) < 1.7 , \qquad b = 3.5 \quad \text{GeV}^{-2}$$

Similiar behaviour is observed in the other studies. This variation of the slope of the differential cross-section with the mass of the produced system is displayed in Fig. 79 (for the "deuteron stripping" experiment[79]) and summarized in Table XV (from the Bonn-Hamburg-Munich experiment[78]). One sees for the diffractive channel (or rather, the $I_t = 0$, $I_{p\pi} = 1/2$ channel), that the slope at threshold is very high ($\sim 2 \times$ elastic slope, $b \sim 15$ GeV^{-2}), and falls very fast with increasing mass up to $M^2 \sim 2$ GeV^2, at which point the slope is $\sim$ 4-5 GeV^{-2} and remains rather constant for further increases in mass. The $I_t = 3/2$ slopes are not very dependent on mass, and both $I_t = 1/2$, 3/2 slopes do not change much with energy.

Fig. 80 shows the mass plot of $(p\pi^-)$ system produced by a high energy neutron beam from the AGS (mean momentum $\sim$ 23 GeV/c) on complex nuclear targets.[81] The same smooth low mass enhancement is observed, produced with a characteristically coherent differential cross-section from the various nuclear targets.

The decay angular distribution of the $p\pi^-$ system has been studied in each of these experiments. Typical results are shown in Fig. 81, where the Jackson angular distribution is shown for various t and M cuts. The data indicate that for small mass and small t, the angular distributions are rather isotropic, but as mass or t increase, the distributions become more complex, reflecting an increasing complexity of the spin structure in the $(p\pi^-)$ system.

As one selects larger t, the mass distributions begin to reflect the presence of the well-known isobars--$D_{13}(1520)$, $F_{15}(1688)$--and the angular distributions may be well explained in terms of the known angular momentum of the expected resonances. However, the increased complexity <u>in the small</u> t <u>data</u> does not accompany any clear mass structure--the mass distributions remain smooth, just moving to larger mean masses as the t-cut is increased.

To summarize the data on $N \to N\pi$:

- a large cross-section for producing $I = 1/2$ $(N\pi)$ state is observed,
- the process involves $I = 0$ exchange,
- has a very slow energy dependence of the cross-section,
- has a very steep $d\sigma/dt$ for low masses; the slope decreases as the mass increases,
- no resonance structure is observed for the small t, steep $d\sigma/dt$, low mass component; as one looks at larger and larger t's, the expected resonances are observed,
- this low mass process is observed to proceed coherently on nucleii.

B. $N \to N\pi\pi$ dissociation

Another strong diffractive channel for nucleons is observed to be $N \to (N\pi\pi)$. Typical mass plots are shown in Figs. 82 and 83, where a large low mass enhancement is seen, with some structure at ~ 1450 MeV and 1700 MeV. These are associated with the production of resonances, but only represent a fraction of the total low mass system.

The cross-section for the production of this $N\pi\pi$ system is observed to be almost flat as a function of energy, falling like $p^{-0.4}$.

The differential cross-section is strongly peaked, and displays the same feature discussed above in $N\pi$--i.e. as the mass of the $(N\pi\pi)$ system increases from threshold the $d\sigma/dt$ become flatter. This is summarized in Table XVI. It is interesting to note that the $(N\pi\pi)$ and $(N\pi)$ slopes seem to agree well, for a given mass of the baryon system. These studies also show that if the mass spectrum is examined for larger t values (e.g. $t > 0.1$ GeV^2), the resonance signals become much clearer (just as discussed above for the $N\pi$ system).

Finally, there is strong evidence for the coherent production of this low mass $(N\pi\pi)$ system. We will be hearing more of this in Gobbi's talk[82] at the Conference.

In summary, the $N \to N\pi$, $N\pi\pi$ reactions display the same properties.

C. Nucleon dissociation at high energies

Having reviewed the data on diffraction dissociation of the nucleon at (5-30) GeV/c energies, let us look at a few results from NAL. Several experiments have found evidence for the reaction

$$pp \to pN^*$$

at high energies, where N^* refers to the phenomena we have been discussing above.

First, the NAL US-USSR collaboration[83] using the solid state detectors to identify the recoil proton from 'beam-hydrogen gas jet' collisions to study elastic scattering, have also measured the missing mass spectrum. This belongs more properly in the chapter on Inclusive Diffraction, but it is interesting to refer to it here, since it measures in the low mass region and ties on nicely to what we have been discussing with respect to $d\sigma/dt$, and s-dependence of the cross-sections. (We will discuss this experiment again in the inclusive section, to review some recent results on $dp \to dX$ at 100-400 GeV/c.)

The missing mass spectrum is shown in Fig. 84. The resolution in missing mass is dominated by the angular resolution of the detectors and is typically $\pm$ 100 MeV in the resonance region. The four histograms are the MM^2 distributions measured by four different counters placed at different angles (near 90°) to the incident proton beam, for an incident beam momentum of 200 GeV/c. Data were taken at 175, 200 and 400 GeV/c. The arrows mark the positions of known isobars which could be diffractively excited N(1450), N(1560), N(1688), ... A preliminary analysis of the data indicate the cross section in the resonance region is independent of energy. In particular, the cross-section in the 1400 MeV region exhibits a very steep t dependence, e^{-15t}, and that the NAL cross-section is the same to within 20% as that measured at 20 GeV/c.

Further, the $\pi^- p$[84] and pp[85] bubble chamber experiments at 205 GeV/c have both studied the exclusive four body reactions--

$$\pi^- p \to \pi^- \pi^+ \pi^- p$$

$$pp \to p\pi^+ \pi^- p$$

and have isolated fairly clean samples. The mass distribution of the $(p\pi^+\pi^-)$ system is shown in Figs. 85 and 86 for these two processes, and clearly shows the low mass enhancement, with some evidence of N(1450) and N(1700) structure. The proton experiment also shows the strong $\Delta\pi$ component of this low mass region, just as is observed at low energies.

Figure 87 shows the topological cross-section for inelastic 2 prong reactions, from pp interactions from (12-300) GeV/c. The cross-section is falling with increasing energy. Also shown as a shaded band, is the estimate of the diffractive component in the two prong topology from model fits to the high energy multiplicity distributions and topological cross-sections (Miettinen,[86] Harari[87]). The isospin analysis from the Bonn-Hamburg-Munich group provides the cross-section for the $(I_t = 0, I(N\pi) = 1/2)$ process up through 24 GeV/c, at which point the 2-body diffractive cross-section is about equal to the predicted total 2 prong cross-section. However, if the $N \to N\pi$ cross-section keeps falling like $p^{-0.5}$--which it does up to 24 GeV/c--then would predict ~ 0.9 mb at 200 GeB/c, or about half the total topological limit.

(Another rumor from London-SFM group studied $pp \to p\pi\pi^+$ at $\sqrt{s} = 53$ GeV, and see cross-section falling off like $p^{-0.5}$ up to 1500 GeV/c. They also see many of the same features discussed in this section for $N \to N\pi$ diffraction--

- slow σ variation (mentioned already),
- sharp $d\sigma/dt$, being very steep for small mass, and flattening out as $M(n\pi^+)$ increases,
- $\cos\theta_J^{pn} > 0$--smooth structureless low mass bump, where θ_J is the Jackson polar angle,
- $\cos\theta_J^{pn} < 0$--begin to see resonance structure in the mass plot.)

D. Hyperon dissociation

Before leaving the baryon system, we report the observation of a threshold enhancement in the reaction

$$\Sigma^- + Z \to \Lambda\pi^- + Z$$

at 24.6 GeV/c from the NAL-Yale hyperon beam group at BNL.[88] The mass spectrum for the $\Lambda\pi^-$ system is shown in Fig. 88--it is interesting to see the same smooth, structureless, low-mass enhancement in this process as we have been discussing for nucleon diffraction.

3. Meson Dissociation

A. Cross-sections

For meson diffraction dissociation we have two basic processes to be studied

$$\pi N \to (3\pi)N \qquad \text{(IV.3)}$$

$$KN \to (K\pi\pi)N \qquad \text{(IV.4)}$$

The cross-section for reaction (IV.3) is displayed in Fig. 89 from 2 GeV/c up through 205 GeV/c. The energy dependence of this data is very mild above 5 GeV/c, with a distinct flattening off at high energy. The high energy data is dominated by the $N \to (N\pi\pi)$ diffraction discussed above in Chapter IV.2 and the meson dissociation $\pi \to 3\pi$. Typical mass distributions for the 3π system are shown in Fig. 82 for $\pi^\pm p$ at 16 GeV/c[77] (from a bubble chamber study), Fig. 90 for $\pi^- p$ at 40 GeV/c (from a spark chamber spectrometer experiment at Serpukov),[89] and in Fig. 91 for $\pi^- p$ at 205 GeV/c (from a HBC experiment at NAL).[84] All spectra show a rapid rise of the cross-section to form a broad peak called the A_1, followed by a shoulder at around 1700 MeV called the A_3. For data cut on larger t values (e.g. $t > 0.2$ GeV^2 another structure becomes very prominent--the A_2 meson. The A_1 and A_2 regions are observed to decay into $\rho\pi$, while the A_3 region is associated with the $f\pi$ system. (There is evidence from the Washington-Berkeley $\pi^- d$ HBC experiment[90] at 15 GeV/c of a $g\pi$ enhancement around 1900 MeV, which they name the A_4.)

The s- and t-dependencies of the reaction (IV.3) have been studied as a function of (3π) mass, and the results are summarized in Table XVII. The energy dependence of the cross-section as a function of mass, evaluated above 11 GeV/c, are given in the last column of the table, and indicate rather flat energy dependence--being very similar to the elastic cross-section energy dependence for small 3π masses, $(\sigma \propto p^{-.3})$ and falling just slightly faster for masses in the neighborhood of 2000 MeV, $(\sigma \propto p^{-.5})$.

The energy dependence of the three enhancement regions--the A_1, A_2 and A_3 regions--is given in Figs. 92, 93 and 94 from (5-40) GeV/c. Fitting the cross-section to $\sigma \propto p^{-n}$ they find

$$n(A_1) = 0.40 \pm 0.06$$

$$n(A_2)^{\text{natural}} = 0.51 \pm 0.05$$

$$n(A_2)^{\text{unnatural}} = 2.1 \pm 0.2$$

$$n(A_3) = 0.57 \pm 0.2$$

It is interesting that the A_2 cross-section (supposedly mainly vector and tensor exchange) has such a similar energy dependence to the A_1 and A_3 regions (which are thought to be produced by Pomeron exchange).

The fact that the A_1 energy dependence in Table XVII, and in the above fit are somewhat different implies that the $\sigma(A_1)$ flattens out at higher energies. This is confirmed by the 205 GeV/c $\pi^- p$ experiment, which reports a cross-section for $0.8 < M(3\pi) < 1.2$ GeV as 160 ± 40 μb. At the foot of Table XVII this is compared to the 25 and 40 GeV/c cross-sections.

The energy dependence of reaction IV.4 is shown in Fig. 95 for $K^0 p \to Q^0 p$.† The cross-section for Q^0 production is quite flat from 5 GeV/c-12 GeV/c,[91] having a momentum dependence of $p^{-.59\pm.16}$. Complementary data on Q^+ production is shown in Fig. 96 from the "world K^+ collaboration."[92] The energy dependence from (2.5-12.7) GeV/c is studied as a function of the $(K\pi\pi)$ mass, in 40 MeV steps from 1200-1500 MeV. All six mass intervals exhibit the same behaviour, with an average momentum dependence of $p^{-.60\pm.05}$. The $K^- \to Q^-$ data (for $M_Q < 1.5$ GeV), show a somewhat flatter dependence, with $\sigma \propto p^{-.3\pm.09}$.

†The $K_S^0\pi^+\pi^- p$ reaction cross-section rises rapidly from threshold, and then falls off as $p_{lab}^{-1.2}$. This is somewhat more rapid than the equivalent reactions for K^+p and K^-p, and is presumably due to the fact that the $K^\pm p$ reactions have substantial contributions from proton diffraction, $(p \to p\pi\pi)$, at the nucleon vertex, while such a process is forbidden in the K_L^0 experiment due to the change of C at the $K_L^0 \to K_S^0$ vertex.

A CERN bubble chamber collaboration (CERN-Brussels-Krakow)[93] have performed an isospin decomposition for the diffractive processes $K \to K\pi\pi$, $N \to N\pi\pi$ at 5.0 and 8.2 GeV/c. The various charge states for $(K^*\pi)$ and $(\Delta\pi)$ were selected from the following reactions--

$$K^+p \to K^+\pi^-\pi^+p$$

$$K^0\pi^+\pi^0p$$

$$K^0\pi^+\pi^+n \ .$$

They find that the $K\pi\pi$ system is dominated by the $I = 1/2$ amplitude, which is constant in magnitude between 5 and 8.2 GeV/c, as one would expect for a diffractive process. The mass distributions for the $I = 1/2$ and $3/2$ amplitudes are shown in Fig. 97. The low mass $K\pi\pi$ enhancement--the Q region--is clearly seen in the $I = 1/2$ data, and quite absent for the $I = 3/2$ data.

So we see that the cross-sections for these diffractive processes are quite flat as a function of energy, and that they fall off only slightly faster than the elastic scattering cross-sections themselves. The data exhibit another feature of the elastic cross-sections discussed in Chapter II--namely, the equality of particle and antiparticle cross-sections. Cornille and Martin[40] predicted that asymptotically this ratio should be 1, even for inelastic diffractive two body processes.

In Fig. 98 the ratio of the cross-section for $K^0p \to Q^0p$ and $\bar{K}^0p \to \bar{Q}^0p$ is shown as a function of momentum from (2-12) GeV/c. The equal components of K^0 and $\bar{K}^0$ in the K_L^0 beam, for this experiment, allow a comparison of these cross-sections to be made over the entire energy region free from problems of relative normalization between the strangeness states. The ratio is consistent with a constant value of 0.99 ± 0.08 over the entire energy region. Similar studies have been performed around 16 GeV/c for $\pi^\pm \to (3\pi)^\pm$ in HBC[94] and wire spark chamber[95] experiments, with the result,

$$R = \frac{\pi^- p \to (3\pi)^- p}{\pi^+ p \to (3\pi)\, p} = 1.00 \pm 0.07,\ 0.94 \pm 0.12 \ .$$

B. Differential cross-sections

The (3π) data angular distributions have been analyzed to determine the spin-parity amplitudes involved in the reaction. These analyses are summarized below.

The A_1 region--(the 1100 MeV enhancement)--is associated with $J^P = 1^+$, s-wave $\rho\pi$ decay. (See the amplitudes in Fig. 99.) The phase of this wave shows very little energy dependence with respect to any of the background waves, and gives no indication of behaving like a Breit-Wigner resonance amplitude--see Fig. 99. The differential cross-section for this region (selected in mass and only taking the 1^+ s-wave part of the data), is plotted in Fig. 100--where the slope is shown as $e^{-(6.7\pm.8)t}$.

The A_2 region is identified as $J^P = 2^+$, with a d-wave $\rho\pi$ decay mode. The amplitude and phase of this wave is shown in Fig. 101, where the 2^+ phase with respect to background is seen to move rapidly through the resonance mass, as would be expected from a Breit-Wigner amplitude. The mass and width is found to be $M = (1315 \pm 5)$ MeV, and $\Gamma = (115 \pm 15)$ MeV. The differential cross-section, for the 2^+ amplitude in the A_2 region, is shown in Fig. 102, and exhibits a dip in the forward direction. The data are fit with $d\sigma/dt \propto |t|\, e^{-bt}$ with $b = (8.6 \pm 1.2)\ \mathrm{GeV}^{-2}$.

A similar analysis in the A_3 region is shown in Fig. 103, where the enhancement is assigned $J^P = 2^-$, and associated with an s-wave $f\pi$ system. The mass and width are found to be $M = (1650 \pm 30)$ MeV, and $\Gamma = (300 \pm 50)$ MeV. Again the phase shows no mass dependence, like the $A_1(1^+)$ wave, and not like the resonant 2^+ A_2 wave. (Purdue[97] has reported finding a phase variation in $\pi^+p \to (3\pi)^+p$ in contradiction to the above result from CERN-IHEP (Ascoli) analysis[96] of $\pi^-p \to (3\pi)^-p$; however, Morrison[18] has reported that his CERN HBC collaboration in analysing both $\pi^\pm p \to (3\pi)^\pm p$ at 16 GeV/c see no phase movement for the 2^-A_3 phase; same for LBL.[98]) The production distribution for the 2^- events in the A_3 region, and the background events, are shown in Fig. 104, where the enhancement data is shown to be more peripheral ($b = 9.9 \pm 1.2\ \mathrm{GeV}^{-2}$) than the background $b = (6.4 \pm 0.6\ \mathrm{GeV}^{-2})$.

The slope of the differential cross-sections, and the dependence on $M(3\pi)$ has been mentioned above (Table XVII). Further data on this effect are given in Table XVIII for both π^+p and π^-p at 16 GeV/c. It is interesting to note that there is not much sign of shrinkage for these slopes--see Table XIX --the small t, small (3π) mass slope being the same at 16 GeV/c and at 40 GeV/c

Similar analysis of the decay distribution have been performed for the $(K\pi\pi)$ system--a typical set of amplitudes is shown in Fig. 105, where the dominant wave for the Q region is seen to be the $J^P = 1^+$, and where the phase of this wave moves only slowly with energy--like the A_1.

Clear evidence for the low mass diffractive enhancement in $K \to K\pi\pi$ is given in Fig. 106 from a 14.3 GeV/c K^-p bubble chamber experiment.[99] The mass of $(K^*\pi)$ is plotted against the mass of $K\pi$ system. Two points are of interest--a) the $K\pi\pi$ system couples strongly to $K^*(890)\pi$ and $K^*(1420)\pi$, b) the low mass enhancement is quite absent in the charge exchange reaction $K^- \to (\bar{K}^0\pi^+\pi^-)$, where only the 3-body decay of the K^*_{1420} is observed. (The $K^*(1420)$ is the SU(3) partner of the A_2 resonance discussed above in the 3π data.)

The differential cross-section from this same data is shown in Fig. 107 where the distinct difference in slopes between the diffractive Q-region and the Regge exchange $K^*(1400)$ region is demonstrated.

The dependence of the slope of the differential cross-section on the mass of the $(K\pi\pi)$ system is shown in Fig. 108 for $K^0 \to Q^0$ and $\bar{K}^0 \to \bar{Q}^0$, and in Fig. 109 for $K^- \to Q^-$. The slope values for the $S = -1$ data are in good agreement. This effect is very similar to that observed in the $\pi \to 3\pi$ and $N \to N\pi$, $N\pi\pi$ data discussed above.

Finally, the inelastic diffractive reactions exhibit the cross-over phenomenon in the differential cross-sections. We discussed this effect in Chapter II--it is caused by a C odd Regge exchange contribution to the process

in addition to the dominant Pomeron exchange. This additional contribution gives rise to different slopes in the differential cross-section for particle and for antiparticle scattering. An example of this phenomenon is shown in Fig. 110 where 13 GeV/c K^+p and K^-p elastic scattering data from the SLAC wire spark chamber spectrometer experiment are displayed.[58] A clear cross-over of the two cross-sections is seen for momentum transfers, $t \sim 0.2$ GeV^2. Similar behaviour is observed for $\pi^\pm p \to (3\pi)^\pm p$ around 16 GeV/c from the SLAC wire chamber experiment[95] and from the CERN 16 GeV/c $\pi^\pm p$ HBC experiment[94] --see Fig. 111. Again, for KN reactions we show the cross-over for K^0 in Fig. 112, and for $K^\pm p$ in Fig. 113. The diffraction dissociation data is much less precise than the elastic data, but the positions of the cross-overs are consistent with the corresponding elastic reaction cross-over. Also, the change in slope between the particle and the antiparticle process is similar in elastic and in the inelastic reactions--see Table XX.

4. Summary

- In summary, we have seen that $N \to N\pi$, $N\pi\pi$; $\pi \to 3\pi$; $K \to K\pi\pi$ reactions exhibit large low mass enhancements. The cross-sections for the various processes are listed in Table XXI and compared to the elastic reactions. The inelastic processes seem to fall off a little faster than the corresponding elastic reaction. It is not clear whether this difference is important (or real), or just due to the technical difficulty of determining an "A" cross-section above background (or even knowing what an A cross-section really means!). However, it is clear that these inelastic diffractive processes are much more like the elastic reactions than the typical Regge exchange processes where cross-sections fall off like $p^{-1.5}$ or faster.
- The angular distributions for these inelastic diffractive processes are sharply peaked with slopes about twice the slope for elastic scattering for threshold mass of the diffracted system, and flattening out to a slope value of about half the elastic scattering slope for masses about 1000 MeV above threshold. The slopes for some specific mass states are summarized in Table XXII. It appears that the same regularities found among the elastic slopes are to be seen in the inelastic slopes.
- These reactions all exhibit the cross-over phenomenon in $d\sigma/dt$ very similar to the elastic reactions and also have $\sigma(Ap) = \sigma(\bar{A}p)$.

It is interesting to see how similar the elastic and inelastic diffractive processes are with respect to total cross-section and differential cross-section behavior.

5. Final Comment on Exclusive Diffraction Dissociation

I have isolated this section from the general conclusions since it is a mixture of personal opinion and a summary of known facts. However, it may be helpful, if only to stimulate argument and catalyze you to forming your own "picture."

We know that the pion, kaon and proton all produce low mass enhancements which have the following features:

- mainly $I = 1/2$;
- mainly $I = 0$ in t-channel;
- smooth, featureless bump, rising quickly from threshold;
- cross-section only weakly s-dependent;
- can be produced coherently on nuclear targets;
- no sign of well-known resonance structure;
- sharp $d\sigma/dt$ with slope about twice the elastic slope at threshold, falling as the mass of the produced system increases, until about 1 GeV above threshold it is rather flat, with slope about half the elastic slope;

- we also know that for larger momentum transfers, one sees signs of resonance structure in the mass distribution, and in the decay angular distributions. The πd, Kd experiments see clear signs of $D_{13}(1500)$, $F_{15}(1700)$ when making larger t cuts--they also see zero phase difference between these two production amplitudes, as would be expected from diffraction production;
- there is also good evidence that for the small t smooth enhancement, the angular momentum in the decay is simplest (i.e. s-wave) for threshold masses and becomes more complex as the mass increases;
- if cuts are made on the decay angle of the $N\pi$ decay system for $N \to N\pi$, for $\cos\theta_J^{NN} > 0$, see only the smooth bump, but for $\cos\theta_J^{NN} < 0$, begin to see the usual resonances being produced;
- we have neglected the process $\gamma p \to \pi^+\pi^- p$ in our discussion of inelastic diffraction, because $\gamma \to \rho$ was dealt with separately. However, here we have a reaction in which accidentally the "elastic" processes take place above the threshold for inelastic diffraction. However, there is a well-known diffractive non-resonant background below the rho meson, well described by the Drell diagram. It displays all the features we have learned of the other low mass diffractive processes. (An example of the dependence of slope on mass is shown in Fig. 114.)

So we suggest that we have the following situation--there are two components in diffractive reactions: 1) a dissociation of the incoming beam, and 2) diffractive production of resonances. The cross-section for dissociation starts at quasi-two-body threshold and rises rapidly followed by a long tail as a function of mass. (See Fig. 115.)

Following Lubbatti and Moriyasu[100] we may think of the dissociation as the coupling of the incident (or target) particle to a whole string of virtual states

$$\pi \to \pi\rho, \quad \pi f, \quad --$$

$$N \to N\pi, \quad \Delta\pi, \quad --$$

and in the collision, it picks up some longitudinal momentum to make up the change in mass.

With these excited states populated, the particle has an effective size larger than its "ground state" size. As the mass of the excited state increases, the momentum distribution associated with the excited state increases and there will be a reciprocal decrease in the size of the hadron (from the uncertainty principle). A reasonable measure of the mean square momentum might be $(M^2 - M_i^2)$ where M is the mass of the excited state and M_i is the mass of the constituents. Then $R^2 \sim (M^2 - M_i^2)^{-1}$.

Lubbatti and Moriyasu have plotted the known slopes we have discussed above in this form--see Fig. 116--and find that the data seem to fall on universal curves.

There are deviations at the known resonances, and we might think of their being different anyway--that is, as having a size of their own.

With respect to the second component--we know in $N \to N\pi$, $\Delta\pi$ where we have a solid knowledge of the N^* spectrum from s-channel studies, that there are resonances produced diffractively. Given the success of the whole structure of SU(3) and quark model classification schemes, it seems highly probable that A_1 and Q mesons do exist. The problem of experimentally isolating this signal from the dissociation background is very difficult (like sorting out ρ photoproduction from Drell background if the non-resonant $\pi\pi$ background was the dominant amplitude).

Perhaps with Omega, MPS and LASS systems coming into operation,[101] we will be able to see independent signs of these states from analysis of reactions like

$$\pi p \to Q\Lambda$$

$$Kp \to A_1\Lambda$$

or as SPEAR II, DORIS and PEP come along, in production experiments like

$$e^+e^- \to \pi A_1$$
$$\bar{K}Q \ .$$

Perhaps one of the more direct ways we will find out what is going on in diffractive processes will be from analysis of the Caltech-LBL-SLAC $\pi^{\pm}p$ experiment[102] with a hybrid spark chamber--bubble chamber set-up. They are studying the baryon break-up for processes where a fast beam-like pion leaves the bubble chamber and triggers the downstream system--in particular they will have good information on $p \to p\pi\pi$. See Fig. 117. An analysis of the $N\pi\pi$ amplitudes obtained from this t-channel experiment and their comparison with the detailed amplitudes for the same state obtained in the SLAC-LBL s-channel phase shift analysis[103] should allow great insight into diffraction processes and perhaps throw some light on this two component hypothesis.

We will return to a discussion of the dynamics of diffraction at the end of the section on Inclusive Scattering.

V. RULES OF DIFFRACTION

1. Introduction

As we discussed in the Introduction we have very little theoretical understanding of the diffractive process, and our main guide as to whether a process is diffractive or not, is often how well it obeys our list of phenomenological "rules."[12]

These rules are listed below.

a) energy independent cross sections (to factors of $\ln s$)

b) sharp forward peak in $d\sigma/dt$

c) particle cross sections equal to antiparticle cross sections

d) factorization

e) mainly imaginary amplitude

f) exchange processes characterized by the quantum numbers of the vacuum in the t-channel (i.e. $I = 0$, $C = +1$). Also, the change in parity in the scattering process follows the natural spin-parity series $(-1)^J$ or $P_f = P_i \cdot (-1)^{\Delta J}$, where ΔJ is spin change.

g) the spin structure in the scattering is s-channel helicity conserving (SCHC).

In Chapters II, III and IV we have seen points (a), (b), (c), (e) all borne out by the data. We now examine the other points.

2. Quantum Numbers in Pomeron Exchange (point f) above):

The "rules" for diffractive processes said that, from a t-channel point of view, the Pomeron would carry the quantum numbers of the vacuum (i.e. $C = +1$, $I = 0$ exchange). How well does the data support this assertion?

(a) I = 0 character:

We know from amplitude analysis of elastic scattering[104] (which we suppose to be mainly diffractive) that the dominant amplitude is the non-flip isoscalar t-channel amplitude. We also know that processes involving a change of charge in the scattering (and hence $I \neq 0$ in the t-channel) have cross sections which fall quite rapidly with energy and do not have the character of diffractive reactions.

Below we consider two examples of $I = 0$ character of diffractive processes from inelastic scattering:

The reactions $\pi^- p \to N\pi\pi$ were studied at 16 GeV/c by the ABBCCHW collaboration[105] and the $N\pi$ mass spectra are shown for the various possible charge combinations (see Fig. 119). The $(N\pi)^+$ combinations (i.e., $p\pi^0$, $n\pi^+$) which can be produced with no charge exchange and hence accessible from $I = 0$ exchange in the t-channel, exhibit a large low mass enhancement in the (1400-1700) MeV range. This enhancement has an almost energy-independent cross section and is related to the diffractive excitation of N^*'s. The $(N\pi)^-$ combinations (i.e. $p\pi^-$, and $n\pi^-$ respectively), which cannot be reached with $I = 0$ exchange, have no low mass diffractive enhancement.

A similar example[105] is shown in Fig. 120 where 10 GeV/c $K^- p \to \bar{K}(N\pi\pi)$ reactions have been studied. Again the $(N\pi\pi)^+$ mass spectrum shows a low mass enhancement associated with the diffractive production of excited N^*, while the $(N\pi\pi)^0$ spectrum shows no such structure.

Thus we see quite clearly that the observation of diffractive phenomena is closely connected with $I = 0$ in the t-channel.

(b) C = +1 character:

To examine this property we compare the $K^- p \to K^-(p\pi\pi)$ data already displayed in Fig. 120 above, to data on $K_L^0 p \to K_S^0(p\pi\pi)$ of approximately the same energy, from the SLAC bubble chamber experiment.[91] The data is selected to isolate out the peripheral $p \to p\pi\pi$ reaction mechanism and the resulting $(p\pi\pi)$ mass spectrum is shown in Fig. 121. The low mass diffractive enhancement in the K^- reaction is not observed in the K_L^0 data, although these two reactions are so very similar. The difference lies in that the K_L^0 and K_S^0 are eigenstates of C with opposite sign and therefore the t-channel exchange in the K_L^0 reaction must carry $C = -1$. This may be viewed as evidence of the $C = +1$ character of diffractive processes.

(c) Spin-parity changes:

As per our "rules" we expect that diffraction will proceed most simply with no change of spin or parity for either the target or projectile particles, but that if there is a change it will follow the natural spin-parity sequence, viz.

$$P_f = P_i(-1)^{\Delta J}$$

This may be thought of as picking up angular momentum in the "Pomeron-diffracting-particle" scattering.

This is a phenomenological rule,[106] whose main claim to correctness is that there are no known diffractive processes which violate it. There exists rigorous proof for the spin zero case, but there is no general theorem for the more interesting spin situations.

The main evidence for justification for this "rule" is negative in nature (as mentioned above); however, one recent confirmation of the rule comes from a bubble chamber experiment on $\pi^- n \to \pi^- \pi^- p$ at 11.7 GeV/c by the Riverside group.[107] They observe diffractive production of N^*'s decaying into $p\pi^-$ final state. The analysis is free from complications of π-π resonance effects and deals with the well understood two-body elastic decay of the N^*; (i.e. it avoids, the complication of previous studies which have observed diffractive production of $N^* \to N\pi\pi$, and then applied assumptions about two-body decays into $\Delta\pi$ final states). The Riverside results show production of P_{11}, D_{13}, F_{15} N^*'s (i.e. the correct parity sequence for the "rule") and no sign of the D_{15} state. Further, the production phase between the D_{13} and

F_{15} processes was found to be 0^0, in agreement with the hypothesis of diffractive production.

On the negative side, three threats to the rule existed over the last few years--vector K^* production by K's, tensor A_2 production by π's and axial vector B production by γ's. Each of these processes violates the natural spin-parity sequence, but claims of "diffraction-like" properties had been made. We discuss them at more length below:

(i) $K^*(890)$ production:

At the Oxford conference[108] data on $K^-p \to K^{*-}_{890}p$ was reported implying that the cross section, which had been falling like p_{lab}^{-2} up to 8 GeV/c actually flattened out to an almost constant value for higher energies. This was taken as evidence of Pomeron contribution to K^* production.

However, new data up to 16 GeV/c is now available,[109] and the cross section seems to fall like p_{lab}^{-1} beyond 8 GeV/c and the production and decay characteristics are in good agreement with isoscalar, natural spin parity exchange. Presumably ω^0 exchange takes over from π exchange at the higher energies, and this "threat" to the parity rule has disappeared.

(ii) A_2 production:

There have been suggestions for some time that perhaps the A_2 meson is produced via Pomeron exchange, thus violating our simple rule of natural spin-parity excitation in diffraction processes. Kruse et al.[96] have submitted an analysis of A_2 production in bubble chamber data in the energy range from (5-25) GeV/c. There is also a paper from Ascoli et al.[96] on A_1, A_2, and A_3 production at 40 GeV/c. The facts are summarized below:

i. The A_2 cross-section falls off as $p^{-0.8\pm0.08}$ in the (5-25) GeV/c range;

ii. The relative energy dependence of A_1, A_2, and A_3 between 25 GeV/c and 40 GeV/c are essentially the same;

iii. The natural parity exchange contribution to A_2 production falls off as $p^{-0.57\pm0.09}$;

iv. The t-channel exchange in A_2 production is mainly isoscalar;

v. The s-dependence of the cross section implies an effective intercept, $\alpha_{eff}(0) \sim 0.7$;

vi. An analysis of the shrinkage of the $J^P = 2^+ A_2$ differential cross-section yields an $\alpha_{eff}(0) \sim 0.8$.

The energy dependence and α_{eff} values quoted above are more in agreement with a strong Pomeron contribution to A_2 production than the vector, and tensor meson contributions one expected. However, we must understand at least one other fact before throwing away our current picture of Pomeron processes--the energy dependence for the A_2 cross section as measured in the $K\bar{K}$ decay mode seems to be faster than $p_{lab}^{-1.0}$. This is a clean reaction in which to study A_2 production with very little background, and the observed momentum dependence is very much in agreement with that expected for meson exchange in the t-channel. Several experiments should be reporting new cross-sections for $A_2 \to K\bar{K}$ within the near future, and we wait impatiently for their results. Another indication that A_2 is not diffractively produced comes from the differential cross-section shown in Chapter IV--it was well fit with $d\sigma/dt \propto |t|e^{-bt}$, with a forward turnover.

(iii) Photoproduction of the B-Meson:

Finally, in this section on "bogey-men," we deal with the photoproduction of the B-meson.[110] The reaction $\gamma p \to Bp$ violates the natural spin-parity series expected in diffractive processes, yet the B signal is observed with the same strength at 2.8, 4.7, and 9.3 GeV. The energy independent cross-section has encouraged speculation as to the validity of the simple rules on spin couplings for the Pomeron.

However, the statistics on these observations are rather limited, each energy point having a cross section of (1.0 ± 0.4) μb. One could accommodate quite a variety of energy dependences within these measurements. It is an important reaction and to be followed with interest, but the present

results are not strong enough to call our ideas on Pomeron coupling to question--at least not yet. (This effect is most probably the diffractive production of a ρ' meson (coupling strongly to $\pi\omega$), with a mass close to the B-meson.

For the moment the rule seems to be obeyed.

(d) G-parity:

It is interesting to observe that G-parity is strongly recognized in diffractive processes. For π reactions, one sees strong diffractive cross-section for 3π, 5π but not 4π final states. This observation is confirmed in coherent processes with π on nuclear targets.

Perhaps an even more interesting example is the relative coherent production of A_1 and B systems in π^- experiment at 11.7 GeV/c in a heavy liquid bubble chamber.[111] These two systems have the same $J^P = 1^+$, but A_1 has $G = -1$ like the π, while the B Has $G = +1$. The experiment observes strong coherent A_1 production, with a cross-section of $\approx$ 2mb/nucleon, while there is no evidence of B- production with an upper limit of < 30 μb/nucleon.

The Pomeron seems to care about G-parity.

3. Spin Structure in Diffractive Processes (point g) above):

Our "rules" assert that diffractive processes are s-channel helicity conserving (SCHC). This hypothesis derives from the early experimental work of the SLAC-Berkeley-Tufts group[112] on their study of ρ^0-meson photoproduction with the polarized photon beam, at 4.7 GeV. They found that the diffractively produced ρ^0-meson maintained the photon helicity in the s-channel. Gilman and co-workers[113] then hypothesized that all diffractive processes conserved s-channel helicity and showed that the understanding of the πN scattering amplitudes at that time was consistent with that assumption.

New data on $\gamma p \to \rho^0 p$ at 9 GeV from the SBT group,[71] and measurements of the R, A parameters in πN and NN scattering by a Saclay group[114] confirm, in the main, the early conclusions. The new experiments are discussed in more detail below.

It is interesting to note that if s-channel helicity conservation really holds, then the old "lore" that the Pomeron behaves in the energy dependence of cross-sections like a particle of spin 1, but has the couplings of a particle of spin 0, cannot be true. SCHC requires quite specific couplings in the t-channel--in general helicities will flip and there must be quite specific relations between the t-channel spin flip and non-flip couplings.

The density matrix elements from the new SBT experiment at 9.3 GeV[71] are shown in Fig. 122. They confirm the dominant behaviour as being SCHC and show that it holds out to larger t than previously observed. However, the ρ_{10} element (i.e. SCH flip) is quite definitely non-zero as is shown more clearly in Fig. 123. It was confirmed that the effect was real and not due to a scanning bias, by rotating the plane of polarization of the incident photons with respect to the bubble chamber camera axis; no change in the result was found. Further, they find when isolating the separate exchange amplitudes that the effect belongs to the natural-parity exchange amplitude. It is also found that the magnitude of the effect does not change rapidly with energy. All these factors imply that there is a small helicity flip amplitude, of about 15% the SCHC amplitude, which may be associated with Pomeron exchange. Results of their analysis of the helicity flip contribution are given in Table XXIII.

The Saclay experiment[114] studied $\pi^{\pm}p$ scattering at 6, 16 GeV/c from a polarized proton target. The recoil proton was detected in a spark chamber polarimeter. The spin rotation parameters R and A were measured. Actually good measurements of R were obtained and A found from the relation $P^2 + A^2 + R^2 = 1$, using the existing precision measurements of the polarization (P), in p-p scattering. Rough measurements of A were taken to resolve the

quadratic ambiguity in the above equation. They find A to be close to +1 as expected from SCHC.

At 6 GeV/c, an amplitude analysis[104] was performed using all the available data on total and elastic πN cross sections, differential cross-sections, charge exchange cross sections, polarization for elastic and charge exchange reactions and their own new R and A parameters. Results for the isoscalar flip and non-flip amplitudes are shown in Fig. 124. The flip amplitudes has a kinematic zero in the forward direction but is certainly nonzero at larger t. For the region of $t > 0.2$ GeV^2, they find the ratio of flip to non-flip amplitude to be 0.17 ± 0.2 at 6 GeV/c.

There is not sufficient πN scattering data to perform a complete amplitude analysis at 16 GeV/c but a reasonable choice of solutions gives the flip to non-flip ratio, at 16 GeV/c, to be 0.14 ± 0.03. That is, the πN data shows that SCHC is the dominant amplitude but that again a small (~ 15%) helicity flip amplitude is present and that it is isoscalar and weakly s-dependent--presumably associated with the Pomeron. It is important to remember that although the $\gamma \to \rho$ experiment and this πN experiment are both measuring 15% helicity flip amplitudes which are isoscalar and weakly energy dependent, they are <u>not</u> measuring the same thing; the photon experiment measures the spin structure at the meson vertex while the πN experiment measures the spin structure at the nucleon vertex.

The Saclay group also measured R, A parameters for p-p scattering at 6, 16 GeV/c,[114] and found the parameters consistent with dominance of SCHC. There is not sufficient data to perform an amplitude analysis for p-p scattering, but it is clear that this data would be consistent with a small helicity flip amplitude.

Finally, we must consider the spin structure for inelastic processes. Table XXIV summarizes recent work on this question.[12,14] It shows that the vector meson photoproduction behaves very much like elastic scattering--SCHC in the main, but with a small helicity violating amplitude. The various diffraction dissociation processes do <u>not</u> conserve s-channel helicity. Most of them are much more close to t-channel helicity conservation, but in general do <u>not</u> conserve that either. Thus, although their inelastic processes looked very much like elastic reactions from the point of view of cross section and differential cross sections, they have bery different spin structure. This difference may be due to the fact that these processes are perhaps not really particle production, but kinematic enhancements, or alternatively, may be due to the spin change that occurs in these inelastic processes and the complex t-channel spin structure of the Pomeron.

4. Factorization

If we really believed that diffraction reactions are dominated by the exchange of a simple Pomeron, we should be able to factorize, or separate, the different vertices appearing in these processes. It is interesting to test how well the cross-section data supports the factorization hypothesis. Below we examine several tests:

(1) A simple factorization test involving the isospin of the breakup of the low mass $N\pi$ enhancement may be performed, checking whether $\frac{\sigma(pp \to p(n\pi^+))}{\sigma(pp \to p(p\pi^0))}$ is actually 2. Studies on 19 GeV/c pp interaction report[115] this ratio as 1.9 ± 0.2.

(2) Another test is found in the three sets of reactions, shown in Fig. 125, involving the excitation of the proton to $N^*(1688)$ in π^-, K^- or p^- interactions. These cross-sections should have the same ratio with respect to elastic scattering, independent of the nature of the incident particle. The results of the test are shown in Fig. 126 where the ratio $\left[\frac{Ap \to AN^*(1688)}{Ap \to Ap}\right]$ is plotted against momentum transfer, for two energies--8 and 16 GeV/c. Factorization is observed to hold within 20% and even works well as a function of momentum transfer at least out to $t \sim 0.2$ GeV^2.[105]

(3) Consider the processes illustrated in Fig. 127, with elastic pion

and proton scattering at the upper vertex, and proton diffraction into proton plus zero, one, two or three pions at the bottom vertex. The ratio between cross-sections for reactions involving the upper two vertex processes should be the same, independent of which of the four bottom vertices they interact. That is, $R_1 = \sigma(\pi p \to \pi p)/\sigma(pp \to pp)$ should equal $R_2 = \sigma(\pi p \to \pi(p\pi^0))/\sigma(pp \to p(p\pi^0))$ etc.

The cross-section for each of the bottom vertices was isolated in 16 GeV/c $\pi^- p$ and 19 GeV/c pp bubble chamber experiments,[116] using the Van Hove Longitudinal Phase Space analysis[117] to isolate the diffractive components. The results are given in Table XXV. Good agreement is observed.

(4) Another interesting test of factorization in diffractive processes is shown schematically in Fig. 128. If the Pomeron contribution were well behaved and factorizable, we would expect the ratio of cross-sections for each of the upper vertex processes--$\gamma \to \rho^0$, $\pi \to \pi$, $p \to p$--being joined in turn to both of the bottom vertex process--$p \to p$, $p \to (p\pi^+\pi^-)$--to be equal. That is, we would expect to find

$$R_1 = \frac{\sigma(\gamma p \to \rho p)}{\sigma(\gamma p \to \rho p \pi\pi)}, \qquad R_2 = \frac{\sigma(pp \to pp)}{\sigma(pp \to pp\pi\pi)}, \qquad R_3 = \frac{\sigma(\pi p \to \pi p)}{\sigma(\pi p \to \pi p \pi\pi)}$$

The diffractive component for these reactions was again isolated using the LPS analysis.

The experimental values[118] for R_1, R_2 and R_3 are given in Table XXVI for three different energy regions. The agreement is surprisingly good.

(5) We may use the results of the various isospin amplitude studies discussed in Chapter IV to further test factorization. The integral over t of the isoscalar t-channel amplitude leading to the $I = 1/2$ final state $(N\pi)$ system is calculated for incident π, K and proton collision, $(\int |M_0^{1/2}|^2\, dt)$. The ratio $R(H) = [\sigma(Hp \to H(N\pi))/\sigma(Hp \to Hp)]$, where $H = \pi$, K, p. We expect $R(\pi) = R(K) = R(p)$ if the factorization holds. The results are given in Table XXVII, where again quite remarkable agreement is found.[119] (The agreement is even better when one notes that the 24 GeV/c pp point includes some I = 1 t-channel exchange contribution since no pn data were available to do the t-channel I-spin decomposition.)

(6) An interesting factorization test has been made possible by the study of the four body exclusive reaction in pp and $\pi^- p$ collisions at 205 GeV/c.[120] The diffraction of the target proton into a $(p\pi^+\pi^-)$ system has been isolated in each experiment--see Fig. 129.

The cross-section for $\pi p \to \pi(p\pi\pi)$, $\sigma_1 = (180 \pm 36)\ \mu b$

The cross-section for $pp \to p(p\pi\pi)$, $\sigma_2 = (370 \pm {}^{40}_{140})\ \mu b$

The cross-section for $\pi^- p$ reaction is $\alpha g^2_{\pi\pi\mathbb{P}} * g^2_{pN^*\mathbb{P}}$

The cross-section for the pp reaction is $\alpha g^2_{pp\mathbb{P}} \times g^2_{pN^*\mathbb{P}}$

Now

$$\begin{aligned}
\frac{\sigma_1}{\sigma_2} &= g^2_{\pi\pi\mathbb{P}} \cdot g^2_{pN^*\mathbb{P}} / g^2_{pp\mathbb{P}} \cdot g^2_{pN^*\mathbb{P}} \\
&= g^2_{\pi\pi\mathbb{P}} / g^2_{pp\mathbb{P}} \\
&= \frac{\sigma(\pi p \to \pi p)}{\sigma(pp \to pp)}, \text{ or } \frac{\sigma_{el}(\pi p)}{\sigma_{el}(pp)} \\
&= \frac{3.0 \pm 0.3}{6.8 \pm 0.2} \\
&= 0.44 \pm 0.05
\end{aligned}$$

while σ_1/σ_2 are measured to be ~ 0.5.

(7) A final example comes from a study of inclusive scattering at 25 and 40 GeV/c at Serpukov. The CERN-IHEP collaboration[89] measured

$$\pi^- p \to X^- p$$

$$K^- p \to X^- p$$

with their missing mass spectrometer. The cross-sections $(d^2\sigma/dt\, dx)$ are shown in Fig. 130 where the dashed line represents the pion data, and the circles represent the kaon cross-sections. If factorization holds, we expect

$$\left[\frac{\frac{d\sigma}{dx}(\pi^- p)}{\frac{d\sigma}{dx}(K^- p)}\right] = \left[\frac{\sigma_T^{inel}(\pi^- p)}{\sigma_T^{inel}(K^- p)}\right] .$$

Integrating over t, they find the left-hand side of this equation to be 1.20 ± 0.09, while the right-hand side is 1.18 ± 0.04.

To summarize, we have learned that factorization in diffractive processes--elastic, diffraction dissociation and leading particle inclusive reactions--is surprisingly good, holding to ~ 20%.

It would be interesting to have data on an even wider variety of processes, and more importantly, with rather better accuracy. At intermediate energies, we know that non-leading effects such as cuts, are quite important and at high energies the observations of rising cross sections have killed any idea of simple single pole dominance of the interactions--thus, we expect breaking of factorization to occur, maybe even at the 10% level. It would be very interesting to have experiments of sufficient accuracy to observe this breaking, and perhaps even see some s-dependence to the breaking of factorization.

VI. INCLUSIVE SCATTERING

1. High Energy Inclusive pp Scattering

A. Missing mass distribution

It has been known for some time that inclusive pp scattering at high energy is characterized by a large quasi-elastic peak which is associated with the diffractive production of high mass states[121] (see Fig. 131). It is interesting to study the energy, mass and momentum transfer dependencies of this process to learn more of the dynamics of diffraction. A considerable amount of new data on this topic has become available recently.

In Fig. 132 the missing mass plots from the NAL bubble chamber experiments [122] are given. The HBC pictures are scanned for slow protons which can be identified by their ionization; for those events so identified the missing mass is then calculated. The lowest masses are seen to be produced with almost constant cross-section between 100 and 400 GeV/c.[123] For larger masses the cross-section is falling almost linearly with energy. An alternative display is in terms of the Feynman x variable, the fractional longitudinal momentum, p_L/p_{max} or $x = (1 - M^2/s)$. The 100 and 400 GeV/c data are shown, plotted as a function of x, in Fig. 133.[124] From this plot, we see the cross-section for $x \approx 1$ increasing with energy, as it must if the cross section at small masses is constant in energy. This region is presumably the classical diffraction dissociation region. For $x \sim .6$ to $.8$ region the cross-section scales in x. The intermediate region of $x \sim .95$ seems to show some energy dependence indicating that the quasi-elastic peak does not quite scale in x at these energies.

The 200 GeV/c missing mass data[125] is shown again in Fig. 134 and broken down in the various topological contributions in Fig. 135. The cross-section in the small mass region (up to masses of 4 GeV), is seen to fall off like M^{-2} and the diffraction peak is developed by peaks in each of the lower

topological cross-sections. It also appears that the mean mass of the diffractive peak increases as the topology or multiplicity, n, increases. The total cross-section of this low mass diffraction peak is estimated at ~ 6 mb, independent of energy.

The same behavior is observed at ISR energies where the CHLM[122,126] and ACGHT[127] groups have demonstrated the existence of the low mass diffractive enhancement. In Fig. 136 the missing mass distribution from the two arm spectrometer ACGHT experiment, is shown. They are able to make a rough multiplicity assignment, using a scintillation counter hodoscope round the aperture of each spectrometer. There is clear evidence for the increase of mean mass in the diffractive peak as the multiplicity increases.

It is interesting to note that the term "low mass" peak is purely relative and that these diffractive peaks include masses up to 7 GeV.

Figure 13 shows the missing mass spectrum from the Columbia-Stony Brook experiment at NAL.[128] This experiment uses polyethelene and carbon targets and detects the recoil proton in an array of solid state counters. The normalization is effected by counting the d, T, He^3 and He^4 production in both the polyethelene and carbon targets simultaneously with the protons, thus allowing for a very accurate subtraction and hence reliable proton cross-sections.[129] The resolution in missing mass squared is very good, being of order of 1 GeV^2 near $x \sim 1$, whereas the CHLM group has $\delta M^2 \sim 9$ GeV^2 and the ACGHT group has $\delta M^2 \sim 20$ GeV^2. Their missing mass plot shows a very sharp peak with some structure around 3-4 GeV^2 and becoming essentially flat for masses above 16 GeV^2.

This missing mass distribution is quite different from the ISR data. Part of this difference is due to the missing mass resolution of the different experiments, but part is also due to the fact the measurements have been made at <u>different</u> t values; the ISR experiment has typically $t \sim 0.8$ GeV^2, while the NAL experiment had $t \sim 0.06$ GeV^2. We will come back to this point later.

B. <u>Energy dependence, or scaling</u>

The energy dependence of the quasi-elastic pp scattering has been studied at NAL from (50-400) GeV/c by Rutgers-Imperial College group.[139] The recoil proton is detected and identified in a scintillation counter telescope with a total absorption counter. The momentum of the proton is determined from time of flight measurements over 186 cm flight path.

The invariant cross-section, for four different t values, is given in Fig. 138 for five energies between 50 and 400 GeV. For x values close to 0.8 there is very little energy dependence, while for x values around 0.9, close to the quasi-elastic peak, quite considerable variation is observed through this energy region. In Fig. 139 the invariant cross-section is plotted against $s^{-1/2}$ for the four t ranges measured, for x values of 0.83 and 0.91. Again substantial s-dependence is clearly visible.

They fit the data to the form

$$s \frac{d^2\sigma}{dt\, dM^2} = A(x)\, e^{b(x)t} [1 + B(X)\, s^{-1/2}] \; .$$

This form represents the data well, with b being essentially independent of x and having a value of ~ 6 GeV^{-2}. The best fit to the data gave

$x = 0.83$	$A = 71 \pm 7$ mb/GeV^2	$B = 1.9 \pm .7$ GeV
$x = 0.91$	$A = 66 \pm 3$ mb/GeV^2	$B = 4.3 \pm .4$ GeV

Through the NAL energy range, there is ~ 20% change in the cross-section for x values near unity, and the fits to the data imply that the variation remaining in the cross-section through the ISR energy range will be less than 10%.

The fall-off in the cross-section for $x \sim .95$ as measured in the four NAL HBC experiments and discussed above in Fig. 133 is also compatible with this s-dependence.

The experimental results from the CHLM group[126] at the ISR are given in Fig. 140 and show that in this region the cross-section is observed to scale to within 10%. Note that both the ISR and NAL experiments are performed at intermediate t values.

In summary then, the invariant cross-section $s(d^2\sigma/dt\, dM^2)$ is observed to be almost energy independent for x values of order 0.8 from 50 GeV/c through 2500 GeV/c; for $x \sim 0.9$ the cross-section is observed to have a component with $s^{-1/2}$ dependence which amounts to a 20% effect through the NAL energy region ((50-400) GeV/c), but which is $< 10\%$ effect through the ISR range (200-2500 GeV/c).

C. Momentum transfer dependence

The momentum transfer dependence of the production of the diffraction peak has been studied at NAL by the bubble chamber experiments[122] and the Columbia-Stony Brook experiment[128] and at the ISR by the CHLM[126] and ACGHT[127] groups.

The t-dependence as a function of the missing mass squared, $(x = 1 - M^2/s)$, is shown in Fig. 141 from the 200 GeV/c HBC experiment.[125] For small masses, the slope of the inelastic diffractive scattering is close to, but a little less than, the elastic scattering slope. As the masses increase, the slope decreases, until one reaches masses corresponding to an x value of ~ 0.9. For masses beyond that there seems to be only a weak M dependence left.

In Fig. 142 the t-dependence of the diffraction peak is shown, from experiments at NAL and the ISR. The cross-section is exponential but with at least two slopes. The dashed line shows a fit which behaves like e^{-7t} at small t and e^{-4t} at large t.

D. Aside on the missing mass distribution

From the above discussion it seems plausible that the differential cross-section, $d\sigma/dt$, is mass dependent. The diffraction peak studied in Fig. 142 contains a wide range of masses (up to $M^2 \sim 50$ GeV^2) and the two exponential shape of that $d\sigma/dt$ may be just a reflection of this mass dependence. Such a dependence would imply that the shape of the missing mass distribution would change for different t values, and perhaps account for some of the difference between the ISR[126,127] and NAL (Columbia-Stony Brook)[128] mass plots (Fig. 137). Indeed, if one assigns an e^{-7t} dependence to the peak masses, and an e^{-4t} dependence to the large mass region $(M^2 \sim 20$ GeV$^2)$ then quantitative agreement between the measured missing mass distributions results.

Further, if such a dependence exists then the peak to shoulder ratio (low mass to high mass ratio) should be seen to change for measurements at different t. In Figs. 143, 144 the missing mass squared distribution as measured by the CHLM group[126] at the ISR, for four different t ranges is shown. Clear evidence of this effect is observed.

Thus it seems that in fact the different missing mass distributions are in good agreement--there exist three separate regions in the mass plot:

1. The threshold region $(x \approx 1.0)$ where the cross-section, $d^2\sigma/dt\, dx$, is growing linearly with s (i.e., scaling in M^2) and has a steep t dependence;

2. The diffraction peak $(1.0 > x > .9)$ where the cross-section is nearly constant in s--some 20% variation in the NAL region (50-400) GeV/c and less than 10% variation at the ISR (200-2500) GeV/c, and with a $d\sigma/dt$ that depends on M^2, becoming flatter as M^2 increases.

3. Multiparticle production region $(.8 < x < .2)$, where the cross-section seems essentially independent of s and where $d\sigma/dt$ is rather flat $(\sim e^{-4t})$ and varying slowly with s and M^2.

The mass dependence in the diffraction peak appears to be compatible with a $1/M^2$ fall off:

1. The 200 GeV/c HBC expt. (Ref. 125)(see Fig. 134).
2. ACGHT group[127] at ISR find $d\sigma/dM^2 \propto (M^{-2})^{1.15\pm.1}$.
3. CHLM group[126] at ISR find $d\sigma/dM^2 \propto (M^{-2})^{0.98\pm.1}$.
4. Columbia-Stony Brook[128] at NAL find $d\sigma/dM^2$ compatible with M^{-2}.

E. Back to momentum transfer studies

Above we had shown that there was evidence that the slope of the differential cross-section for the diffraction peak became flatter as the diffracted mass increased, and that the $d\sigma/dt$ for the whole peak (averaging over all masses) was exponential but with at least two slopes.

In Fig. 145 the s-dependence of the $d\sigma/dt$ is studied. The data comes from the Rutgers-Imperial College group[130] at NAL. For $x = 0.87$ the differential cross-section, $d\sigma/dt$, is shown for $s = 108$ and $752\ \mathrm{GeV}^2$. Essentially no energy dependence is observed, at these x values.

The $d\sigma/dt$ as measured by the Columbia-Stony Brook group[128] at NAL, for missing mass squared around $40\ \mathrm{GeV}^2$ is shown in Fig. 146, together with data from Rutgers-Imperial College[130] and from the CHLM[126] group at ISR. Good agreement is observed between the measurements. A flattening of the cross-section is observed for small t values ($t < .2\ \mathrm{GeV}^2$). For smaller masses, this effect becomes a turnover in the very forward direction, with a maximum to the cross-section at $t \sim 0.1\ \mathrm{GeV}^2$, as shown in Fig. 147. Again the data comes from the Columbia-Stony Brook experiment.[128] Corrected data from a previous run by the same group at 200 GeV/c is also shown.[131]

Similar behaviour is observed in some preliminary data from the (100 + 400) GeV/c HBC experiments at NAL.[132] In Figs. 148 and 149 the p_T^2 distribution is shown for small masses and large masses respectively. The low mass spectrum shows the same tendency to a forward turnover as the NAL counter experiment, whereas the distribution for large missing masses seems to be quite linear.

2. Pion Diffraction Scattering

The first systematic study of high energy pion-proton collisions has been reported by the Berkeley-NAL collaboration working on a 205 GeV/c $\pi^- p$ exposure of the 30 NAL HBC.[133,134] Their results are briefly outlined below.

They have analyzed the exclusive process

$$\pi^- p \to \pi^- \pi^+ \pi^- p$$

and claim to have an event sample with less than 25% background. They see strong evidence of the pion diffracting into 3π, and the target proton diffracting into a $(p\pi^+\pi^-)$ system, Figs. 150 and 151. The cross-section for both these processes is estimated to be 1.5 mb.

In addition, the diffraction of a $\pi \to \pi^*$, shown schematically in Fig. 152, has been studied using the same technique as in the p-p HBC experiments. The pictures were scanned for events in which a slow recoil proton could be identified by ionization. This selection works well for proton momenta up to 1.5 GeV/c. The missing mass distribution obtained from these events is shown in Fig. 153. A low mass peak is observed, extending out to $M^2 \sim 20\ \mathrm{GeV}^2$, associated with the diffractive excitation of the incoming pion.

The mass dependence is shown in Fig. 154, where over a substantial range of masses, the data are consistent with a $1/M^2$ fall-off.

In Fig. 155, the composition of this low mass diffractive peak by topology is presented and as in the p-p studies, one remarks that only the lowest multiplicities contribute to the peak. Again, the central value moves to larger masses as the multiplicity increases. The mean multiplicity in the diffraction peak is about half that of the overall multiplicity ($\langle n_d \rangle^{\mathrm{charged}} \sim 4$, $\langle n_{\mathrm{all}} \rangle^{\mathrm{charged}} \sim 8$) and increases with M^2.

The differential cross-section, $d\sigma/dt$, is shown by topology in Fig. 156 and for two different mass regions in Fig. 157. No turnover in the forward direction is observed, nor any sizable mass dependence of the slope.

In all these features the pion diffraction data show the same trends as the proton diffraction. Below, the invariant cross sections for $\pi^- p \to X^- p$ and $pp \to pX^+$ are shown with a relative normalization set to compare the x distributions. (See Fig. 158.) Again good agreement is observed.

3. Multiplicity in Inclusive Collisions

As we noted earlier when discussing the structure of the low mass diffractive peak, these events are characterized by a smaller multiplicity, n, than the average. The NAL HBC experiments[122] report that the mean diffractive multiplicity, $\langle n_d \rangle$ is about half the total mean multiplicity, i.e.

$$\langle n_d \rangle \sim \frac{1}{2} \langle n_{all} \rangle .$$

A similar study in the $\pi^- p$ 205 GeV/c bubble chamber experiment[84] finds the diffractive multiplicity, $\langle n_d \rangle = 3.8 \pm 0.2$ while the total multiplicity, $\langle n_{all} \rangle = 8.02 \pm 0.12$. The frequency distribution is given in Fig. 159. At higher energies, the CHIM group[126] at the ISR report that the mean charged multiplicity $\langle n \rangle$ is 2.8 ± 0.5 for $x > 0.99$, while for $x \sim 0.8$ it is measured as $\langle n \rangle \sim 6.7 \pm 1.0$, in good agreement with the NAL bubble chamber conclusions.

Both the p-p and $\pi^- p$ HBC groups at NAL have found an interesting correlation of multiplicity with energy available in the collision. They plot the multiplicity for diffractive reactions as a function of the mass squared of the excited system.

They then plot the mean charged multiplicity of the entire reaction as a function of available energy in the center of mass, and find both sets of data fall on the same curve. The results of the pion experiments are shown below in Fig. 161, but the proton experiments at 100, 200 and 300 GeV/c exhibit the same behaviour.

The implication is that the final multiplicity depends on the available energy but not on whether the initial state consisted of a pion and a proton or of a Pomeron and a proton.

While discussing the multiplicity distributions it is interesting to ask what we can learn of diffraction from their frequency distributions and their correlations.

For diffractive processes, we expect to find a large rapidity gap between the leading particle and the fragments of the excited system. (Rapidity is defined as $y = \frac{1}{2} \ln[(E + p_L)/(E - p_L)]$, where p_L is the longitudinal momentum of a particle and E is its energy. A useful variable which approximates y for high energy particles is $\eta = \ln \tan(\theta/2)$.) We would therefore expect to find a "typical diffraction event" to look like Fig. 162 in rapidity space. Other inelastic processes are expected to be characterized by rather uniform distributions in rapidity space, on average. (See Fig. 163.)

The Pisa-Stony Brook collaboration[135] at the ISR have studied the multiplicity distribution in high energy p-p collisions, measuring the angles of each charged particle in a large counter hodoscope system. They group their events according to the total multiplicity, and characterize each event by two numbers--they throw away the largest and smallest rapidities and then calculate a mean rapidity and a dispersion, for what is left. The two variables are defined

$$\bar{\eta} = \Sigma(\eta_i/n-2)$$

$$\delta(\bar{\eta}) = \sqrt{\frac{\Sigma(\eta_i - \bar{\eta})^2}{n - 3}}$$

We may now expect diffractive events to show large values of $\bar{\eta}$ and a small dispersion about this $\bar{\eta}$, while the other inelastic events should be centered at $\bar{\eta} = 0$, and with a broad dispersion.

A three-dimensional presentation of the same plot for two energies--the lowest and highest available at the ISR, $\sqrt{s} = 23.6$ and 62.8 GeV--is shown in Fig. 165. Again, for low multiplicities the diffractive component ($\bar{\eta}$

large and sharp), is seen to dominate over the non-diffractive component. As the multiplicity increases their roles reverse. As one goes to larger energies the diffractive component contributes to larger and larger multiplicities. These correlations plots are a nice independent verification of the presence of the diffractive component and a confirmation of several of the properties derived from the magnetic spectrometer studies.

4. Single Particle Inclusive Studies at Low Energy (i.e. $p < 50$ GeV/c)

The high energy single particle inclusive experiments from NAL and the ISR have shown the existence of a large energy independent cross-section for the production of a low mass peak. This process is assumed to be diffractive excitation of the target or projectile and has a cross-section almost equal to the elastic scattering cross-section (i.e. $\sigma_{diff} \sim 6$ mb). At the highest energies this low mass peak in fact includes rather large masses--up to 7 GeV. The low mass peak is made up mainly from low multiplicity channels and the mean charged multiplicity is about half the total charge multiplicity for all processes. The multiplicity increases with increasing mass. For recent review see Ref. (13).

It is interesting to see what can be learned in similar processes at lower energies. Two groups have presented such data in the last year--the CERN-Serpukov collaboration[89] on the missing mass studies at 25 and 40 GeV/c for π^- and K^- beams, and a CERN bubble chamber experiment[136] on $\pi^+ p \rightarrow$ anything at 8, 16 and 23 GeV/c.

The x distribution (where $x = p_{11}/p_{11}^{max}$) for the π^+ at all three energies from the CERN HBC experiment[136] are shown in Figs. 167, 168 and 169. One can clearly observe the build up of the diffractive $x \approx 1$ peak as the energy increases, but it is interesting to notice that the peak is fed only by the 2 prong and the 4 prong topologies. They show that indeed only three exclusive reactions make up $\sim 80\%$ of the forward peak cross sections--

$$\pi^+ p \rightarrow n\pi^+\pi^+$$
$$\pi^+ p \rightarrow p\pi^+\pi^0$$
$$\pi^+ p \rightarrow \pi^+\pi^+\pi^- p \ .$$

The x-distributions for these processes are shown in Figs. 170 and 171 where events were selected to emphasize the diffractive phenomena, by choosing only those in which the π^+ is the only particle going forward in the c.m.s. and all other particles are going backwards. These contributions are shown as the heavy lines in Figs. 170 and 171. The shaded area in Fig. 171 represents events in which the proton is the only particle going backwards in the c.m.; these events correspond to dissociation of the incoming pion.

The sum of the contributions from the proton diffraction dissociation in the three exclusive reactions studied above, is compared to the diffractive peak obtained in the ISR p-p scattering experiments in Fig. 172. The ISR data were extrapolated to low transverse momenta (where the HBC data exists) under the assumption that

$$E \frac{d^3\sigma}{dp^3} = A(x)\ e^{-B(x)p_\perp^2}$$

and then integrated over the entire $p_\perp$ range. (The ISR data was taken for $0.7 < p_\perp < 1.2$ GeV/c.) They further assumed factorization of the diffraction dissociation process and scaled down the p-p cross-sections by

$$\left(\frac{\sigma^T_{pp}}{\sigma^T_{\pi^+ p}} \right)^2 = 3.08$$

to compare to the $\pi^+ p$ cross-sections.

The errors associated with these extrapolations are large and indicated on Fig. 172 as the hatched band. The data indicate that within 20-30% one can observe scaling of the forward peak in energy range, $s = 31$ to 2000 GeV^2.

This scaling conclusion is also verified by the CERN-Serpukov experiment.[89] The missing mass spectrum for $\pi^- p$ collisions is shown in Fig. 173. Production of peaks in the A_1, A_2 and A_3 regions are observed but no furthe

narrow high mass structure is seen. The invariant cross-sections $d^2\sigma/dt\,dx$ and $d\sigma/dx$ are compared in Fig. 174. The cross-sections scale (i.e. are seen to be independent of s for a given x) and the ratio

$$\frac{\frac{d\sigma}{dx}(25\ \mathrm{GeV/c})}{\frac{d\sigma}{dx}(40\ \mathrm{GeV/c})} \quad \text{for} \quad -0.90 < x < -0.75$$

is given as 1.01 ± 0.03. Also the slope of the cross-section in t is observed to be independent of energy--see Fig. 175.

The same apparatus was used in the study of the reaction $K^-p \to X^-p$ at 25 and 40 GeV/c. The missing mass distribution is shown in Fig. 176. The Q region is the only structure observed. The shape of the cross-section in t is observed to be energy independent and very similar to the π^-p distribution (the dashed line)--see Fig. 177. The question of scaling was also addressed for the K^- experiment and the invariant cross-sections are shown in Fig. 178 as a function of x. The scaling hypothesis holds well for this reaction, too. The dashed line represents the invariant cross-section for the pion data and lies somewhat about the K^- cross-section. However, if factorization is assumed then the π and K data are observed to be in good agreement--

$$\frac{\frac{d\sigma}{dx}(\pi^-p)}{\frac{d\sigma}{dx}(K^-p)} = \frac{\sigma^T_{incl}(\pi^-p)}{\sigma^T_{incl}(K^-p)}$$

$$1.20 \pm 0.07 \quad 1.18 \pm 0.04$$

Another interesting measurement from Serpukov has been done by Derevshchikov et al.[137] who have studied the proton diffraction region from high energy pions--

$$\pi^-p \to \pi^-X \quad \text{for} \quad 0.9 < x < 1.0\ ,$$

and for pion momenta of 42 GeV/c and 51 GeV/c. The invariant cross-sections are shown in Fig. 166 where the sharp diffractive peak at $x \sim 1.0$ is seen.

The data exhibit the same general behavior as pp scattering. It will be interesting to see higher energy data from NAL, to see if the s-dependence matches that of pp scattering.

5. Conclusions

In conclusion, the single particle inclusive studies have shown the existence of a large energy independent cross-section for the production of a low mass peak. The process is assumed to be diffraction excitation of the target or projectile and has a cross-section almost equal to the elastic scattering cross-section (i.e. $\sigma_D \sim 6$ mb). The peak extends up to quite large masses (for example, at ISR energies, it extends up to 7 GeV), and seems to have a M^{-2} fall off. This diffractive peak is made up mainly from low multiplicity events, the mean multiplicity in the peak being about half the mean multiplicity for all events. The multiplicity increases with the mass of the diffracted system. The s-dependence of the cross-section for the peak is very slow, exhibiting a small component with $s^{-1/2}$ behavior, which causes ~ 20% fall in cross-section through NAL (50-400 GeV/c), but which is less than a 10% through the ISR range (200-2500 GeV/c). The momentum transfer behaviour of the diffraction peak is consistent with an exponential fall off, in which the slope decreases as the mass of the diffracting system increases. (This behaviour is very reminiscent of the exclusive diffraction reactions.) Very similar properties are observed for the diffraction of pions and for protons.

Finally, the reports from London bring results from Cool et al.'s[138] measurements on $pd \to Xd$ through the energy range of NAL. By observing the recoil deutron from a deuterium gas jet target, they assure $I = 0$ exchange in the proton excitation. They study the diffraction scattering region for $x > 0.93$.

As in the $pp \to px$ experiment, discussed in Chapter IV above, they observe structure at small missing mass, but for $M \sim 2$ GeV they find the spectrum falling off like M^{-2}. They also find the cross-section independent

of energy, namely,

$$M^2 \frac{d\sigma}{dM\,dt} \quad \begin{cases} \text{flat in } s \\ \text{flat in } M \end{cases} \quad (\text{for } M > 2 \text{ GeV}).$$

The region below 2 GeV they estimate has a total cross-section at 300 GeV of around 0.75 mb, compared to ~ 1 mb at 20 GeV. This resonance diffraction region exhibits the flat energy dependence we expect.

For the data above 2 GeV, integration over t gives a cross-section, $\sigma \sim (0.7\ \text{mb}/M^2)$, and now integrating over M, they find $\sigma \sim \ln s$, with the single diffraction cross-section at 305 GeV, $\sigma_{SD} \sim 3$ mb.

If they subtract off from the inelastic cross-section, the diffractive component indicated here, the resulting non-diffractive inelastic cross-section is flat through the NAL-ISR range, i.e. $\sigma_{inel} - 2\sigma_{SD} - \sigma_{DD}$ = constant as function of s. So in addition to the other properties defined above, this new NAL experiment gives more weight to the suggestion that the rise in the total cross-section observed in the ISR region is due to the expanding phase space of the diffraction process, and the constancy of the cross-section at each individual mass.

VII. TRIPLE REGGE PHENOMENOLOGY

1. Which Terms are Important?

Analysis of the single particle distributions at high energies may be done through the application of triple-Regge theory. One wants to calculate the cross-section for processes of the type (a) in Fig. 179. Applying an equivalent of the optical theorem in $2 \to 2$ body scattering, the total cross-section is then given by the square of the forward scattering amplitude--so for processes of the type (a) we square the forward amplitude by multiplying by itself, shown diagrammatically in Fig. 179(b). This is then approximated by the triple-Regge diagram--Fig. 179(c).

The cross-section obtained from this exercise is then written as

$$s \frac{d^2\sigma}{dt\,dM^2} = \sum_{1,2,3} \frac{R_{123}(t)}{s} \left(\frac{s}{M^2}\right)^{\alpha_1(t)+\alpha_2(t)} M^{2\alpha_3(0)}$$

$$= \sum_{1,2,3} \left(\frac{1}{s}\right)^{1-\alpha_3(0)} R_{123}(t) \left(\frac{s}{M^2}\right)^{\alpha_1(t)+\alpha_2(t)-\alpha_3(0)}$$

It is supposed that such a description should be valid for (s/M^2) and M^2 large.

One then tries to fit the data as a function of s, M^2 and t with an appropriate selection of the trajectories α_1, α_2 and α_3 (see Fig. 179). For Pomeron exchanges, P, $\alpha(0)$ is taken to be 1, and for Regge terms, R, $\alpha(0)$ is taken to be 1/2. Excluding interference terms, there are four leading terms to be used in fitting the data--PPP, PPR, RRP, and RRR. The s-dependence for fixed x and M^2-dependence of each is summarized in Table XVIII and in Fig. 180.

If the PPP contribution is not zero,[139] it is expected to dominate at large s and large M^2. Fits to the ISR data[140] show that the data is compatible with substantial PPP coupling, but important contributions from the other trajectories are also required and the fits are by no means unique.

The most systematic attempts to study the triple-Regge question have been performed by the Rutgers-Imperial College Group at NAL,[130,141] and the CHLM group at the ISR.[140,20] Fox[5] has recently given a critical review of this field (recommended reading). In the meantime, we will follow the work of these two experimental groups with the single "Fox caution" kept in mind--it is probably not a good approximation only to keep the four leading terms--appreciable interference effects should be expected.

The Rutgers-Imperial College data spans a large range in the important variables:

$$100 \leq s \leq 750 \text{ GeV}^2$$
$$0.14 \leq t \leq 0.38 \text{ GeV}^2$$
$$5 \leq s/M^2 \leq 12.5$$

and has already been discussed (in Chapter VI) with respect to the scaling behaviour of the cross-section. The wide energy range available in this experiment allows a clean separation of the energy dependent terms, PPR and RRR, from the energy independent terms, PPP and RRP.

The data was divided into four t intervals--$0.14 < t < 0.18$, $0.18 < t < 0.22$, $0.22 < t < 0.28$, $0.28 < t < 0.38$ GeV^2, and fit to the triple-Regge cross-section formula given above, with the couplings being left free in each t interval.

Five fits were attempted: (1) in which the four leading triple-Regge terms were used with $\alpha_P = 1 + 0.25\,t$ and $\alpha_R = 0.5 + t$. This fit was quite poor, not reproducing the dip structure for $x \sim 0.88$. It is interesting to note that the PPP term exhibits a dip in the forward direction with a maximum at $t \sim 0.2$ GeV^2--see Fig. 181; (2) which uses the same trajectories as in fit (1) but only fits the data for $x > 0.84$. This fit is much better but still not very good. The PPP term still shows the forward turnover; (3) in which the trajectory of the RRP terms is taken to be $\alpha = 0.2 + t$ (after Miettinen and Roberts)[142] to allow for the effects of lower lying trajectories. This provides a much better fit to the data, but now the PPP term has no forward turnover--see Fig. 181; (4) is very similar to fit (3) but an explicit parametrization is used for a $\pi\pi P$ term (due to Bishari)[143], together with the four leading triple Regge terms with conventional trajectories. This gives a rather good fit to the data, and no forward structure to the PPP term; (5) in which the RRP term is replaced by an exponential e^{-cx}, as suggested by Capella et al.[144] This provides the steeper x-dependence required by the data and indeed this parametrization gives the best fit. Again, the PPP term shows no forward turnover--see Fig. 181.

It is interesting to note that despite the uncertainty and variation in the PPP term between the several fits tried, the energy dependent term--PPR--seems very stable, quite model independent and rather well determined.

In summary, a clear separation between the s-dependent and s-independent terms has been observed. For the s-dependent terms the RRR contribution is small and negligible, while the PPR contribution is well determined. The energy independent part requires both the PPP and RRP terms, and no unambiguous isolation if the PPP coupling seems possible at this time. Fits with conventional trajectories yielded a PPP coupling which peaked for $t \sim 0.2$ GeV^2 and turned over in the forward direction, while better fits to the data (with modified trajectories) had a quite structureless PPP t-dependence. Therefore not much light can be shed on the question of whether g_{PPP} vanishes at $t = 0$. To make more progress in studying the triple-Regge phenomenology and in particular to identify unambiguously the PPP contribution new data extending further into the diffraction peak, to x values nearer 1, are urgently required.

Sens[20] fits the CGHL group data, which is characterized by:

$s = 1995$ GeV^2	$0.5 < x < 0.82$	$0.7 < P_T < 1.2$ GeV/c
$= 551$ GeV^2	$5 < M^2 < 30$ GeV^2	$.15 < P_T < 1.25$ GeV/c
$= 930$ GeV^2	$7 < M^2 < 50$ GeV^2	$.45 < P_T < 1.65$ GeV/c

The medium x data at $s = 1995\ \mathrm{GeV}^2$ were fit assuming that by this high an energy RRR components had died out, and only one term is dominating the cross-section, namely, the RRP contribution. This may be justified by inspection of Fig. 182, which shows s-independence in the medium x region (0.5-0.7), from $\sqrt{s} = 23$ GeV to $\sqrt{s} = 53$ GeV. Terms like RRR, or interference terms may be expected to be small, or at least to contribute less than 20%, to the cross-section.

For this one term we may rewrite the triple Regge relationship:

$$E \cdot \frac{d^3\sigma}{dp^3} = \frac{M_0^2}{16\pi^2 s} \cdot G_{ffp}(t)\left(\frac{s}{M^2}\right)^{2\alpha_f(t)} \cdot \left(\frac{M^2}{M_0^2}\right)^{\alpha_p(0)}$$

where f is the effective meson trajectory in the RRP term.

Taking $M_0^2 = 1$ and $\alpha_p(0) = 1.0$, this reduces to

$$E\frac{d^3\sigma}{dp^3} = \frac{G_{ffp}(t)}{16\pi^2} \cdot \left(\frac{M^2}{s}\right)^{1-2\alpha_f(t)}$$

The data at $s = 1995\ \mathrm{GeV}^2$, when fitted to this form, give

$$\alpha_f(t) = 0.45 + 0.75\ t,$$

and the results are plotted in Fig. 183. The dashed line gives the sensitivity of the data to the more usual unit slope of the meson trajectory.

At high x, the data is a mixture of diffraction dissociation and high momentum fragments from the pion production region. This is especially true in a poor resolution situation. Sens subtracts out the high momentum fragments assuming they are well explained by the RRP term just determined above.

The M^2-distribution is shown in Fig. 184 and the extrapolated fragmentation component under the diffraction peak is shown as the "background" curve.

The mass spectrum falling like M^{-2} (see Fig. 184), and the s-independence of the cross-section for $x \sim 1.0$ shown in Fig. 185, suggests that the peak may be dominated by the PPP term. See Table XXVIII for M^2, x and s-dependence of the different terms.

Sens then assumes only the PPP term, which gives

$$E \cdot \frac{d^3\sigma}{dp^3} = \frac{G_{ppp}(t)}{16\pi^2} \cdot \left(\frac{M^2}{s}\right)^{1-2\alpha_p(t)}$$

Fitting the data near $x = 1$, and making sure to remove the elastic scattering contamination of the data, allowing for the momentum resolution of the spectrometer and subtracting the high momentum fragmentation "background" using the RRP term, finally yields the Pomeron trajectory

$$\alpha_p(t) = 1 + 0.2t$$

shown in Fig. 186.

This trajectory was compared to that derived from a study of elastic scattering assuming Pomeron dominance of the two-body reaction--

$$\frac{d\sigma}{dt} = f(t)\cdot s^{2\alpha_p(t)-2}$$

Using elastic scattering data at $s = 551{,}930\ \mathrm{GeV}^2$ they find good agreement wit this Pomeron trajectory (shown as crosses, (x), on Fig. 186). This is also in good agreement with the best overall fit to all elastic pp scattering above $s = 100\ \mathrm{GeV}^2$, which gave $\alpha' \sim 0.275\ \mathrm{GeV}^{-2}$. (See Chapter II.)

This analysis shows that the triple Regge framework allows a consistent description of the data, but as Fox[5] points out, there are are so many paramete and the correlations in the data are so strong that it is difficult to learn anything at present.

2. Decoupling of the Triple Pomeron Term as $t \to 0$.

The question of the vanishing of the triple Pomeron coupling as $t \to 0$ is always of interest, and should be addressed before leaving the triple Regge chapter.

Abarbanel et al.[139] have shown that the triple Pomeron coupling $g_p(t)$ is given by

$$g_p(t) = \frac{(16\pi)^{1/2} \cdot G_p(t)}{\sqrt{\sigma_T} \cdot \sqrt{d\sigma/dt_{el}}}$$

where

$$E \cdot \frac{d}{dp^3}(\text{diffractive}) = \frac{1}{\pi} \cdot G_p(t) \cdot \frac{s}{M^2}$$

and

$$\frac{d\sigma}{dt\,dx} = G_p(t) \cdot \frac{1}{s} \cdot \left(\frac{s}{M^2}\right)^{2\alpha_p(t)} \cdot (M^2)^{\alpha_p(0)}$$

and where σ_T, $d\sigma/dt\big|_{el}$ are the asymptotic values of the cross-sections. (This is strictly only true for $\alpha_p(0) = 1$.)

This may be rewritten in the following way

$$\frac{1}{16\pi} \cdot \frac{1}{2\alpha_p'(0)} \cdot g_p^2(0) \leq 1 - \alpha_p(0) .$$

The Abarbanel et al. paper points out that if the Pomeron is a factorizable simple pole, that the above triple Pomeron relation cannot be self consistent unless $\alpha_p(0) < 1$ or $G_p(0) = 0$.

Hence the interest in the question of whether PPP vanishes at $t = 0$.

The data of Columbia-Stony Brook[128,129] discussed in Chapter VI, and shown again below as Fig. 187, show a dip at small t for $8 < M^2 < 14\ \text{GeV}^2$. This dip is not present for larger $(20 < M^2 < 60\ \text{MeV}^2)$ or smaller masses. The interpretation of this turnover as a zero in g_{ppp} may be justified by--

- $8 < M^2 < 14\ \text{GeV}^2$ region is roughly optimal for seeing the triple Pomeron term at this energy. At lower masses the PPR term is domiant, while at larger masses the RRP term is important,
- the value of $(d\sigma/dtdM^2)$ is non-zero for $t = 0$, but is in agreement with many of the fits for PPR and RRP contributions. (See Fox's review of all these fits.) However, away from $t = 0$ there seems to be a need for an extra contribution to the (PPR and RRP) to fit the data--is this an indication of the presence of the PPP term?

Before accepting that $g_{ppp} \to 0$ as $t \to 0$ as fact, we should notice several other points:

- First, if we use the extrapolated value of the PPP term (going to $t = 0$ with an exponential) from the Sens analysis,[20] and put $G_p(0)$ into the formula derived above, we find

$$1 - \alpha_p(0) \geq \frac{10^{-3}}{2\alpha_p'(0)}$$

which implies for $0.05 < \alpha' < 0.5$, the Pomeron intercept must lie in the range

$$0.99 < \alpha_p(0) < 0.999$$

Clearly this is not too serious a departure from $\alpha(0) = 1$.

This means that the self-consistency equations do not demand that the triple Pomeron coupling have a sharp turnover as $t \to 0$.

If fact, if we write

$$\alpha_p(t) = 1 - \epsilon + \alpha_p(0) \cdot t$$

then for $\alpha' = 0.25\ \text{GeV}^{-2}$, $\epsilon \geq 2.10^{-3}$. This changes the definition of the cross-section

$$\frac{d\sigma}{dt\,dx} = s^{-\epsilon} \cdot G_p(t) \cdot \left(\frac{s}{M^2}\right)^{1+2\alpha_p'(t)-\epsilon}$$

For small values of ϵ, as those indicated, the scale breaking is very small. For $\epsilon < 10^{-2}$ the cross-section is still well approximated by a logarithmic growth. Indeed the $s^{-\epsilon}$ factor contributes only a 2% correction between $s = 200$ and $3000\ \text{GeV}^2$. Therefore, the cross-section increases with s in this energy range.

- We may also take the PPP term obtained in the Sens fit,[20] and extrapolate to the t-range measured by the Columbia-Stony Brook experiment at NAL.[129] Sens has attempted this comparison, adding to the PPP terms his RRP term (to account for high momentum fragmentation protons). The result is shown in Fig. 188.

  For $5 < M^2 < 30$ GeV^2--the region of Sens high energy fit--the agreement may be interpreted as confirmation that down to $t \sim 0.056$ GeV^2 there is no sign of $G_{ppp}(t)$ turnover.

- Finally, what do the bubble chamber experiments say on the question of the forward dip? (This question was reviewed in Chapter VI in discussing the t-dependence of the inclusive scattering.)

The 200 GeV/c $\pi^- p$ and pp experiments looking at $d\sigma/dtdM$ see no sign of a forward turnover for small masses--(i.e. the $8 < M^2 < 14$ GeV^2 region studied in the Columbia-Stony Brook experiment). The data are repeated below in Figs. 189 and 190. The pp experiment does observe some flattening of the t-distribution for M^2 above 25 GeV^2.

Vander Velde,[145] in a summary of all four pp experiments (102, 205, 303, 405 GeV/c) reports that for the broad hump region (i.e. $0.9 > x > 0.5$), the $d\sigma/dt$ is exponential with a slope of $\exp(-8.5P_T^2)$, and the region of large mass in the diffraction peak ($x > .9$ but $M^2 > 10$GeV^2) is also quite exponential with slope $\exp(-7P_T^2)$. However, in studying the four prong data they do observe a dip in the forward direction for $P_T^2 \leq 0.4$ GeV^2 for $M^2 < 10$ GeV^2. Beyond $P_T^2 \sim 0.05$ GeV^2 the data are exponential with a slope of $\exp(-10P_T^2)$. See Fig. 191.

The bubble chamber data do not help to clarify this question. It is important to establish the existence of the dip firmly, and then by studies of its s- and M^2-dependence attempt to associate it with one of the triple Regge terms contributing to the process. In this way, we may see some progress on the question of whether the triple Pomeron coupling vanishes as $t \to 0$. As mentioned before, unambiguous determination of the triple Pomeron term needs experiments measuring s-, t- and M^2-dependences well inside the diffraction peak for x nearer 1.0.

VIII. IMPACT PARAMETER ANALYSIS OF HIGH ENERGY SCATTERING

1. Summary of Data

a) σ_T increases by $(10 \pm 2\%)$ in NAL-ISR energy range.
σ_{el} increases by $\sim 10\%$ in NAL-ISR energy range.
σ_{inel} is responsible for most of rise in σ_T, it grows by $\Delta\sigma \sim 3.3$ mb ($\sigma_{inel} = 32.3 \pm .4$ mb at $\sqrt{s} = 23.4$ GeV and $35.6 \pm .5$ mb at 53 GeV).

b) Real part of elastic scattering amplitude at $t = 0$ changes sign around $p \sim 300$ GeV/c crossing from negative to positive values.

c) Small t slope of $d\sigma/dt$ (i.e. $|t| < 0.15$ GeV^2), is steep ~ 12 GeV^{-2}, and grows like $\ln s$. Parametrizing this shrinkage in terms of a Pomeron trajectory yields $\alpha' = (0.27 \pm 0.05)$GeV^{-2}.

d) The slope of $d\sigma/dt$ changes rapidly by $\Delta b \sim 2$ GeV^{-2} around $t \sim 0.15$ GeV^2. The cross-section for larger t values shows weak energy dependence.

e) The break in $d\sigma/dt$ observed in the 10-30 GeV/c energy region for $t \sim 1.3$ GeV^2 develops into a beautiful diffraction minimum, at high energy.

f) Production of a low mass peak in inelastic scattering with an s-independent cross-section; the peak extends up to masses of about 7 GeV at ISR energies and seems to behave like M^{-2}.

g) The cross-section for the inelastic diffractive process is found to grow like $\ln s$, and to account for a substantial part of the rise in the total cross-section; (one experiment indicates that the inelastic cross-section minus the single and double diffractive contributions is a constant from NAL through ISR).

h) The multiplicity in diffraction scattering is lower than for other processes--typically the mean diffractive multiplicity is about half the total mean multiplicity. This multiplicity increases with the mass of the diffraction excited system.

i) The differential cross-section, $d^2\sigma/dM^2dt$, is peaked and consistent with an exponential behaviour where the slope is a function of the mass of the diffracted system, $d^2\sigma/dM^2dt \propto \exp(-b(M^2)\cdot t)$. The slope, $b(M^2)$, falls from a value close to twice the elastic value for low masses, to ~ 4 GeV^{-2} for the high mass tail.

j) The properties of pion diffraction, $(\pi \to \pi^*)$, and proton diffraction, $(p \to p^*)$, are observed to be very similar.

2. Elastic Scattering Analysis

In Chapter I we discussed diffraction scattering as the shadow of inelastic processes and through s-channel unitarity arrived at the relation--

$$\mathrm{Im}\, T_{fi} = G_{el} + G_{inel}$$

where T_{fi} is the elastic amplitude and G_{el}, G_{inel} the elastic and inelastic overlap functions.

From the measured data on $d\sigma/dt$ for pp elastic scattering one can determine $\mathrm{Im}\, b_{el}(s,t)$ and $\mathrm{Re}\, b_{el}(s,t)$. Most simply one can assume pure imaginary, non-flip for the elastic amplitude and solve for $\mathrm{Im}\, b_{el}(t)$ directly from the data. The next stage in sophistication is to attempt to find $\mathrm{Re}\, b_{el}(t)$. The real part is known only at $t = 0$, but a reasonable estimate of the phase is obtained by assuming that the imaginary part of the scattering amplitude vanishes for $t \sim 1.3$ GeV^2 dip, and the measured cross-section gives the real part at that t-value. Using smoothness to connect, one may estimate $\mathrm{Re}\, b_{el}(t)$. (It turns out not to be at all sensitive to the phase assumed.)

Given the elastic amplitude, one may use the s-channel unitarity equation to find $G_{inel}(t)$--see Fig. 192.

Here we see the inelastic overlap function changing sign as a function of t, for $t \sim 0.6\ \mathrm{GeV}^2$, and a second zero for $t \sim 2.2\ \mathrm{GeV}^2$. The change of sign shows how important are the phases of the many open channels, in making up the inelastic overlap function.

Perhaps one sees more clearly what is going on, if we Fourier-Bessel transform the $\mathrm{Im}\ b_{el}(s,t)$ and $\mathrm{Re}\ b_{el}(s,t)$ into b-space (i.e. impact parameter space). We may then find $G_{inel}(s,b)$ from the relation

$$\mathrm{Im}\ b_{el}(s,b) = \frac{1}{4}\ |b_{el}(s,b)|^2 + G_{inel}(s,b)\ .$$

Figure 193 shows the result for the total, elastic and inelastic overlap functions using the ISR pp scattering at $\sqrt{s} = 53$ GeV. (This is from the analysis of Pirila and Miettinen,[16,17] but all of the analyses are in fairly good agreement.) The "blackness" of the proton is observed to be ~ 94% of the unitarity black disc limit, and the inelastic overlap looks like a gaussian with average radius a little less than 1 fermi. On closer inspection, G_{inel} flattens out near $b = 0$, and has a long tail.

This long tail of the $G_{inel}(b)$, (or $\mathrm{Im}\ b_{el}(b)$--as for large b they are the same), is directly related to the sharp break in $d\sigma/dt$ at $t = 0.15\ \mathrm{GeV}^2$. There is much discussion as to the origin of this tail--2π contributions, dissociation, etc.

The dip at $t \sim 1.3\ \mathrm{GeV}^2$ is related to the flattening of G_{inel} as $b \to 0$, but the corresponding effect in the elastic amplitude is very difficult to see. (Remember, the cross-section at the dip is between six and seven decades down from $d\sigma/dt|_0$, so it does not take a big change in the elastic amplitude). It is also interesting to note that if $G_{inel}(s,b)$ did not level off near $b \sim 0$, it would violate unitarity. This suggests that absorptive effects are at least partially responsible for the small b flattening.

It is of interest to study the s-dependence of the overlap function--the same analysis was performed for $\sqrt{s} = 21$, 30, 44 and 53 GeV. The results are shown in Fig. 194, where we see that the radius grows ~ 5% through this energy range, but that the absorption at $b = 0$ stays constant at 94% of its unitary value. So the protons are getting bigger not blacker.

In addition, if we look at where G_{inel} changes between 53 and 31 GeV, we find that the increase in the inelastic cross-section comes from a narrow region, a ring around 1 fermi. Perhaps it is not so surprising if we remember that the increase in the elastic cross-section comes mainly from the small t region--i.e. for large impact parameters. (See Fig. 194.)

3. Inelastic Diffractive Scattering: Impact Parameter Analysis

The measurements of the inclusive proton spectra at NAL and the ISR show that at high energies inelastic diffractive scattering and non-diffractive scattering populate different regions of phase space. This suggested that it may be useful to consider their contributions to the elastic scattering separately. Hence the inelastic overlap may be split into two parts--

$$G_{inel}(t) = G_{prod}(t) + G_D(t)$$

Rewriting the s-channel unitarity relation, we have--

$$\mathrm{Im}\ T_{fi}(t) = G_{el}(t) + G_D(t) + G_{prod}(t)\ ,$$

where $G_{prod}(t)$ is the shadow of the non-diffractive particle production processes and G_D the same for the diffractive part.

The analysis closely parallels the elastic study above, except now have to take into account spin and helicities in the inelastic scattering while "no flip only" was taken in the elastic case. Sakai and White[146] have done a careful analysis of this case--they assume that as the mass of the excited system grows, the spins involved grow quite rapidly.

They also assume that the diffraction scattering conserves helicity in the t-channel. (The data discussed in Chapter V showed that the data favour TCHC over SCHC, but still shows some violation. However, Miettinen points out that the impact analysis is not crucially dependent on rigourous TCHC, but merely demand substantial SCH flip--which the data certainly confirms.)

Sakai and White fit the $(d^2\sigma/dM^2dt)$ for the single particle spectra and find that the diffractive shadow $G_D(s,b)$ has a peripheral profile, and that diffraction occurs at the edge of the absorption region around $b \sim 1$ fermi. See Fig. 195. (Note that if SCHC had been assumed, the impact profile for diffraction would have been central. Further note that the large b tail is ascribed to central inelastic amplitude in this model. G_{in} dominates for $b < 1f$ and for $b > 1f$.)

4. Slope-Mass Correlation

This association of the diffractive production with peripheral impact parameters allows a very natural explanation of the observed correlation of the slope of the diffraction peak with the mass of the system. The production from a ring at large impact parameters will contribute a term $(e^{at} J_{\Delta\lambda}(R\sqrt{-t}))$ to the differential cross-section, $d^2\sigma/dM^2dt$, where $\Delta\lambda$ is the helicity flip involved in the scattering and where the exponential accounts for the smearing of the edge of the ring.

When the mass is close to threshold, the spin (J) is low and the contribution of helicity flip amplitudes are small. For this situation the shape of the amplitude is given by $J_0(R\sqrt{-t})$, which for $R \sim 1$ fermi gives a zero at $t - 0.2\ GeV^2$. This would mean that the very steep slope for the low mass diffraction is caused by a zero at small t values in the dominant helicity amplitude, and not by a large value of the exponential slope, a.

As the mass of the system increases, this zero becomes washed out by contributions of the flip amplitude, and/or real parts--as the mass increases the spin increase and the helicity flip amplitudes grow--flattening out the cross section, $d\sigma/dt$. See Fig. 196.

It will be interesting to see inelastic diffraction data from NAL at small mass and over large enough a t region to convincingly see this structure. At these energies the real parts should be small enough that if this is really what is going on, we should see the characteristic J_0 structure in the $d\sigma/dt$.

There is some confirmation of this suggestion, from two bubble chamber experiments--one on $pp \to pn\pi^+$ at 19 GeV/c[147]--see Fig. 197--and the other on $np \to p\pi^-p$ at 12.5 GeV/c[79]--see Fig. 198. For small masses of the diffractively excited $(N\pi)$ system there are signs of small t structure.

However, for the moment only a hint.

5. Rise of σ_T

In the summary of the data, we found that the rise in σ_T comes from σ_{inel} mainly, and that it originates for large impact parameters--from a narrow ring around $b \sim 1$ fermi.

We have also argued that the inelastic diffraction is peripheral and comes from a narrow ring around $b \sim 1$ fermi.

Further we have several experiments which indicate that the diffractive cross-section increases like $\ln s$, and could account for the increase in the total cross-section.

It is very tempting to tie all of these points together; to be sure we would like to have $G_D(s,b)$ at several energies to find where the increase in diffraction comes from. This is a necessary precaution, because one can imagine a situation where the increase is due to a central contribution but which produces a peripheral increment to the total amplitude.

Consider the case of σ_{inel} being constant, but the elastic differential cross-section shrinks. This causes G_{inel} to fall at $b = 0$ and go up for large b. If, as the energy increases, we add a new central contribution then

the new total G_{inel} at the higher energy could be compensated such that G_{inel} has not changed at $b = 0$, and the difference of the two G_{inel} would peak at ~ 1 fermi (i.e. have produced a peripheral increase in G_{inel} from a new central piece, plus a shrinking elastic amplitude). See Fig. 199.

6. Conclusion

Finding the reason for this phenomenon of rising total cross-section is one of the most interesting questions in particle physics. It is clear that the rise is not due to the saturation of unitarity (Froissart, Chen-Wu), but which of the several other possible mechanisms nature is using is far from clear Is it due to an expanding core?, or to an expanding ring around the edge of the absorption region?, or to an increasing blackness of this outer ring? (or something else?). Defining the specific amplitude and mechanism for the growing cross-section is a very tantalizing and fundamental question!

IX. CONCLUSIONS

Having completed a review of the data on diffractive processes, we now collect together some of the questions raised in the preceding chapters.

1. Total Cross-sections--what is the asymptotic behaviour? Do they continue to rise with increasing energy or do they approach a constant value at high energy? See Fig. 200.

   Some useful insight on this matter will come from:

   -study of the "early rising" K^+p cross-sections through the NAL energy range;

   -good measurements of the magnitude of the real part of the forward scattering amplitude in p-p scattering at highest energies of the ISR;

   -watching for changes in the s-dependence of σ_{el}, σ_{el}/σ_{tot}, b (the slope of the forward cross-section) for all processes through the NAL energy range;

   -watching the energy dependence of the difference in total cross-section for particle and antiparticle processes through the NAL range, to see if (and when), the Pomeranchuk theorem will be satisfied.

2. Elastic Cross-section--are there really two components to the Pomeron? There are three interesting areas to watch here:

   -study of the s-dependence of the small t cross-section, especially for the K^+p system, though NAL energies. (Do we find diffractive amplitudes with upward curvature at small t?)

   -study of the s-dependence of the larger t cross-section and of the diffractive dips, to provide more information on the "central collisions." (Do K^+p, $\gamma \to \phi$, $\pi^{\pm}p$ reactions show deep diffraction dips? If so at what t-values and how do they move with energy?)

   -the determination of the real part of the elastic scattering amplitude at all t values--see Davier's lectures.[104]

3. Inelastic Diffraction Scattering--here we have quite a long list of interesing questions:

-understand the two components of exclusive diffraction (the threshold kinematic amplitude and the diffractive production of resonant states), and their relationship to each other;

-from studies at NAL energies of low mass exclusive diffraction, determine whether the slope-mass correlation is caused by a zero in the amplitude at small t (which gets filled in as the mass grows and spin structure gets more complicated), or is due to a real shrinkage of an exponential cross-section as masses go to threshold.

-understand the anomalous nuclear absorption in diffractively produced systems, wherein the absorption cross-section for (3π) and (5π) states is the same as a single pion, $(K\pi\pi)$ like the K and $(N\pi\pi)$ like the nucleon. (See the lecture of B. Gobbi.[82])

-where are the meson resonances, which correspond to the diffractive N^* production? Hoepfully, with new tools becoming available[101] we will be able to study A_1 and Q production in non-diffractive channels--

$$K^- p \to A_1 \Lambda,\ Q^- \Delta^+$$

$$\pi p \to Q\,\Lambda,\ A_1 \Lambda$$

$$e^+ e^- \to \pi A_1,\ \bar{K} Q\ .$$

-is the inclusive diffractive amplitude peripheral? Is the increase in this amplitude, with increasing energy, peripheral or central? Does the increase in the diffractive cross-section account for the observed rising total cross-section?

-if we think of the proton as an almost black disc with an edge contribution, are the disc and the edge both growing with energy? If so, how fast? Does the edge get blacker?

-for a better understanding of the triple Regge picture experiments covering a large s- and t-range and measuring x-values from $x \sim 0.8$ right up to almost 1.0 are required. Such studies should also allow a better discussion of the question of the decoupling of the triple Pomeron coupling at small t values.

4. Factorization--we know from studies of two-body processes around 10 GeV/c that secondary processes (cuts, absorption, double exchanges, etc.) are important, and further the rising total cross-sections observed at high energies exclude a simple pole description. These observations lead us to expect a breakdown of factorization. It would be interesting to have good experiments, with a few percent accuracy, to observe this breakdown and attempt to follow any s-dependence of the violation.

5. Comment on the s-Dependence of the Impact Structure of Pomeron

Since s-channel unitarity relates elastic and inelastic behaviour at a given impact paramter through the equation:

$$\mathrm{Im}\, f_{el}(s,b) = f_{el}(s,b) + f_{inel}(s,b)$$

we have to be prepared for the impact structure of Pomeron to change with energy, despite our prejudice as to its constancy.

We know that the total inelastic cross-section is flat (slowly rising--but maybe if take out the diffraction dissociation contribution, then it would be flat). But we also know that there are different reaction channels contributing at any two energies s_1 and s_2, being driven by quite different mechanisms. For example, at 10 GeV/c we have mainly quasi-two-body processes, which are very peripheral, while at 1000 GeV/c it is not mainly quasi-two body and I do not think peripheral--i.e. although the total inelastic cross-section is flat, the distribution in b-space will probably change--therefore the diffractive b structure must change (since one is the shadow of the other).

Perhaps there is a neat collaboration in the turning-on of the diffractive dissociation piece, which is peripheral and inelastic, and which feeds the Pomeron such that it picks up what is disappearing as the Regge two-body processes die out with increasing energy. (I think this is unlikely given the respective energy dependencies.)

At any rate, a study of the change of the impact parameter structure of the Pomeron, and of the inelastic processes which are coming in or dying out, may allow a deeper understanding of what diffraction is and how the proton is built up.

TABLE I

"OLD" REGGE POLE PARAMETRIZATION

$$\sigma_t(\pi^- p) = 21.3 + 17.6\ p^{-1/2}\ \text{mb}$$
$$\sigma_t(\pi^+ p) = 21.3 + 11.2\ p^{-1/2}$$
$$\sigma_t(K^- p) = 17.1 + 17.1\ p^{-1/2}$$
$$\sigma_t(K^- n) = 17.1 + 11.45\ p^{-1/2}$$
$$\sigma_t(K^+ p) = 17.1$$
$$\sigma_t(K^+ n) = 17.1$$
$$\sigma_t(\bar{p}p) = 37.4 + 50.7\ p^{-1/2}$$
$$\sigma_t(pp) = 37.4 + 7.4\ p^{-1/2}$$
$$\sigma_t(\gamma p) = 94.1 + 79.9\ p^{-1/2}\ \mu\text{b}$$
$$\sigma_t(\gamma n) = 94.1 + 53.6\ p^{-1/2}$$

TABLE II

THE VALUES OF THE PARAMETERS A AND n RESULTING FROM THE FITTING OF THE TOTAL CROSS-SECTION DIFFERENCES ABOVE 3 GeV/c TO THE FORMULA

$$\Delta\sigma = A p_{lab}^{-n} .$$

(The errors shown in the table have been evaluated taking into account statistical and systematic errors.)

Cross-section differences	A (mb)	n
$\Delta(\pi^{\mp} p)$	4.0 ± 0.3	0.32 ± 0.02
$\Delta(K^{\mp} p)$	18.1 ± 0.3	0.54 ± 0.02
$\Delta(K^{\mp} n)$	$13\ 0 \pm 0.4$	0.67 ± 0.02
$\Delta(p^{\mp} p)$	63 ± 2	0.64 ± 0.02
$\Delta(p^{\mp} n)$	49 ± 7	0.61 ± 0.05

TABLE III

ELASTIC DIFFERENTIAL AND TOTAL CROSS-SECTIONS MEASURED BY THE CERN-ROMA COLLABORATION

$\sqrt{s}$ (GeV)	$\lvert t\rvert$ (GeV^2) $\times 10^{-3}$	$(d\sigma/dt)_t$ (mb/GeV^2)	$b^{a)}$ (GeV^{-2})	$\epsilon = e^{b\lvert t\rvert}$ Extrapolation factor$^{b)}$	$(d\sigma/dt)_{t=0}$ (mb/GeV^2)	σ_t (mb)	$\sigma_{el}^{c)}$ (mb)	σ_{in} (mb)
23.4	8.1	71.0 ± 1.5	11.8	1.10 ± 0.004	78.1 ± 1.7	39.1 ± 0.4	6.8 ± 0.2	32.3 ± 0.4
30.5	13.5	71.0 ± 1.6	12.3	1.18 ± 0.007	83.8 ± 1.9	40.5 ± 0.5	7.0 ± 0.2	33.5 ± 0.4
44.8	17.5	73.8 ± 1.7	12.8	1.25 ± 0.010	92.3 ± 2.2	42.5 ± 0.5	7.5 ± 0.3	35.0 ± 0.5
52.8	23.0	70.6 ± 1.8	13.1	1.35 ± 0.014	95.4 ± 2.6	43.2 ± 0.6	7.6 ± 0.3	35.6 ± 0.5

a) The values of the forward slope b are obtained by fitting the Serpukhov and the ISR results on the hypothesis that $b \propto \ln s$.

b) The extrapolation factor ϵ increases with energy because the elastic scattering events are measured at a fixed angle, and thus at a momentum transfer $|t|$ which increases by a factor of about three when the energy is increased. The error on ϵ is obtained by assuming a very generous error $\Delta b = \pm 0.5\ GeV^{-2}$ on the interpolated values of b. The fitted errors are half of the error chosen.

c) The elastic cross-section σ_{el} is obtained from the quoted values of $(d\sigma/dt)_{t=0}$ and the shape of the differential cross-section as measured by the CERN-Roma and the Aachen-CERN-Genova-Harvard-Torino collaborations.

TOTAL CROSS-SECTIONS MEASURED BY THE PISA-STONY BROOK COLLABORATION

$\sqrt{s}$ (GeV)	Detected cross-section	Increment for elastic losses (mb)	Increment for inelastic losses (mb)	η	σ_t (mb)
23.4	38.66 ± 0.79	0.54 ± 0.10	0.10 ± 0.02	1.017 ± 0.003	39.30 ± 0.79
30.5	39.93 ± 0.81	0.75 ± 0.10	0.17 ± 0.04	1.023 ± 0.004	40.85 ± 0.82
44.8	40.69 ± 0.84	1.54 ± 0.15	0.34 ± 0.10	1.047 ± 0.006	42.57 ± 0.86
52.8	40.53 ± 0.83	1.95 ± 0.20	0.50 ± 0.12	1.060 ± 0.008	42.98 ± 0.84
62.8					44.0 ± 0.8

TABLE IV

LUMINOSITY INDEPENDENT MEASUREMENT OF $\sigma_T(pp)$ AT THE ISR

p (GeV/c)	σ_T (mb)
11.8	40.5 ± 1.0
15.4	40.3 ± 1.0
22.6	42.6 ± 1.1
26.6	43.1 ± 1.2

TABLE V

RESULTS ON PROTON-PROTON TOTAL CROSS-SECTIONS, ELASTIC CROSS-SECTIONS AND ρ

P_1 (lab) (GeV/c)	$P_1 + P_2$ (GeV/c)	$\sqrt{s}$ (GeV)	σ_{tot} (mb)	σ_{el} (mb)	ρ
102		13.9	39.7 ± 1.5	6.9 ± 1.0	
200		19.4	39.5 ± 1.1	6.92 ± 0.4	
303		23.9	39.0 ± 1.0	7.2 ± 0.4	
	15.4 + 15.4	30.6	40.3 ± 2.0	6.8 ± 0.6	
	11.8 + 11.8	23.5	38.9 ± 0.7	6.7 ± 0.3	+0.02 ± 0.05
	15.4 + 1 .4	30.6	40.2 ± 0.8	6.9 ± 0.4	+0.03 ± 0.06
	11.8 + 11.8	23.5	39.3 ± 0.8		
	15.4 + 15.4	30.6	40.9 ± 0.8		
	22.6 + 22.6	44.9	42.6 ± 0.9		
	26.6 + 26.6	52.8	43.0 ± 0.8		
	11.8 + 11.8	23.5	39.1 ± 0.4	6.8 ± 0.2	
	15.4 + 15.4	30.6	40.5 ± 0.5	7.0 ± 0.2	
	22.6 + 22.6	44.9	42.5 ± 0.5	7.5 ± 0.3	
	26.6 + 26.6	52.8	43.2 ± 0.6	7.6 ± 0.3	

TABLE VI

NEW ELASTIC CROSS-SECTIONS

p (GeV/c)	Group	σ_{el} (mb)	
25	CERN-IHEP	3.35 ± .06	$\pi^- p$
32.8	IHEP	3.91 ± .22	
35.4	IHEP	3.48 ± .36	
40.0	CERN-IHEP	3.32 ± .06	
42.0	IHEP	3.23 ± .10	
45.3	IHEP	3.44 ± .19	
48.6	IHEP	3.22 ± .12	
54.7	IHEP	3.35 ± .17	
205.0	NAL-LBL-Berkeley	3.03 ± .30	
25.0	CERN-IHEP	2.46 ± 03	$K^- p$
40.0	CERN-IHEP	2.33 ± .03	
25.0	CERN-IHEP	8.7 ± .2	$\bar{p}p$
40.0	CERN-IHEP	7.2 ± .3	

TABLE VII

ENERGY DEPENDENCE OF ELASTIC CROSS SECTION

$\sigma \propto p^{-n}$

Particle	Exponent, n	Range of Fit
π^-	-0.25 ± .02	(5-40) GeV/c
π^+	-0.28 ± .06	(5-40) GeV/c
K^-	-0.26 ± .03	(5-40) GeV/c
K^+	-0.09 ± .03	(4-15) GeV/c
$\bar{p}$	-0.42 ± .03	(5-40) GeV/c
p	-0.26 ± .02	(5-30) GeV/c

TABLE VIII

RATIO OF ELASTIC TO TOTAL CROSS-SECTION, $(\sigma_{el}/\sigma_{tot})$

	p_{lab} (GeV/c)	Ratio
π^-	5.5	.188 ± .005
	55.0	.138 ± .007
π^+	7.0	.192 ± .004
	16.0	.170 ± .006
K^-	10	.140 ± .003
	40	.126 ± .014
K^+	5	.225 ± .024
	15	.196 ± .017
p	6	.294 ± .006
	60	.187 ± .008
	200	.174 ± .005
	1000	.176 ± .007
$\bar{p}$	8.0	.225 ± .012
	16.0	.185 ± .010
	40.0	.178 ± .018

TABLE IX

RATIO OF $\dfrac{\sigma(Xp \to Xp)}{\sigma(\bar{X}p \to \bar{X}p)}$

Ratio \ Momentum (GeV/c)	5	10	40
$R(\pi^-/\pi^+)$	1.01 ± .06	1.00 ± .02	1.03 ± .02
$R(K^-/K^+)$	1.09 ± .06	0.94 ± .09	1.01 ± .03
$R(\bar{p}/p)$	1.26 ± .06	1.19 ± .04	1.05 ± .11

TABLE X

RESULTS ON THE EXPONENTIAL SLOPE b IN ELASTIC PROTON-PROTON SCATTERING AT THE CERN ISR. THE ERRORS INCLUDE AN ESTIMATE OF THE SYSTEMATIC CONTRIBUTIONS TO THE ERROR

$P_1 + P_2$ (GeV/c)	$\sqrt{s}$ (GeV)	$\lvert t\rvert \leq 0.15$ GeV^2		$\lvert t\rvert \geq 0.15$ GeV^2	
		t-range (GeV^2)	slope b (GeV^{-2})	t-range (GeV^2)	slope b (GeV^{-2})
10.8 + 10.8	21.5	0.05 -0.09	11.6 + 0.3	0.14-0.24	10.4 ± 0.2
15.5 + 15.5	30.6	0.05 -0.09 0.015-0.06	11.9 ± 0.3 13.0 ± 0.7	0.14-0.24	10.9 ± 0.2
22.5 + 22.5	44.9	0.05 -0.09 0.03 -0.12 0.01 -0.05	12.9 ± 0.2 12.9 ± 0.4 12.6 ± 0.4	0.14-0.24	10.8 ± 0.2
26.5 + 26.5	52.8	0.06 -0.11 0.04 -0.16 0.01 -0.06	12.4 ± 0.3 13.0 ± 0.3 13.1 ± 0.3	0.17-0.31	10.8 ± 0.2
31.4 + 31.4	62.6	0.01 -0.06	13.1 ± 1.0		

TABLE XI

$\pi^- p$ ELASTIC SLOPES

p (GeV/c)	t-Range (GeV^2)	Slope, b (GeV^{-2})
	$\left[\frac{d\sigma}{dt} \propto e^{-bt}\right]$	
14	$.05 < t < .78$	7.7 ± .03
55	$.05 < t < .53$	8.8 ± .2
205	$.03 < t < .60$	9.0 ± .7
	$\left[\frac{d\sigma}{dt} \propto e^{-bt-ct^2}\right]$	
3.0	$.05 < t < .44$	7.61 ± .11
3.7		7.60 ± .12
5.0		7.66 ± .09
6.0		7.70 ± .08
14.0	$.05 < t < .78$	8.26 ± .10
25	$.1 < t < .6$	9.07 ± .32
40		9.63 ± .31

TABLE XII

PARAMETERS OF ELASTIC SCATTERING (25 AND 40 GeV/c) - $\left(\frac{d\sigma}{dt} = \frac{d\sigma}{dt}\right)_0 e^{bt+ct^2}$

	p_{inc}	Events	b	c	χ^2/pts	$(d\sigma/dt)_{t=0}$	CTP	σ_{el}
π^-	25	8600	9.07 ± 0.32	2.4 ± 0.6	34/38	28.6 ± 2.6	31.6 ± 0.3	3.35 ± 0.06
	40	9300	9.63 ± 0.31	2.9 ± 0.5	38/38	29.8 ± 2.6	30.1 ± 0.3	3.32 ± 0.06
K^-	25	12400	8.71 ± 0.21	2.4 ± 0.4	34/38	19.9 ± 1.6	22.1 ± 0.2	2.46 ± 0.03
	40	15400	8.90 ± 0.23	2.8 ± 0.4	36/38	19.0 ± 1.5	21.2 ± 0.2	2.33 ± 0.03
$\bar{p}$	25	12000	12.8 ± 0.4	2.3 ± 0.8	25/33	108 ± 9	112 ± 1	8.7 ± 0.2
	40	4400	12.2 ± 0.7	2.0 ± 1.4	28/33	85 ± 9	101 ± 1	7.2 ± 0.3

TABLE XIII

t-DEPENDENCE OF SHRINKAGE IN ELASTIC $\pi^- p$, $K^- p$, and $\bar{p}p$ SCATTERING

($2\alpha'$ GeV^{-2})

	t = 0	-0.1	-0.2	-0.3	-0.4 (GeV^2)
π^-	0.72 ± 0.18	0.52 ± 0.12	0.35 ± 0.08	0.23 ± 0.05	-0.08 ± 0.06
K^-	0.73 ± 0.16	0.54 ± 0.12	0.38 ± 0.08	0.20 ± 0.06	0.00 ± 0.08
$\bar{p}$	-0.8 ± 0.2	-1.1 ± 0.1	-1.0 ± 0.1	-1.4 ± 0.2	-2.0 ± 0.2

TABLE XIV

RESULTS OF FITTING THE CROSS SECTIONS. FITS OF THE TYPE A exp(Bt) WERE MADE TO THE $\pi^{\pm}$ AND $K^{\pm}$ CROSS SECTIONS FOR THE RANGE $0.05 \leq -t \leq 0.44$ GeV^2; THE FORM A exp(Bt + Ct^2) WAS USED FOR p AND FOR $\bar{p}$ DATA OVER THE INTERVALS 0.05 to 1.0 GeV^2 AND 0.05 TO 0.44 GeV^2, RESPECTIVELY. THE SUPERSCRIPTS ± REFER T O THE CHARGE OF THE INCIDENT PARTICLE. ERRORS SHOWN INCLUDE STATISTICAL ERRORS AND UNCERTAINTY IN THE CORRECTIONS FOR SINGLE COULOMB SCATTERING.

Beam	p_{beam} (GeV/c)	A^+ mb/GeV^2	B^+ GeV^{-2}	GeV^{-4}	χ^2 per degree of freedom	A^- mb/GeV^2	B^- GeV^{-2}	C^- GeV^{-4}	χ^2 per degree of freedom
π	3	52.7 ± 1.2	7.03 ± .12		17/19	55.6 ± 1.1	7.61 ± .11		24/19
	3.65	44.8 ± 1.0	6.75 ± .12		20/19	51.5 ± 1.2	7.60 ± .12		14/19
	5	39.4 ± 0.7	6.94 ± .09		24/19	44.1 ± 0.7	7.66 ± .09		32/19
	6	37.1 ± 0.7	7.08 ± .10		14/19	40.2 ± 0.6	7.70 ± .08		33/19
K	3	17.5 ± 0.4	3.64 ± .11		24/19	38.7 ± 0.9	7.96 ± .13		16/19
	3.65	17.1 ± 0.5	4.12 ± .12		29/19	33.9 ± 0.8	7.57 ± .13		22/19
	5	16.2 ± 0.4	4.62 ± .10		23/19	28.9 ± 0.6	7.65 ± .10		24/19
	6	15.7 ± 0.4	4.87 ± .11		12/19	27.0 ± 0.7	7.57 ± .13		18/19
p	3	117.0 ± 2.3	7.80 ± .15	2.66 ± .20	19/26	299 ± 19	12.2 ± .8	-5.7 ± 2.4	28/18
	3.65	110.1 ± 2.4	8.29 ± .16	3.06 ± .22	23/26	264 ± 20	12.1 ± 1.0	-7.6 ± 3.0	12/18
	5	97.3 ± 2.0	8.46 ± .16	2.66 ± .22	22/26	194 ± 14	11.4 ± 1.0	-5.9 ± 2.9	15/18
	6	91.2 ± 1.9	8.63 ± .16	2.50 ± .23	31/26	198 ± 22	12.4 ± 1.5	-2.5 ± 4.0	19/18

TABLE XV

SLOPE PARAMETER b[GeV^{-2}] OF THE SQUARE ISOSPIN AMPLITUDES AT 12 AND 24 GeV/c IN pp → (Nπ)p

(Nπ) Mass interval [GeV]	I = $\frac{1}{2}$ (Nπ)-state 12 GeV/c	I = $\frac{1}{2}$ (Nπ)-state 24 GeV/c	I = $\frac{3}{2}$ (Nπ)-state 12 GeV/c	I = $\frac{3}{2}$ (Nπ)-state 24 GeV/c
1.08-1.32	11.7 ± 0.6	9.6 ± 0.6	10.1 ± 0.6	9.1 ± 1.2
1.32-1.44	8.4 ± 0.5	8.8 ± 0.6	8.7 ± 1.1	9.7 ± 1.5
1.44-1.56	6.1 ± 0.5	6.4 ± 0.6	8.2 ± 1.6	
1.56-1.80	4.4 ± 0.4	3.8 ± 0.4	8.3 ± 1.2	11.2 ± 1.3
1.80-2.28	4.4 ± 0.4	3.7 ± 0.7	10.1 ± 1.2	

TABLE XVI

CROSS SECTION $(d\sigma/dt')_{t'=0}$ AND SLOPE PARAMETER b, FOR THE REACTIONS $\pi^{\pm} p \to (\pi^{\pm}\pi^{\mp})p$ and $\pi^{\pm} p \to \pi^{\pm}(p\pi^{\pm}\pi^{\mp})$ at 16 GeV/c, AS A FUNCTION OF (3π) AND (p$\pi\pi$) MASS

Mass, GeV	$\pi^- p \to \pi_f^-(\pi_s^-\pi^+ p)$ $\left(\frac{d\sigma}{dt'}\right)_0 \cdot \frac{mb}{GeV^2}$	$\pi^- p \to \pi_f^-(\pi_s^-\pi^+ p)$ b, GeV^{-2}	$\pi^+ p \to \pi_f^+(\pi^+\pi^- p)$ $\left(\frac{d\sigma}{dt'}\right)_0 \cdot \frac{mb}{GeV^2}$	$\pi^+ p \to \pi_f^+(\pi^+\pi^- p)$ b, GeV^{-2}
All	1.4 ± 0.2	5.9 ± 0.4	1.6 ± 0.2	6.5 ± 0.5
1.2 -1.52	0.63 ± 0.08	11.7 ± 1.2	0.65 ± 0.08	11.8 ± 1.2
1.52-1.64	0.26 ± 0.03	7.5 ± 0.6	0.35 ± 0.05	8.3 ± 0.9
1.64-1.80	0.30 ± 0.03	4.7 ± 0.3	0.29 ± 0.04	4.6 ± 0.7
1.80-2.08	0.17 ± 0.03	2.5 ± 0.9	0.26 ± 0.04	5.3 ± 0.8
2.08-3.20	0.18 ± 0.03	4.0 ± 0.8	0.17 ± 0.03	3.7 ± 0.7

TABLE XVII

SLOPE b OF DIFFERENTIAL CROSS-SECTION $d\sigma/dt$, INTEGRATED CROSS-SECTION σ AND EXPONENT n OF THE ENERGY DEPENDENCE FOR THE REACTION $\pi^- p \to \pi^- \pi^- \pi^+ p$ versus 3π MASS. THE SYSTEMATIC ERRORS ARE GIVEN IN PARENTHESES

$m_{3\pi}$ [GeV]	25 GeV/c b [GeV/c^{-2}]	25 GeV/c σ [μb]	40 GeV/c b [GeV/c^{-2}]	40 GeV/c σ [μb]	11-40 GeV/c n [$\sigma \propto P_{inc}^n$]
0.8-1.0	14.3 ± 0.8	36.6 ± 3.3 (3.7)	14.9 ± 0.6	37.3 ± 2.2 (3.7)	-0.31 ± 0.11
1.0-1.1	11.7 ± 0.5	51.6 ± 3.6 (5.2)	12.6 ± 0.5	50.9 ± 2.3 (5.2)	-0.29 ± 0.10
1.1-1.2	10.0 ± 0.4	68.4 ± 3.4 (7.0)	10.7 ± 0.4	64.5 ± 2.2 (6.5)	
1.2-1.3	8.3 ± 0.4	71.7 ± 3.1 (7.6)	8.5 ± 0.4	63.5 ± 2.1 (6.4)	-0.29 ± 0.10
1.3-1.4	7.3 ± 0.4	56.5 ± 2.6 (7.0)	6.1 ± 0.4	53.9 ± 2.1 (5.5)	
1.4-1.5	7.2 ± 0.6	35.6 ± 2.3 (5.0)	7.2 ± 0.5	30.6 ± 1.5 (3.1)	-0.42 ± 0.11
1.5-1.6	6.2 ± 0.6	35.3 ± 2.1 (5.2)	7.2 ± 0.5	33.2 ± 1.5 (3.4)	
1.6-1.8	6.6 ± 0.5	80.9 ± 3.8 (11.0)	7.2 ± 0.3	72.5 ± 2.1 (7.4)	-0.50 ± 0.11
1.8-2.0	5.1 ± 0.6	48.5 ± 3.2 (7.0)	5.6 ± 0.6	44.0 ± 2.1 (4.6)	
	25 GeV/c		40 GeV/c		205 GeV/c
[0.8-1.2]	(157 ± 6) μb		(153 ± 5) μb		(160 ± 40) μb

TABLE XVIII

CROSS SECTION $(d\sigma/dt')_{t'=0}$ AND SLOPE PARAMETER b, FOR THE REACTIONS $\pi^\pm p \to (\pi^\pm \pi^+ \pi^-)p$ AND $\pi^\pm p \to \pi^\pm (p\pi^+\pi^-)$ AT 16 GeV/c, AS A FUNCTION OF (3π) AND $(p\pi\pi)$ MASS

Mass, GeV	$\pi^- p \to (\pi_f^- \pi_s^- \pi^+)p$		$\pi^+ p \to (\pi_f^+ \pi_s^- \pi^+)p$	
	$(\frac{d\sigma}{dt'})_0 \cdot \frac{mb}{GeV^2}$	b, GeV^{-2}	$(\frac{d\sigma}{dt'})_0 \cdot \frac{mb}{GeV^2}$	b, GeV^{-2}
All	4.9 ± 0.4	9.1 ± 0.3	3.7 ± 0.3	7.2 ± 0.3
0.6 -1.0	1.0 ± 0.1	14.6 ± 1.8	0.58 ± 0.05	11.3 ± 0.5
1.0 -1.12	1.2 ± 0.1	11.5 ± 0.8	0.8 ± 0.1	9.6 ± 0.7
1.12-1.28	1.2 ± 0.1	9.8 ± 0.7	1.0 ± 0.1	7.6 ± 0.6
1.28-1.40	0.57 ± 0.06	7.1 ± 0.5	0.40 ± 0.06	5.0 ± 0.6
1.40-3.00	1.3 ± 0.2	7.2 ± 0.7	1.0 ± 0.1	5.7 ± 0.3

TABLE XIX

SLOPE PARAMETER FOR $\pi \to (3\pi)$ AT 16 AND 40 GeV/c

Mass (3π) (GeV)	16 GeV/c (ABBCCH Collab[12])	40 GeV/c (Antipov et al.[24])
(1.0 -1.2)	(10.6 ± 0.9) GeV^{-2}	(11.2 ± 0.9) GeV^{-2}
(1.25-1.45)	(7.1 ± 0.5) GeV^{-2}	(6.7 ± 0.9) GeV^{-2}
	$(0.02 < t < 0.4$ GeV$^2)$	$(0.04 < t < 0.33$ GeV$^2)$

TABLE XX

THE DIFFERENCE IN SLOPE FOR $K^-p \to Q^-p$, $K^+p \to Q^+p$

Mom. (GeV/c)	Elastic Scattering Slope Diff. (GeV^{-2})	Q, Slope Diff. (GeV^{-2})
8	2.70 ± .16	1 ± 1
10	2.05 ± .13	1.8 ± 1.2
(12-14) }	1.60 ± .10	1.7 ± 0.4
13		1.1 ± 0.4
		A, Slope Diff.
		2.0 ± .9
15	1.5 ± 0.8	1.1 ± .8

TABLE XXI

ENERGY DEPENDENCE OF DIFFRACTION PROCESSES,

$\sigma \propto p^{-n}$; (5-20 GeV/c)

Process	Exponent, n
$K^0 \to Q^0$	0.59 ± .16
$K^+ \to Q^+$	0.60 ± .05
$K^- \to Q^-$	0.30 ± .10
$\pi^- \to A_1^-$	0.41 ± .11
$\pi^- \to A_3^-$	0.57 ± .2
$N \to N\pi$	0.5 ± .1
$N \to N\pi\pi$	0.4 ± .06
For Comparison, the Elastic Scattering Energy Dependence is:	
K^+p	~ 0.1
K^-p	~ 0.4
πN	~ 0.2
NN	~ 0.2

TABLE XXII

SLOPE OF DIFFERENTIAL CROSS-SECTIONS

Process	Slope (GeV^{-2})
$\gamma \to \rho$	~ 6-8
$\pi \to A_1$	~ 9-11
$\pi \to A_3$	~ 9
$K \to Q$	~ 5-7
$\bar{K} \to \bar{Q}$	~ 8-10
$N \to (N\pi\pi)_{1400}$	~ 10-11
$N \to (N\pi\pi)_{1700}$	~ 5

For comparison, the elastic slopes are ~

Process	Slope (GeV^{-2})
γN	~ 6
πN	~ 7-9
KN	~ 5-6
$\bar{K}N$	~ 7-8
NN	~ 9-10

TABLE XXIII

s-CHANNEL HELICITY-FLIP AMPLITUDE RATIOS IN THIS EXPERIMENT

AND IN πN SCATTERING FOR $.18 < |t| < .80\ GeV^2$

Amplitude Ratios*	Experimental Values of Density Matrix Elements			
	2.8 GeV	4.7 GeV	9.3 GeV	Average
Photoproduction				
$\lvert T_{01}\rvert^2/\lvert T_{11}\rvert^2 \simeq \rho^0_{00}$	$-.01 \pm .03$	$.07 \pm .02$	$-.01 \pm .02$	$.018 \pm .012$
$\lvert T_{-11}\rvert^2/\lvert T_{11}\rvert^2 \simeq \rho^1_{1-1} + \mathrm{Im}\ \rho^2_{1-1}$	$.04 \pm .05$	$.11 \pm .05$	$-.02 \pm .05$	$.04 \pm .03$
$\mathrm{Im}\ T_{01}/\lvert T_{11}\rvert \simeq 2\ \mathrm{Re}\ \rho^0_{10}$	$.16 \pm .03$	$.12 \pm .03$	$.14 \pm .02$	$.14 \pm .016$
$\mathrm{Im}\ T_{-11}/\lvert T_{11}\rvert \simeq \rho^0_{1-1}$	$-.06 \pm .03$	$-.05 \pm .03$	$-.10 \pm .02$	$-.08 \pm .02$
πN Scattering				
$\lvert F^0_{+-}\rvert/\lvert F^0_{++}\rvert$ Isospin 0 Exchange		6 GeV/c		$.15 \pm .02$

*The nucleon helicities in the photoproduction amplitudes listed are $\frac{1}{2}\ \frac{1}{2}$ (or $-\frac{1}{2}\ -\frac{1}{2}$).

TABLE XXIV

Reaction		p_{lab}(GeV/c)	Group	Analyzer	SCHC	TCHC
$\gamma \to \rho^0$		2.8,4.7,9.3	Ballam et al.	Azimuthal and polar angle of π.	Yes (They report a possible 2% flip contribution.)	No
		(2.7-4.0)	Gladding et al.	Same	Yes ($t < .5$ GeV)	No
		(4-6)	Struczinski et al.	Same	Yes	No
		(9-16)	Bulos et al.	Same	Yes	No
$\gamma \to \omega$		2.8,4.7,7.3	Ballam et al.	Same	Yes	No
$\gamma \to \phi$		2.8,4.7,7.3	Ballam et al.	Same	Consistent	No
	$\pm$	8.16	ABBCH	LPS selection, and polar angle of π	No	No
	$\pm$	16	ABBCCHLVW	Azimuthal study, normal to 3π and polar angle of π	No	No
$\pi \to A_1$	-	5-40	Kruse et al.		No	Slight violation
	-	40	Antipov et al.		No	Slight Violation
	-	4.5	Beketov et al.	Normal to 3π plane	No	Yes
$\pi^- \to A_3^-$		(5-2.5)	Ascoli et al.	π^+ polar angle	No	Yes (but not very strong)
	-	10	ABBCCHLVW	Azimuthal study, and normal to plane and π polar angles	No	No
$K \to Q$	-	14.3	Barloutaud et al.	Normal to $K\pi\pi$ plane, and polar angles of π	No	No
	0	(4-12)	Brandenburg et al.	Normal to $K\pi\pi$ plane	No	Yes (but not very strong)

TABLE XXIV Cont.

Reaction		p_{lab}(GeV/c)	Group	Analyzer	SCHC	TCHC
	1400	10,16	ABBCCHLVW	Azimuthal study, and normal, and polar	Data Insensitive	
	1700	10,16	ABBCCHLVW	Same	No	Yes
$p \to p\pi\pi$	All	8,16	ABBCH	LPS and polar angles of π	No	Yes
	All	25	Chapman et al.	Azimuthal	No	No
	1700	11.6	Oh et al.		No	Yes
	1500		Lamsa et al.	Azimuthal	No	Yes
	1700		Lamsa et al.	Azimuthal	No	Yes
$p \to n\pi$ / $\pi \to 3\pi$	All / All $\pm$	11.0	Evans et al.	Azimuthal	No	No

TABLE XXV

FACTORIZATION TEST IN πN AND pp REACTIONS

$$R_1 = \frac{\sigma(\pi^- p \to \pi^- p)}{\sigma(pp \to pp)} = 0.43$$

$$R_2 = \frac{\sigma(\pi p \to \pi(p\pi^0))}{\sigma(pp \to p(p\pi^0))} = 0.46 \pm .15$$

$$R_3 = \frac{\sigma(\pi p \to \sigma(p\pi^+\pi^-))}{\sigma(pp \to \delta(p\pi^+\pi^-))} = 0.35 \pm .18$$

$$R_4 = \frac{\sigma(\pi p \to \pi(p\pi\pi\pi))}{\sigma(pp \to \delta(p\pi\pi\pi))} = 0.45 \pm .15$$

TABLE XXVI

A FACTORIZATION TEST FOR γp, πp, and pp REACTIONS

	Momentum (GeV/c)		
	(6-10)	(10-14)	(14-18)
$R_1 = \frac{\sigma(\gamma p \to \rho^0 p)}{\sigma(\gamma p \to \rho^0 p\pi^+\pi^-)}$	0.053 ± 0.014	0.035 ± 0.014	0.055 ± 0.024
$R_2 = \frac{\sigma(pp \to pp)}{\sigma(pp \to pp\,\pi^+\pi^-)}$	0.064 ± 0.07	0.061 ± .008	0.060 ± 0.009
$R_3^+ = \frac{\sigma(\pi^+ p \to \pi^+ p)}{\sigma(\pi^+ p \to \pi^+ p\pi^+\pi^-)}$		0.061 ± .006	0.063 ± 0.003
$R_3^- = \frac{\sigma(\pi^- p \to \pi^- p)}{\sigma(\pi^- p \to \pi^- p\pi^+\pi^-)}$		0.052 ± 0.005	0.059 ± 0.003

TABLE XXVII

VALUES OF THE PARAMETERS R(H)

$R(H) = \frac{\sigma[Hp \to H(N\pi)]}{\sigma[Hp \to Hp]}$	p_{lab} [GeV/c]
$R(\pi^\pm) = 0.11 \pm 0.02$	8
$R(\pi^\pm) = 0.11 \pm 0.02$	16
$R(K^-) = 0.10 \pm 0.02$	10
$R(p) = 0.11 \pm 0.02$	12
$R(p) = 0.14 \pm 0.02$	24

TABLE XXVIII

ENERGY AND M^2-DEPENDENCE OF THE VARIOUS TRIPLE COUPLINGS

Triple Regge Term	s-dependence (fixed x)	M^2-dependence, (x-dependence) (fixed s, t)	
PPP	constant	$1/M^2$,	$1/(1-x)$
PPR	$1/\sqrt{s}$	$1/M^3$,	$1/(1-x)^{3/2}$
RRP	constant	constant,	(constant)
RRR	$1/\sqrt{s}$	$1/M$,	$(1/(1-x)^{1/2})$
		$M^2 = (1-x)s$	

References and Footnotes

1. U. Amaldi, Rapporteur's talk at IInd Aix-en-Provence Conference on High Energy Physics, p. 241, 1973.
2. U. Amaldi, "Elastic and Inelastic Processes at the ISR" CERN Report NP-73-19 (unpublished).
3. A. Diddens, "Very High Energy Hadron Experiments" CERN Report 1973 (unpublished).
4. L. Foa, Rapporteur's talk at IInd Aix-en-Provence Conference on High Energy Physics, p. 317, 1973.
5. G. Fox, "Inclusive Structure of Diffraction Scattering," California Institute of Technology Report, CATL-68-413, 1973.
6. F. Halzen, "Model Independent Features of Diffraction," Lectures, 1973.
7. J.D. Jackson, "Lectures on Hadronic Interactions at High Energies," LBL-2079, 1973.
8. G. Kane, "Phenomenology of Diffractive Reactions," Rutherford Laboratory report, PR-20, 1972.
9. G. Kane, "Implications of Experimental Data for Our View of the Pomeron," Michigan report UM-73-10, 1973.
10. G. Kane and J. Hartley, "Towards a General Description of Two-Body Hadron Reactions," Nuclear Physics, B57, 157 (1973).
11. D.W.G.S. Leith, SLAC preprint, SLAC-PUB-1141, invited talk at XVIth International Meeting on High Energy Physics, Batavia, Sept. 1972.
12. D.W.G.S. Leith, SLAC preprint, SLAC-PUB-1263, invited talk at the 8th Rencontre de Moriond, France, March 1973.
13. D.W.G.S. Leith, SLAC preprint, SLAC-PUB-1330, invited talk at Meeting of APS Division of Particles and Fields, Berkeley, August, 1973.
14. D.W.G.S. Leith, SLAC preprint, Supplement to SLAC-PUB-1330.
15. H. Lubatti, Washington University Preprint, VTL-PUB-9.
16. H. Miettinen and E.H. Groot, Talk presented at the VIIIth Rencontre de Moriond, Méribel Les Allues, 1973.
17. H. Miettinen, Invited talk at the IXth Rencontre de Moriond, Méribel Les Allues, 1974, and CERN Preprint, CERN-TH-1864.
18. D.R.O. Morrison, Lectures given at the Vth Hawaii Topical Conference in Particle Physics, 1973, and CERN Preprint, CERN-D.P.II-73-46.
19. K. Moffeit, "Diffractive Processes," SLAC-PUB 1314 (1973), invited talk at the International Symposium on Electron and Photon Physics, Bonn, 1973.
20. J.C. Sens, "Topics in Particle Physics at ISR," Lectures, 1973.
21. N.N. Khuri, Physical Review Letters 30, 1094, 1973.
22. L. Van Hove, Nuovo Cimento 28, 798, 1963 and Review Modern Physics 36, 655, 1964.
23. M.L. Good and W.D. Walker, Physical Review 120, 1854 (1960).
24. In a process $a + b \to a + b$ the square of the total centre of mass energy, s, is given by $s = M_a^2 + M_b^2 + 2M_b E_a^{lab}$, where M is the mass of the particle and E the laboratory energy. For collision on a proton target at energies about 5 GeV, this reduces to $s \sim 2p_{lab}$ where p_{lab} is the laboratory momentum of the incident particle.
25. V. Barger and R.J.N. Phillips, Nuclear Physics B32, 93 (1971).
26. G. Giacomelli, Rapporteur's talk at XVIth International Conference on High Energy Physics, Chicago, 1972.
27. S. Gjesdal et al. See reference 26.
28. J. Badier et al. See reference 26.
29. A.S. Belousov et al. See reference 26.
    D.O. Caldwell et al. See reference 26.
    T.A. Armstrong et al. See reference 26.
    J. Ballam et al. See reference 26.
30. U. Amaldi et al. Physics Letters 44B, 112 (1973).
31. S.R. Amendolia et al. Physics Letters 44B, 119 (1973).
32. G.B. Yodh, T. Pal and J.S. Trefil, Physical Review Letters 28, 1005 (1972).

33. T. Kycia, Paper presented at the 1974 SLAC Summer Institute Topical Conference--see these proceedings.

34. U. Amaldi et al. See reference 30.

35. G. Barbiellini et al. Physics Letters B39, 663 (1972) and Physics Letters B35, 355 (1971).

36. J. Chapman et al. Physical Review Letters 29, 1686 (1972).
G. Charlton et al. Physical Review Letters 29, 515 (1972).
T. Dao et al. Physical Review Letters 29, 1627 (1972).

37. D. Bogert et al. NAL Preprint 73/57 (1973).

38. D. Ritson, Talk presented at the SLAC Summer Institute, 1974--see these proceedings.

39. A. Martin, Physical Review 129, 1432 (1963) and Nuovo Cimento 42, 930 (1966).

40. H. Cornille and A. Martin, Physics Letters 40B, 671 (1972).

41. R.A. Carrigan, Physical Review Letters 24, 168 (1970).

42. U. Amaldi et al. Paper presented to the APS Division of Particle and Fields Meeting, Berkeley, August 1973.

43. G. Barbiellini et al. Physics Letters B39, 663 (1972); Physics Letters B35, 355 (1972).

44. V. Bartenev et al. NAL PUB 73/54.

45. A. Böhm et al. Physics Letters B49, 491 (1974).

46. J. Engler et al. CERN Preprint, 1973.

47. G. Beznogikh et al. Nuclear Physics B54, 97 (1973) and JINR preprint.

48. V. Hungerbuehler et al. Paper presented to the Berkeley APS Meeting of the Division of Particles and Fields, August 1973.

49. A.R. Dzierba et al. Physical Review D7, 725 (1973).

50. Yu. M. Antipov et al. Paper presented to the IInd Aix-en-Provence Conference on High Energy Physics, Sept. 1973.

51. R. Campbell et al. Nuclear Physics B64, 1 (1973).

52. See G. Kane's work in references 8, 9, 10.

53. M. Davier, Physics Letters B40, 369 (1972).

54. W.D. Walker et al. Physical Review 7, 2554 (1973).

55. P. Caso et al. Paper submitted to the XIV International Conference on High Energy Physics, Vienna (1968).
N.N. Biswas et al. Physical Review Letters 18, 273 (1967).

56. L. Barbaro-Galtieri, Private communication.

57. I. Ambats et al. Argonne preprint ANL/HEP-7329.

58. G. Brandenburg et al. Private communication.

59. V. Bartenev et al. NAL preprint NAL-73/73.

60. U. Amaldi et al. Physics Letters 43B, 231 (1973).

61. N.N. Khuri and T. Kinoshita, Physical Review 137B,, 720 (1965).

62. W. Bartel and A.N. Diddens, CERN Internal Report NP 73-4 (1973).

63. V.D. Apokin et al. IHEP preprint.

64. H. Cheng, J.K. Walker and T.T. Wu, Physics Letters B44, 283 (1973).

65. V. Barger, K. Geer, R.J.N. Phillips, Nuclear Physics B47, 29 (1972).

66. J.W. Allcock, N. Cottingham and C. Michael, CERN preprint TH-1765 (1973).

67. L. Durand and R. Lipes, Physical Review Letters 20, 637 (1968).

68. T.T. Chou and C.N. Yang, Physical Review Letters 20, 1213 (1968).

69. S. Frautschi and B. Margolis, Nuovo Cimento 56A, 1153 (1968).

70. J. Ballam et al. Physical Review Letters 24, 960, 1970.

71. J. Ballam et al. SLAC preprint SLAC-PUB-1092.

72. F. Bulos et al. Paper presented to XVIth International Meeting on High Energy Physics, Chicago (1972), and R. Giese, Ph.D. Thesis, Stanford University (1973).

73. G. Chadwick et al. SLAC preprint SLAC-PUB-1093.

74. For a discussion of these experiments see reference 12.

75. R. Anderson et al. SLAC preprint SLAC-PUB-1086.

76. H.J. Besch et al. Paper presented to the International Symposium on Electron and Photon Interactions at High Energies, Bonn, August 1973.

77. P. Bosetti et al. Nuclear Physics B62, 1 (1973).

78. K. Böckmann et al. Bonn University preprint, PIB-3-27 and paper presented to the IInd Aix-en-Provence Conference on Elementary Particle Physics, September 1973.

79. J.W. Cooper et al. Michigan preprint, UMBC 74-1.

80. D. Lissauer et al. Physical Review D6, 1852 (1972).

81. M. Longo et al. Physics Letters 36B, 560 (1971).
J.C. Vander Velde et al. Nuclear Physics B45, 1 (1972).

82. B. Gobbi, Invited talk at the 1974 SLAC Summer Institute Topical Conference --these proceedings.

83. V. Bartenev et al. "Diffraction Excitation of Nucleon Resonances in pp Collisions at Incident Proton Energies from (174-400) GeV/c," paper submitted to the APS Division of Particles and Fields Meeting, Berkeley, August 1973, and NAL preprint.

84. G.S. Abrams et al. Berkeley preprint LBL-2112.

85. M. Derrick et al. Argonne preprint, ANL/HEP-7332.

86. M. Miettinen et al. Physics Letters B43, 61 (1973).

87. H. Harari et al. Physics Letters B43, 49 (1973).

88. V. Hungerbuehler et al. Yale University preprint, and paper presented to the IInd Aix-en-Provence Conference on Elementary Particles, September 1973.

89. Yu. M. Antipov et al., Series of papers summarized by W. Kienzle in a paper presented to Joint CERN-IHEP Scientific Council, IHEP, Protrino, May 1973.

90. H.H. Bingham et al. Washington University preprint, VTL-PUB-16.

91. G. Brandenburg et al. SLAC PUB 1038 and Nuclear Physics B.

92. H.H. Bingham et al. Paper presented to the XVIth International Meeting on High Energy Physics, Batavia, September 1972.

93. CERN-Brussels-Krakow Collaboration. Paper presented to the XVIth International Meeting on High Energy Physics, Batavia, September 1972.

94. ABBCH Collaboration, Paper presented to the XVIth International Conference on High Energy Physics, Chicago, September 1972.
J. Ballan et al. SLAC preprint, SLAC-PUB-900.

95. P. Baillon et al. Paper presented to the XVIth International Conference on High Energy Physics, Chicago, September 1972.

96. G. Ascoli et al. Physics Review E7, 669 (1973).
U. Kruse et al.. Paper submitted to the XVIth International Conference on High Energy Physics, Chicago, September 1972.
Yu. M. Antipov et al. Nuclear Physics B63, 153 (1973).

97. G. Thompson et al. Physics Review Letters 32, 331 (1974).

98. M. Tabak et al. Berkeley preprint LBL-3010.

99. R. Barloutand et al. Saclay preprint, D.PhPE 73-01.

100. H.J. Lubatti and K. Moriyasu, Washington preprint, VTL-PUB-18.

101. D.W.G.S. Leith, Invited talk at the IVth International Conference on Experimental Meson Spectroscopy, Boston, April 1974 and SLAC-PUB-1440.

102. C. Peck et al. Caltech-SLAC Collaboration, private communication.

103. D.J. Herndon et al. LBL-1065 (Rev)/SLAC PUB 1108 (Rev), and A.H. Rosenfeld et al. LBL 2633/SLAC-PUB-1386, and R.J. Cashmore et al. LBL 2634/SLAC-PUB-1387.

104. See lectures by M. Davier in these proceedings.

105. D.R.O. Morrison, Rapporteur's talk, Kiev Conference and CERN/D.Ph.II/Phy 71-10 and 70-6.

106. D.R.O. Morrison, Physical Review 165, 1699 (1968).

107. Y. Oh et al. Paper submitted to XVI International Conference on High Energy Physics, Batavia, 1972.

108. See R. Barloutaud, Rapporteur's talk at Oxford Meeting on High Energy Physics, 1971.

109. Y. Goldschmidt—Cleremont, Review talk at the XVIth International Conference on High Energy Physics, Batavia, 1972.

110. J. Ballam et al. Paper presented to the Cornell International Conference on Electrons and Photons.

111. R. Arnold et al. Paper presented to the XVIth International Conference on High Energy Physics, Batavia, September 1972.

112. J. Ballam et al. Physical Review Letters 24, 960, 1970.

113. F. Gilman et al. Physics Letters 31B, 387, 1970.

114. A. de Lesquer et al. Physics Letters 40B, 277 (1972).
G. Cozzika et al. Physics Letters 40B, 281 (1972).
J. Deregel et al. Paper submitted to XVIth International Conference on High Energy Physics, Batavia, 1972.

115. O. Danielson et al. University of Stockholm preprint, 1971.

116. S. Ljung et al. Paper submitted to XVIth International Conference on High Energy Physics, Batavia, 1972.

117. W. Kittle, S. Ratti and L. Van Hove, Nuclear Physics B30, 333, 1971.

118. F. Liu et al. SLAC preprint, SLAC-PUB-1047.

119. H. Lubatti, Mini-review talk presented at IInd Aix-en-Provence Conference on Elementary Particle Physics, September 1973.

120. F. Winkelman, Physics Letters 48B, 273 (1974).

121. M.G. Albrow et al. CERN preprint, and paper submitted to the XVIth International Conference on High Energy Physics, Batavia, September 1972.

122. There are four HBC pp experiments at NAL: (a) 102 GeV/c--Michigan-Rochester collaboration; (b) 205 GeV/c--ANL-NAL collaboration; (c) 303 GeV/c--NAL-UCLA collaboration; (d) 405 GeV/c--Michigan-Rochester collaboration.

123. From a compilation by J. Whitmore (private communication).

124. J. Vander Velde (private communication).

125. S.J. Barish et al. ANL/HEP 7338 and paper presented to the APS Division of Particles and Fields Meeting, Berkeley, August, 1972.

126. M.G. Albrow, et al. CERN preprint, December 1972.

127. Aachen-CERN-Harvard-Genoa-Torino report, communicated by G. Goldhaber.

128. R. Schamberger et al. Paper submitted to the APS Division of Particles and Fields Meeting, Berkeley, August 1973.

129. S. Childress, et al. Paper submitted to the APS Division of Particles and Fields Meeting, Berkeley, August 1973.

130. K. Abe et al. "Measurement of $pp \to pX$ between 50 and 400 GeV/c," paper submitted to the APS Division of Particles and Fields Meeting, Berkeley, August 1973.

131. This data was originally presented in preliminary form at the Vanderbilt Conference on Inclusive Processes at High Energy, 1973. Corrections for instrumented failure have changed the cross-sections in the forward direction.

132. J. Vander Velde (private communication).

133. G.S. Abrams et al. LBL-2112 and paper submitted to the APS Division of Particles and Fields Meeting, Berkeley, August 1973.

134. F.C. Winkelmann et al. LBL-2113 and paper submitted to the APS Division of Particles and Fields Meeting, Berkeley, August 1973.

135. J. Bellettini et al. Paper presented to the IInd Aix-en-Provence Meeting on Elementary Particle Physics, September 1973.

136. R. Stroynowski, CERN/D.PhII/PHY-73-13.

137. Derevshchikov et al. See reference 4.

138. R. Cool et al. Paper presented at the XVIIth International Conference on High Energy Physics, London, July, 1974.

139. Abarbanel et al. Phys. Rev. Letters 26, 937 (1971); Ellis et al. Phys. Rev. D6, 1347 (1972).

140. CERN-Holland-Lancaster-Manchester Group, M.G. Albrow et al. CERN preprint; A. Capella et al. SLAC report no. SLAC-PUB-1252. References to earlier work may be found in this paper.

141. K. Abe et al. "Determination of Triple-Regge Coupling from a Study of Reaction $pp \to pX$ between 50 and 400 GeV/c," paper submitted to the IInd Aix-en-Provence International Conference on Elementary Particles, September 1973.

142. H.I. Miettinen and R.G. Roberts, Rutherford Lab Preprint RPP/T/40 (1973).

143. M. Bishari, Phys. Letters 38B, 510 (1972).

144. A. Capella et al. Orsay Preprint 72/73.

145. J. Vander Velde. Invited talk presented at the Vth International Conference on High Energy Collisions, Stony Brook, 1973.

146. N. Sakai and J.N.J. White, Nuclear Physics B59, 511 (1972) and Max-Plank Institute Preprint, June 1973.

147. Scandinavian Collaboration--unpublished data. Reviewed by H. Miettinen in references 16, 17.

Figure Captions

Fig. 1. Schematic of several peripheral and central amplitudes, and how they transform from impact parameter space to momentum transfer space.

Fig. 2. Schematic of the effect on the scattering amplitude in momentum transfer space, of adding extra partial waves.

Fig. 3. Illustration of the s-channel unitarity equations.

Fig. 4. Relationship between the total, elastic and inelastic overlap functions.

Fig. 5. Plots of hadron total cross-sections versus $(p_{lab})^{-1/2}$. The straight lines represent a Regge pole parametrization of the σ_T data below 30 GeV/c.

Fig. 6. Plot of the photon total cross-section data versus $(p_{lab})^{-1/2}$.

Fig. 7. Energy dependence of the $p^{\pm}$, $K^{\pm}$, $\pi^{\pm}$ cross-sections on hydrogen, up through 65 GeV.

Fig. 8. Energy dependence of Λp and Λn total cross-sections.

Fig. 9. Total photon cross-sections up through 30 GeV.

Fig. 10. Possible asymptotic energy dependence of the total cross-section.

Fig. 11. Total p-p cross-section as measured at Serpukov and the CERN ISR.

Fig. 12. The total pp cross-section measurements compared to the lower bound obtained from studies of cosmic-ray data.

Fig. 13. Energy dependence of the elastic pp cross-section.

Fig. 14. Energy dependence of the elastic $\pi^- p$, $K^- p$, and $p^- p$ cross-sections.

Fig. 15. The energy dependence of the ratio of the elastic to total cross-sections for pp scattering.

Fig. 16. The energy dependence of the ratio of the elastic to total cross-sections for $\pi^- p$ scattering.

Fig. 17. Differential cross-sections, $d\sigma/dt$, taken at (a) the ISR by the ACGHT group, and (b) at NAL by the US-USSR collaboration.

Fig. 18. Energy dependence of the slope of the elastic p-p differential cross-section for two regions of momentum transfer--(a) $|t| < 0.1$ GeV^2, (b) $0.15 \leq |t| \leq 0.5$ GeV^2.

Fig. 19. Compilation of the s-dependence of the slope of the pp scattering cross-section for small momentum transfers (i.e. $|t| < 0.12$ GeV^2).

Fig. 20. The differential cross-section, $d\sigma/dt$, in pp elastic scattering out to very large t, as measured by the ACGHT group at the ISR.

Fig. 21. The differential cross-section for pp elastic scattering from (3-1500) GeV/c. The dashed curve represents the fourth power of the electromagnetic form factor, $G(t) = 1/(1 - t/\mu^2)^2$, with $\mu^2 = 0.71$ GeV^2.

Fig. 22. Normalized differential cross-sections for pp elastic scattering, $(d\sigma/dt)/(d\sigma/dt)_0$, divided by $G^4(t)$ where $G(t)$ is the electromagnetic form factor.

Fig. 23. Differential cross-section for np elastic scattering from (13-21) GeV/c.

Fig. 24. Comparison of pp and np elastic scattering cross-sections at 19 GeV/c.

Fig. 25. Energy dependence of the slope for pp and np elastic scattering from (2-30) GeV/c.

Fig. 26. Slope of the forward neutron-proton elastic scattering cross-section, as a function of energy. The dashed line represents the behaviour of pp scattering in the same t-range.

Fig. 27. Production angular distribution for elastic $\pi^- p$ and $\Sigma^- p$ scattering at 23 GeV/c.

Fig. 28. The differential cross-section for $\pi^- p$ elastic scattering at 14 GeV/c. (Also shown for comparison, are the results of previous measurements at 15 and 16 GeV/c.)

Fig. 29. Differential cross-section for elastic $\pi^- p$, $K^- p$ and $\bar{p}p$ scattering at 25 and 40 GeV/c.

Fig. 30. Shrinkage of the differential cross-section for $\pi^- p$ elastic scattering.

Fig. 31. Two components of the forward elastic cross-section--an exponential part usually associated with the Pomeron contribution, and a "J_0" Bessel function piece which may be associated with the peripheral Regge contribution or with an additional peripheral part of the Pomeron. This second contribution causes an upward curvature in the cross-section at small t.

Fig. 32. The differential cross-section for $K^+ p$ and $K^- p$ elastic scattering at 5 GeV/c.

Fig. 33. The energy dependence of the slope of the cross-section (evaluated at $t = .2$ GeV^2) for elastic $\pi^\pm$, $K^\pm$ and $p^\pm$ scattering in hydrogen.

Fig. 34. The energy dependence of the slope parameter of the Pomeron contribution in $K^+ p$ scattering (shown as the shaded region) and $\pi^\pm p$ scattering (shown as the circles).

Fig. 35. π-π scattering angle distributions in the dipion rest system (θ) and invariant four-momentum transfer squared in π-π scattering for the reactions $\pi^- + p \rightarrow \pi^- \pi^+ + n$ and $\pi^- p \rightarrow \pi^- + \pi^- + \Delta^{++}$. Note that the scales for the sections of $M(\pi\pi)$ are nonlinear.

Fig. 36. Elastic and total cross-section determinations for $\pi^- - \pi^+$ and $\pi^- - \pi^-$ scattering as a function of the dipion invariant mass.

Fig. 37. Differential cross-section for scattering of $\pi^\pm$, $K^\pm$, $p^\pm$ on protons at 3 GeV/c.

Fig. 38. Differential cross-section for scattering of $\pi^\pm$, $K^\pm$, $p^\pm$ on protons at 3.65 GeV/c.

Fig. 39. Differential cross-section for scattering of $\pi^\pm$, $K^\pm$, $p^\pm$ on protons at 5 GeV/c.

Fig. 40. Differential cross-section for scattering of $\pi^\pm$, $K^\pm$, $p^\pm$ on protons at 6 GeV/c.

Fig. 41. Preliminary production angular distribution for 13 GeV/c $K^+ p$ and $K^- p$ elastic scattering.

Fig. 42. a. Production angular distribution for $p^{\pm}p$ elastic scattering at 10.4 GeV/c.
b. Production angular distribution for $K^{\pm}p$ elastic scattering at 10.4 GeV/c.

Fig. 43. Differential cross-section for pp elastic scattering at 50 and 400 GeV, in the very forward direction, showing the Coulomb scattering contribution.

Fig. 44. Differential cross-section for pp elastic scattering at two energies of the CERN ISR in the very forward direction, showing the Coulomb scattering contribution.

Fig. 45. Calculated energy dependence of the ratio of the real to imaginary parts of the forward scattering amplitude in pp elastic scattering, assuming the total cross-section stops rising at 100, 1000, 10,000 and 100,000 GeV, respectively.

Fig. 46. The measured energy dependence of the ratio of the real to imaginary parts of the forward pp scattering amplitude.

Fig. 47. The measured energy dependence of the ratio of the real to imaginary parts of the forward np scattering amplitude.

Fig. 48. The measured energy dependence of the ratio of the real to imaginary parts of the forward π^-p scattering amplitude.

Fig. 49. Two-component amplitudes from the model of Cheng-Walker-Wu,[64] Kane,[8,9,10] Barger-Geer-Phillips,[65] Allcock-Cottingham-Michael.[66] The two contributions are associated with a central process and a peripheral process respectively.

Fig. 50. Two-component amplitudes from the models of Durand-Lipes,[67] Chou-Yang,[68] Frautschi-Margolis.[69] The two components are associated with a pole term and a cut term respectively. The observed structure in the angular distribution comes from the interference of these two contributions.

Fig. 51. Fit to the ISR pp elastic scattering cross-section using the optical model approach of Durand and Lipes.[67]

Fig. 52. Schematic for the vector dominance model description of rho meson photoproduction.

Fig. 53. The decay correlations for $\gamma p \to \rho^0 p$ at 9.3 GeV, in the SLAC-Berkeley experiment using polarized photons.

Fig. 54. The energy dependence of the cross-section for $\gamma p \to \rho^0 p$.

Fig. 55. The cross section for $\gamma p \to \omega p$ as a function of energy, also showing the natural parity (σ^N) and unnatural parity (σ^U) contributions at 2.8, 4.7 and 9.3 GeV.

Fig. 56. The cross-section for the reaction $\gamma p \to \phi p$ as a function of energy.

Fig. 57. The differential cross-section for $\gamma p \to \rho^0 p$ at 9.3 GeV.

Fig. 58. The differential cross-section for $\gamma p \to \rho^0 p$ at energies from 9 to 16 GeV.

Fig. 59. The energy dependence of the slope of the differential cross-section for $\gamma p \to \rho^0 p$.

Fig. 60. Comparison of the data on the forward cross-section for $\gamma p \to \rho^0 p$ at 9 GeV.

Fig. 61. (a) Fits of $d\sigma/dt$ of ρ^0 photoproduction to sum of P and f exchange, utilizing Dual Absorption Model. (b) P and f exchange amplitude slopes as obtained from fits of $d\sigma/dt$. The errors in $\gamma p \to \rho^0 p$ are statistical only. The systematic uncertainties are estimated to be $\pm$ 10%.

Fig. 62. The differential cross section for the reaction $\gamma p \to \omega p$ at 2.8, 4.7 and 9.3 GeV(ϕ) and the natural parity contribution to the differential cross-section (-$\dagger$-).

Fig. 63. Reaction $\gamma p \to p\phi$ at 2.8, 4.7 and 9.3 GeV. Differential cross section (a) 2.8 and 4.7 GeV data combined; (b) 9.3 GeV; (c) shows the experimental values for $d\sigma/dt$ for ϕ photoproduction at 12 GeV as a function of $-t$ from 0.2 to 1.0 $(GeV/c)^2$.

Fig. 64. The differential cross-section for $\gamma p \to \Phi p$ for energies between (2-12) GeV.

Fig. 65. The slope of the differential cross-section for $\gamma p \to \Phi p$ as a function of energy.

Fig. 66. The energy dependence of the cross-section for $\gamma p \to \Phi p$ at $t = 0.6$ GeV^2.

Fig. 67. The elastic pp differential cross-section for momenta between 3 and 16 GeV/c.

Fig. 68. Schematic representation of the amplitudes in the two-component Pomeron model.

Fig. 69. The energy dependence of the cross-section for $\pi N \to \pi\pi N$.

Fig. 70. The energy dependence of $\pi N \to \pi(\pi N)$ where the $I = 3/2$ and $1/2$ πN contributions are displayed separately.

Fig. 71. The separate mass spectra for the $I = 1/2$ and $3/2$ contributions to the reactions $\pi^+ p \to \pi^+ (N\pi)^+$ at 8 and 16 GeV/c.

Fig. 72. The mass spectra for the various exchange isospin and (πN) decay isospin amplitudes in the reactions $\pi^\pm p \to (N\pi)\pi$ at 8 and 16 GeV/c.

Fig. 73. The cross-sections for $pp \to N(N\pi)$ as a function of energy. The contributions for $(N\pi)$ with isospin 3/2 and 1/2 are shown separately.

Fig. 74. The mass spectra in the reaction $pp \to N(N\pi)$, for $I = 0, 1$ in the t-channel, and $(N\pi)$ with isospin 1/2, are shown for incident proton momentum of 12 and 24 GeV/c.

Fig. 75. The mass spectra in the reaction $pp \to N(N\pi)$ for $I = 1$ in the t-channel and $(N\pi)$ with isospin 3/2, are shown for incident proton momentum of 12 and 24 GeV/c.

Fig. 76. (a) Invariant mass of the $p_p\pi^-$ system in the reaction $np \to p_n\pi^- p_p$ at 12.5 GeV/c. The shaded histogram is for events with $M(p_p\pi^-) < M(p_n\pi^-)$.

(b) Invariant mass of the $p_n\pi^-$ system. The shaded histogram is for events with $M(p_n\pi^-) < M(p_p\pi^-)$.

Fig. 77. Mass of the $p\pi^-$ system for $K^+n \to K^+\pi^- p$ at 12 GeV/c.

Fig. 78. The differential cross-section, $d\sigma/dt$, for three ranges of $M(p\pi^-)$, (a) $1.1 < M(p\pi^-) < 1.3$ GeV, (b) $1.3 < M(p\pi^-) < 1.5$ GeV, (c) $1.5 < M(p\pi^-) < 1.7$ GeV. The curves correspond to exponential fits with slopes equal to 14, 8 and 3.5 GeV^{-2}, respectively.

Fig. 79. Slope-mass correlation for $np \to (p_n\pi^-)p_p$. The slope b is determined by fitting the differential cross-section, $d\sigma/dt'$, to $Ae^{bt'}$ in each mass bin, for t intervals ranging from $0.02 < t' < 0.3$ GeV^2 near threshold to $0.05 < t' < 0.6$ GeV^2 in the higher mass bins.

Fig. 80. Mass distributions (events per 10 MeV) for the $p\pi^-$ system observed with carbon, copper, and lead targets. The efficiency of the apparatus vs. mass, shown by the dashed curve in (a), has not been unfolded.

Fig. 81. Distributions in $\cos\theta_J$ and Φ_J for the proton (p_n) in $np \to p_p(p_n\pi^-)$. The distributions are of the Gottfried-Jackson frame. (a) $-t' < 0.1$ GeV^2 and $M(p_n\pi)) < 1.4$ GeV; (b) $-t' > 0.1$ GeV^2 and $M(p_n\pi^-) < 1.4$ GeV; (c) $-t' < 0.1$ GeV^2 and $1.4 < M(p_n\pi^-) < 1.8$ GeV; (d) $-t' < 0.1$ GeV^2 and $1.4 < M(p_n\pi^-) < 1.8$ GeV.

Fig. 82. The mass distribution for $(\pi^\pm\pi^\pm\pi^-)$ and $(p\pi^+\pi^-)$ from the reactions $\pi^\pm p \to \pi^\pm\pi^+\pi^- p$ at 16 GeV/c. Below the ratio of the mass distributions for the π^+p and π^-p reactions are also shown.

Fig. 83. Mass distribution for $(N\pi\pi)$ for π and K induced reactions. The $(N\pi\pi)$ shows familiar resonance structure at low masses.

Fig. 84. Missing mass distribution in $pp \to pN^*$ for an incident proton energy of 260 GeV/c.

Fig. 85. The effective mass distribution for $(p\pi^+\pi^-)$ from 200 GeV/c $\pi^- p \to p\pi^+\pi^-\pi^-$.

Fig. 86. (a) The effective mass distribution for $(p\pi^+\pi^-)$ from 200 GeV/c $pp \to pp\pi^+\pi^-$. (b) and (c) show the mass spectra for the $p\pi^+$ and $p\pi^-$ subsystems.

Fig. 87. The cross-sections for the inelastic two prong events and for the separated isoscalar t-channel, $I = (N\pi)/2$ amplitude, as a function of beam momentum.

Fig. 88. The mass spectrum for $M(\Lambda\pi^-)$ from the reaction $\Sigma^- p \to \Lambda\pi^- p$ at 24.6 GeV/c. The curve is a Monte Carlo calculation of the Deck diagram in the figure.

Fig. 89. The cross-section for $\pi^- p \to \pi^-\pi^-\pi^+ p$ as a function of energy.

Fig. 90. The (3π) and (2π) effective mass distributions from the CERN IHEP experiment on $\pi^- p \to \pi^-\pi^+\pi^- p$ at 40 GeV/c.

Fig. 91. The effective mass distribution of $(\pi^+\pi^-\pi^-)$ from 200 GeV/c $\pi^- p \to \pi^+\pi^-\pi^- p$.

Fig. 92. The energy dependence of the cross-section for $\pi^- p \to A_1 p$ where A_1 is defined as $1000 < M(3\pi) < 1200$ MeV. $\hookrightarrow \rho\pi$

Fig. 93. The energy dependence of the cross-section for $\pi^- p \to A_2 p$ where A_2 is defined as $1200 < M(3\pi) < 1400$ MeV. $\hookrightarrow \rho\pi$

Fig. 94. The energy dependence of the cross-section for $\pi^- p \to A_3 p$ where A_3 is defined as $1500 < M(3\pi) < 1800$ MeV. $\hookrightarrow f\pi$

Fig. 95. The cross sections for the process $K_L^0 p \to K_S^0\pi^+\pi^- p$, and the subprocess $K_L^0 p \to Q^0 p$ as a function of energy.

Fig. 96. The cross section for $K^+ p \to Q^+ p$ as a function of energy for six regions of $(K\pi\pi)$ mass from (1200-1500) MeV.

Fig. 97. The mass distribution for the $K^*\pi$ system from the reaction $K^+ p \to K^*(890)\pi N$ at 5 GeV/c and 8.2 GeV/c for I = 1/2 and I = 3/2 amplitudes separately.

Fig. 98. The ratio of the cross sections $K^0 p \to Q^0 p$ and $\bar{K}^0 p \to \bar{Q}^0 p$ as a function of momentum.

Fig. 99. The energy dependence of the 3π amplitudes in the A_1 region.

Fig. 100. The differential cross section for $\pi^- p \to A^- p$ at 40 GeV/c. The A_1 region is here defined as the 1^+ spin parity amplitude for $1.215 \leq M(3\pi) \leq 1.415$ GeV.

Fig. 101. The energy dependence of the 3π amplitudes in the A_2 region.

Fig. 102. The differential cross-section for $\pi^- p \to A_2 p$ $(A_2 \to \rho\pi)$ at 25 and 40 GeV/c.

Fig. 103. The energy dependence of the 3π amplitudes in the A_3 region.

Fig. 104. The differential cross-section for $\pi^- p \to A_3 p$ $(A_3 \to f\pi)$ at 40 GeV/c.

Fig. 105. The energy dependence of the $K\pi\pi$ amplitudes in the Q and L regions.

Fig. 106. Scatter plot of $M(K\pi)$ against $M(K\pi\pi)$ for $K^- p \to K^- p\pi^+\pi^-$, $\bar{K}^0 p\pi^-\pi^0$ and $\bar{K}^0 n\pi^+\pi^-$ at 14 GeV/c.

Fig. 107. The production angular distribution for low mass $(K\pi\pi)$ in $K^- p \to K^- p\pi^+\pi^-$, $\bar{K}^0 p\pi^-\pi^0$ and $\bar{K}^0 n\pi^+\pi^-$ at 14 GeV/c.

Fig. 108. Exponential slope parameter, b, averaged over the interval $4 < P_{beam} < 12$ GeV/c and plotted versus the mass of the $K^*(890)^+\pi^-$ (squares) and the mass of the $K^*(890)^-\pi^+$ (circles).

Fig. 109. The mass dependence of the slope of the differential cross-section in $K^- p \to Q^- p$ at 14 GeV/c.

Fig. 110. The differential cross-section for $K^+ p$ and $K^- p$ elastic scattering at 13 GeV/c.

Fig. 111. The four-momentum transfer distribution, $d\sigma/dt'$, for the reaction $\pi^\pm p \to (\pi^\pm\pi^\pm\pi^-)p$ in the pion-dissociation sector.

Fig. 112. Differential cross sections for $K^0 p \to Q^0 p$ (squares) and $\bar{K}^0 p \to \bar{Q}^0 p$ (circles) over the momentum range 4 to 12 GeV/c. The scale of the ordinate is determined for neutral Q mesons decaying into $K_S^0\pi^+\pi^-$. The curves result from the following exponential fits:

$$\frac{d\sigma}{dt'}(Q^0 p) = 0.83 \exp(5.9t') \text{ mb/GeV}^2,$$

$$\frac{d\sigma}{dt'}(\bar{Q}^0 p) = 1.36 \exp(9.7t') \text{ mb/GeV}^2.$$

Fig. 113. The differential cross-section for $K^\pm p \to Q^\pm p$ at energies around 14.GeV/c.

Fig. 114. Reaction $\gamma p \to p\pi^+\pi^-$ at 9.3 GeV. Results of fits of the form

$$d\sigma^2/dtdM_{\pi\pi} = \left(d\sigma^2/dtdM_{\pi\pi}\right)_{t=0} \cdot e^{At}$$

in the interval $0.02 \leq t \leq 0.5$ GeV^2. The curve is from the Söding model.

Fig. 115. Mass spectra showing the elastic peak and the threshold enhancement for inelastic diffraction, for π, K, N and γ reactions.

Fig. 116. Plot of the slope of the differential cross-section, b, versus $1/(M^2 - m_i^2)$, where M is the mass of the 3π, $K\pi\pi$ or $N\pi$ diffractively produced systems, and M_i is the sum of the constituent masses.

Fig. 117. Schematic diagram for the peripheral production of $p\pi^+\pi^-$ system.

Fig. 118. Diagrams for the s-channel and t-channel production of $(N\pi\pi)$ systems.

Fig. 119. Mass spectrum for $(N\pi)$ in $\pi N \to \pi\pi N$ at 16 GeV/c.

Fig. 120. Mass spectrum for $(N\pi\pi)$ in $\bar{K}N \to \bar{K}(N\pi\pi)$ at 10 GeV/c.

Fig. 121. Mass spectrum for $(N\pi\pi)$ in $\bar{K}(N\pi\pi)$ collisions; 10 GeV/c K^- and (6-12) GeV/c K_L^0.

Fig. 122. Density matrix elements for ρ^0 photoproduction by polarized photons at 9.3 GeV.

Fig. 123. The momentum transfer dependence of the matrix element, ρ_{10}, for $\gamma p \to \rho^0 p$ at 2.8, 4.7 and 9.3 GeV. This matrix element indicates the presence of a spin flip amplitude.

Fig. 124. The momentum transfer dependence of the flip and non-flip isoscalar πN scattering amplitudes at 6 GeV/c.

Fig. 125. Schematic diagrams for elastic π^-, K^- and $\bar{p}$ scattering and diffractive production of $N^*(1690)$.

Fig. 126. The ratio of the elastic cross-section to the $N^*(1690)$ production cross-section for incident π^-, K^- and $\bar{p}$ at 8, 16 GeV/c, as a function of momentum transfer.

Fig. 127. A schematic of diffractive reactions studied in a test of factorization. The ratios R_1-R_4 refer to the ratio of the cross-section for the reactions when the top two vertices (pion and proton elastic scattering) are joined successively to the bottom four vertices representing proton diffraction into a proton plus zero, one, two or three pions respectively, e.g.

$$R_1 = \frac{\sigma(\pi p \to \pi p)}{\sigma(pp \to pp)} \quad , \quad R_2 = \frac{\sigma(\pi p \to \pi p \pi)}{\sigma(pp \to pp\pi)} \text{ , etc.}$$

Fig. 128. A schematic of diffractive reactions studied in a test of factorization. The ratios R_1, R_2, R_3 refers to the ratio of the cross-sections when each of the upper vertices ($\gamma \to \rho$, $p \to p$, $\pi \to \pi$) is connected with the two lower vertices representing proton diffraction into a proton or a $(p\pi\pi)$ system, respectively.

Fig. 129. Schematic diagrams for the diffractive production of $(p\pi^+\pi^-)$ systems in $\pi p \to (p\pi\pi)\pi$ and $pp \to (p\pi\pi)p$ reactions.

Fig. 130. The invariant cross-section for the process $K^-p \to pX^-$ at 25 and 40 GeV/c as a function of x.

Fig. 131. (a) The invariant cross-section $d^2\sigma/dt\,dx$, as a function of x, for the process $pp \to pX$. The cross-section exhibits a large hump for $0.2 < x < .8$ which is characteristic of the multiparticle production region, then a minimum for $0.8 < x < .9$, followed by a sharp peak for $0.9 < x < 1.0$ which is characteristic of diffractive quasi-elastic scattering shown diagrammatically in (b).

Fig. 132. The missing mass distribution in $pp \to pX$ at 100, 200, 300 and 400 GeV/c, as measured in the NAL HBC experiments.

Fig. 133. The invariant cross-section for $pp \to pX$ as a function of x for the 100 and 400 GeV/c NAL HBC experiments.

Fig. 134. The missing mass distribution in $pp \to pX$ at 200 GeV/c as measured in the NAL HBC experiment.

Fig. 135. The missing mass distribution in $pp \to pX$ at 200 GeV/c for each topology as measured in the 200 GeV/c NAL HBC experiment.

Fig. 136. The missing mass distribution in $pp \to pX$ at the ISR, as measured by the ACGHT group.

Fig. 137. The missing mass distribution in $pp \to pX$ at 300 GeV/c as measured by the Columbia-Stony Brook collaboration.

Fig. 138. The invariant cross-section for $pp \to pX$ as a function of x, for $100 \leq x \leq 750$ GeV^2, as measured by the Rutgers-Imperial College group. Data is presented in four t intervals.

Fig. 139. The invariant cross-section for $pp \to pX$ as a function of $s^{-1/2}$ for x = 0.83 and 0.91.

Fig. 140. The invariant cross-section for $pp \to pX$ as a function of x, for a fixed $P_T = 0.8\ GeV^2$. Data comes from the CHLM group at the ISR, for $\sqrt{s} = 22$, 31 and 45 GeV.

Fig. 141. The differential cross-section, $d\sigma/dt$, for $pp \to pX$, as a function of the missing mass. Data comes from the 200 GeV/c NAL HBC experiment.

Fig. 142. The t-dependence for the production of the diffraction peak in $pp \to pX$ at high energies.

Fig. 143. Missing mass spectra for $pp \to pX$ as measured by the CHLM group at the ISR at $s = 930\ GeV^2$ and for $t = 0.35$, 0.55, 1.05 and $1.75\ GeV^2$.

Fig. 144. Missing mass distribution at fixed t for $\sqrt{s} = 53$ GeV, as measured by the CHLM group at the ISR. Data is presented for $t = 1.2$ and $1.4\ GeV^2$.

Fig. 145. Differential cross-section for $pp \to pX$ for $x = 0.87$ and for $s = 108$ and $752\ GeV^2$.

Fig. 146. Differential cross-section for $pp \to pX$ for missing mass squared $\sim 40\ GeV^2$.

Fig. 147. Differential cross-section for $pp \to pX$ for $8 \leq M^2 \leq 14\ GeV^2$.

Fig. 148. P_T^2 distributions for small missing masses in $pp \to pX$. Preliminary data from the 100, 400 GeV/c NAL HBC experiments.

Fig. 149. (a,b) P_T^2 distribution for large missing masses in $pp \to pX$. Preliminary data from the 100, 400 GeV/c NAL HBC experiments.

Fig. 150. The effective mass distribution of $(\pi^+\pi^-\pi^-)$ from 200 GeV/c $\pi^-p \to \pi^-\pi^-\pi^+p$.

Fig. 151. The effective mass distribution for $(p\pi^+\pi^-)$ from 200 GeV/c $\pi^-p \to p\pi^+\pi^-\pi^-$.

Fig. 152. Schematic diagram for the pion dissociation process.

Fig. 153. The missing mass squared distribution for $\pi^-p \to pX$ at 200 GeV/c.

Fig. 154. The missing mass squared distribution for $\pi^-p \to pX$ at 200 GeV/c.

Fig. 155. The missing mass squared distribution, topology by topology, for $\pi^-p \to pX$ at 200 GeV/c.

Fig. 156. The momentum transfer distribution, topology by topology, for $\pi^-p \to pX$ at 200 GeV/c.

Fig. 157. The momentum transfer distribution for $\pi^-p \to pX$ at 200 GeV/c for $M^2 \leq 10\ GeV^2$ and $10 < M^2 < 40\ GeV^2$.

Fig. 158. Comparison between x dependences for p inclusive invariant cross sections in pp interactions and π^-p interactions. The relativ normalization is arbitrary, o:s = $551\ GeV^2$, $p_\perp \sim .15$ GeV/c (CHLM); ■:s = $380\ GeV^2$, integrated over $p_\perp$ (Berkeley NAL).

Fig. 159. The charged particle multiplicity distribution for $\pi^-p \to$ anything (solid curve), and for pion diffraction (dashed curve).

Fig. 160. Schematic diagram for the diffractive dissociation of an incident particle with a system of charged multiplicity, n, and mass M.

Fig. 161. The mean charged multiplicity for all events, $\pi^-p \to$ anything, is plotted against the square of the available center of mass energy, while the multiplicity of the diffractive system in $\pi^-p \to Xp$, is plotted against the square of the mass of the diffractive system.

Fig. 162. The rapidity spectrum of a "typical" diffractive event.

Fig. 163. The rapidity spectrum of a "typical" non-diffractive event.

Fig. 164. Behaviour of the density of events as a function of $\bar{\eta}$ and $\delta(\bar{\eta})$ (see text) for various charged multiplicities at C.M. energy $\sqrt{s} = 62.8$ GeV. The curves are polynomial interpolation of the points of equal density.

Fig. 165. (a,b) Three dimensional representation of the density of events as a function of $\bar{\eta}$ and $\delta(\bar{\eta})$ for various charged multiplicities at the two extreme ISR energies.

Fig. 166. Derevshchikov et al. data on x dependence of the π^-p interactions of two incident momenta and two p intervals. ×:p_{inc} = 42 GeV/c, o:p_{inc} = 51 GeV/c.

Fig. 167. The x-distribution for the fast forward π^+ in $\pi^+p \to \pi^+$ + (anything at 8 GeV/c. The distribution is broken down topology by topology.

Fig. 168. The x-distribution for the fast forward π^+ in $\pi^+p \to \pi^+$ + (anything) at 16 GeV/c. The distribution is broken down topology by topology.

Fig. 169. The x-distribution for the fast forward π^+ in $\pi^+p \to \pi^+$ + (anything) at 23 GeV/c. The distribution is broken down topology by topology.

Fig. 170. The x-distribution for the forward π^+ in the reactions $\pi^+p \to p\pi^+\pi^0$, $n\pi^+\pi^+$ at 8, 16 and 23 GeV/c.

Fig. 171. The x-distribution for the forward π^+ and backward proton in the reaction $\pi^+p \to \pi^+\pi^-\pi^+p$ at 8, 16 and 23 GeV/c.

Fig. 172. The invariant cross-section, $d\sigma/dt$, for the proton dissociation in $\pi^+p \to \pi^+$ + (anything) at 8, 16 and 23 GeV/c. The ISR pp data are also shown, after being extrapolated to small $p_\perp$ and adjusted for the difference in π^+p and pp total cross-sections (see text for details).

Fig. 173. The missing mass distribution in $\pi^-p \to pX^-$ at 25 and 40 GeV/c.

Fig. 174. The invariant cross-section as a function of x for $\pi^-p \to pX^-$ at 25 and and 40 GeV/c.

Fig. 175. The slope of the differential cross-section for $\pi^-p \to pX^-$ at 25 and 40 GeV/c as a function of x.

Fig. 176. The missing mass distribution in $K^-p \to pX^-$ at 25 and 40 GeV/c.

Fig. 177. The slope of the production angular distribution in $K^-p \to pX^-$ at 25 and 40 GeV/c as a function of x.

Fig. 178. The invariant cross-section for the process $K^-p \to pX^-$ at 25 and 40 GeV/c as a function of x.

Fig. 179. The triple Regge calculation of the single particle inclusive cross-section. (a) is the forward scattering amplitude for the single particle inclusive process, and (b) represents diagrammatically the square of that amplitude, (c) is the triple Regge generalization of diagram (b).

Fig. 180. A qualitative map of the M^2 and x dependence of the triple Regge terms for inclusive proton scattering.

Fig. 181. Plot of G_{PPP} and G_{PPR} versus t for the five fits discussed in the text. For all fits $G_{PPR}(t)$ lies within the shaded band. The shape and magnitude of $G_{PPP}(t)$ depends on the fit assumption.

Fig. 182. Inclusive proton spectra at various ISR energies at fixed p_T versus x.

Fig. 183. The effective meson trajectory obtained in a triple Regge analysis of the data on $pp \to pX$ at $s = 1995$ GeV^2.

Fig. 184. The mass dependence of the forward scattering peak in $pp \to pX$ showing the decomposition into contributions arising from leading protons and from fragmentation protons.

Fig. 185. Inelastic proton spectra at various ISR energies and fixed p_T at high x.

Fig. 186. The effective Pomeron trajectory obtained by fitting the PPP triple Regge term to the $pp \to pX$ data at $s = 551$ and 930 GeV^2 (after correction for elastic contamination, resolution and the contribution of fragmentation protons). The crosses (x), indicate the Pomeron trajectory obtained from an analysis of elastic pp scattering at the same energies.

Fig. 187. The differential cross-section for $pp \to pX$ for $8 \leq M^2 \leq 14$ GeV^2.

Fig. 188. The PPP cross-section obtained from ISR data at $0.15 < t < 1.25$ GeV^2, extrapolated down to $t \sim 0.056$ GeV^2 and compared to the NAL inelastic pp scattering data. The PPP term was obtained in the mass interval $5 < M^2 < 30$ GeV^2.

Fig. 189. The momentum transfer distribution for $\pi^-p \to pX$ at 200 GeV/c for $M^2 < 10$ GeV^2 and $10 < M^2 < 40$ GeV^2.

Fig. 190. The differential cross-section, $d\sigma/dt$, for $pp \to pX$, as a function of the missing mass. Data comes from the 200 GeV/c NAL HBC experiment.

Fig. 191. The P_T^2 dependence of protons from the NAL HBC experiments. 0, 102, 405 GeV/c for four prong or higher multiplicities and with $0.9 < x < 0.6$; • 102, 205, 303, 405 GeV/c for four prong events with $M^2 < 10$ GeV^2.

Fig. 192. The inelastic overlap function calculated from the 1500 GeV/c proton-proton data.

Fig. 193. The impact structure of proton-proton scattering at $\sqrt{s} = 53$ GeV. Shown are Im $h_{el}(s,b)$ and the inelastic and elastic overlap functions extracted from the experimental data. The "black disc limit" indicates the maximum value of the inelastic overlap function allowed by unitarity (i.e., 100% absorption).

Fig. 194. a) Inelastic overlap functions calculated from the $\sqrt{s} = 21, 31, 44,$ and 53 GeV ISR data.
b) Difference of the $\sqrt{s} = 53$ and 31 GeV inelastic overlap functions, $\Delta G_{inel}(s,b)$, showing that the cross-section increase comes from a rather narrow region around 1 fermi.

Fig. 195. The decomposition of the imaginary part of the elastic scattering amplitude into its components assuming t-channel helicity conservation in inelastic diffraction.

Fig. 196. Schematic illustration of the origin of the mass slope correlation in the peripheral model of inelastic diffraction.
a) M^2 small. The non-flip amplitude dominates, faking a steep exponential t-dependence in the small t region.
b) M^2 large. Several helicity amplitudes contribute appreciably. The differential cross-section is much flatter than in the case a).

Fig. 197. Differential cross-section for the process $pp \to pn\pi^+$ at 19 GeV/c for $(n\pi^+)$ masses in the interval (1200-1300) MeV. The curves illustrate the possible peripheral diffraction mechanism: -·-·- is the contribution of the imaginary part of the non-flip amplitude given by $Ae^{at}\,|J_0(R\sqrt{-t})|^2$; ---- is the smooth background (Be^{bt}) which includes real contributions.

Fig. 198. a) The differential cross-section, $d\sigma/dt'$, for $np \to (p\pi^-)p$ at 12.5 GeV/c for $m(p\pi^-)$ less than 1200 MeV.
b) The differential cross-section, $d\sigma/dt'$, for $np \to (p\pi^-)p$ at 12.5 GeV/c for four ranges of $(p\pi^-)$ mass--(a) $M(p\pi^-) < 1300$ Mev, (b) $1300 < M(p\pi^-) < 1450$ MeV, (c) $1450 < M(p\pi^-) < 1600$ MeV, (d) $1600 < M(p\pi^-) < 1800$ MeV.

Fig. 199. Illustrations of how central channels opening up may generate a peripheral $\Delta G_{inel}(s,b)$. (a) The inelastic cross-section stays constant but the elastic differential cross-section shrinks. $G_{inel}(s,b)$ decreases at $b = 0$ and increases at $b > 1$ fermi.
(b) Same as for (a) but some new channels open up causing the inelastic cross-section to rise. The new processes are central, and they compensate the decrease of $G_{inel}(s, b = 0)$ due to shrinkage. As a result the cross-section increase appears peripheral. (c) The difference of the two overlap functions of (b).

Fig. 200. The energy dependence of the total cross-section at high energy--which way will it go?

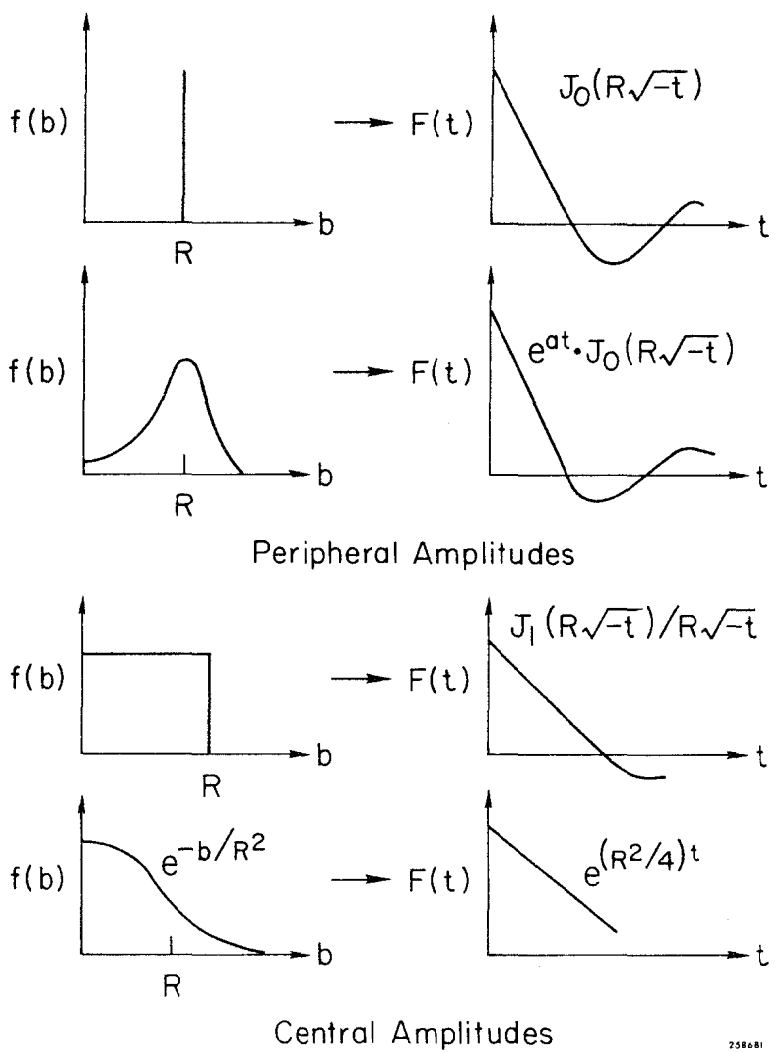

Figure 1

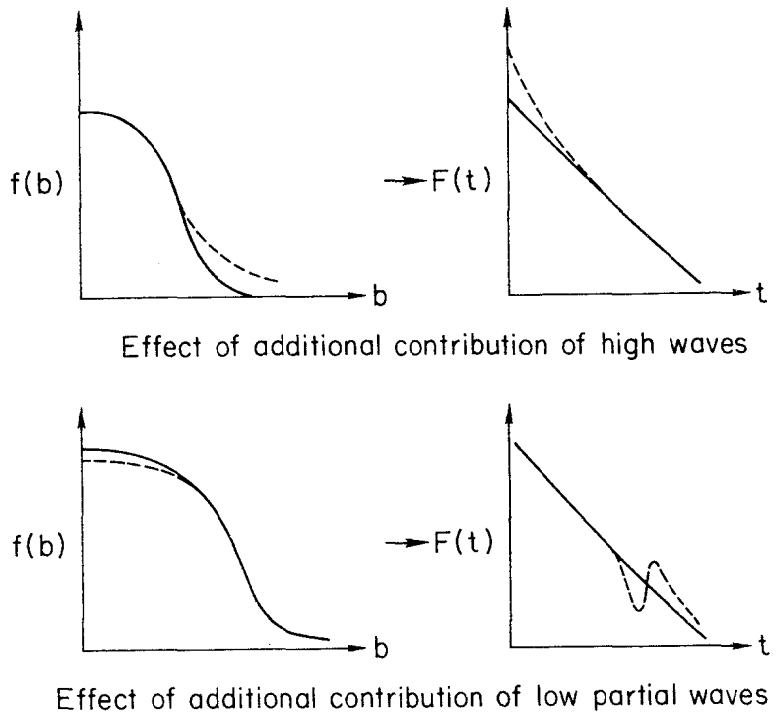

Figure 2

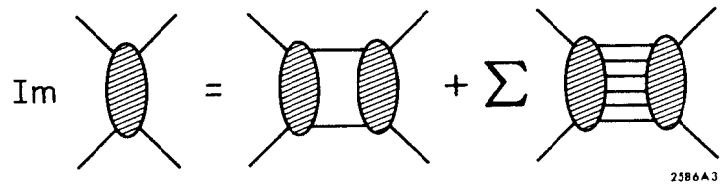

Figure 3

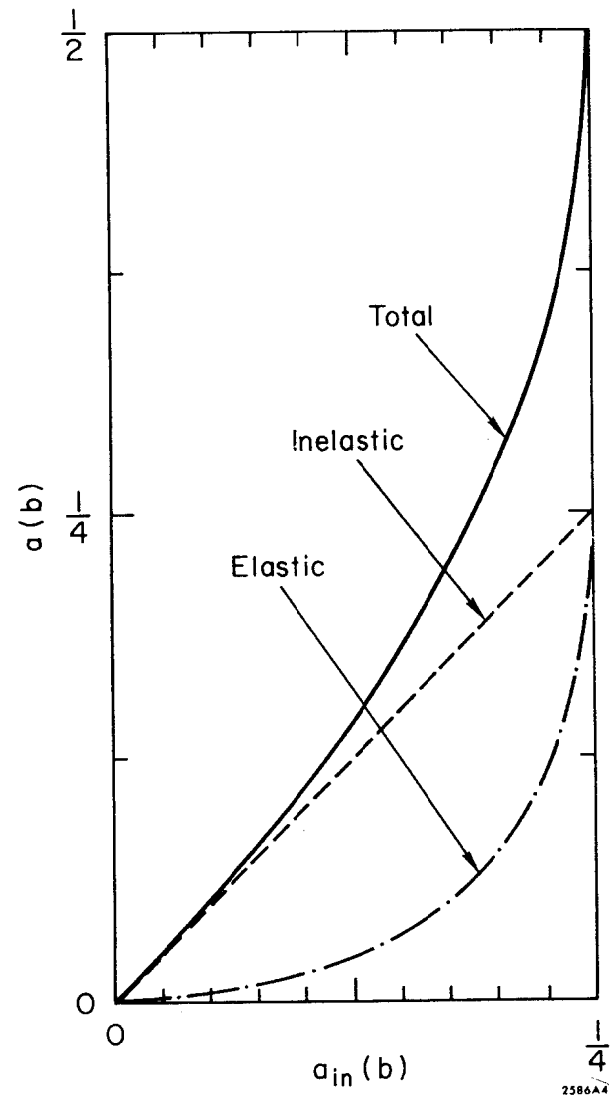

Figure 4

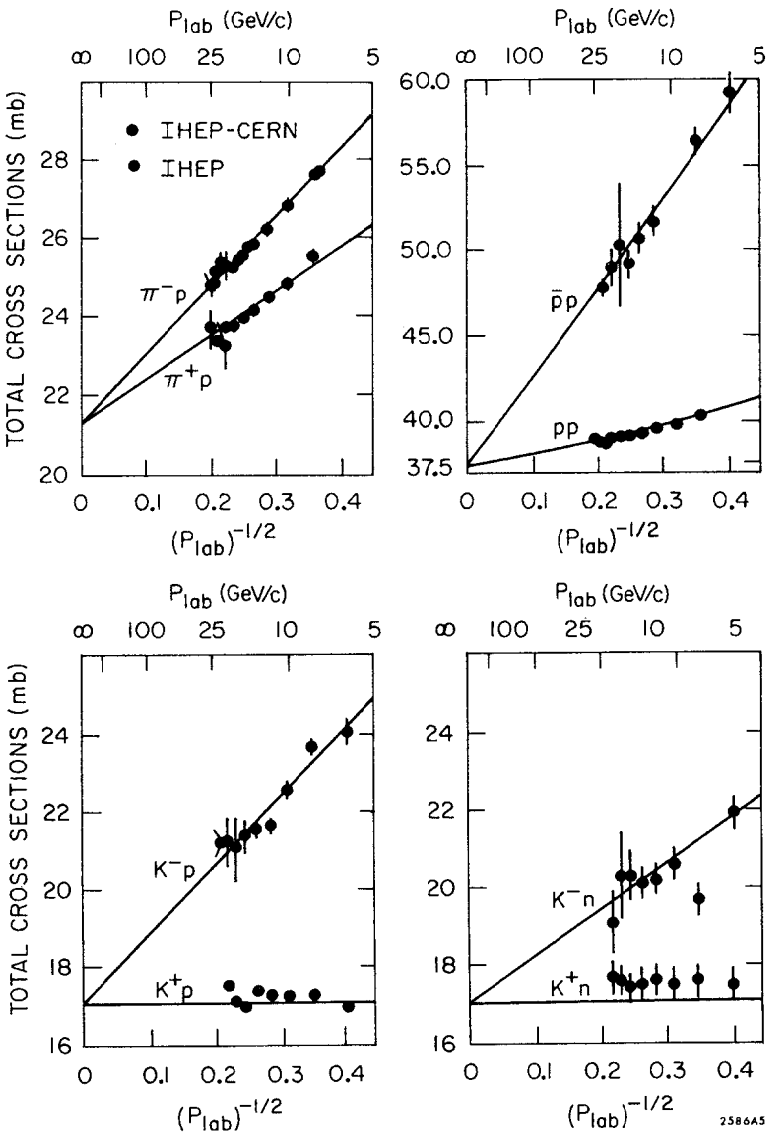

Figure 5

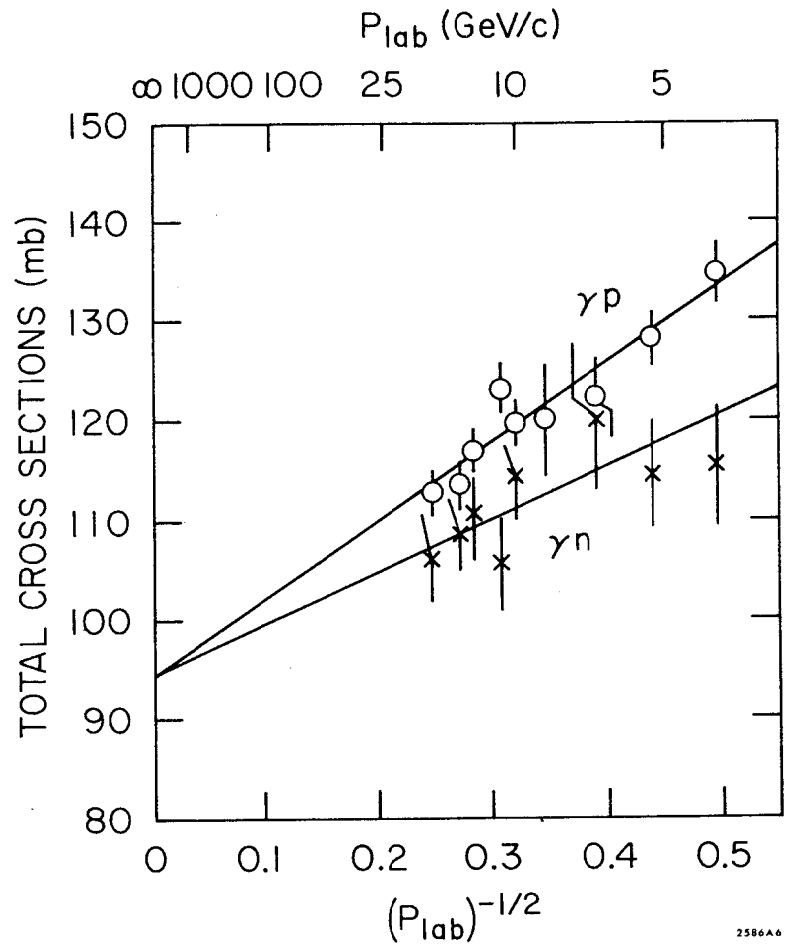

Figure 6

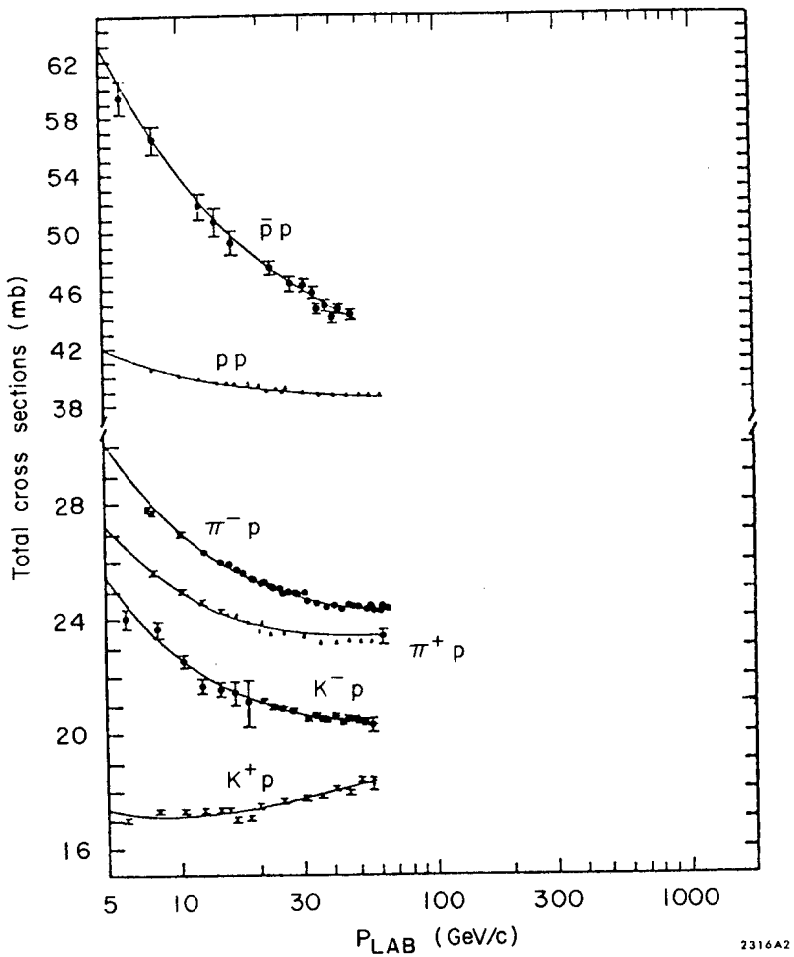

Figure 7

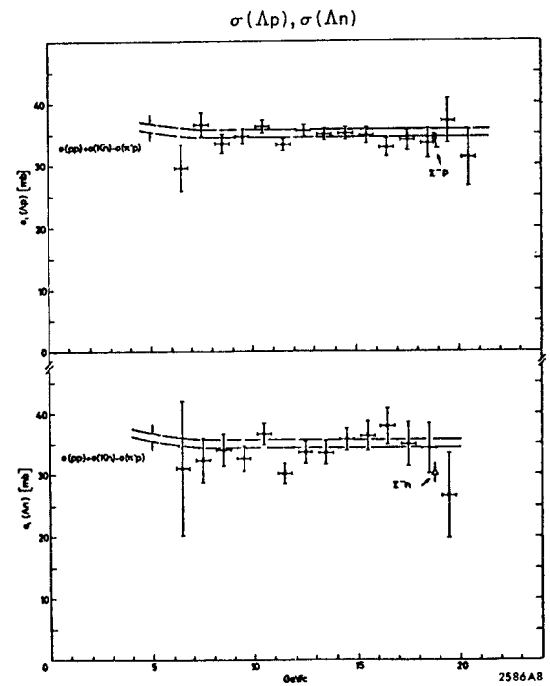

Figure 8

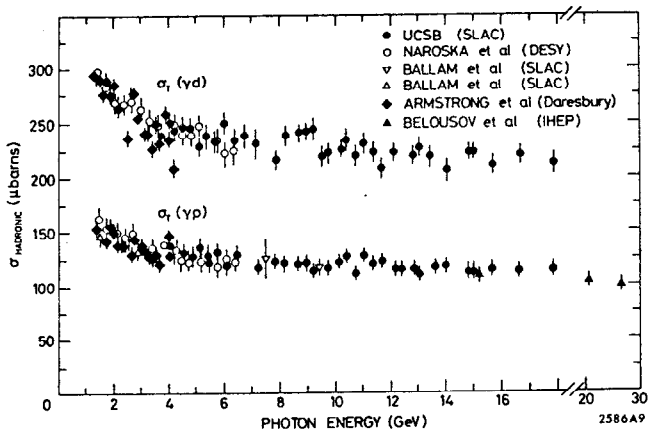

Figure 9

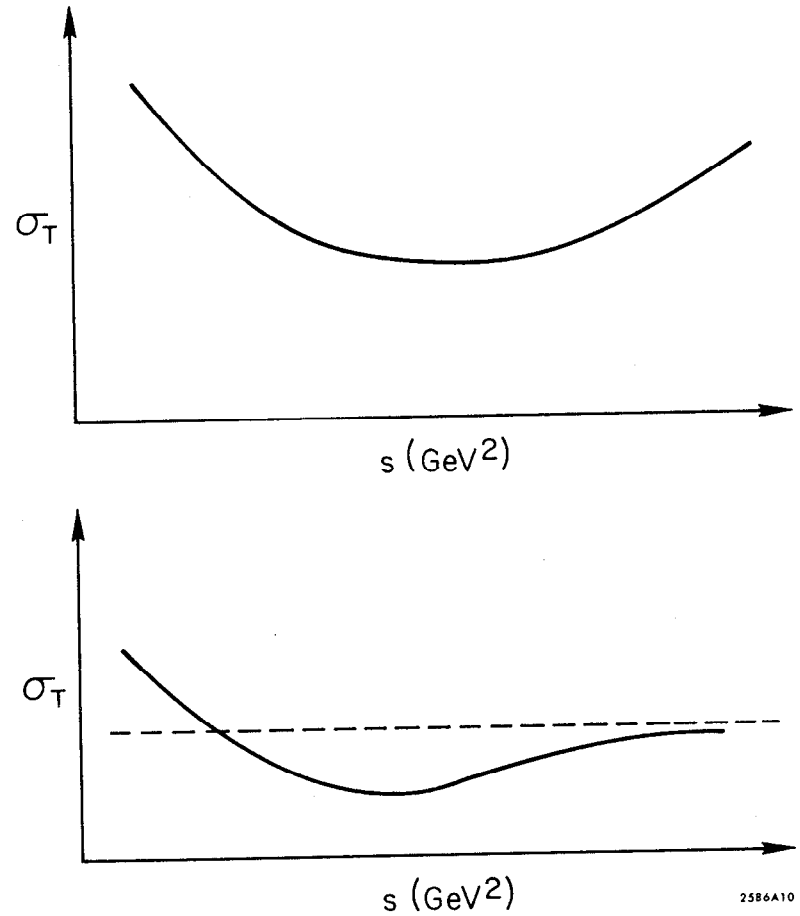

Figure 10

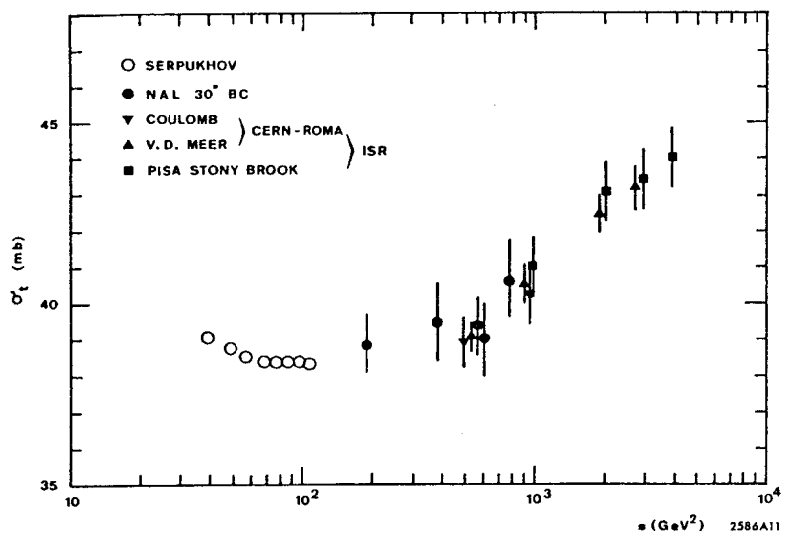

Figure 11

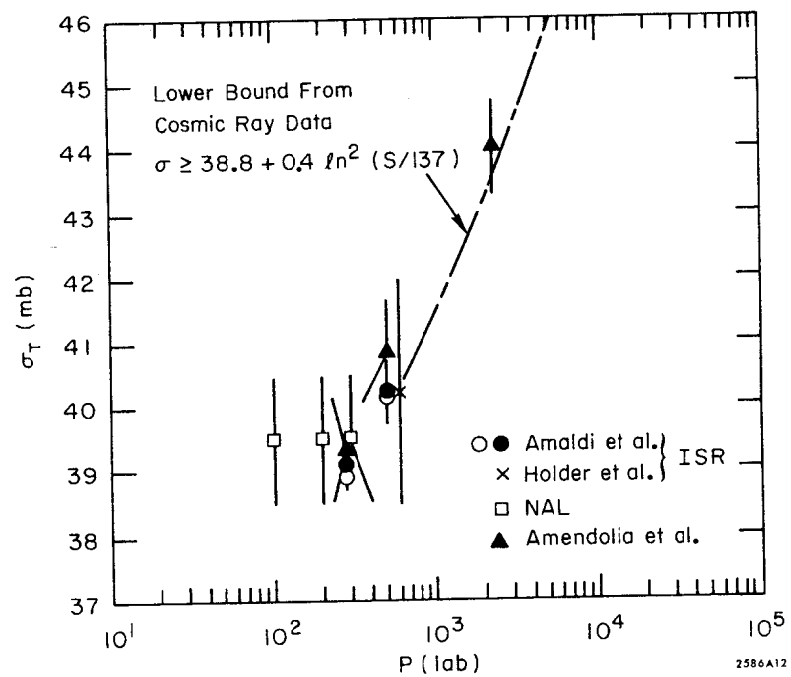

Figure 12

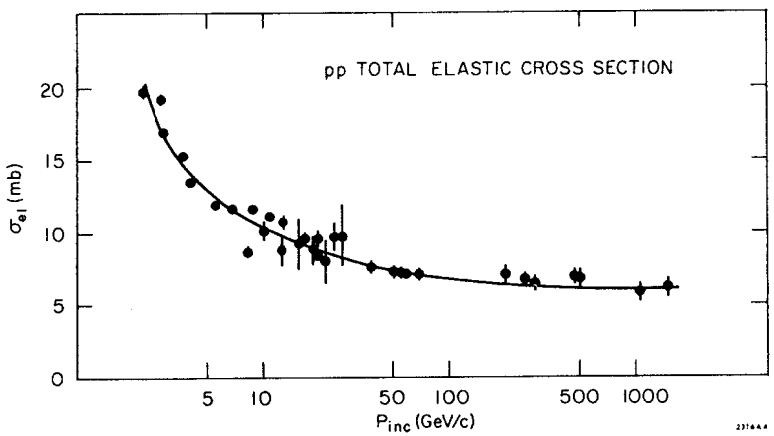

Figure 13

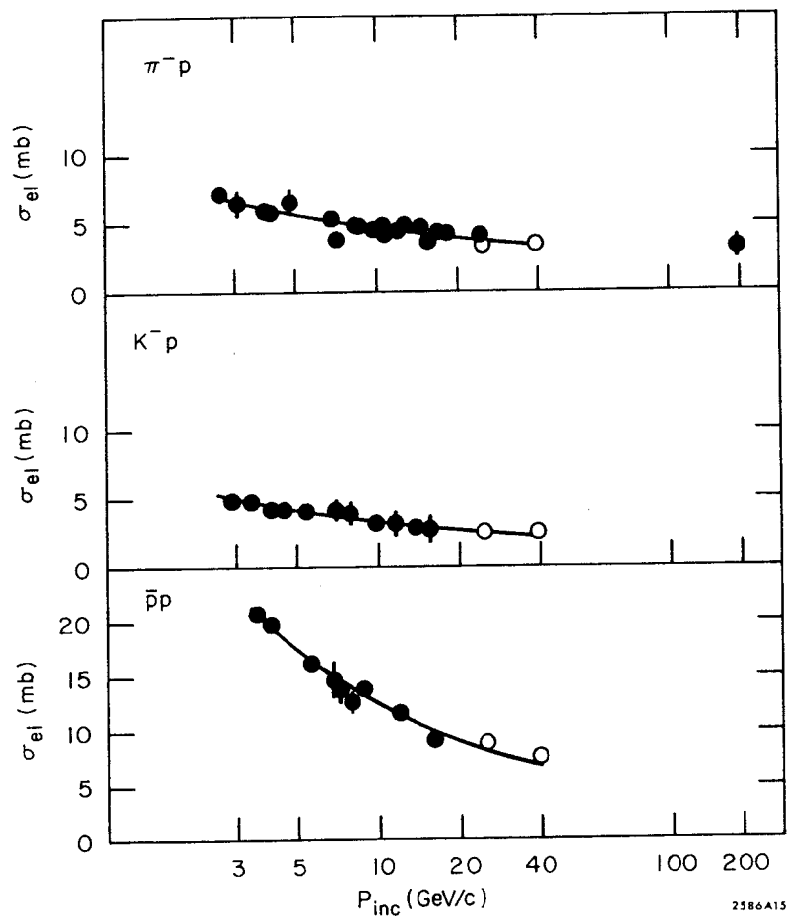

Figure 14

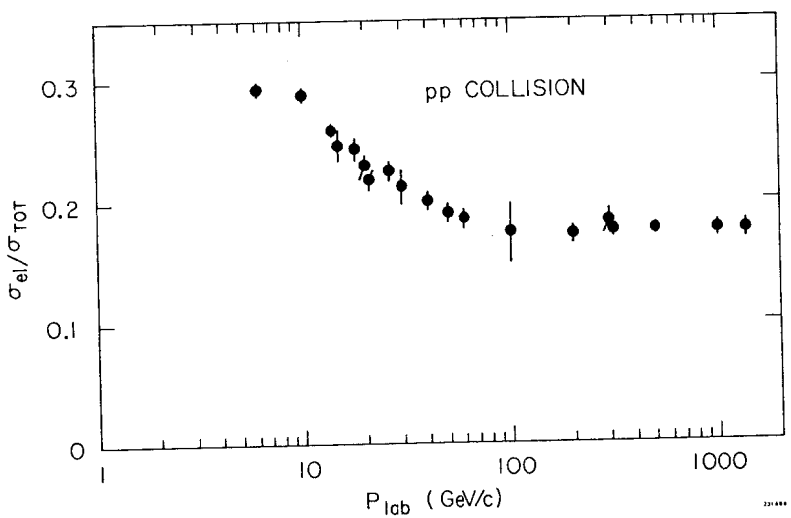

Figure 15

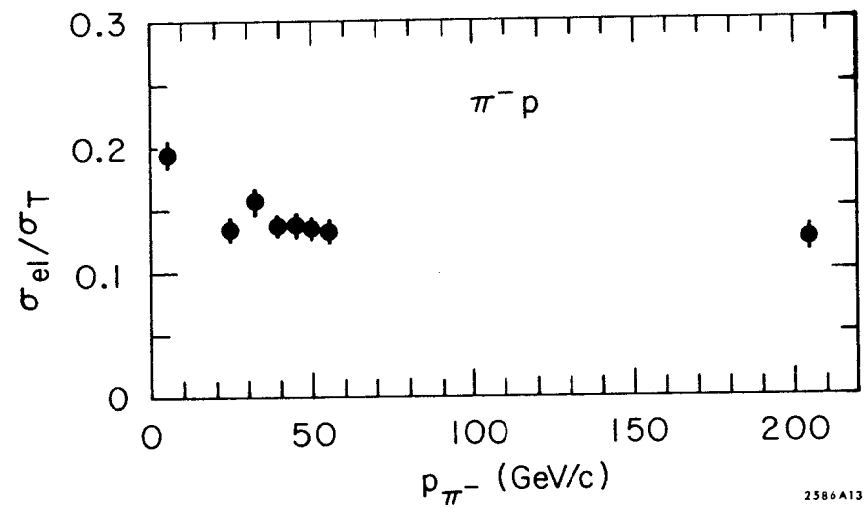

Figure 16

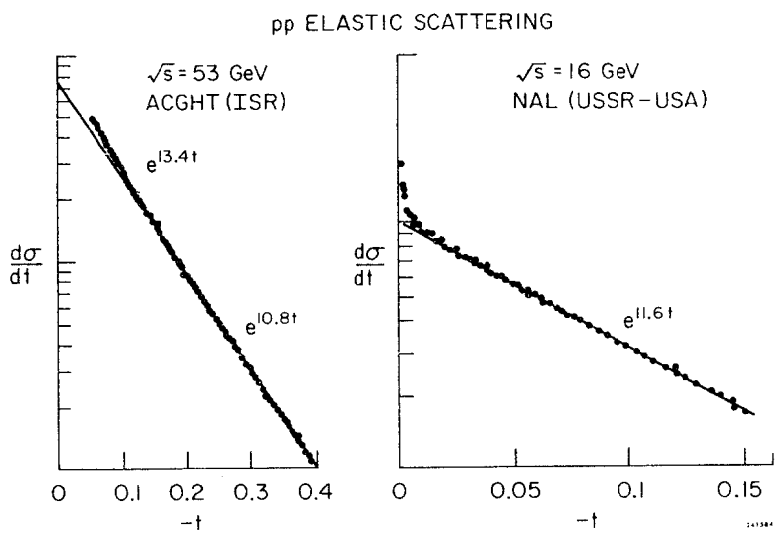

Figure 17

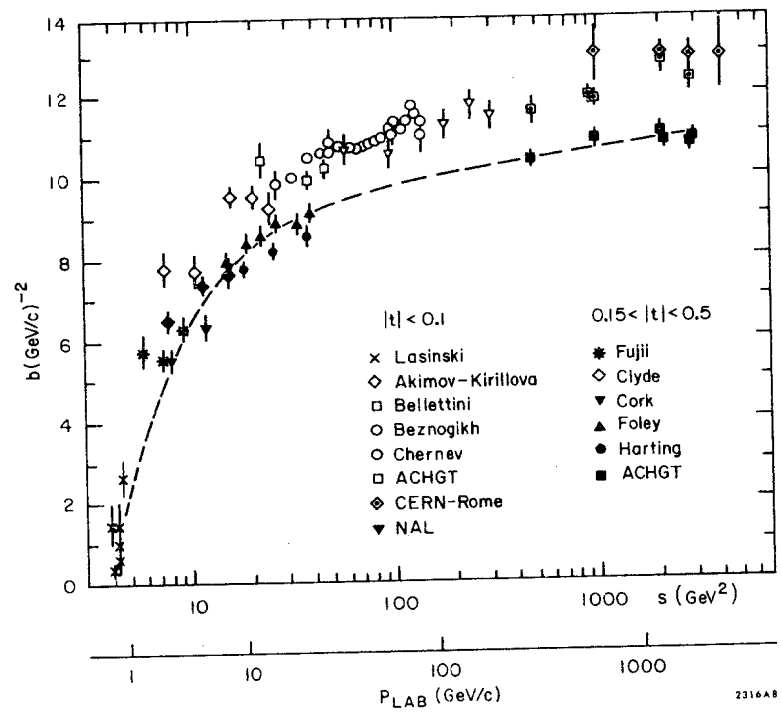

Figure 18

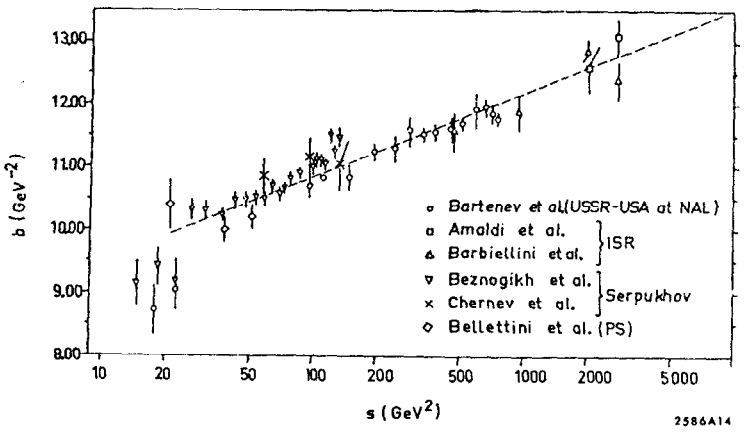

Figure 19

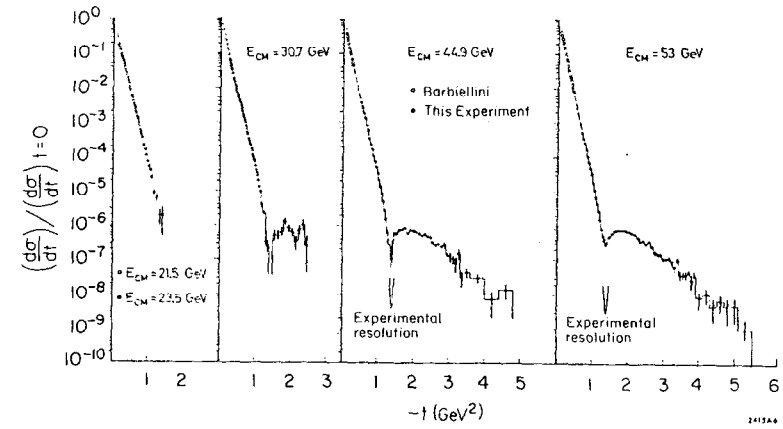

Figure 20

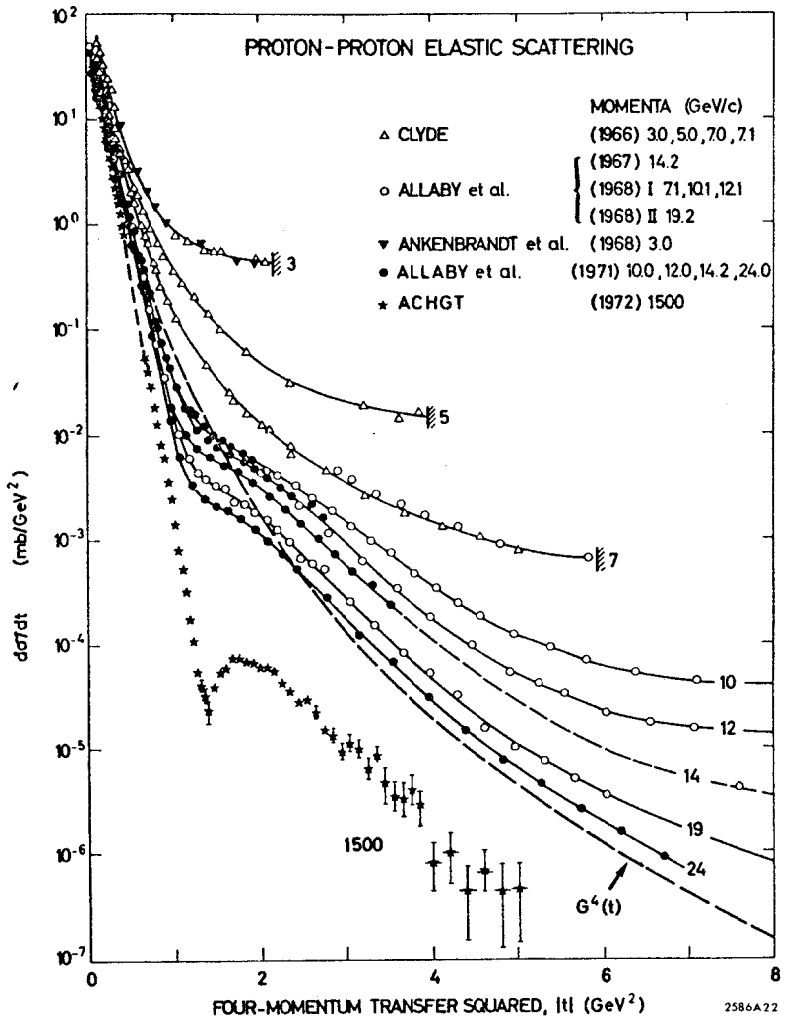

Figure 21

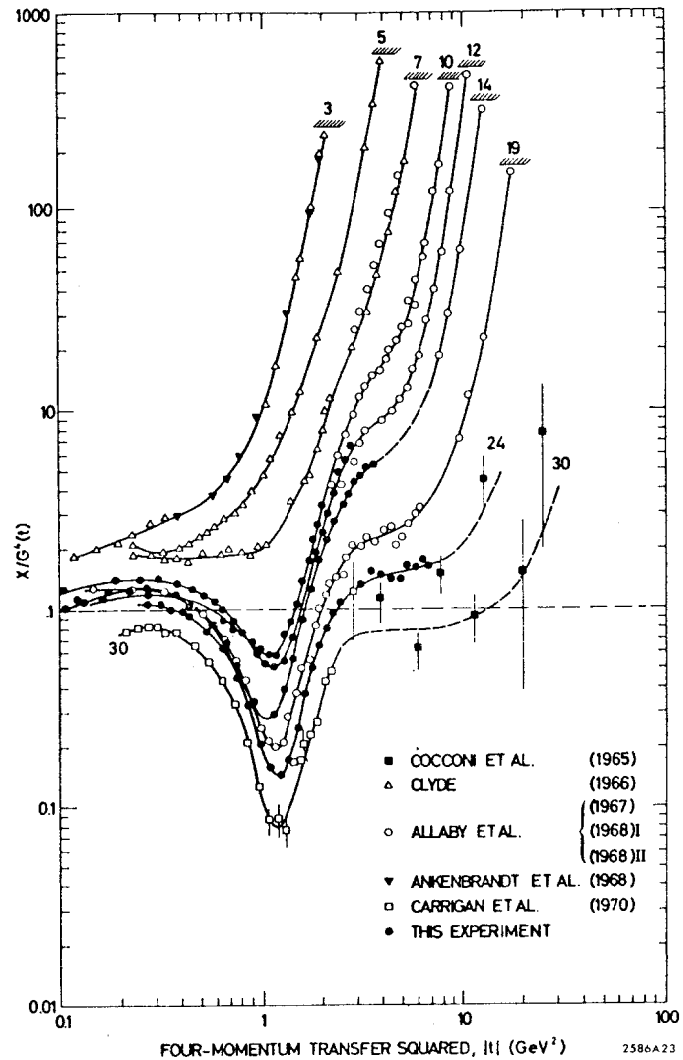

Figure 22

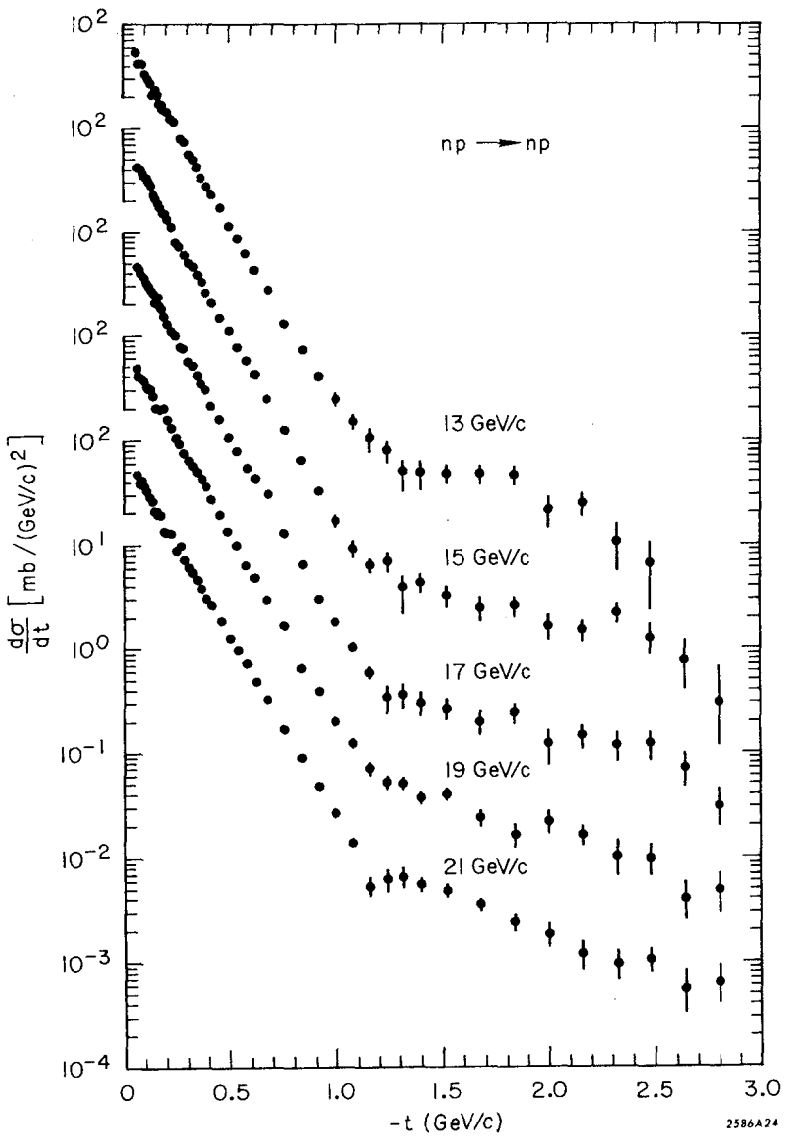

Figure 23

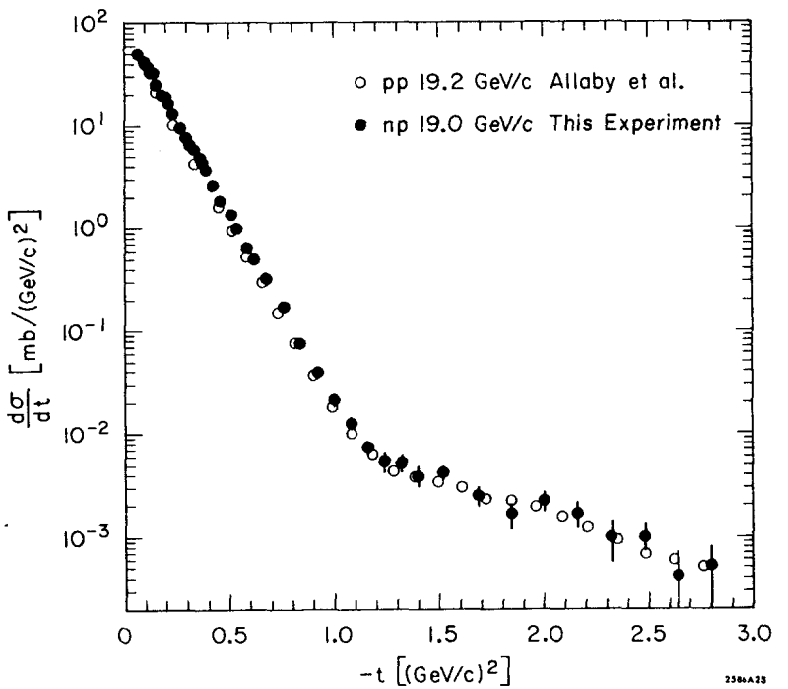

Figure 24

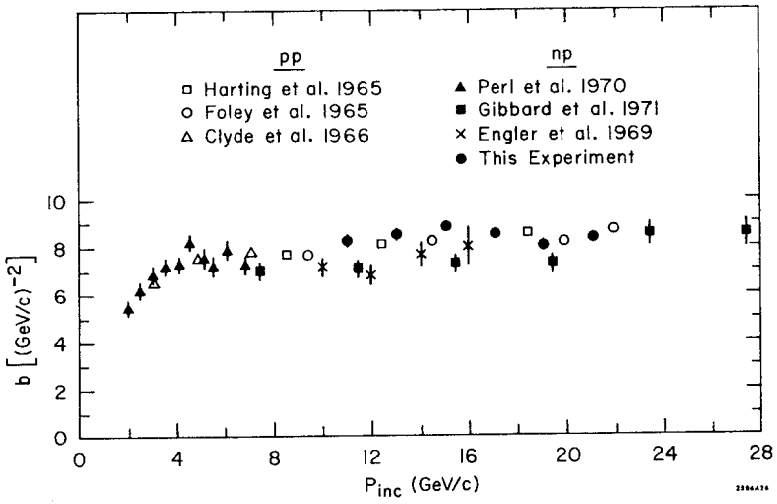

Figure 25

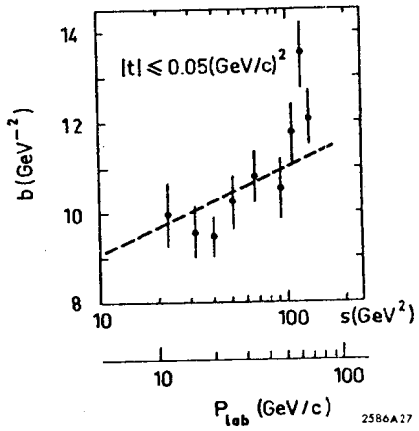

Figure 26

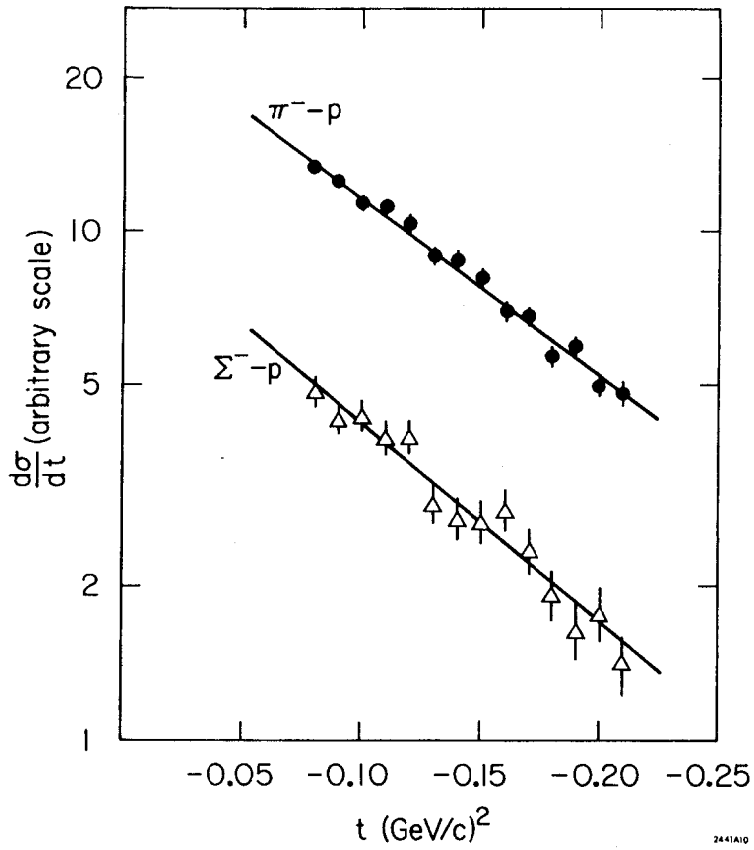

Figure 27

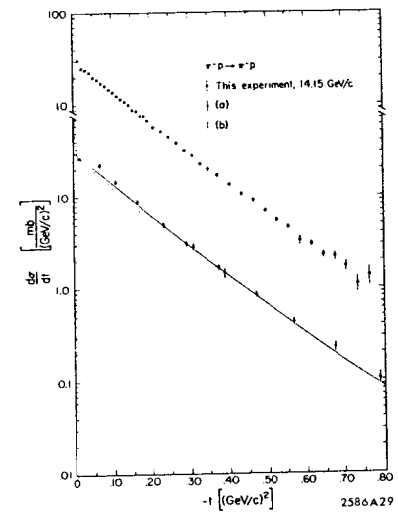

Figure 28

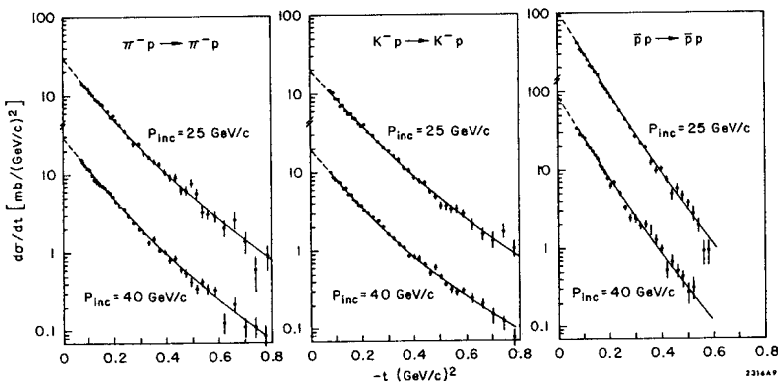

Figure 29

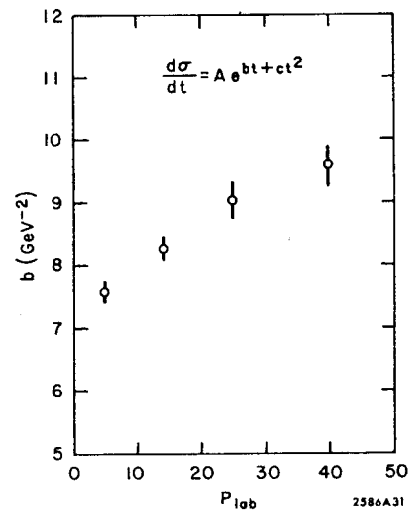

Figure 30

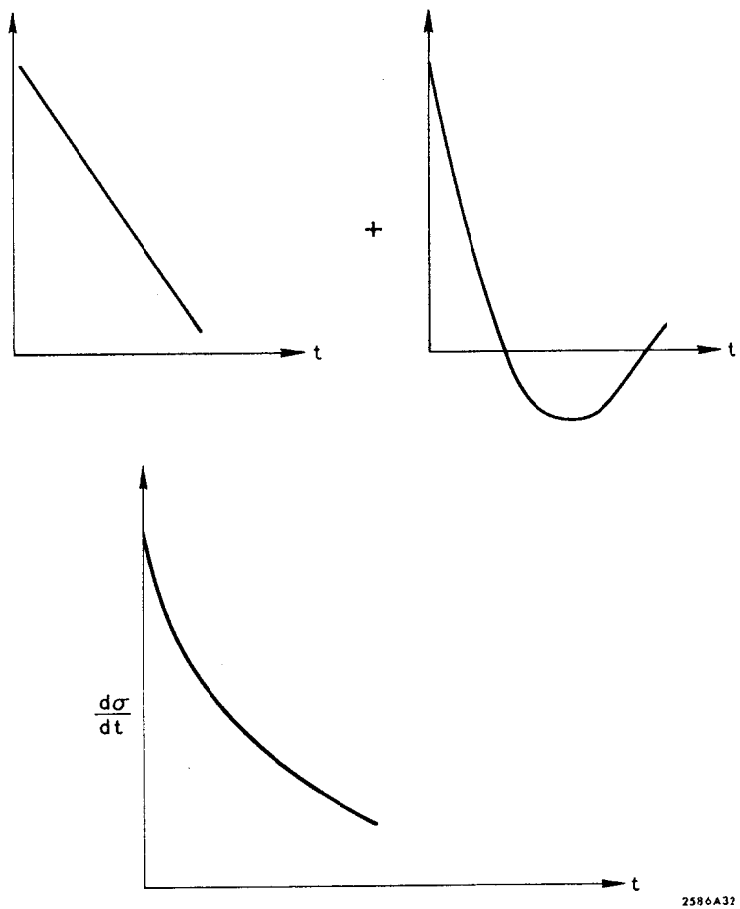
t
+
t
dσ/dt
t
2586A32

Figure 31

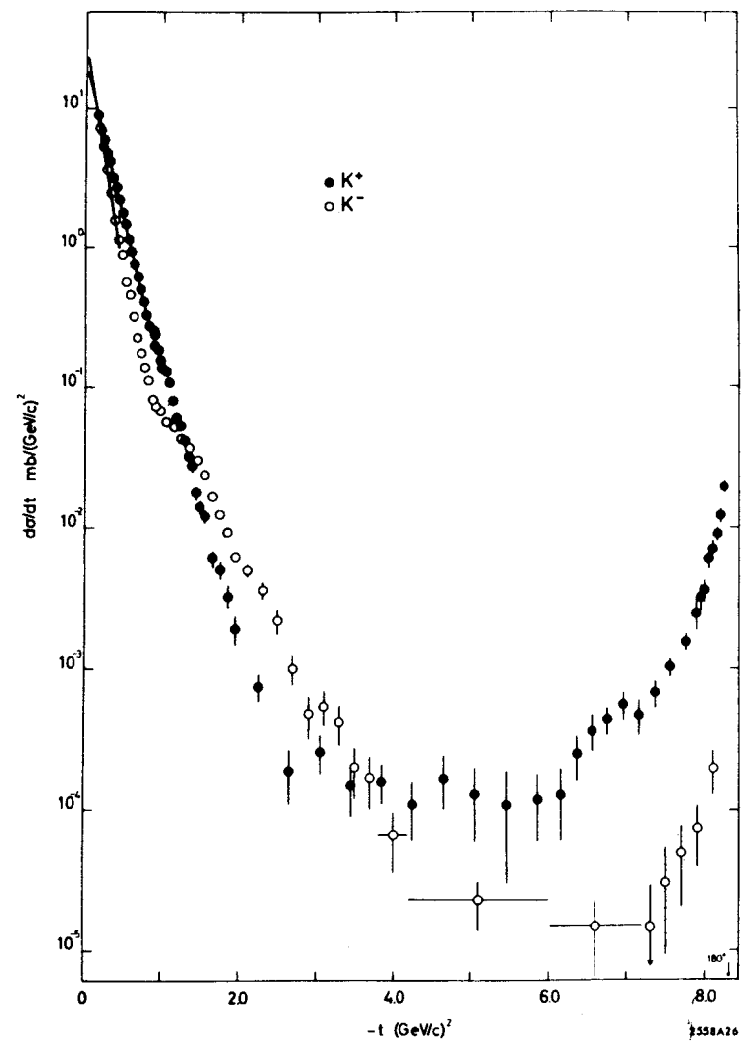
● K+
○ K−
dσ/dt mb/(GeV/c)²
10¹
10⁰
10⁻¹
10⁻²
10⁻³
10⁻⁴
10⁻⁵
0
2.0
4.0
6.0
8.0
-t (GeV/c)²
3558A26

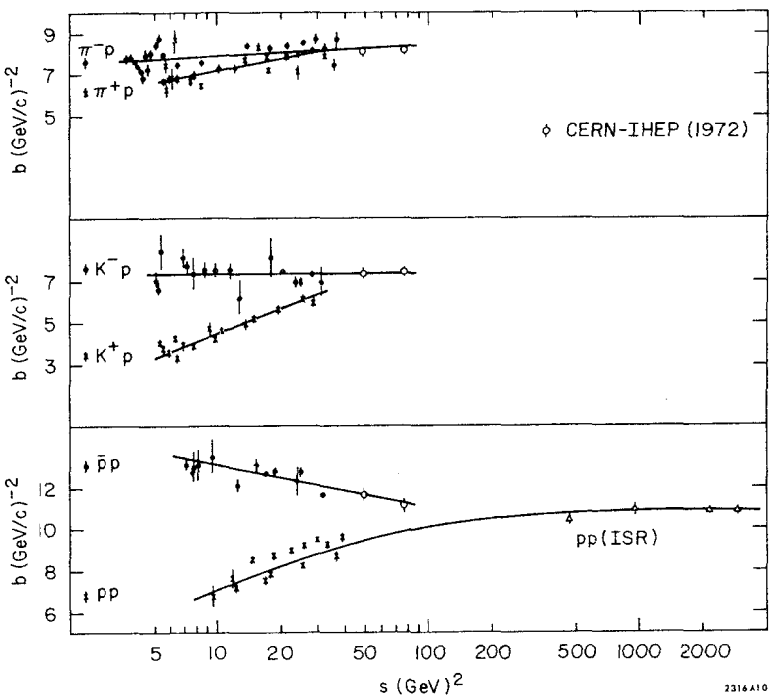

Figure 33

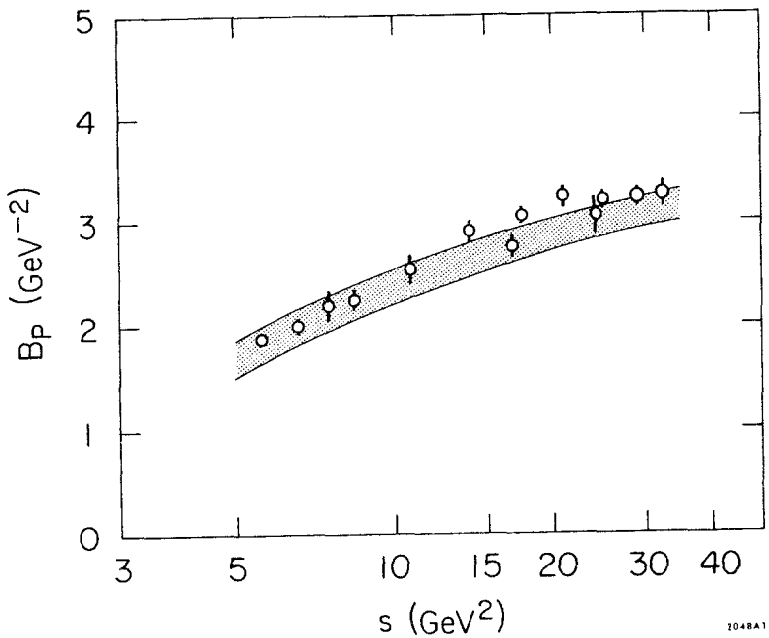

Figure 34

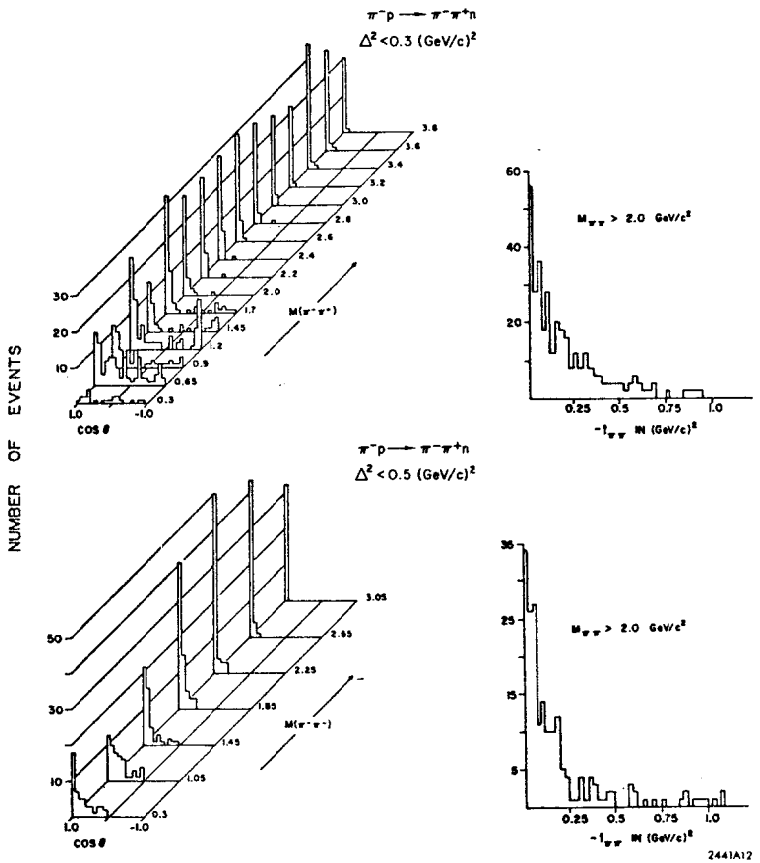

Figure 35

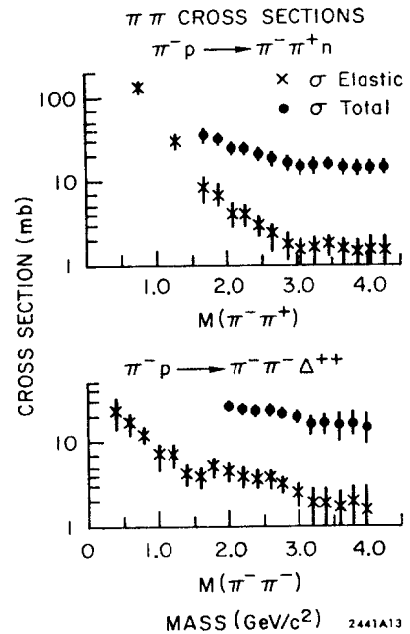

Figure 36

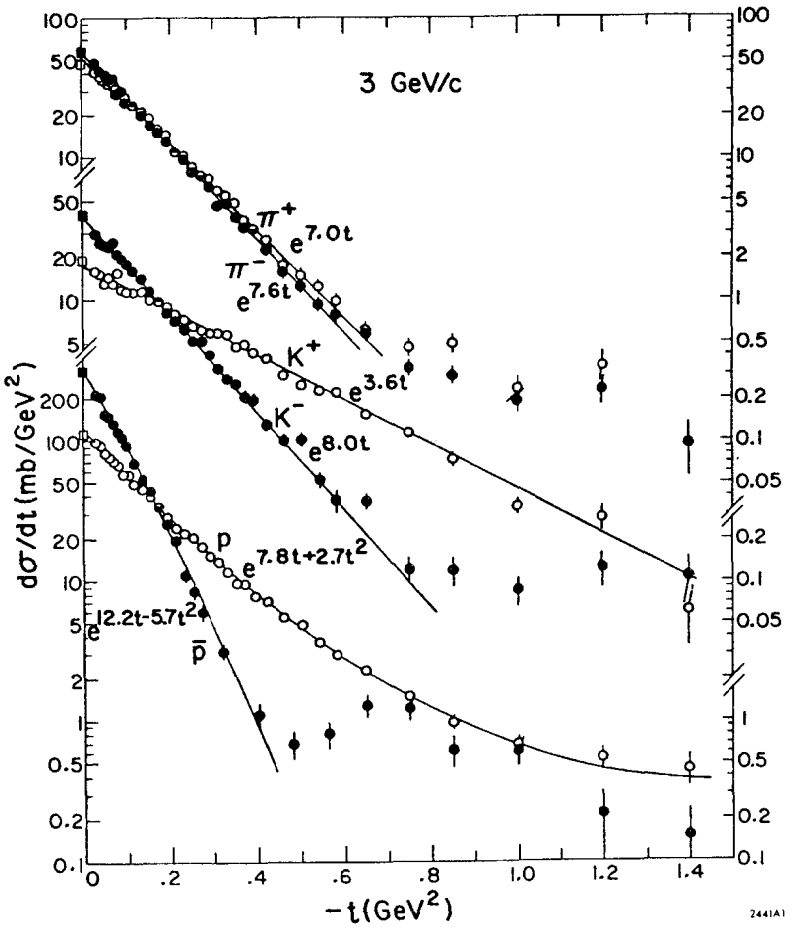

Figure 37

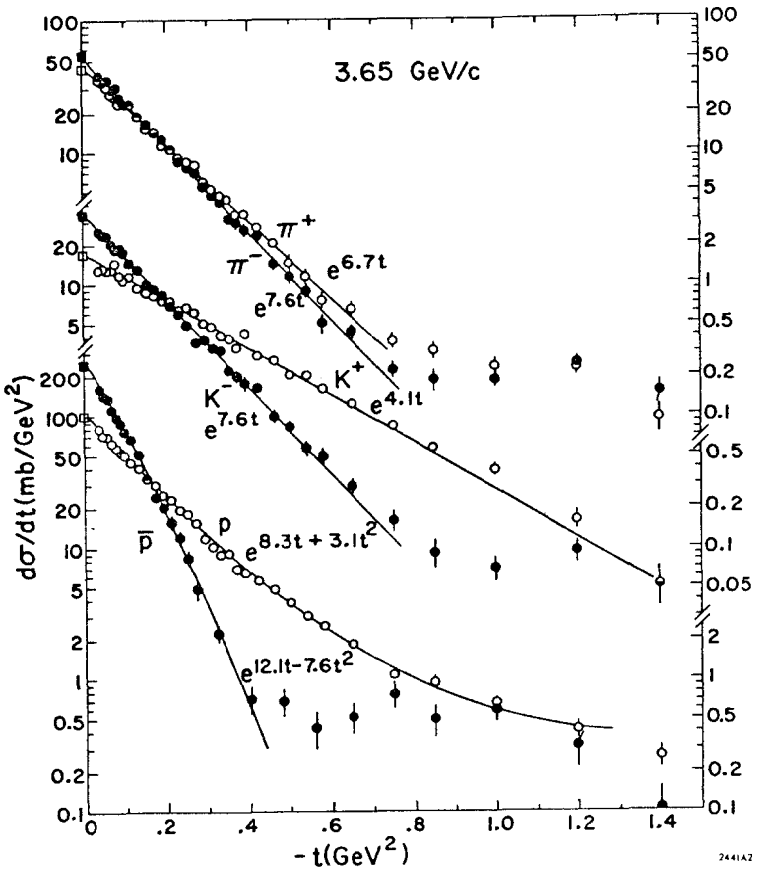

Figure 38

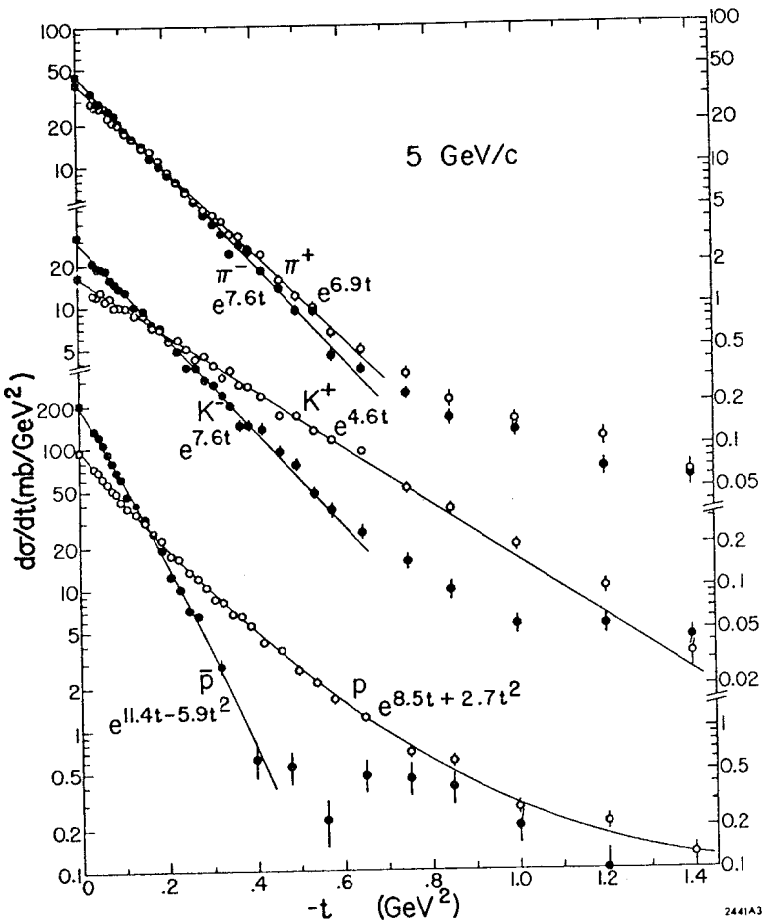

Figure 39

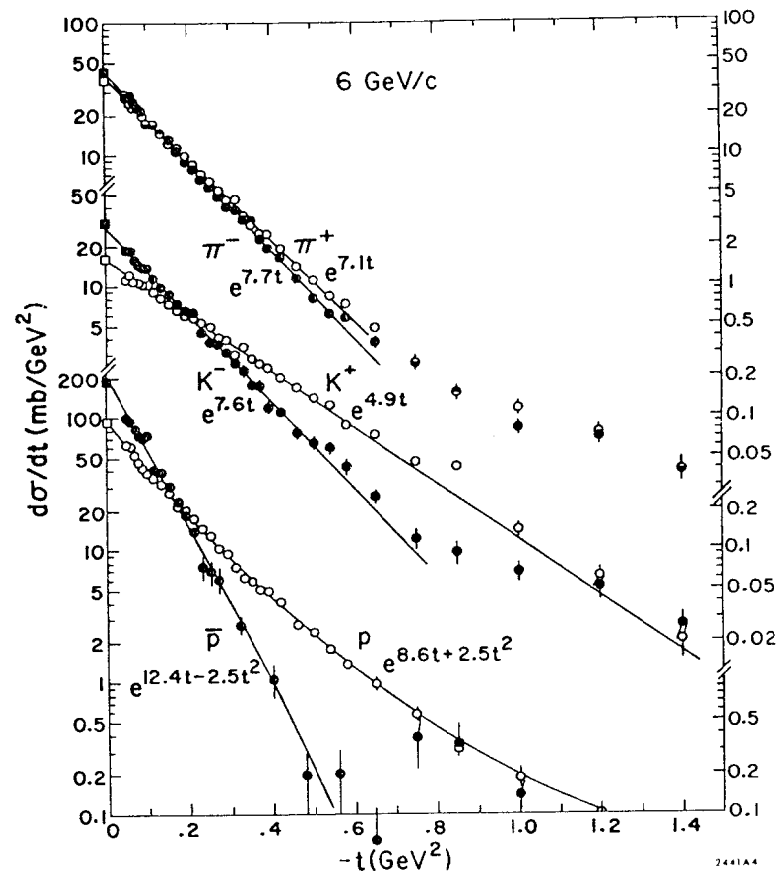

Figure 40

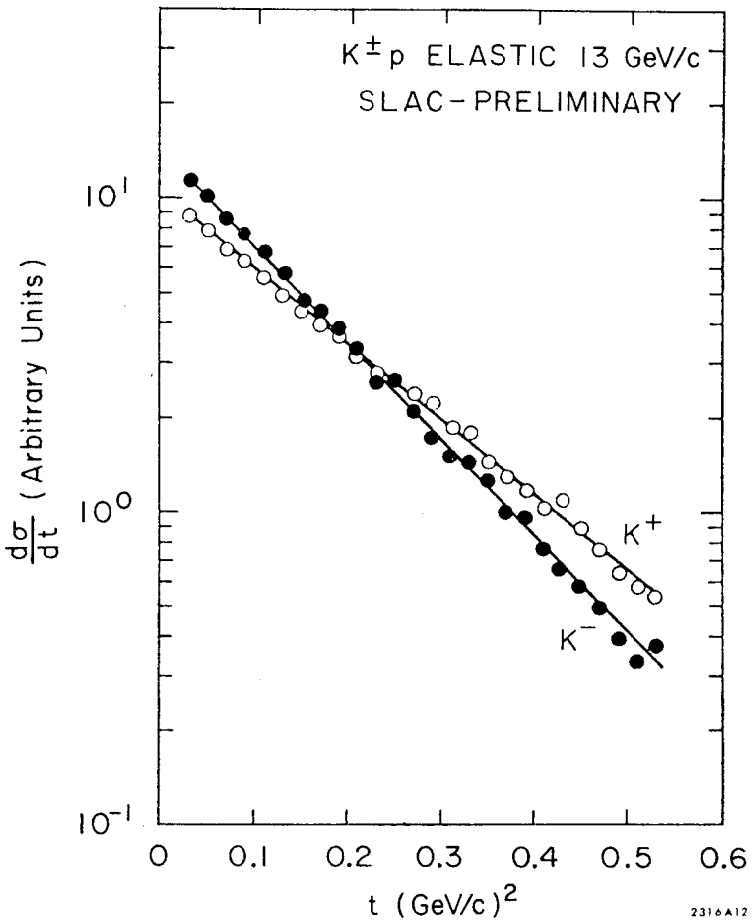

Figure 41

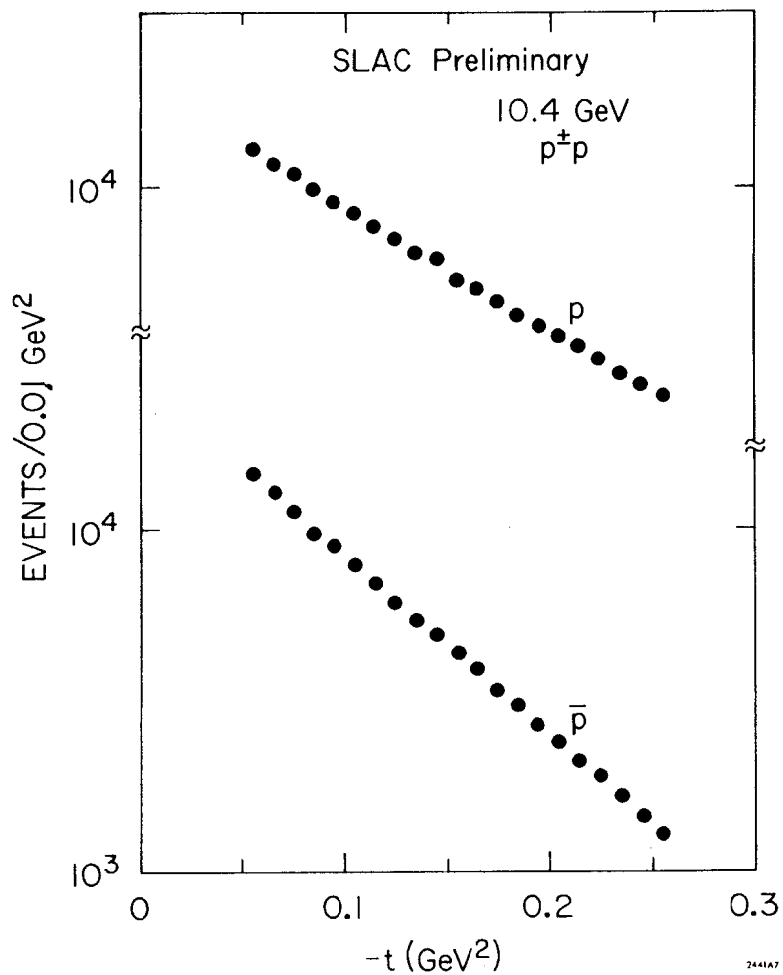

Figure 42a

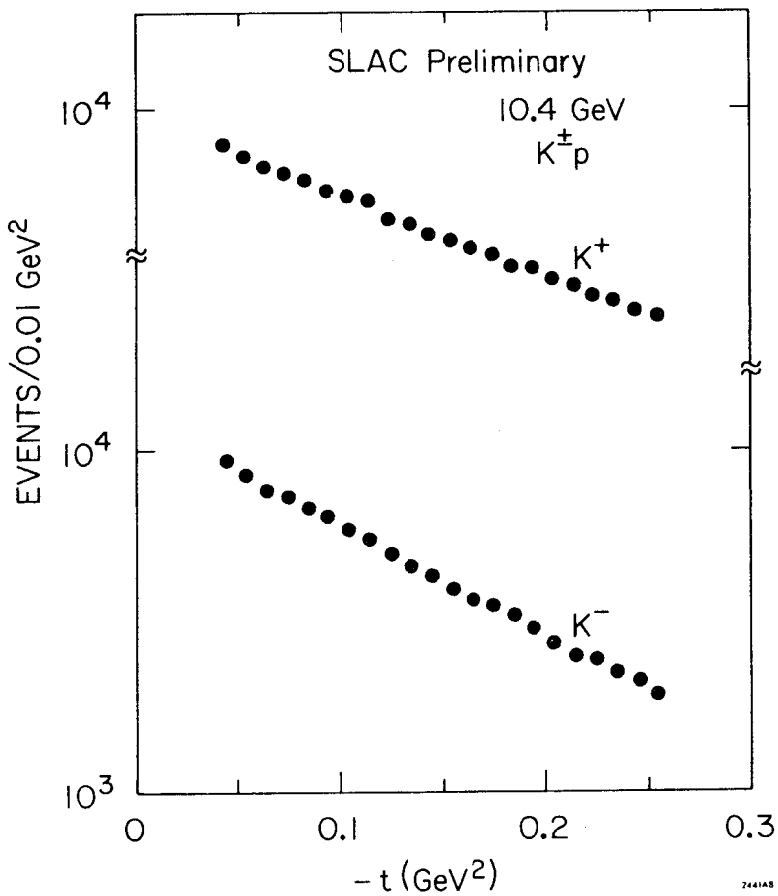

Figure 42b

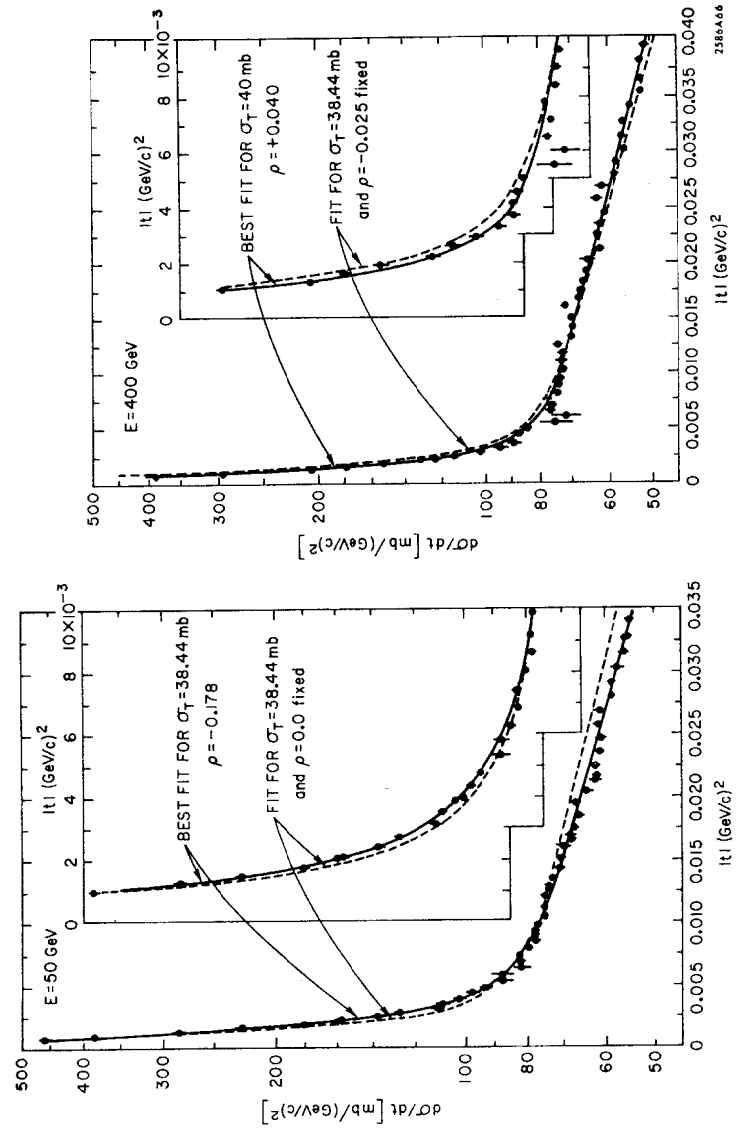

Figure 43

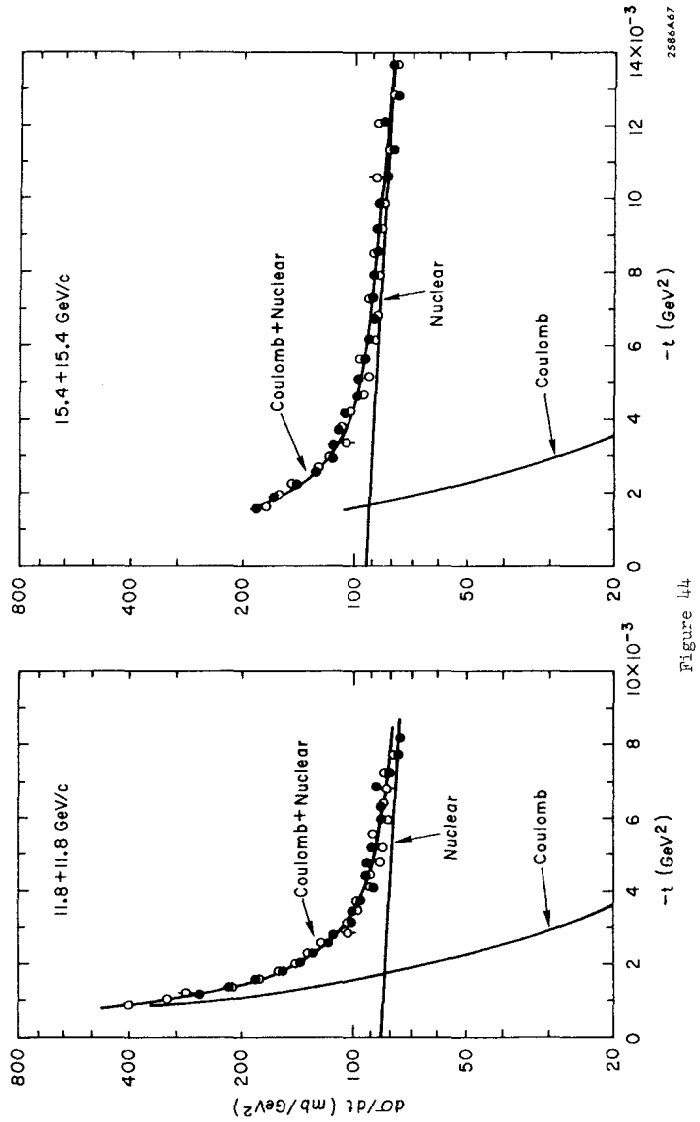

Figure 44

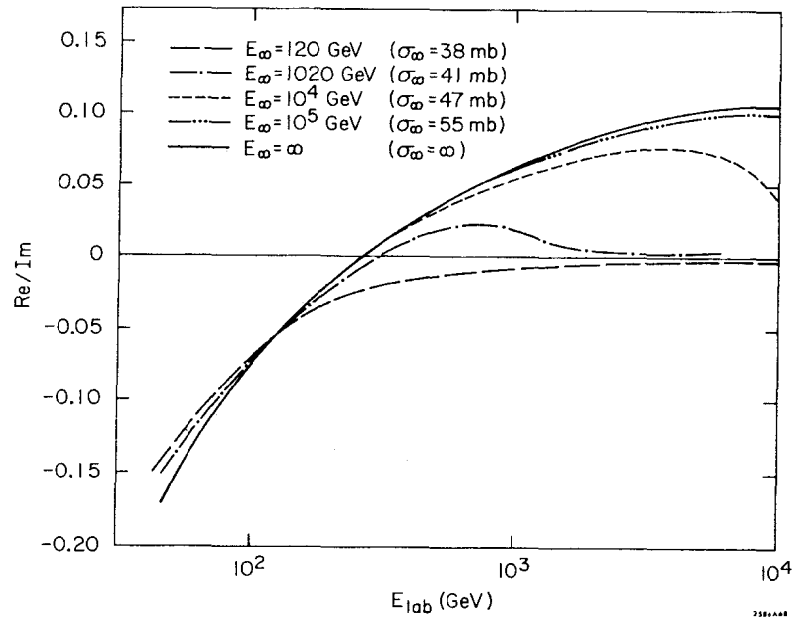

Figure 45

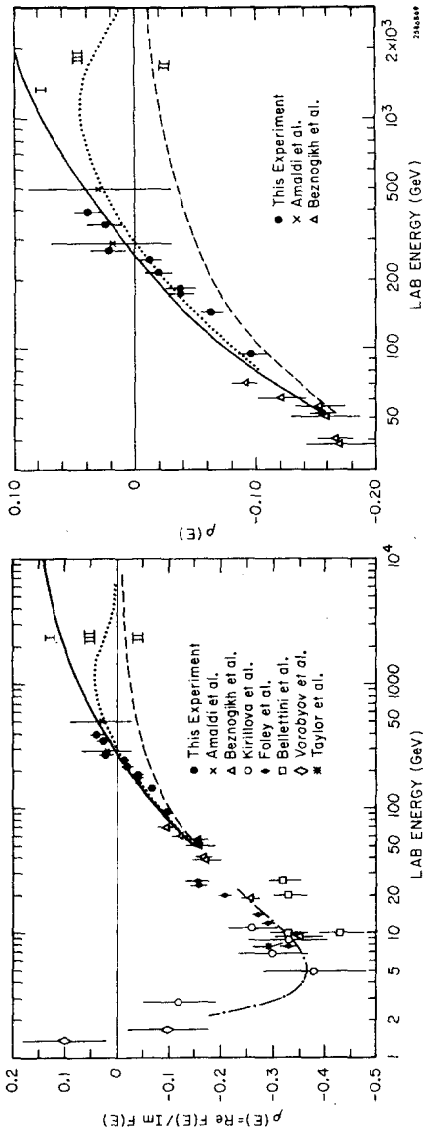

Figure 46

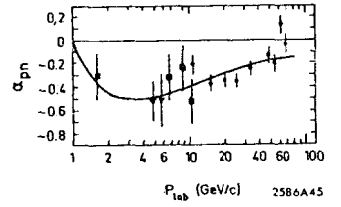

Figure 47

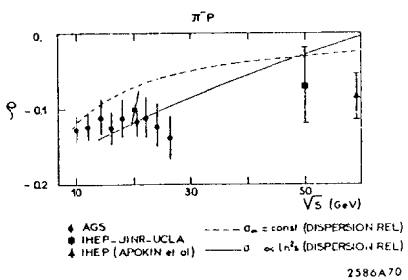

Figure 48

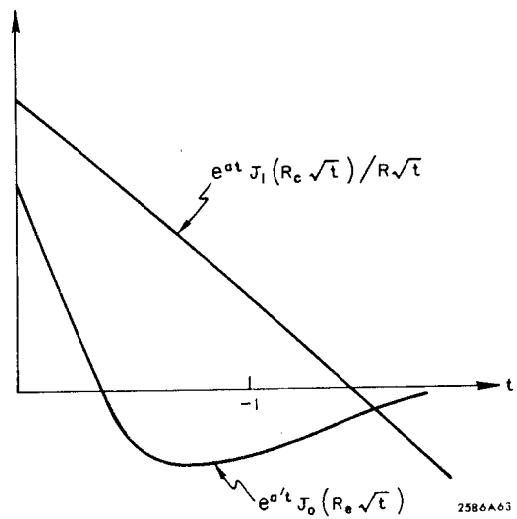

Figure 49

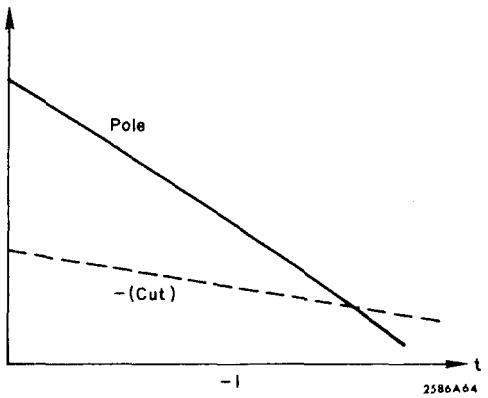

Figure 50

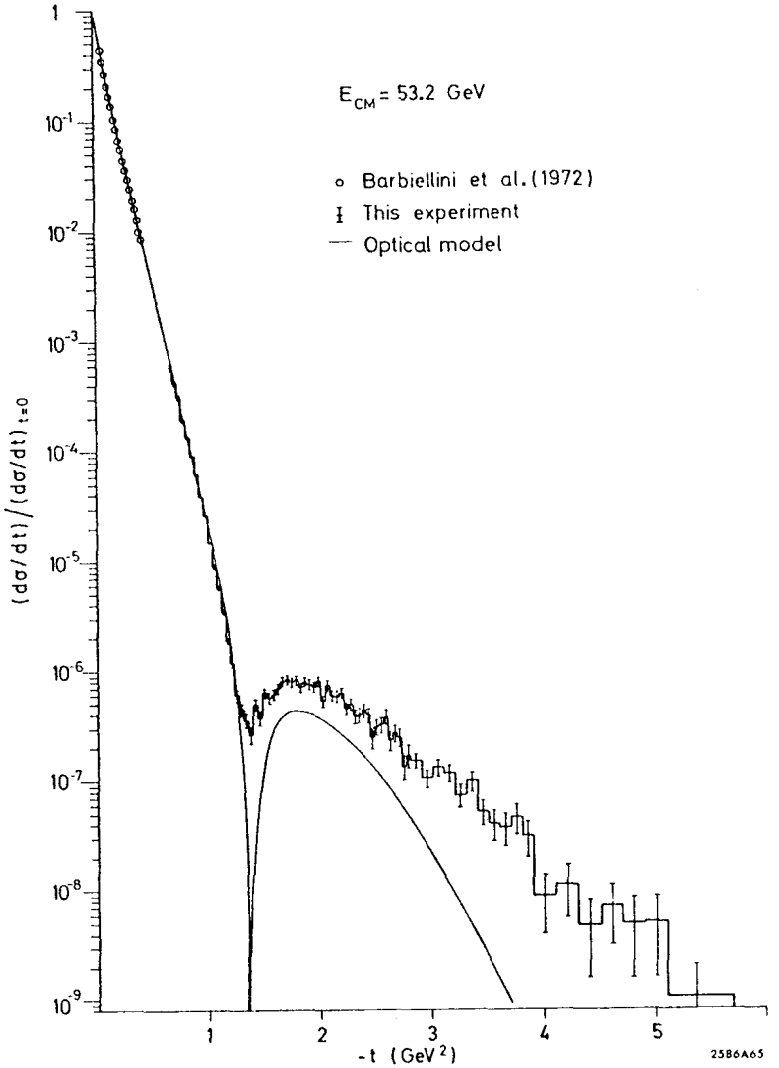

Figure 51

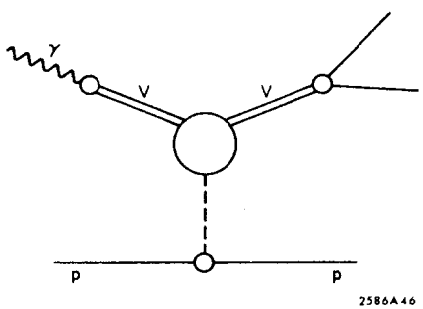

Figure 52

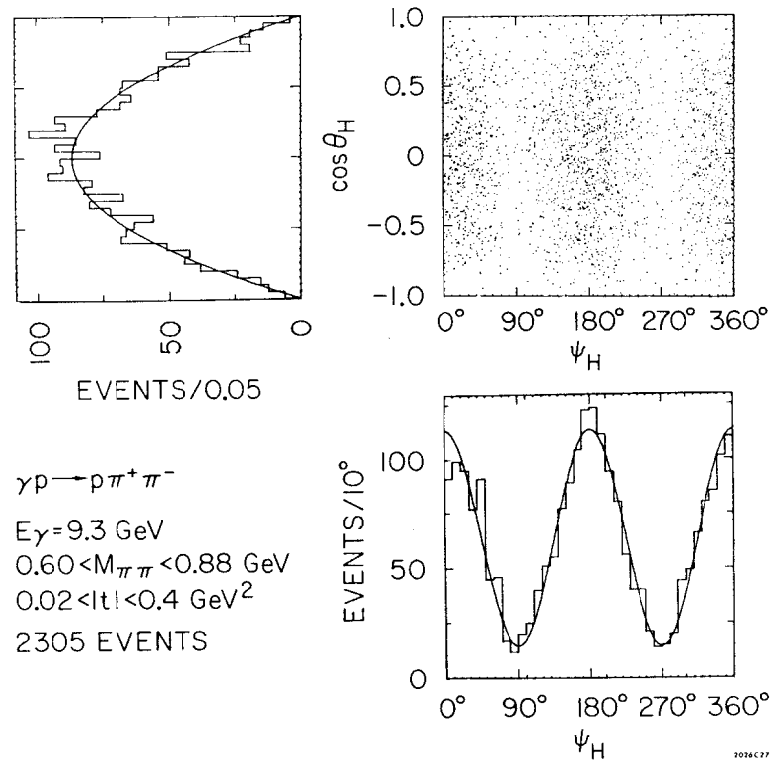

Figure 53

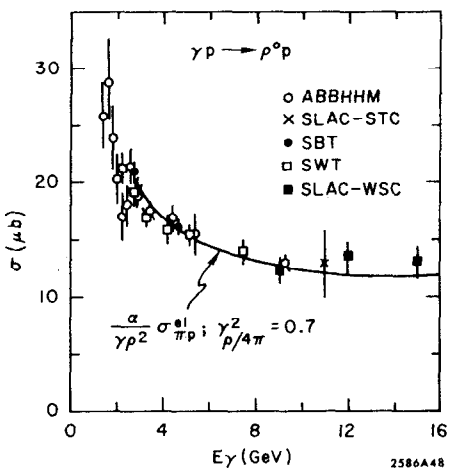

Figure 54

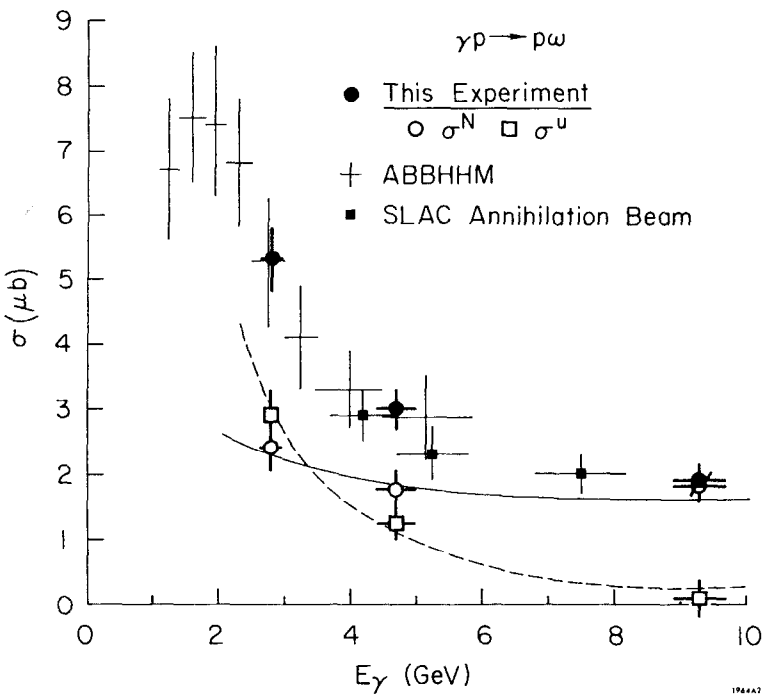

Figure 55

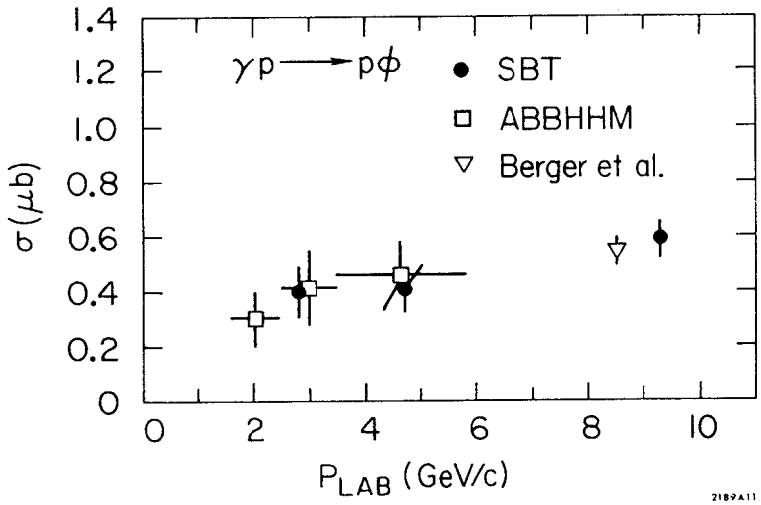

Figure 56

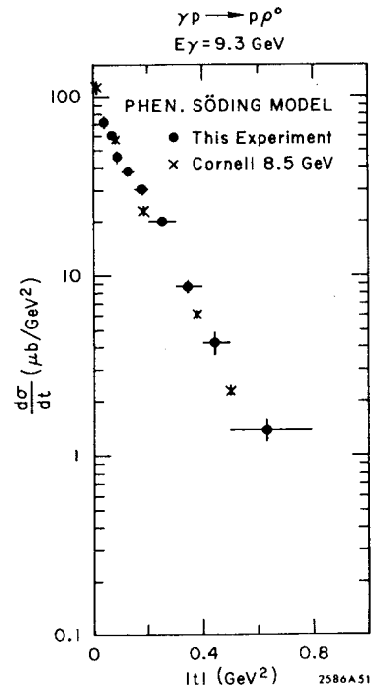

Figure 57

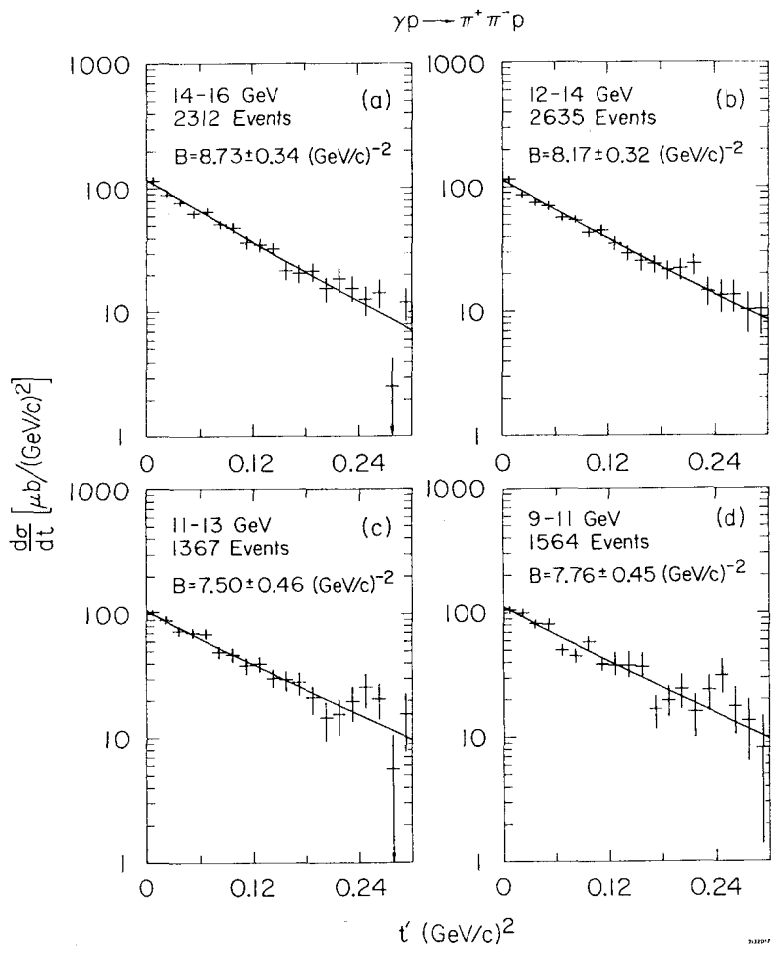

Figure 58

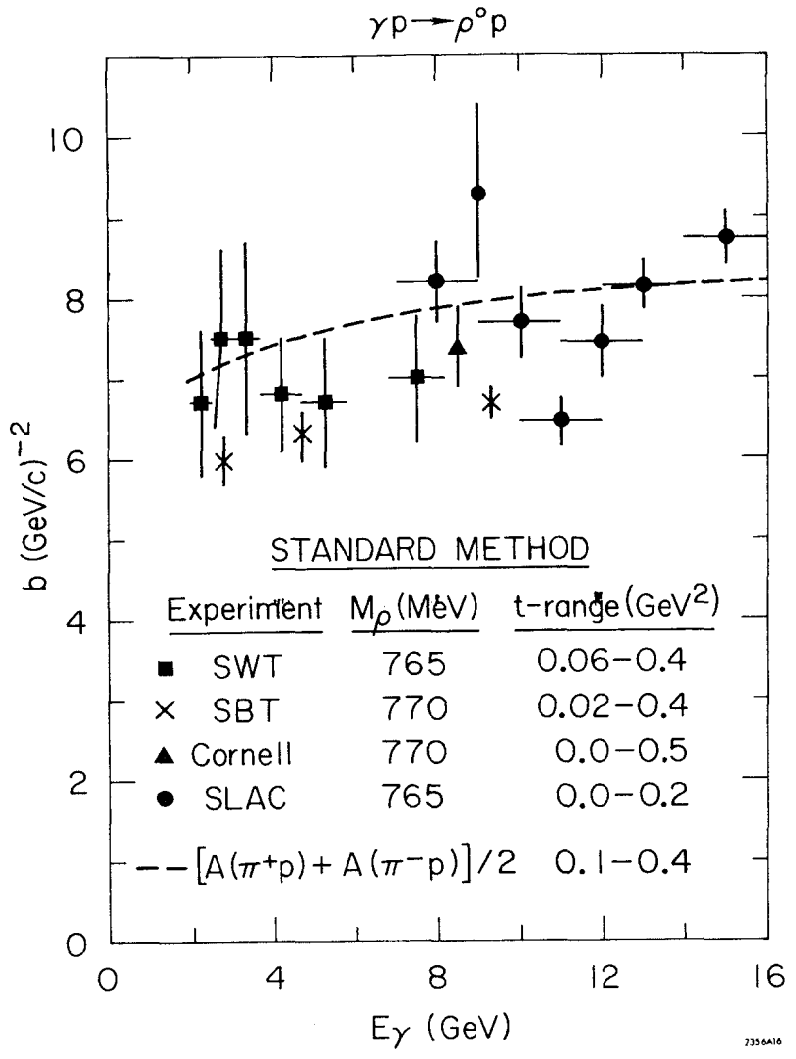

Figure 59

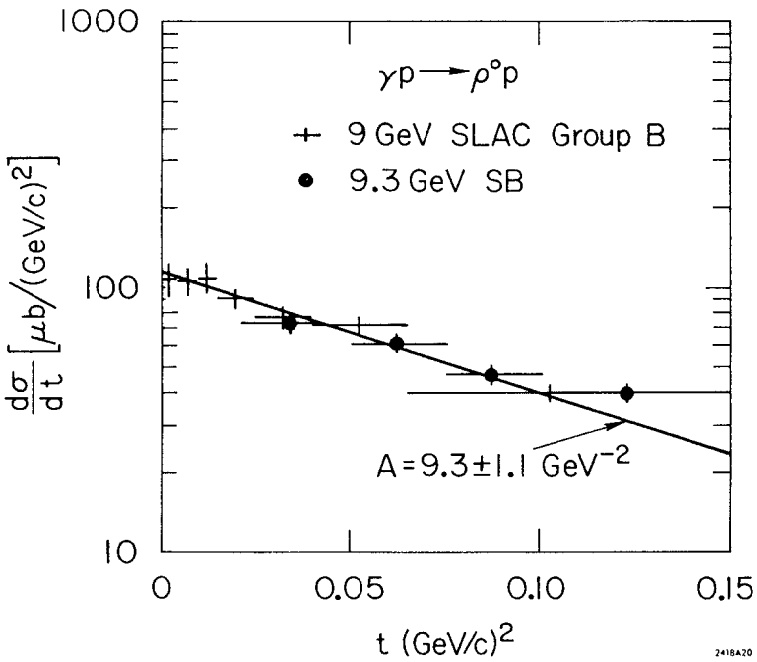

Figure 60

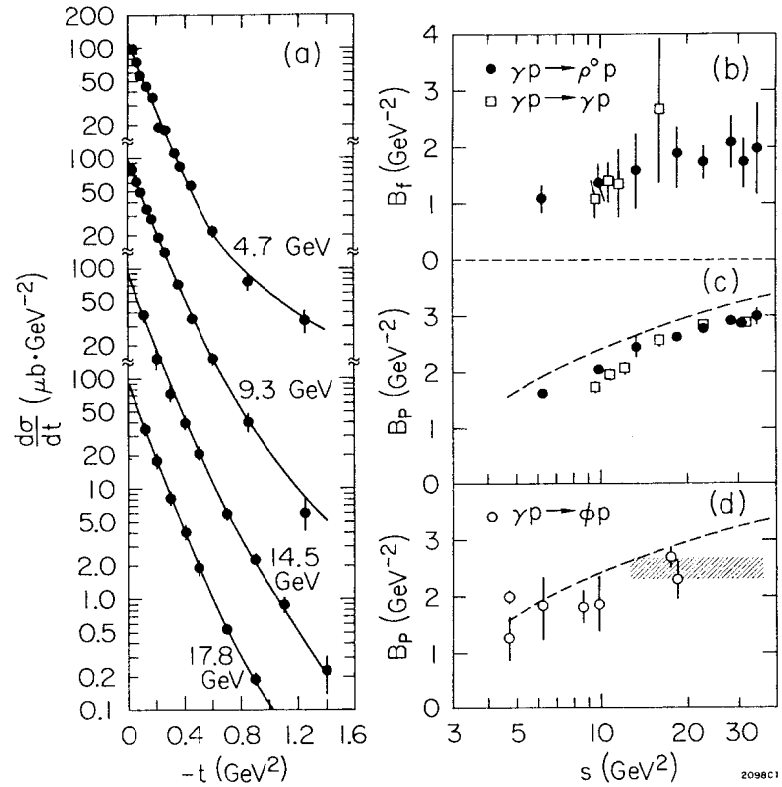

Figure 61

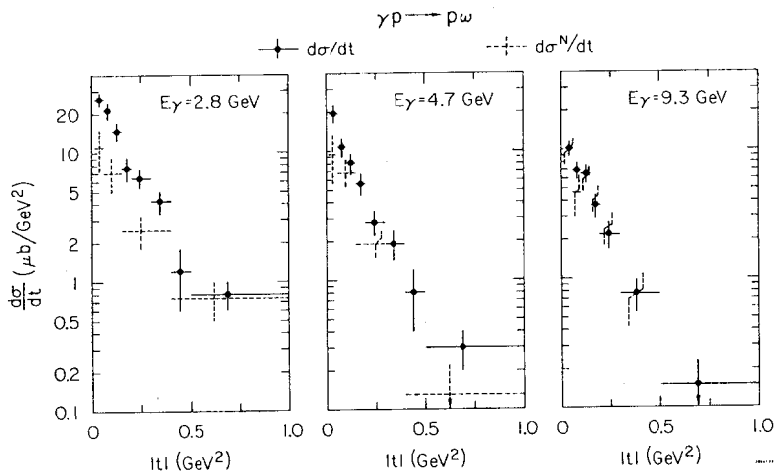

Figure 62

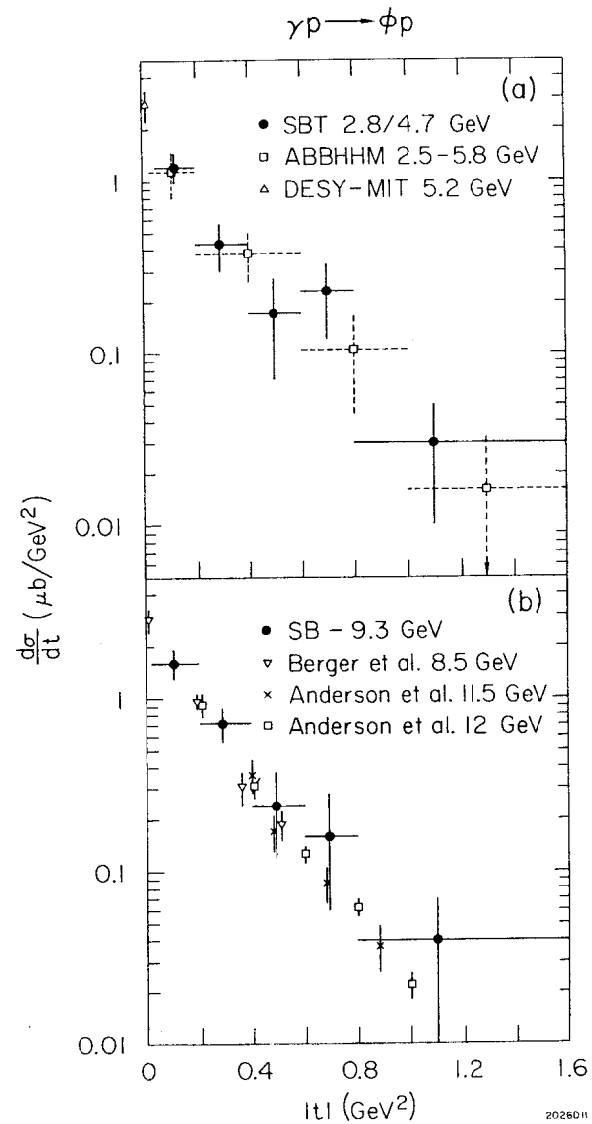

Figure 63

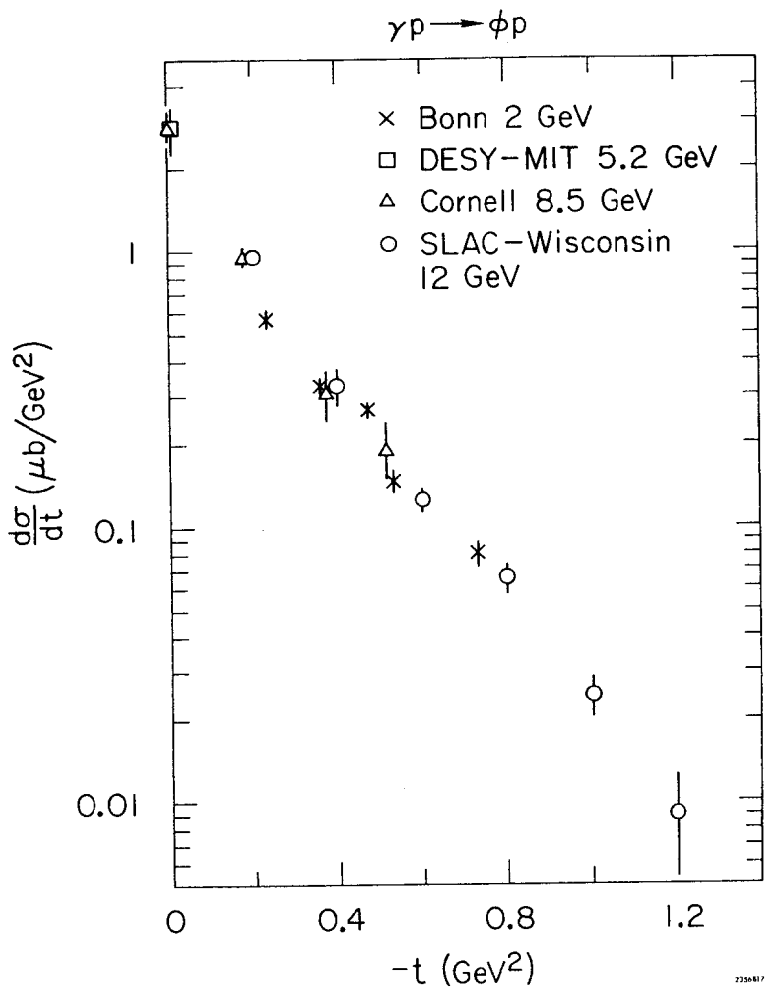

Figure 64

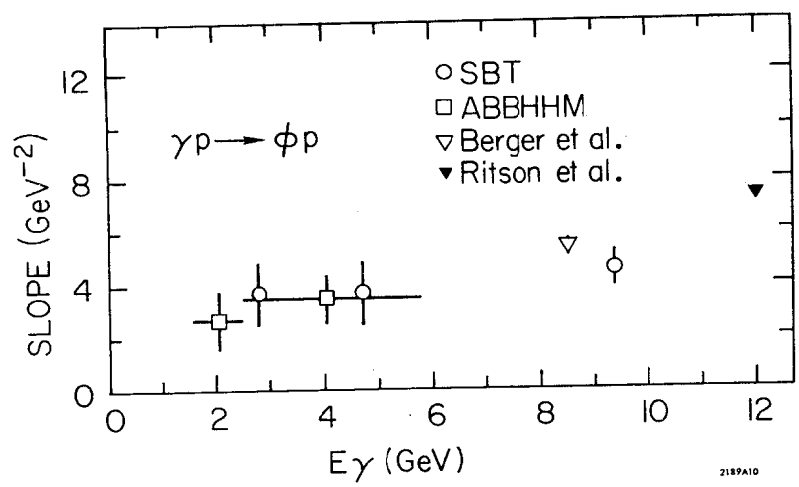

Figure 65

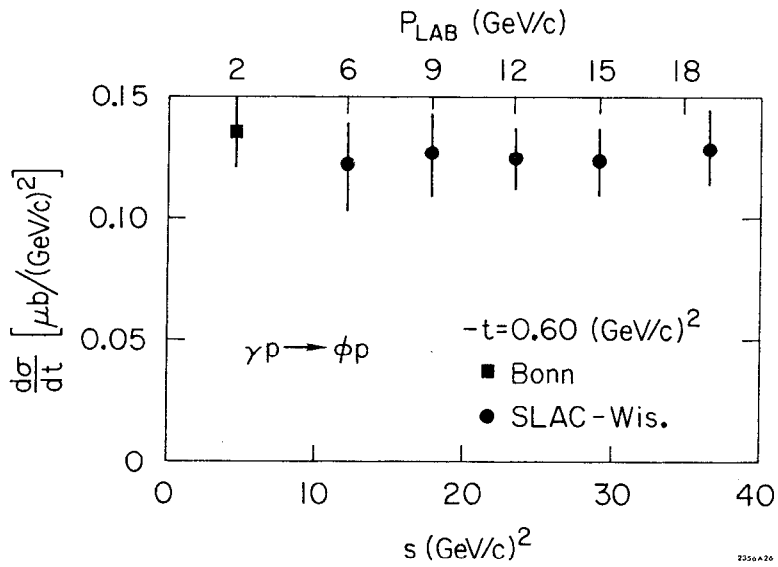

Figure 66

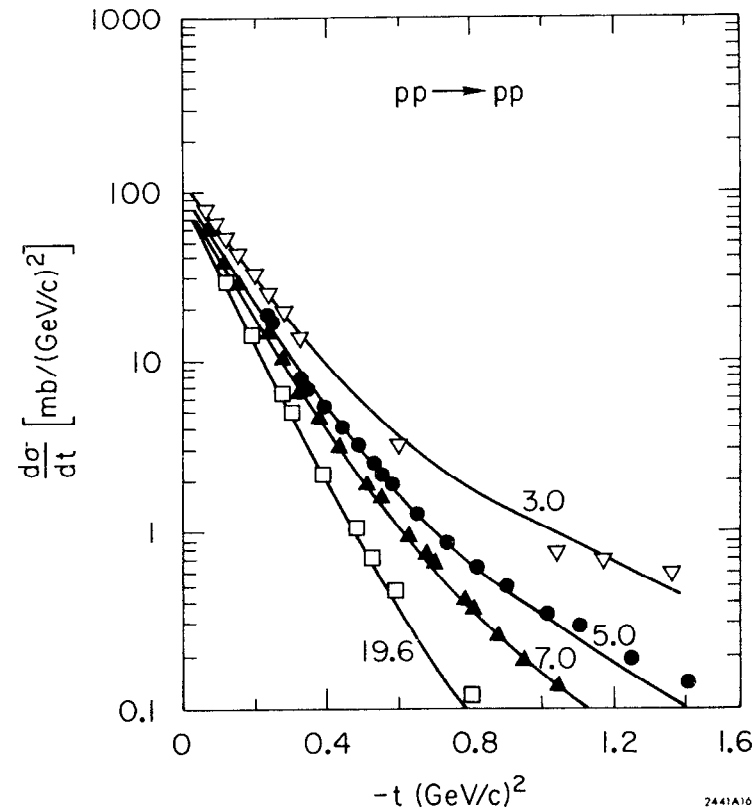

Figure 67

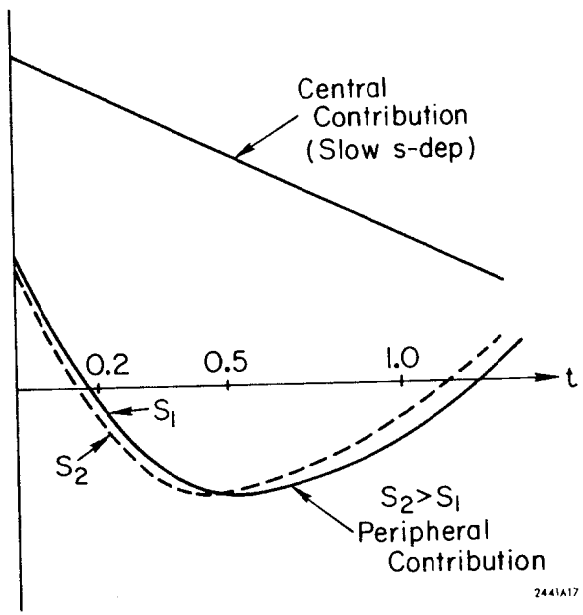

Figure 68

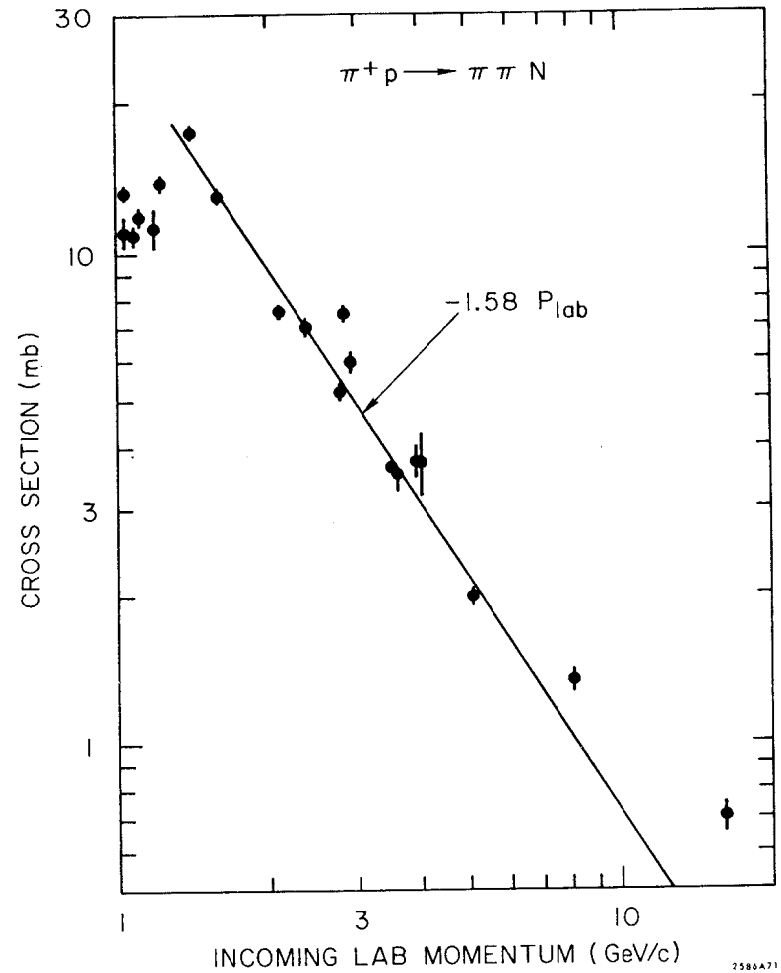

Figure 69

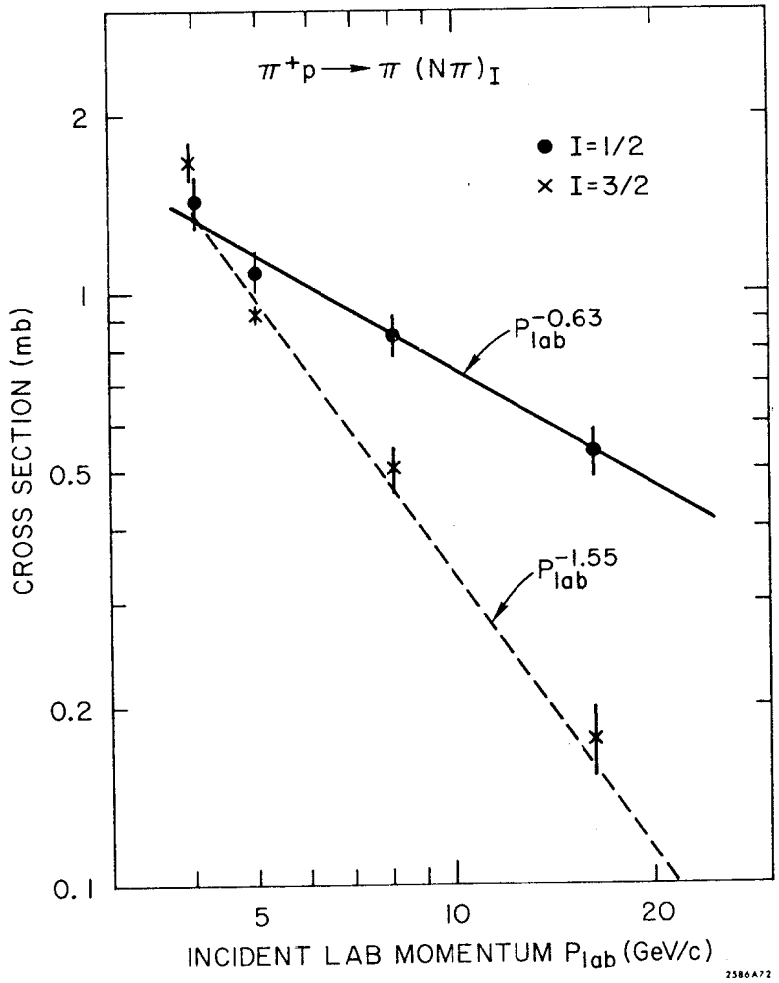

Figure 70

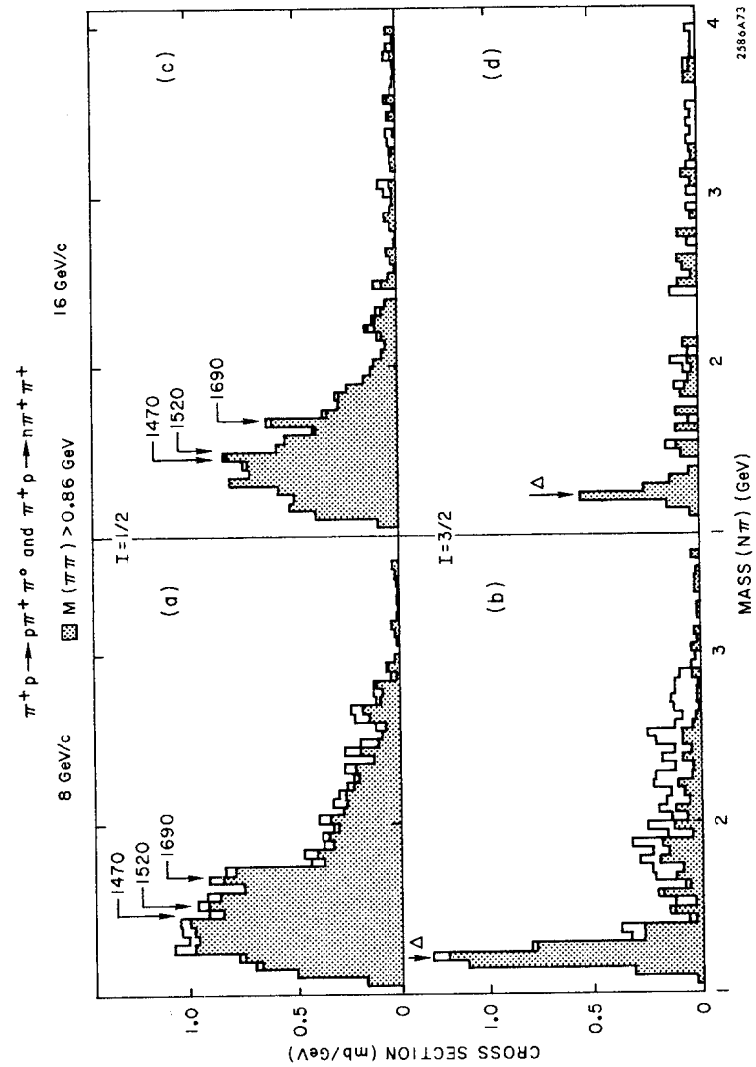

Figure 71

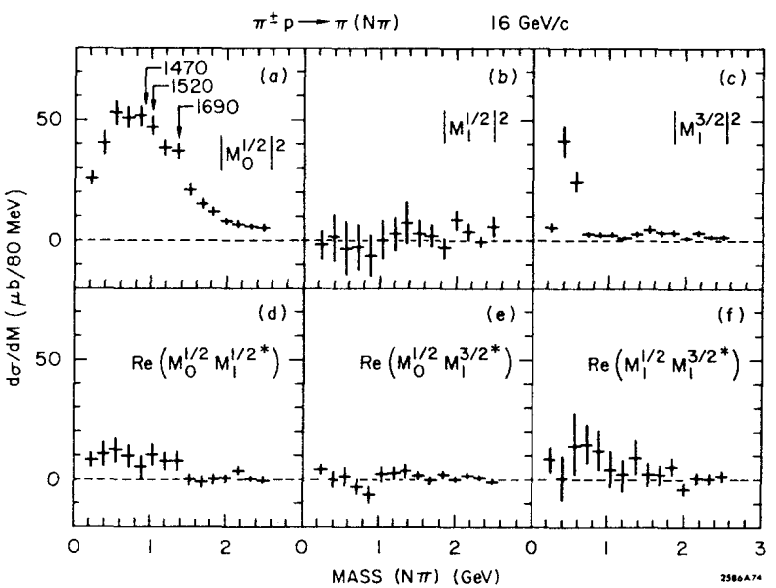

Figure 72

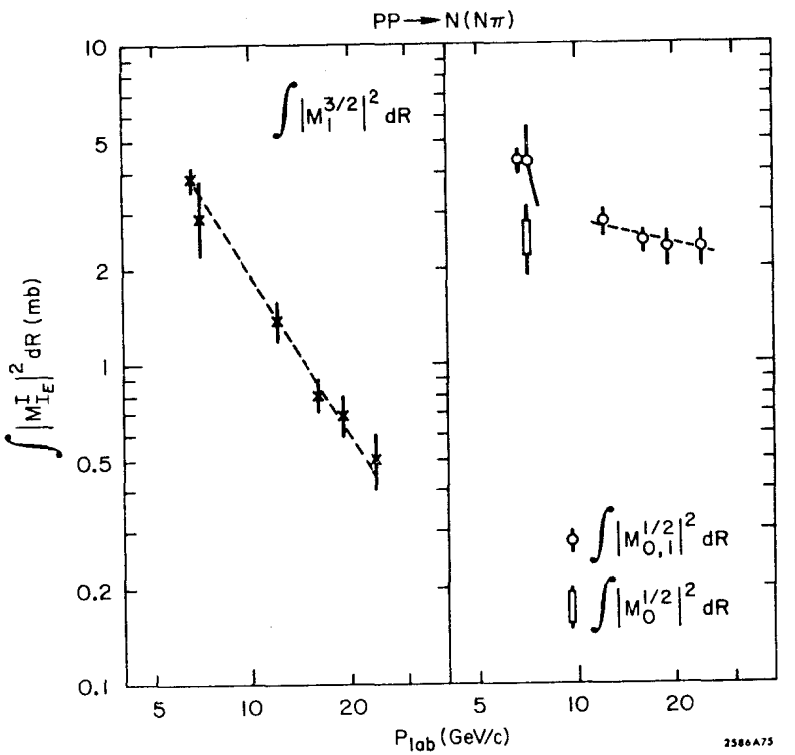

Figure 73

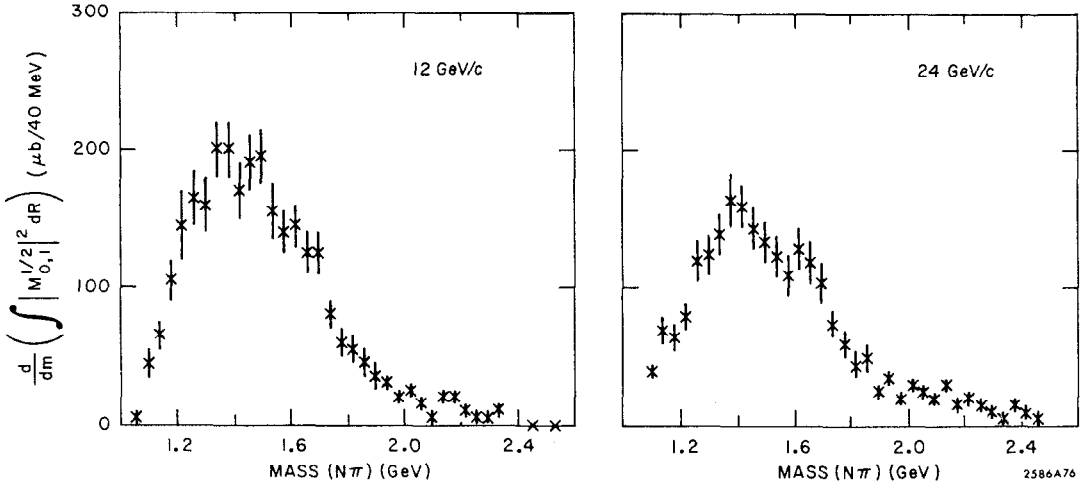

Figure 74

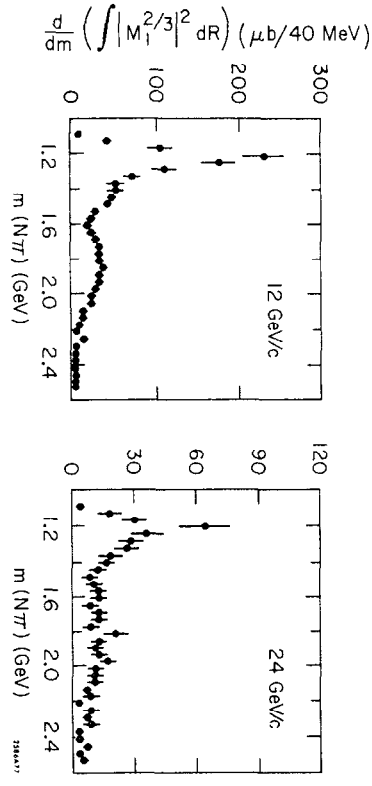

Figure 75

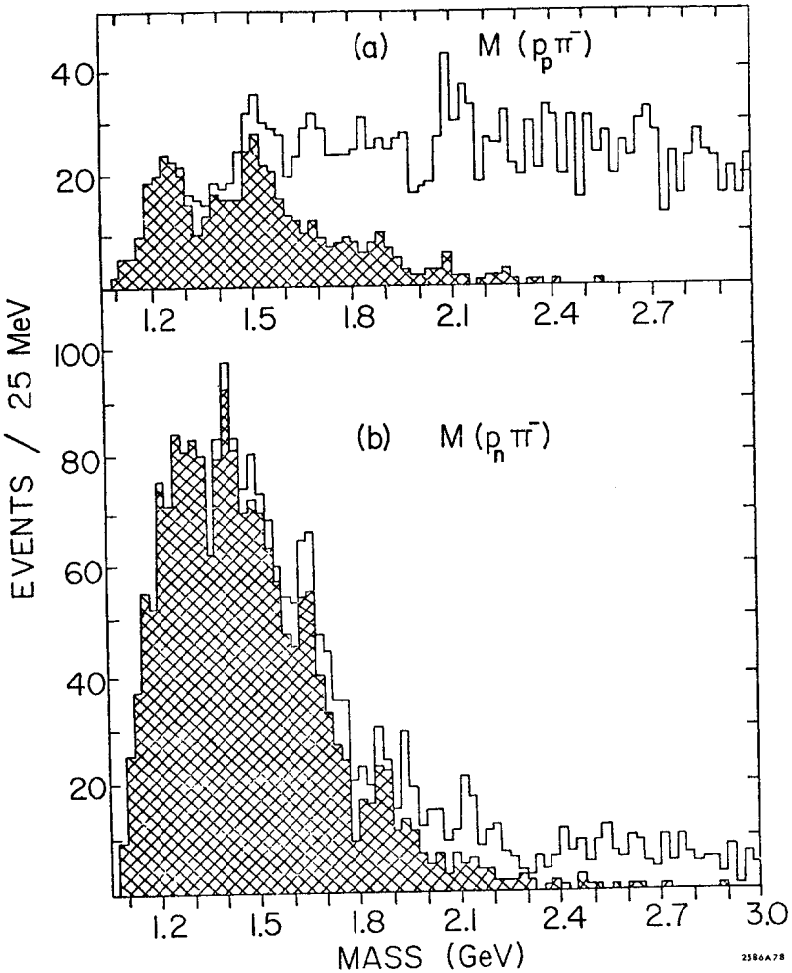

Figure 76

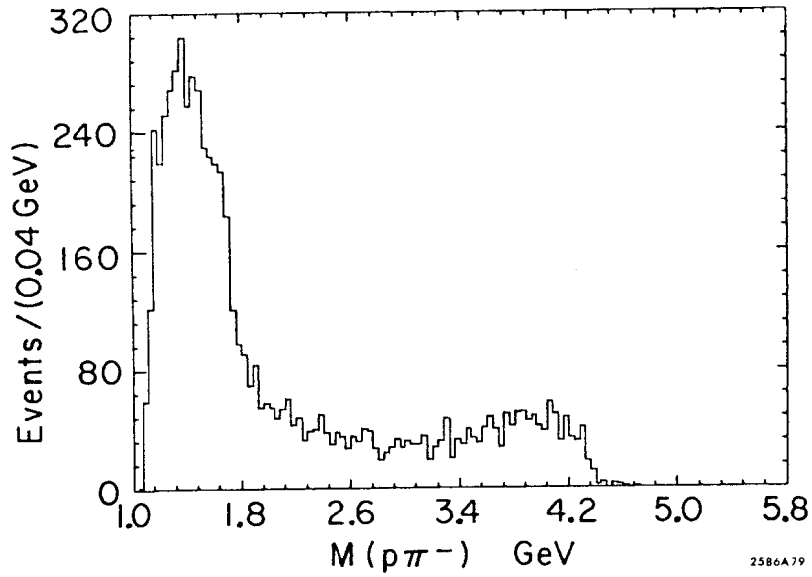

Figure 77

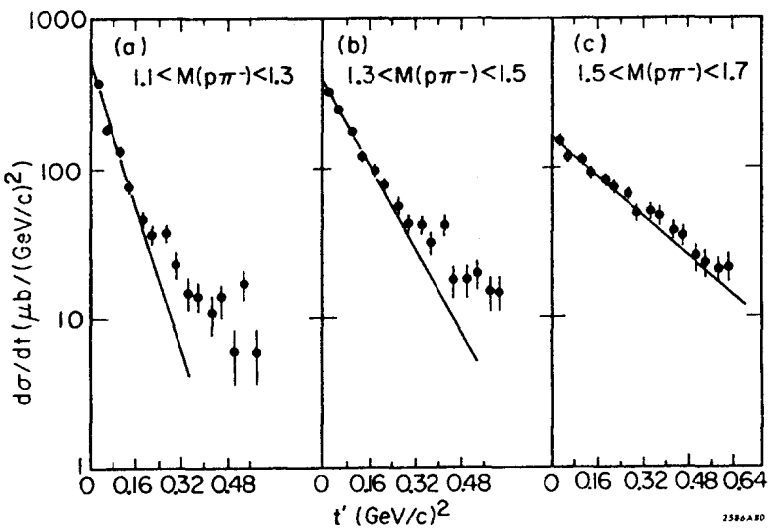

Figure 78

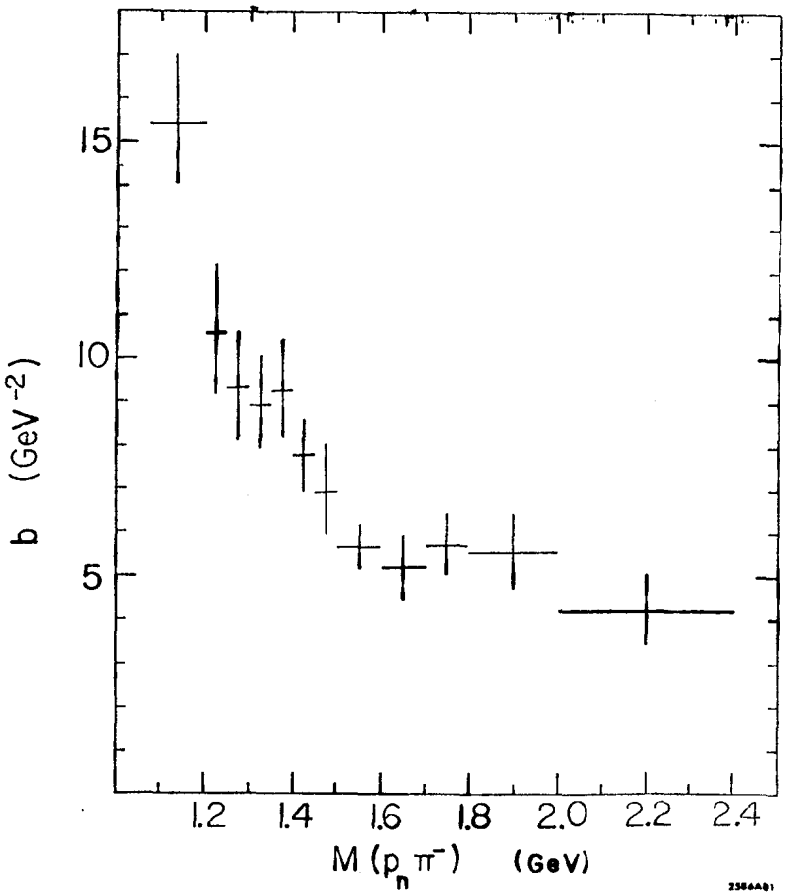

Figure 79

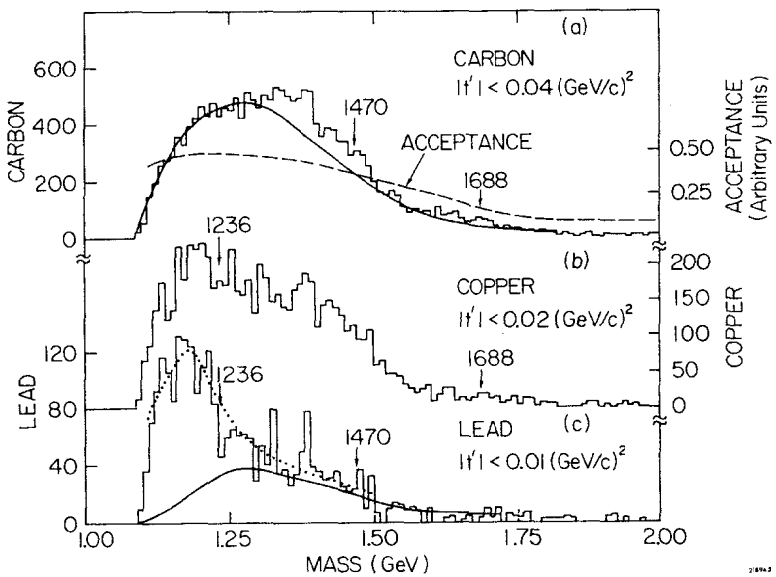

Figure 80

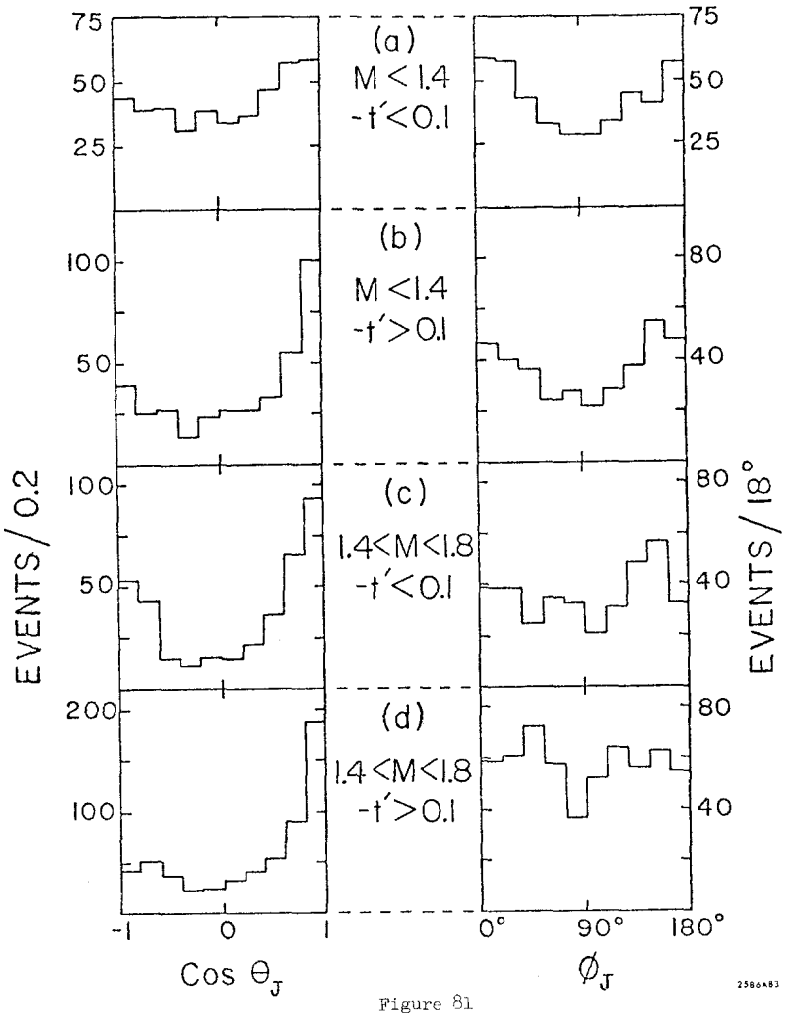

Figure 81

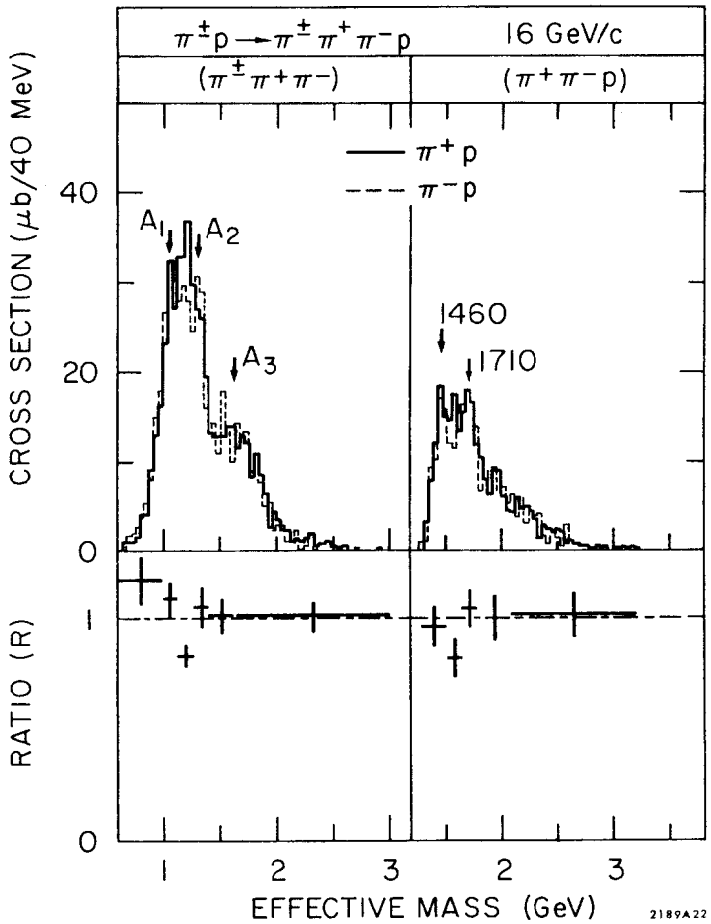

Figure 82

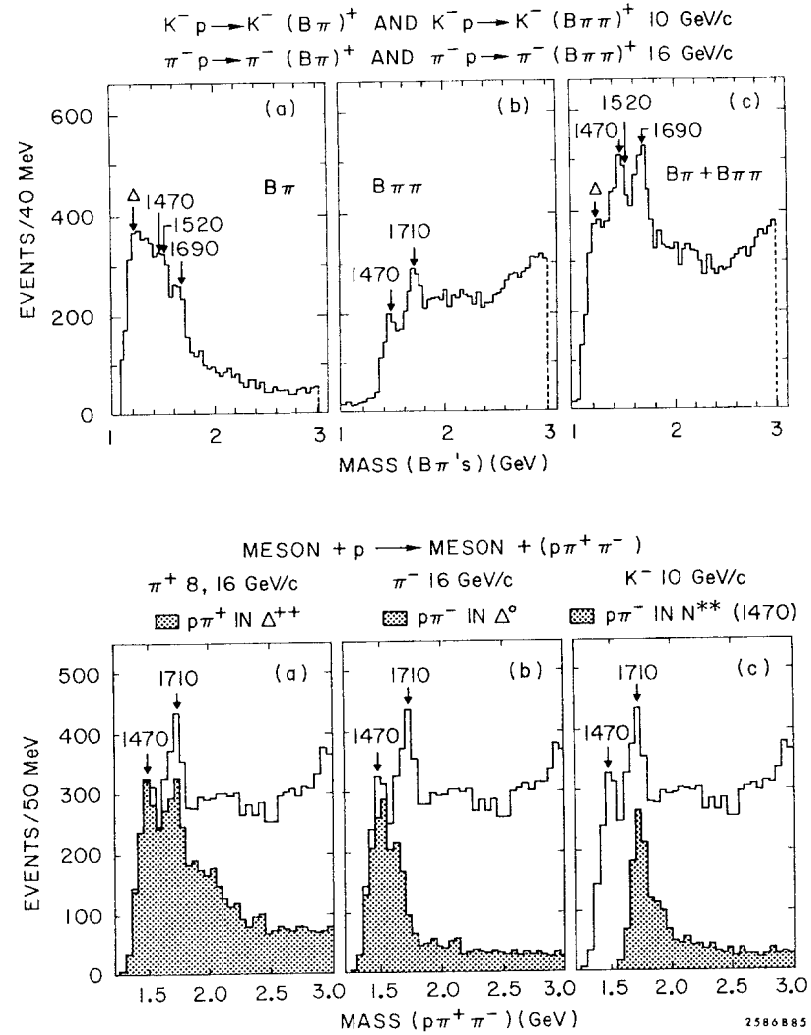

Figure 83

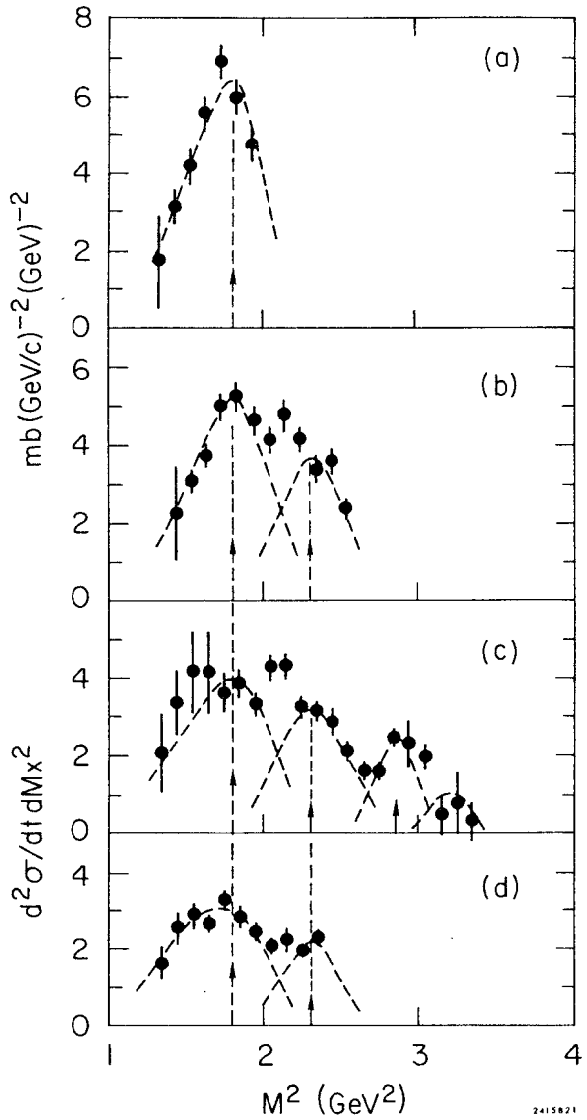

Figure 84

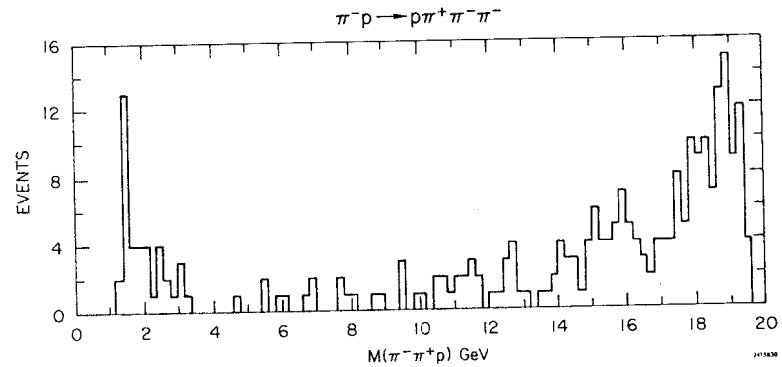

Figure 85

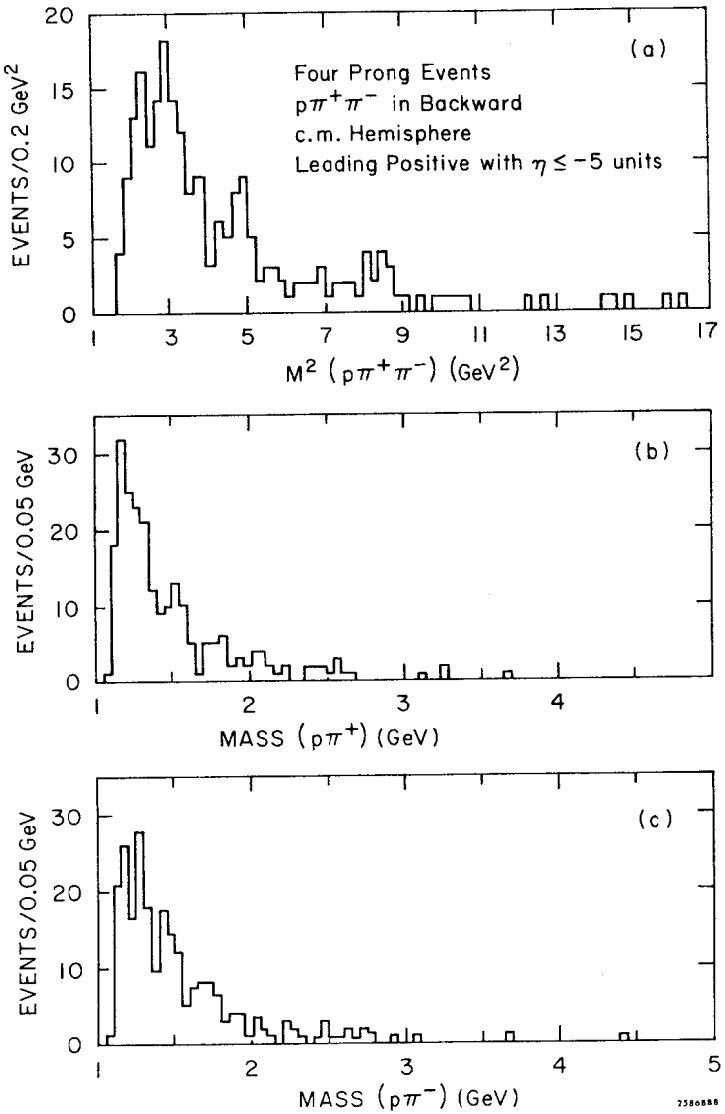

Figure 86

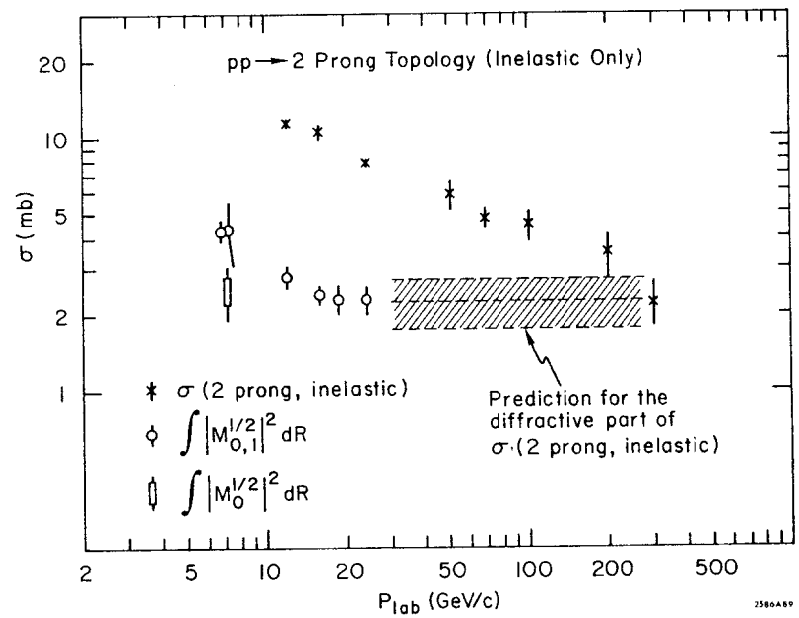

Figure 87

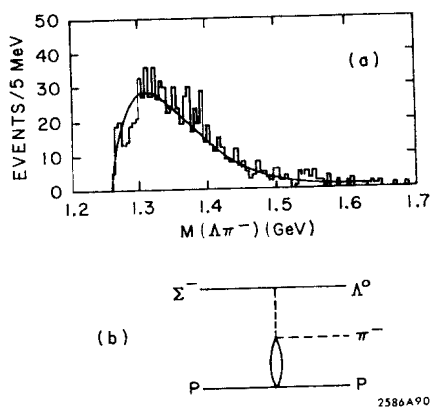

Figure 88

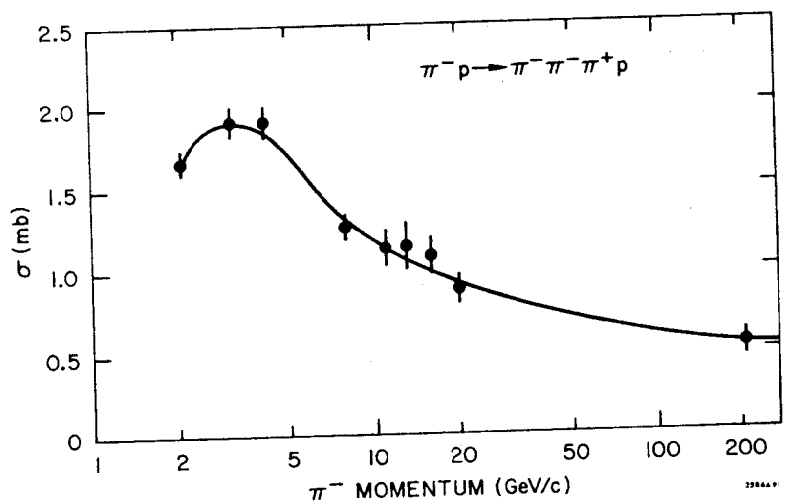

Figure 89

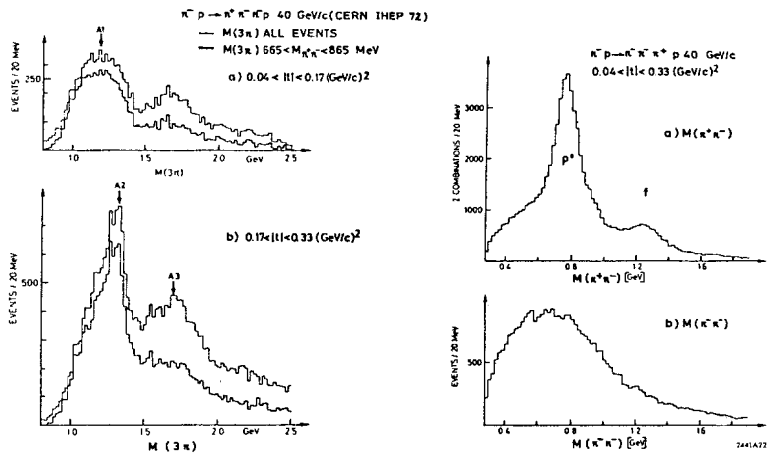

Figure 90

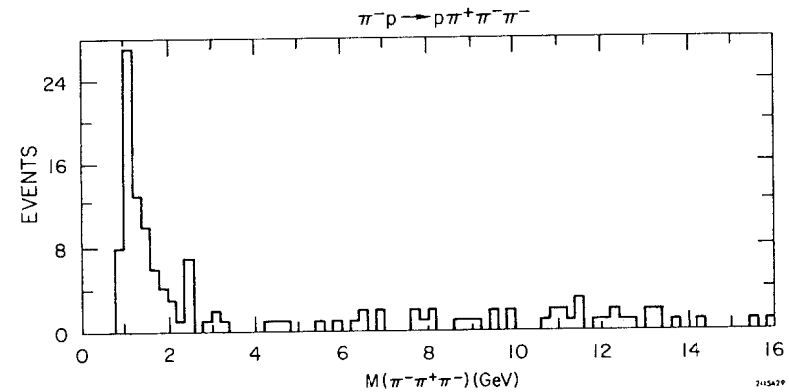

Figure 91

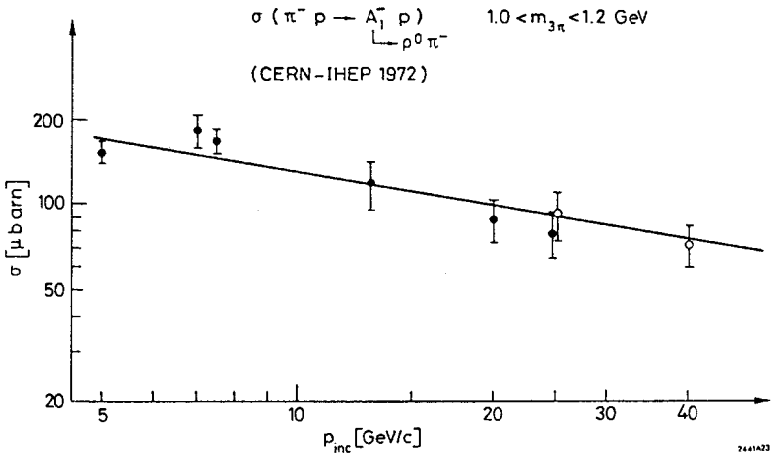

Figure 92

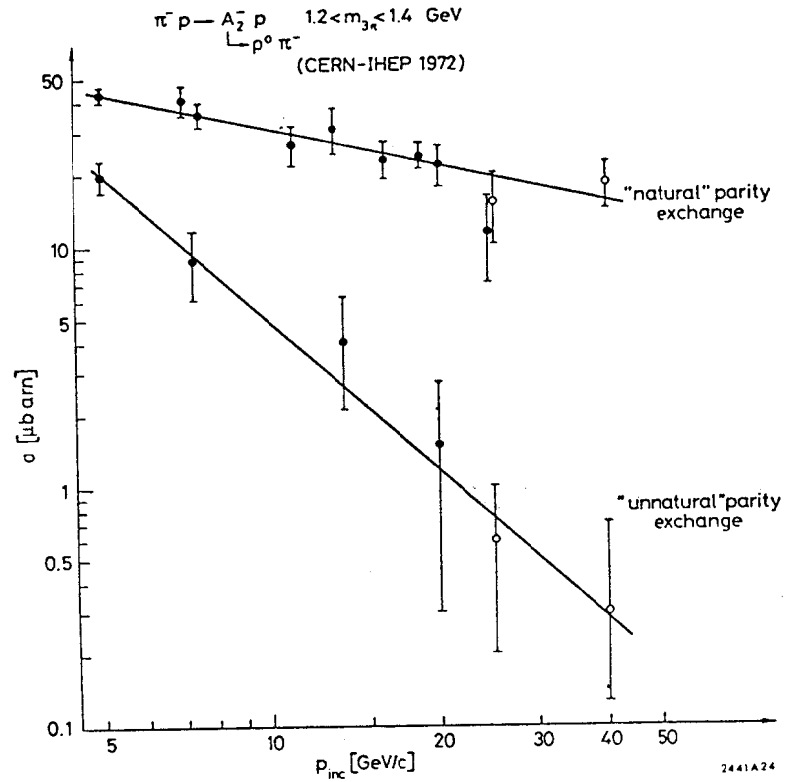

Figure 93

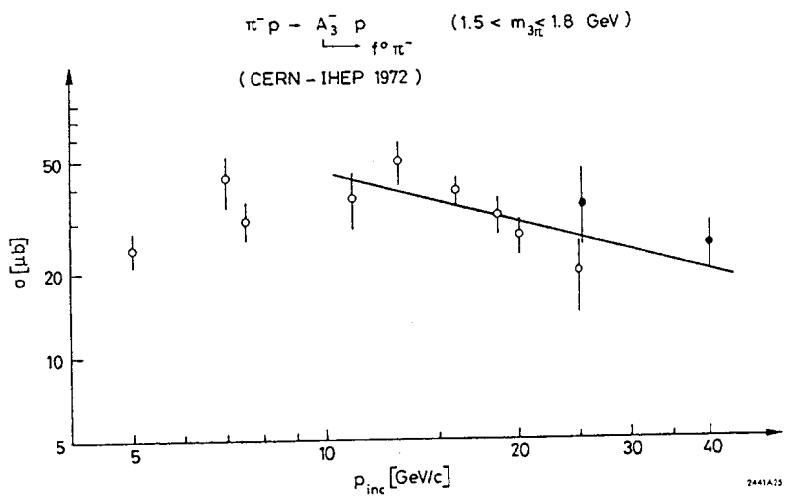

Figure 94

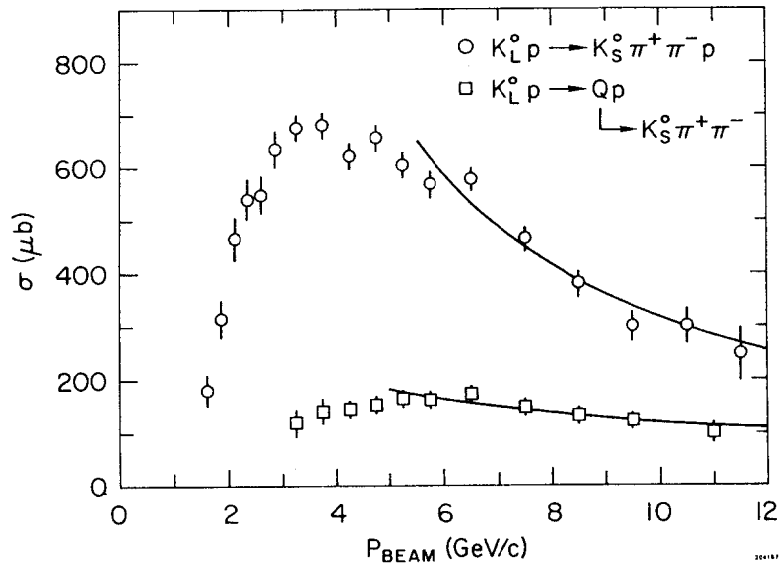

Figure 95

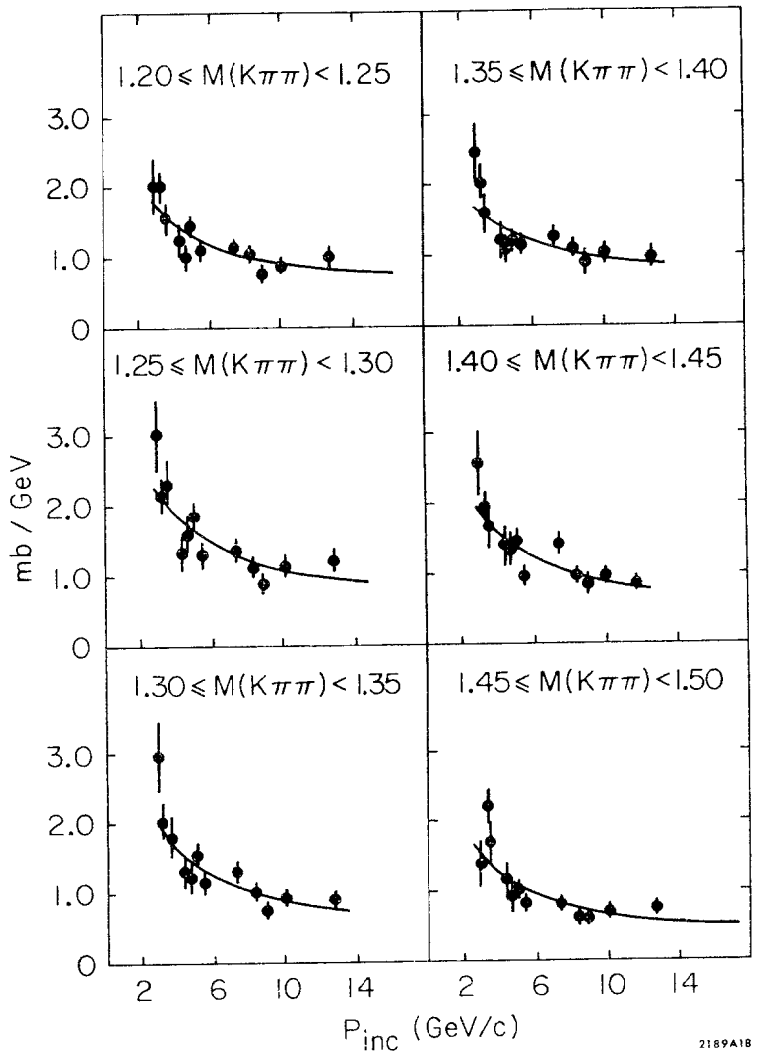

Figure 96

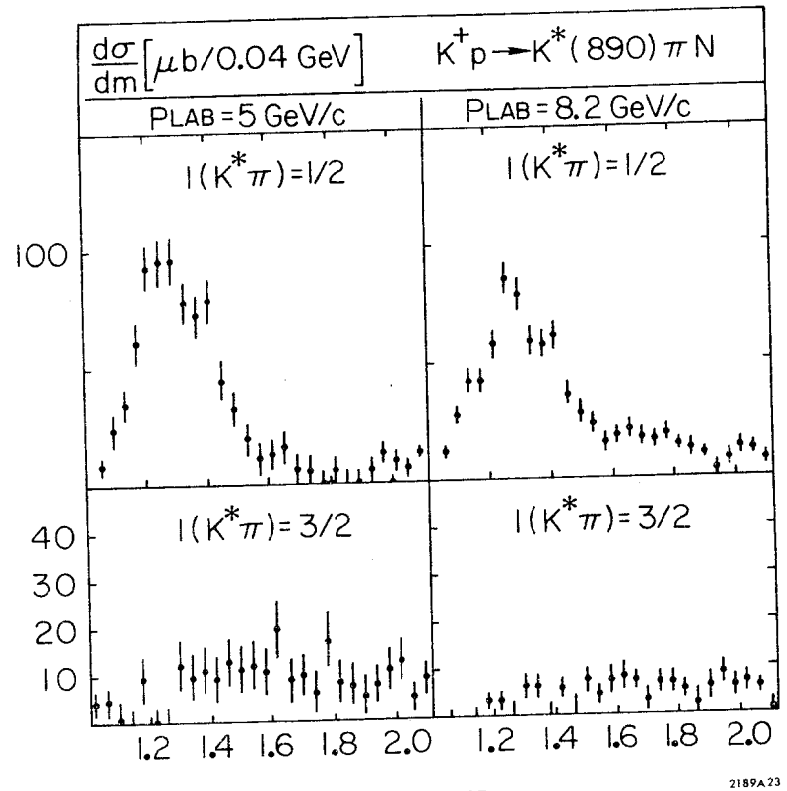

Figure 97

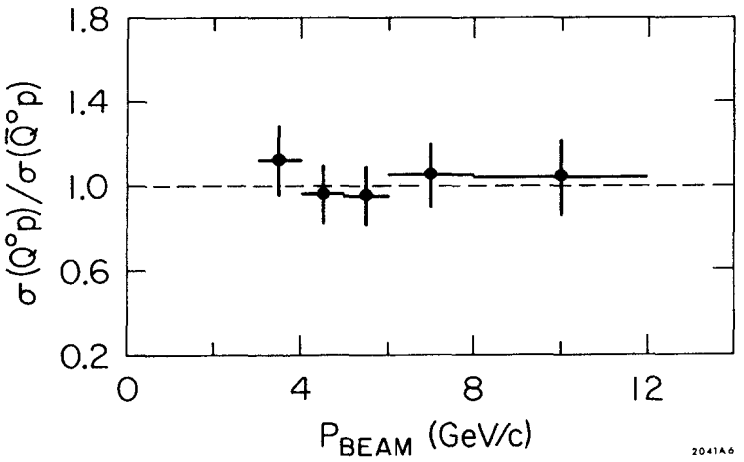

Figure 98

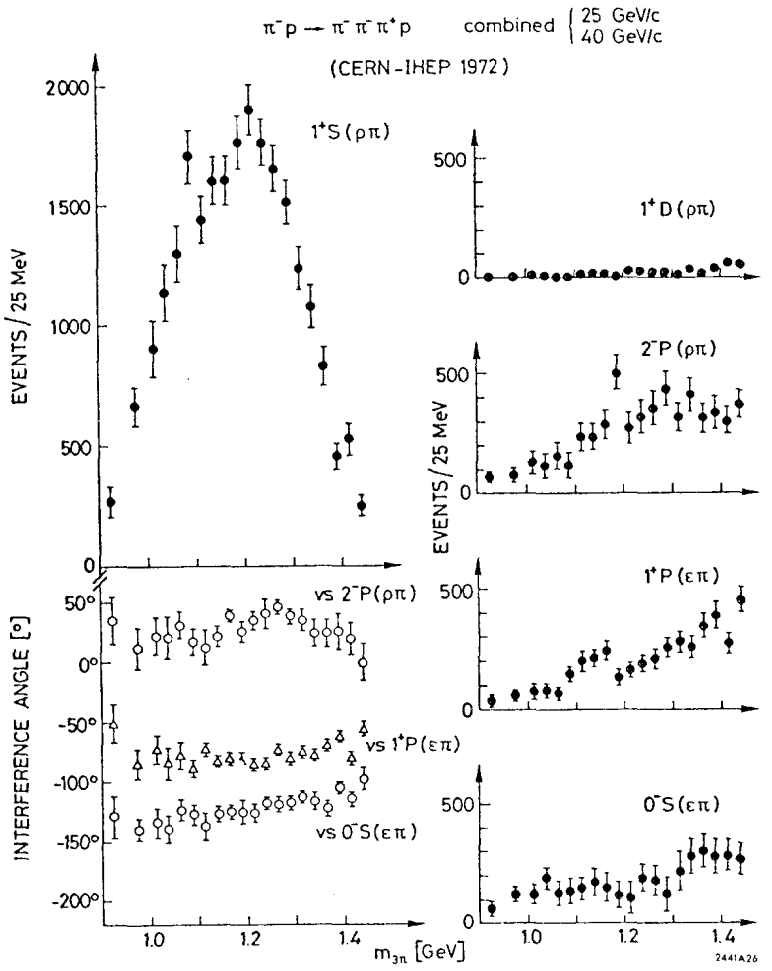

Figure 99

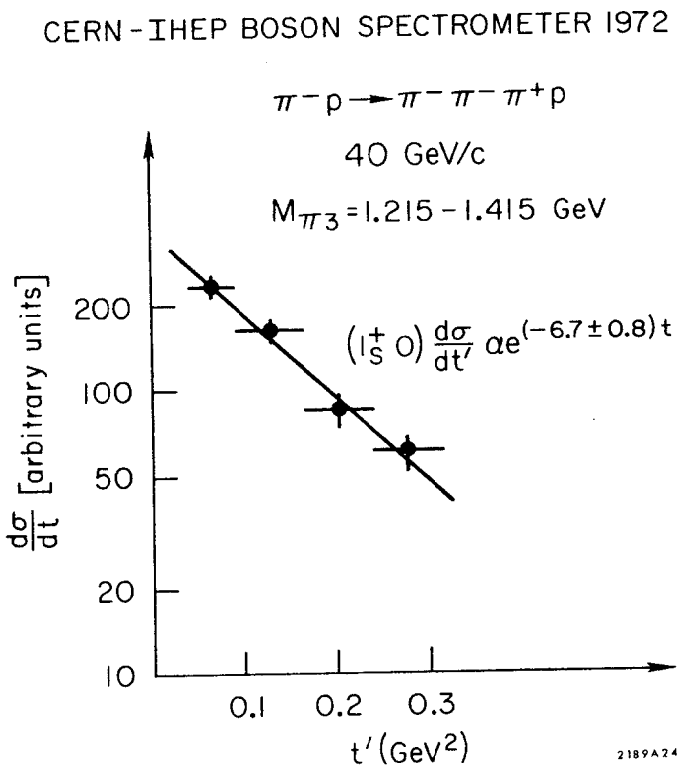

Figure 100

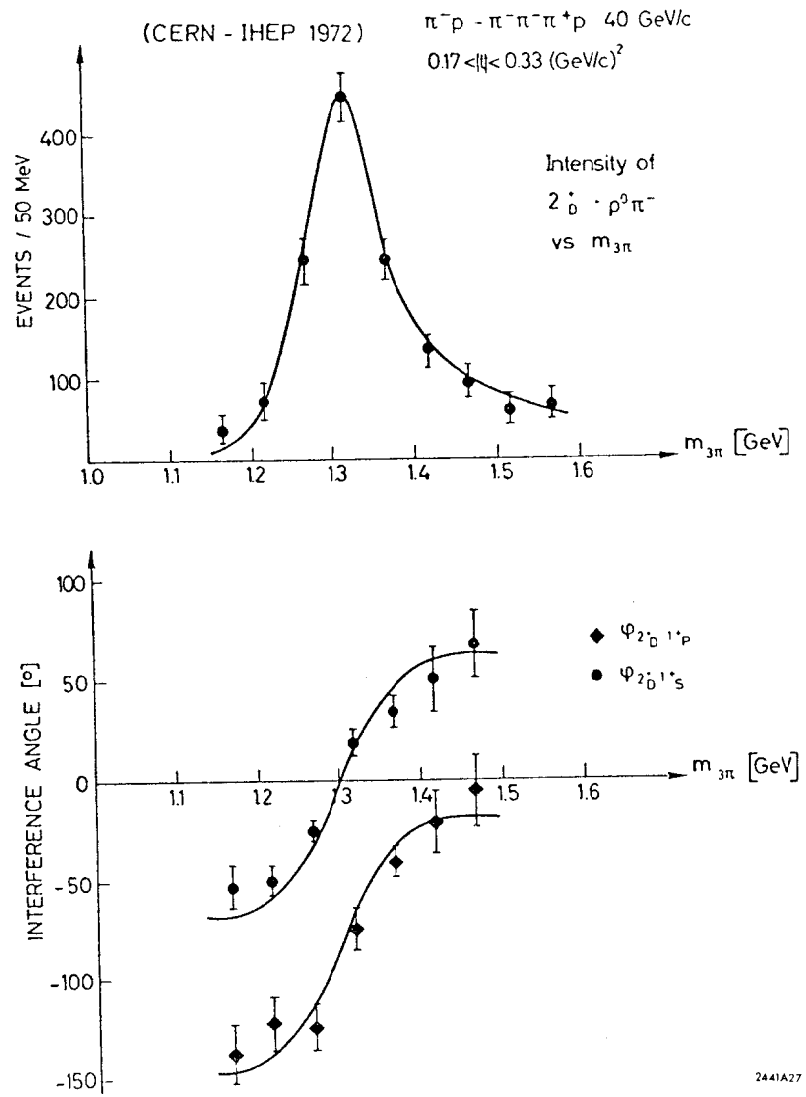

Figure 101

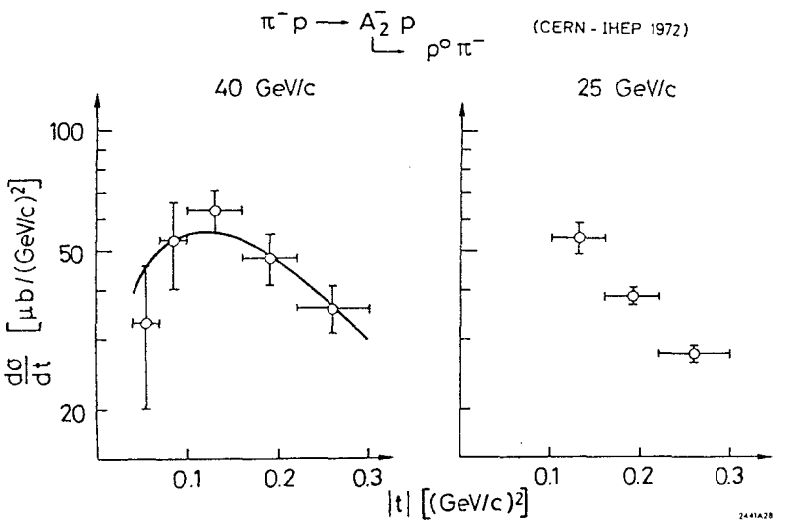

Figure 102

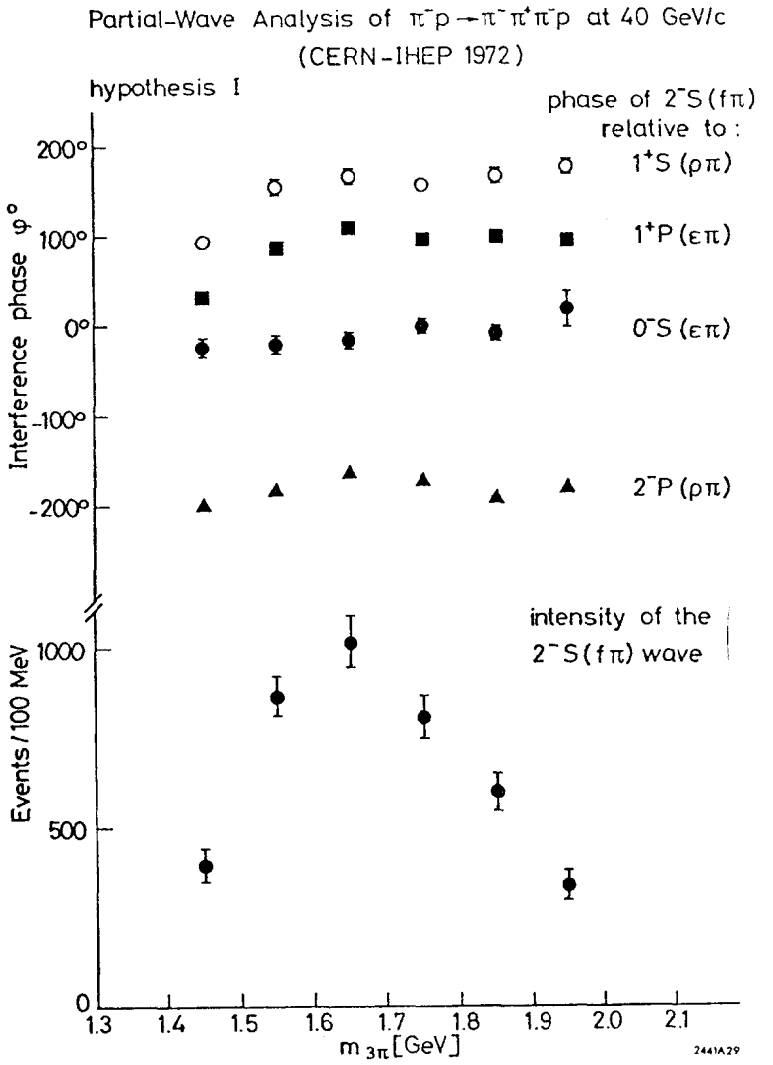

Figure 103

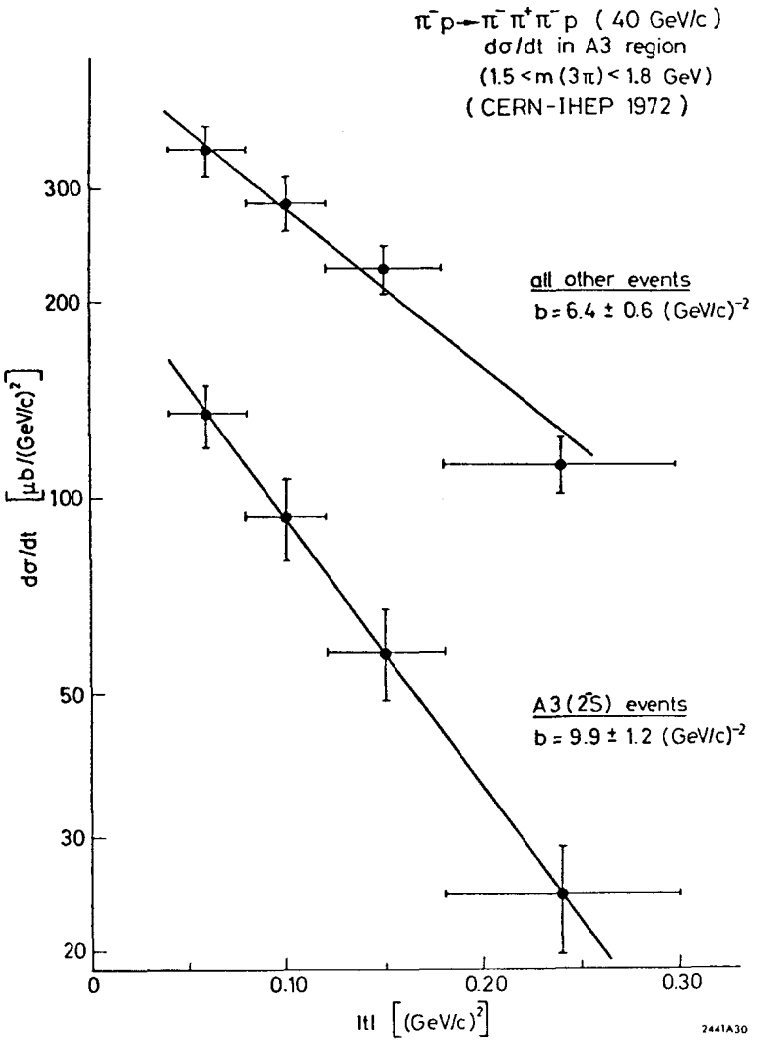

Figure 104

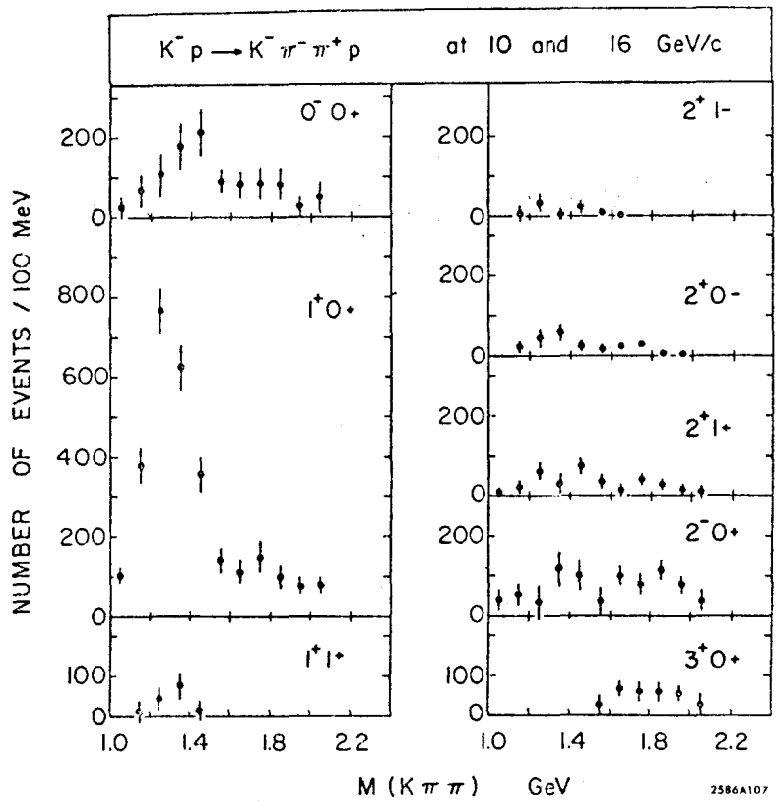

Figure 105

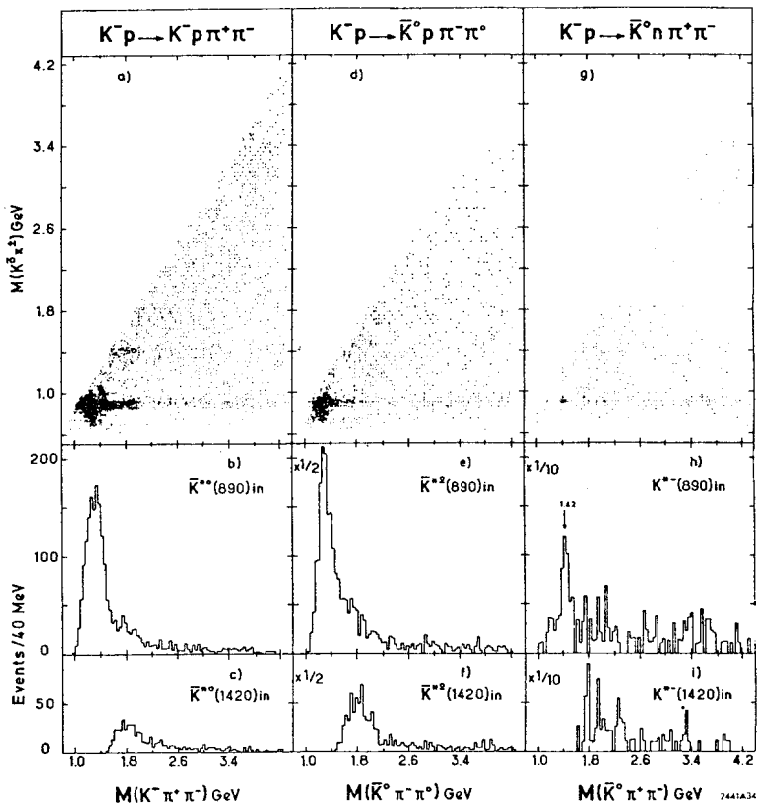

Figure 106

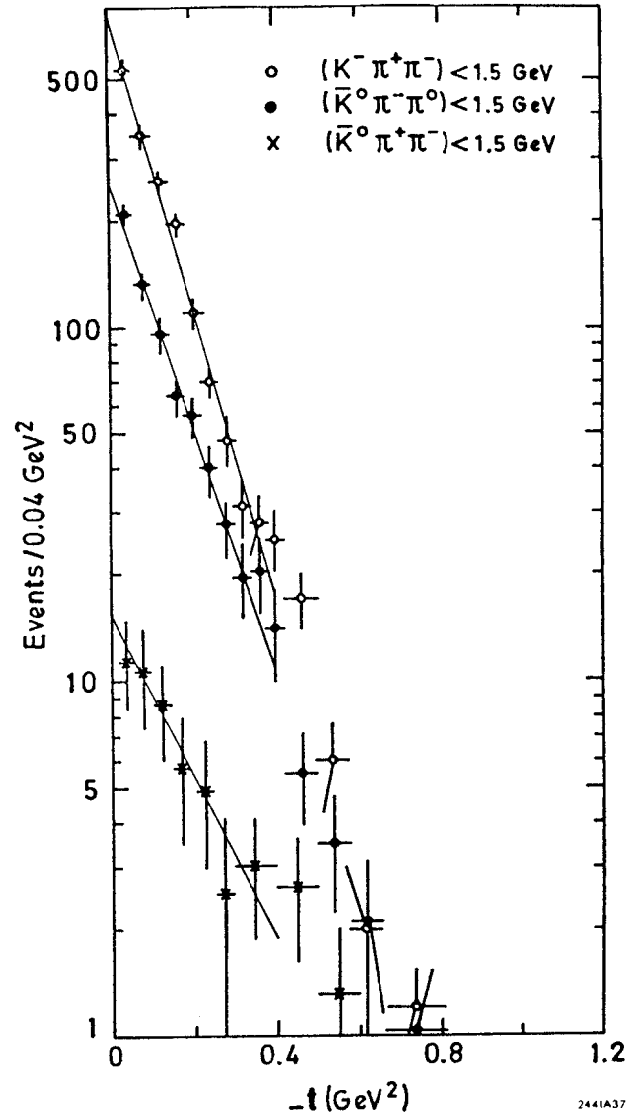

Figure 107

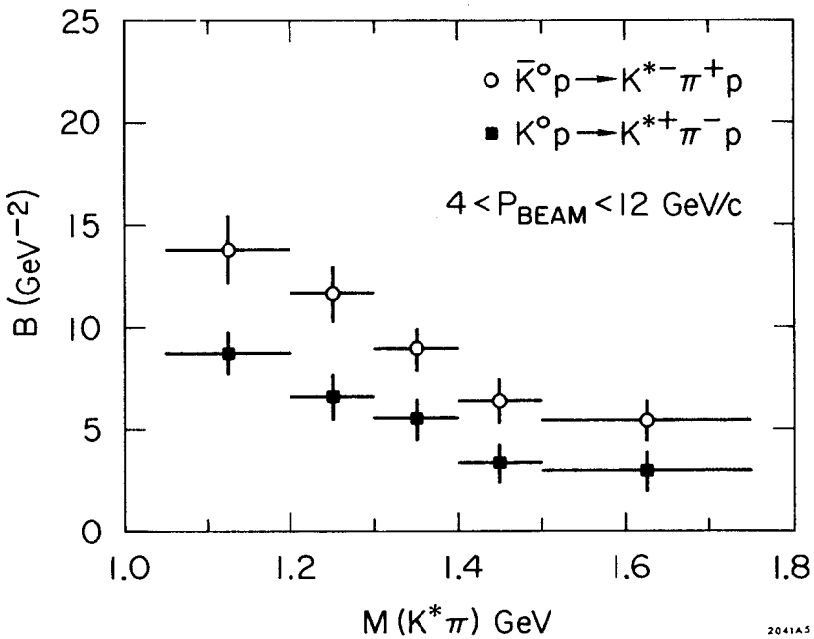

Figure 108

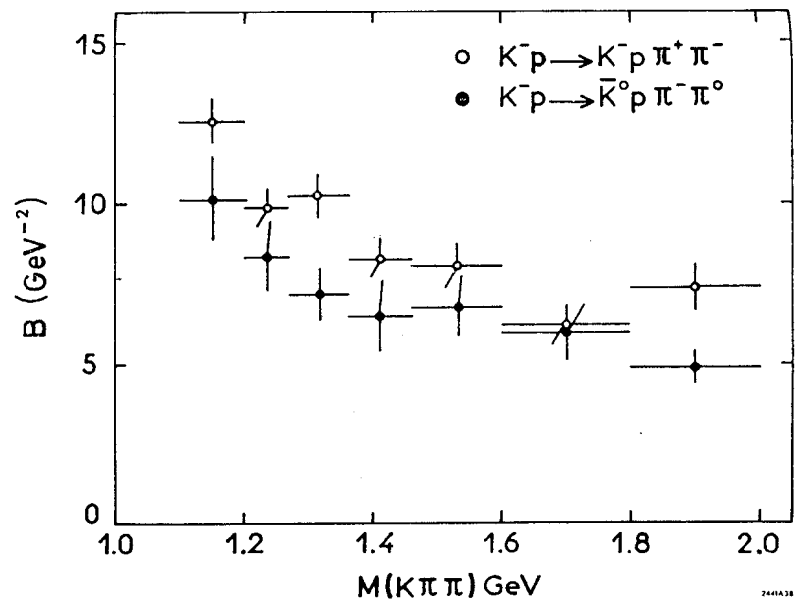

Figure 109

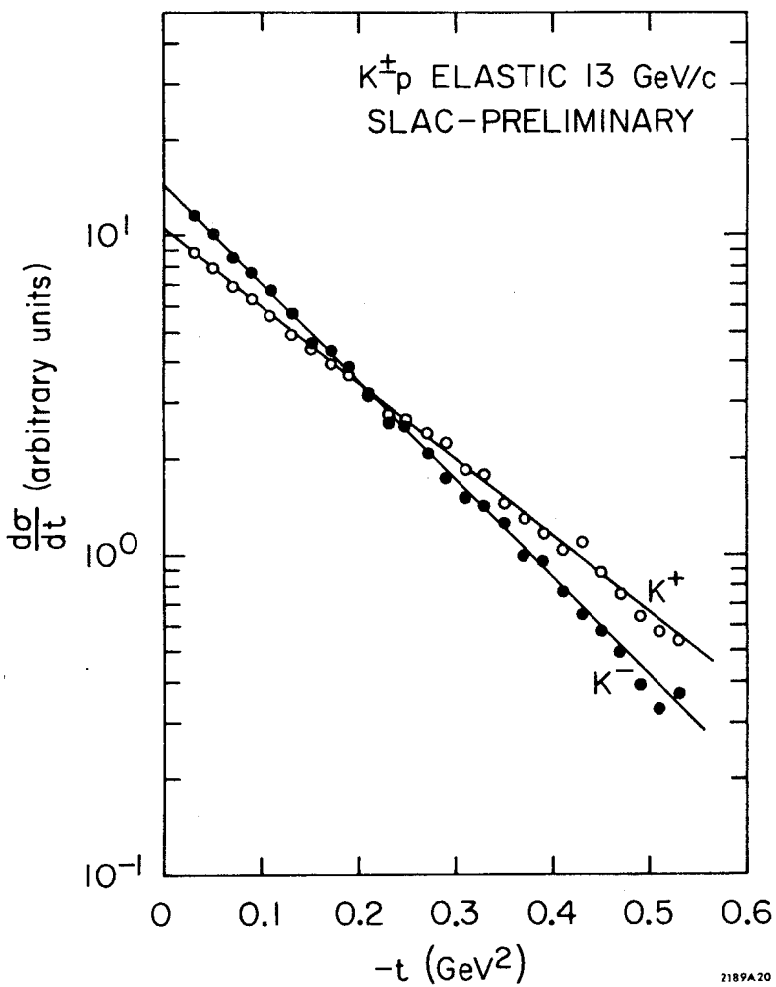

Figure 110

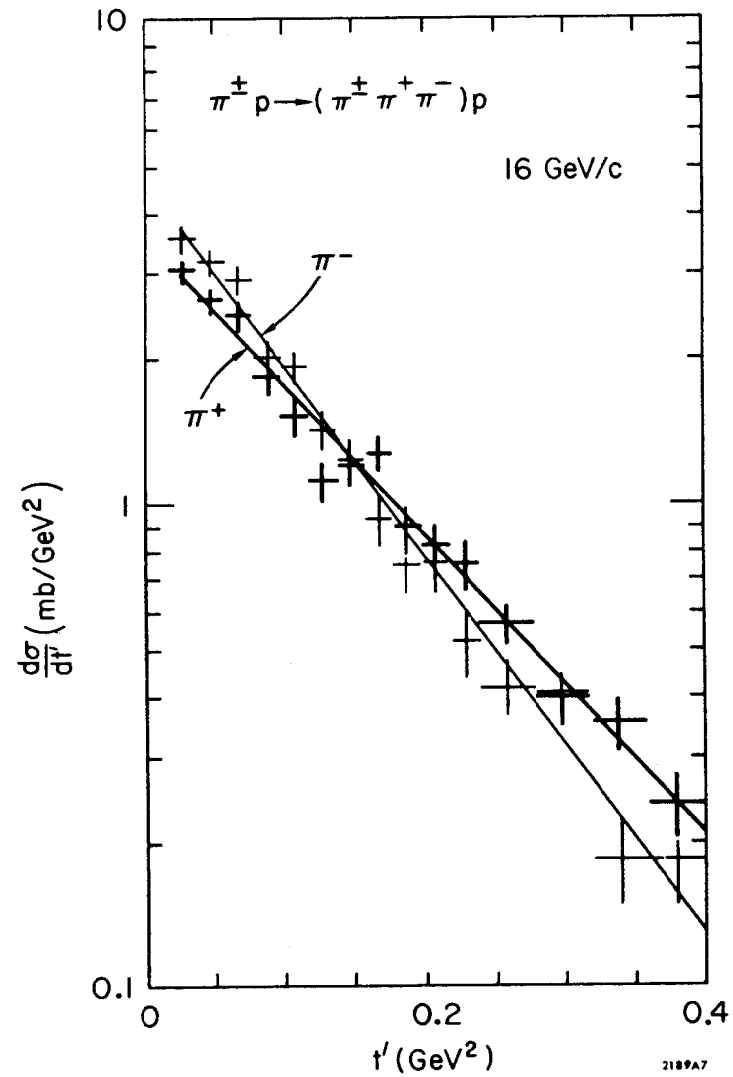

Figure 111

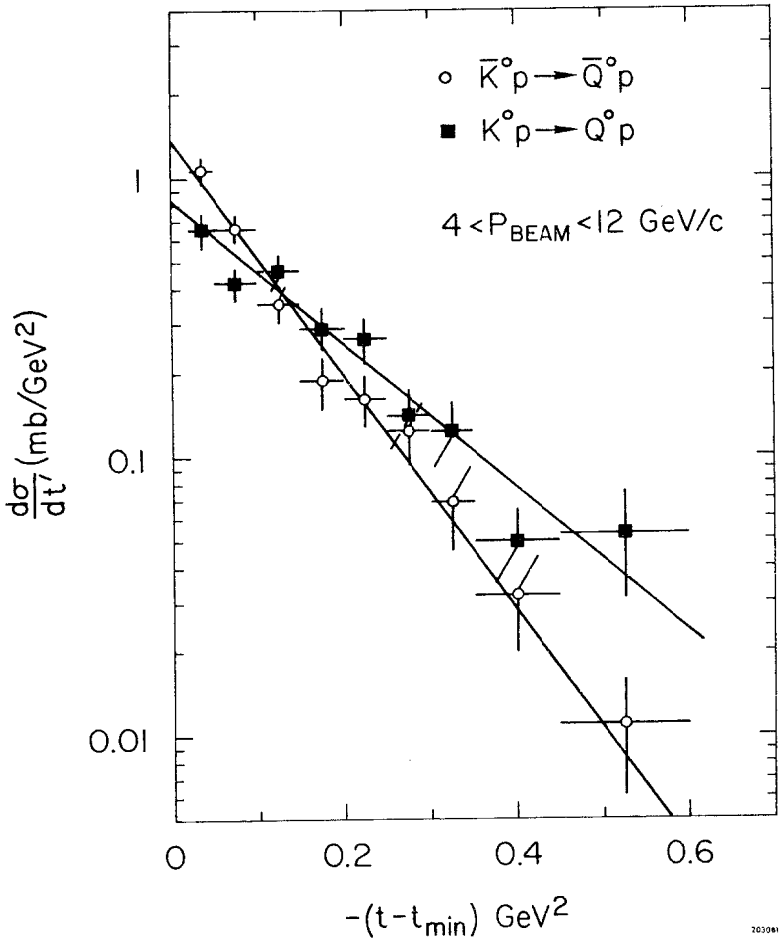

Figure 112

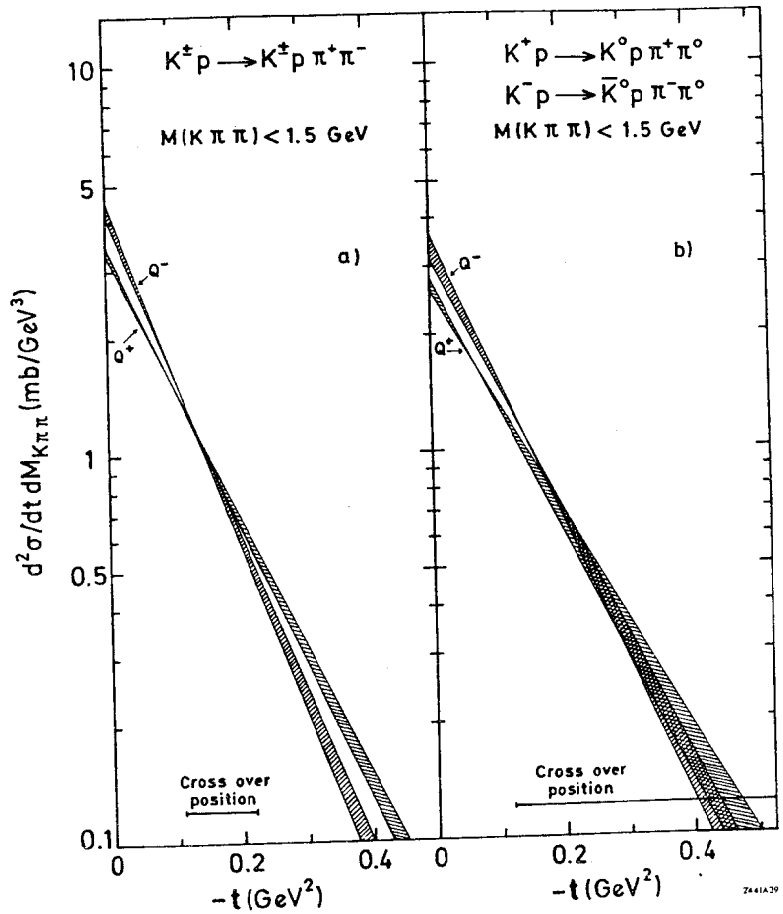

Figure 113

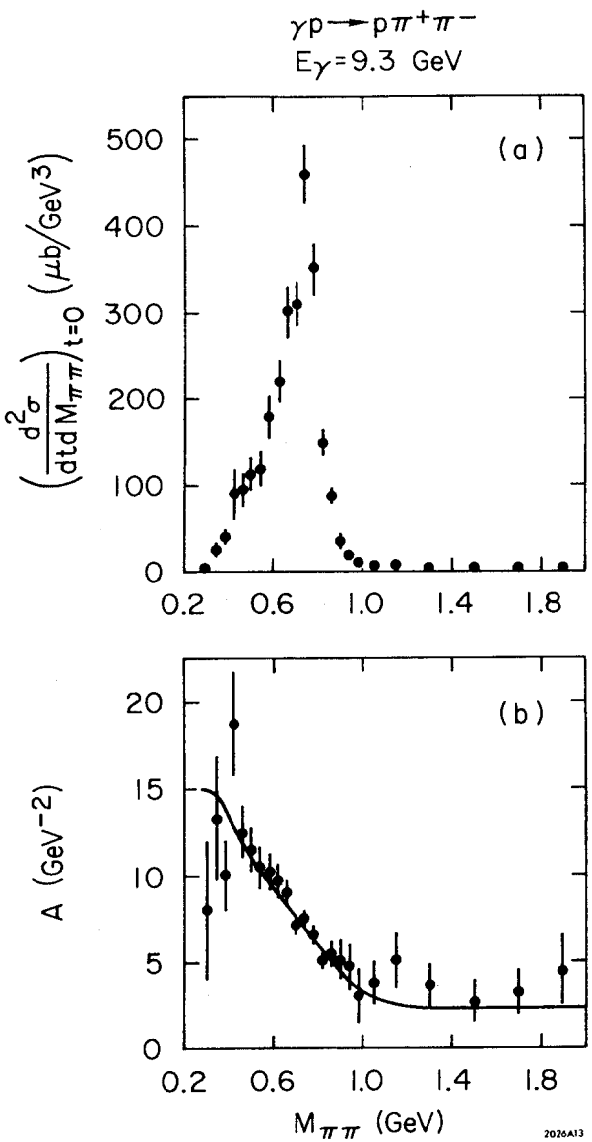

Figure 114

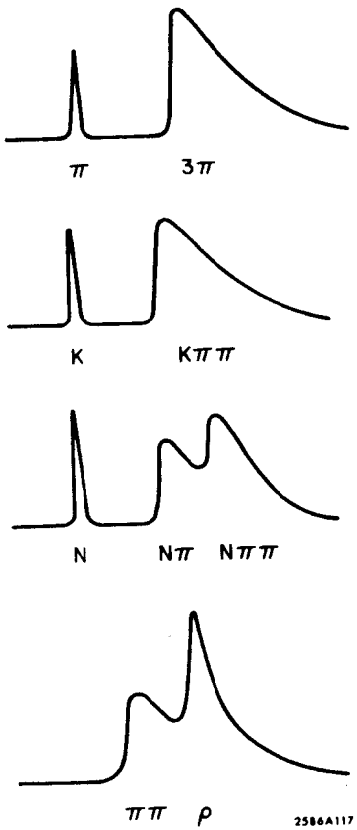

Figure 115

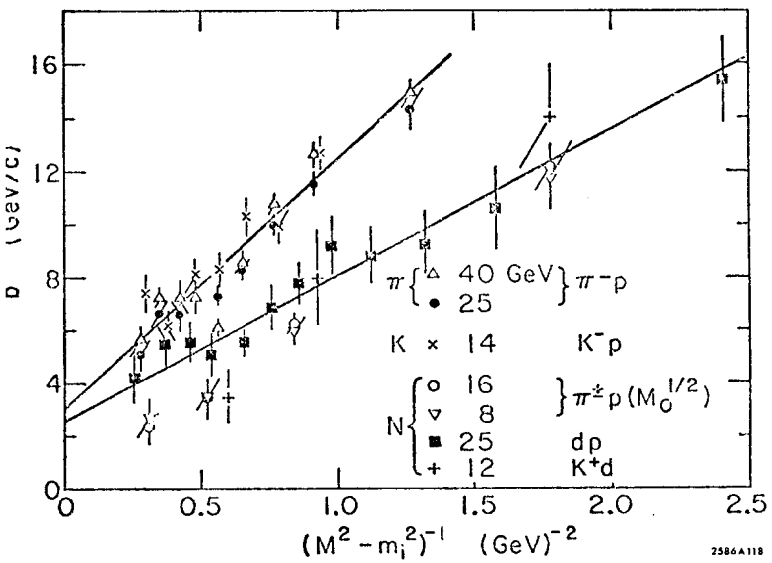

Figure 116

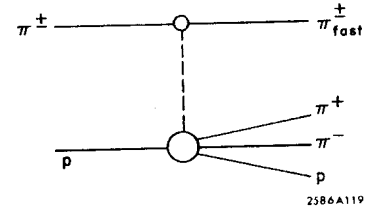

Figure 117

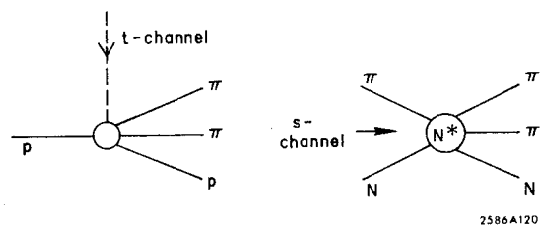

Figure 118

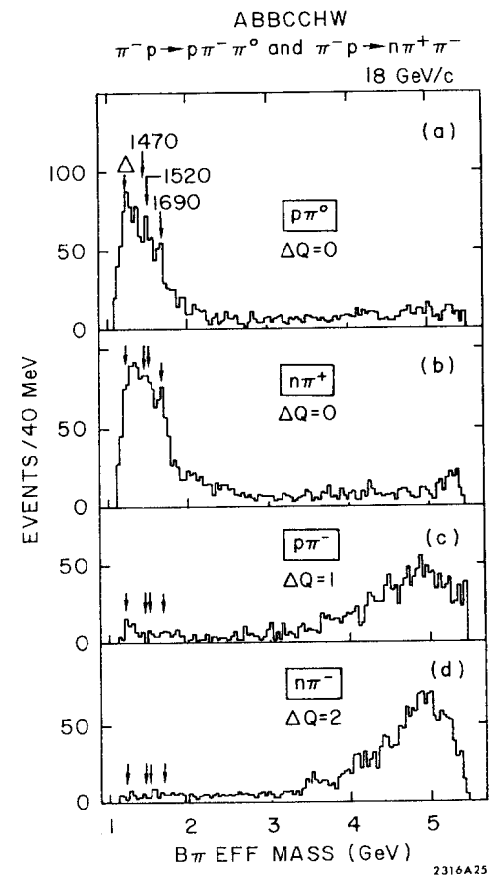

Figure 119

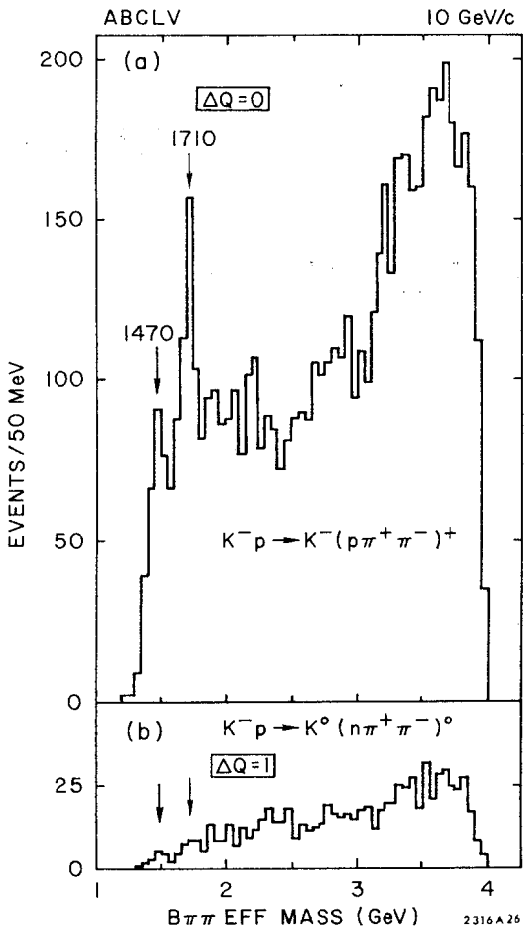

Figure 120

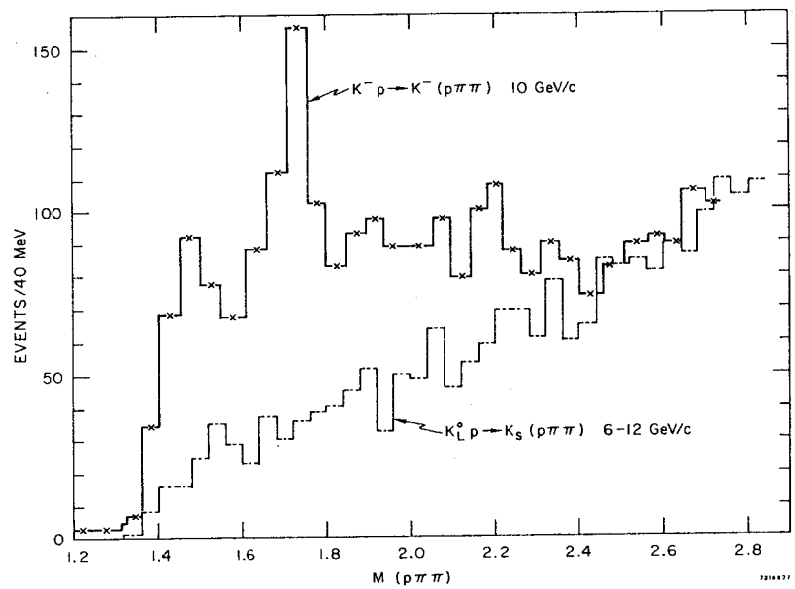

Figure 121

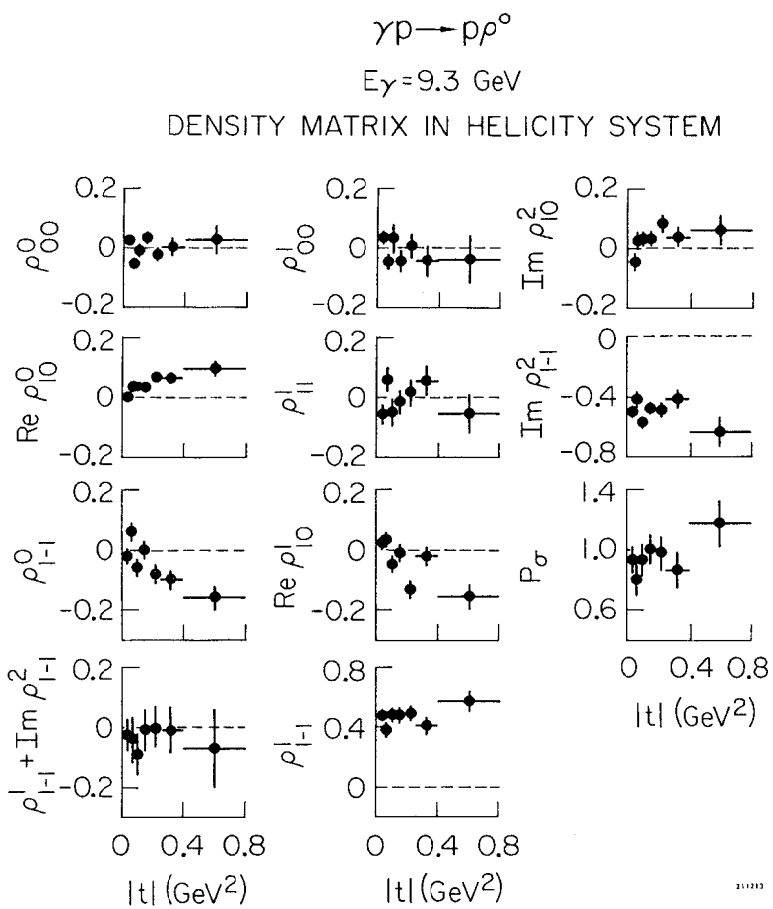

Figure 122

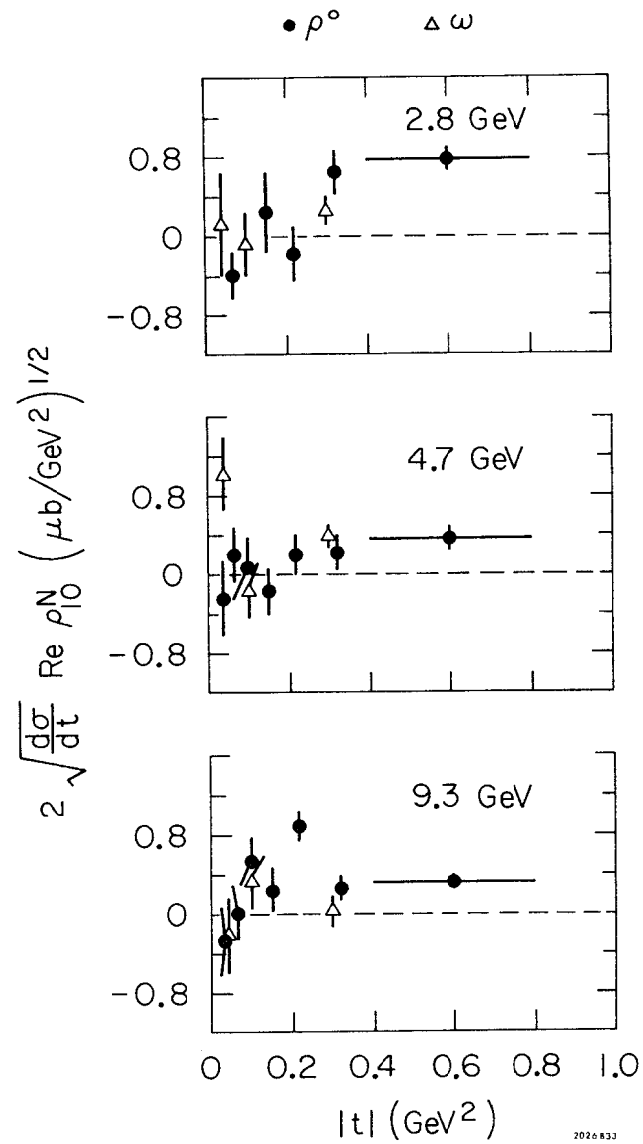

Figure 123

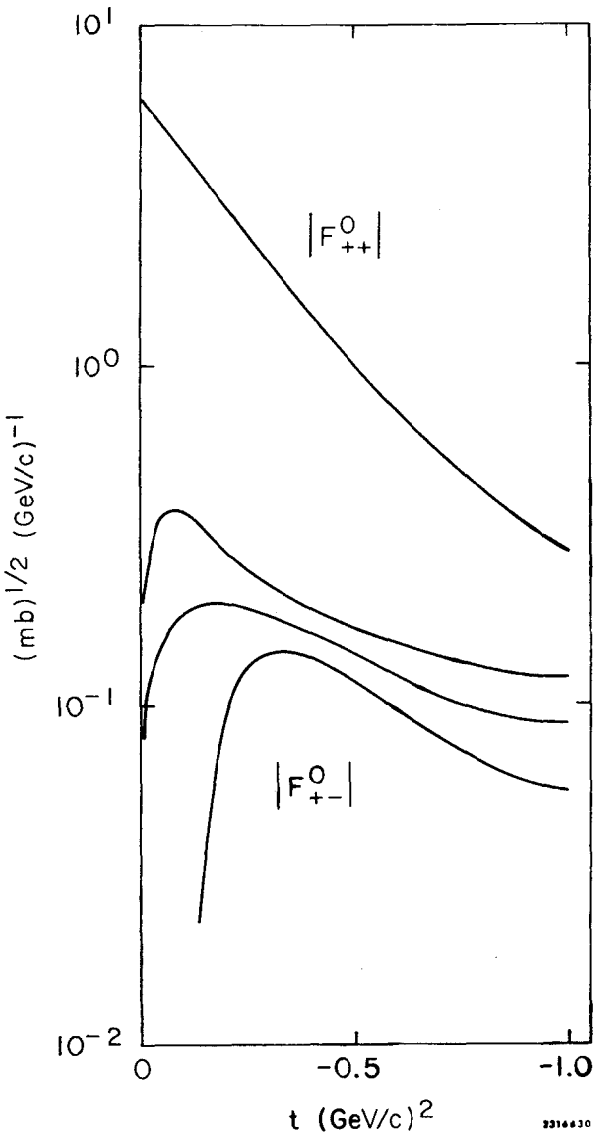

Figure 124

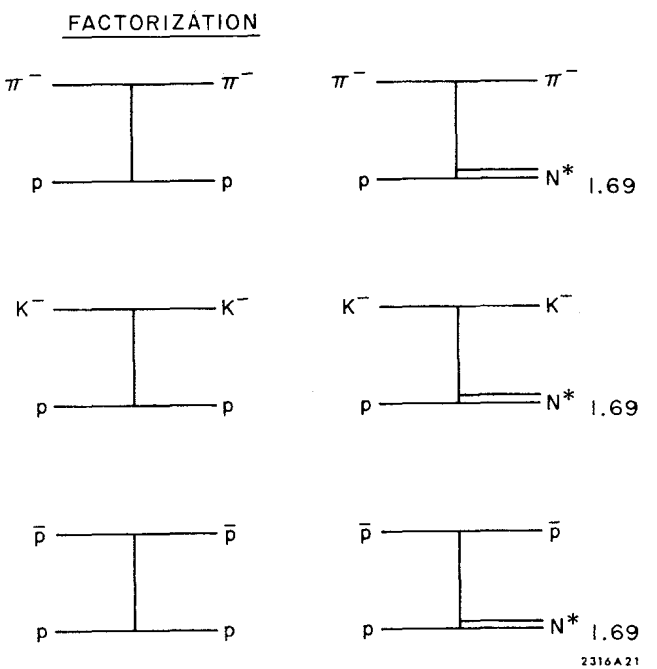

Figure 125

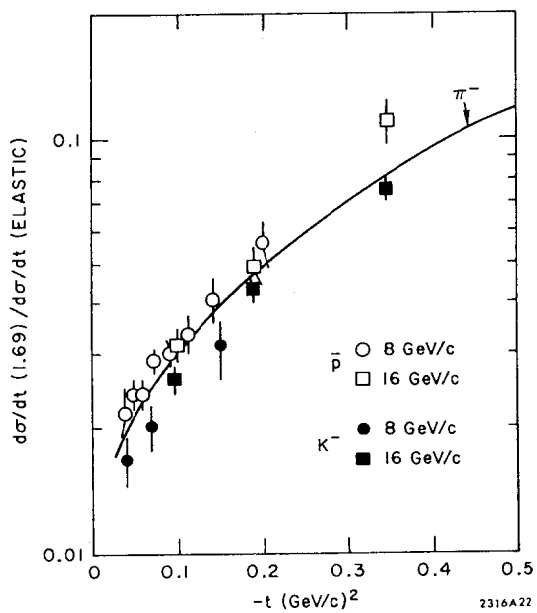

Figure 126

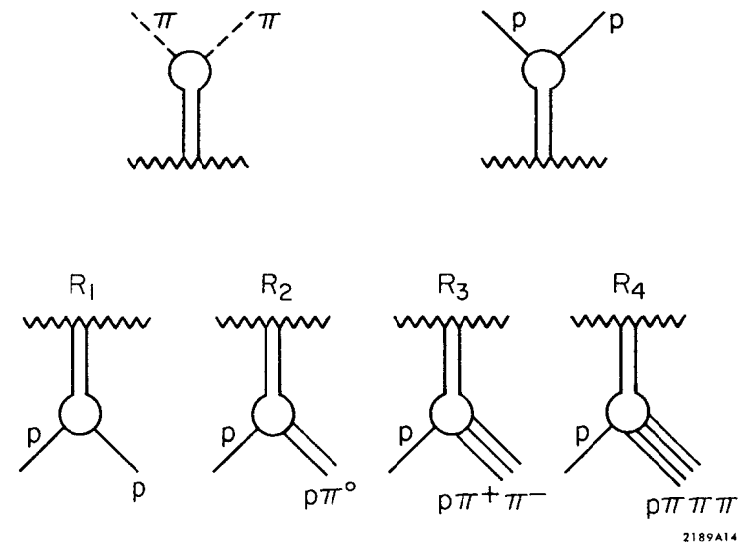

Figure 127

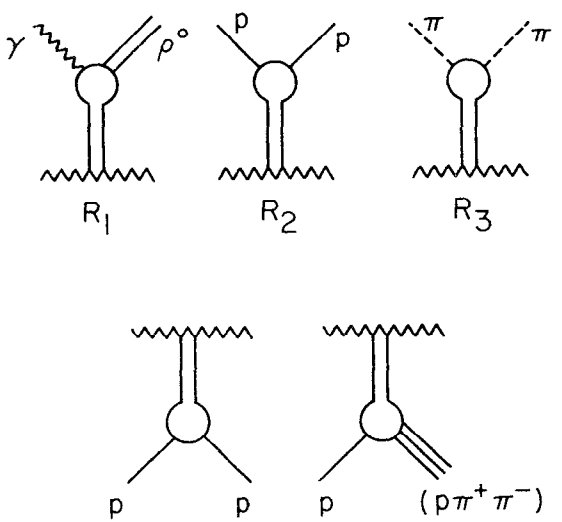

Figure 128

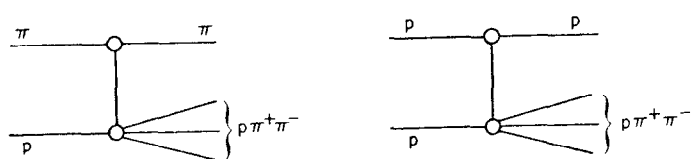

$\sigma_1 = 180 \pm 36\ \mu b$

$\sigma_2 = 370 \pm {}^{40}_{140}\ \mu b$

$\sigma_1 \sim g^2_{\pi\pi\mathbb{P}^*} g^2_{pp^*\mathbb{P}}$

$\sigma_2 \sim g^2_{pp\mathbb{P}^*} g^2_{pp^*\mathbb{P}}$

$$\frac{\sigma_1}{\sigma_2} = \frac{g^2_{\pi\pi\mathbb{P}}}{g^2_{pp\mathbb{P}}} = \frac{\sigma^{elastic}_{\pi p}}{\sigma^{elastic}_{pp}} = \frac{3.0 \pm 0.3}{6.8 \pm 0.2} = 0.44 \pm 0.05$$

$= 0.5.$

2586A131

Figure 129

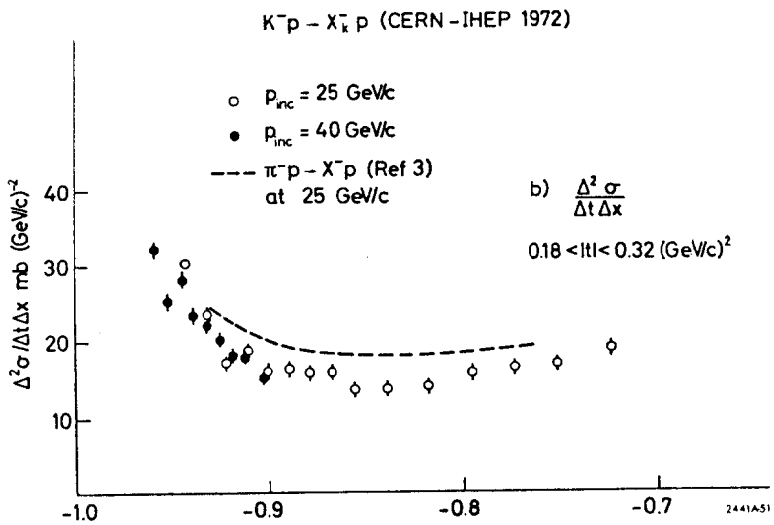

Figure 130

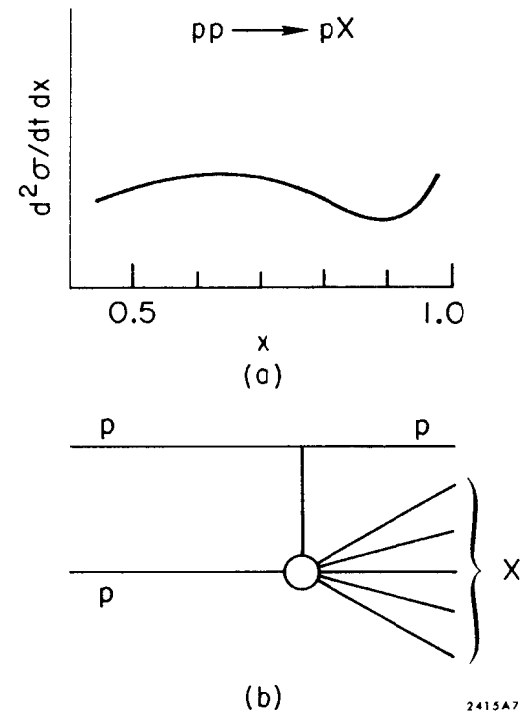

Figure 131

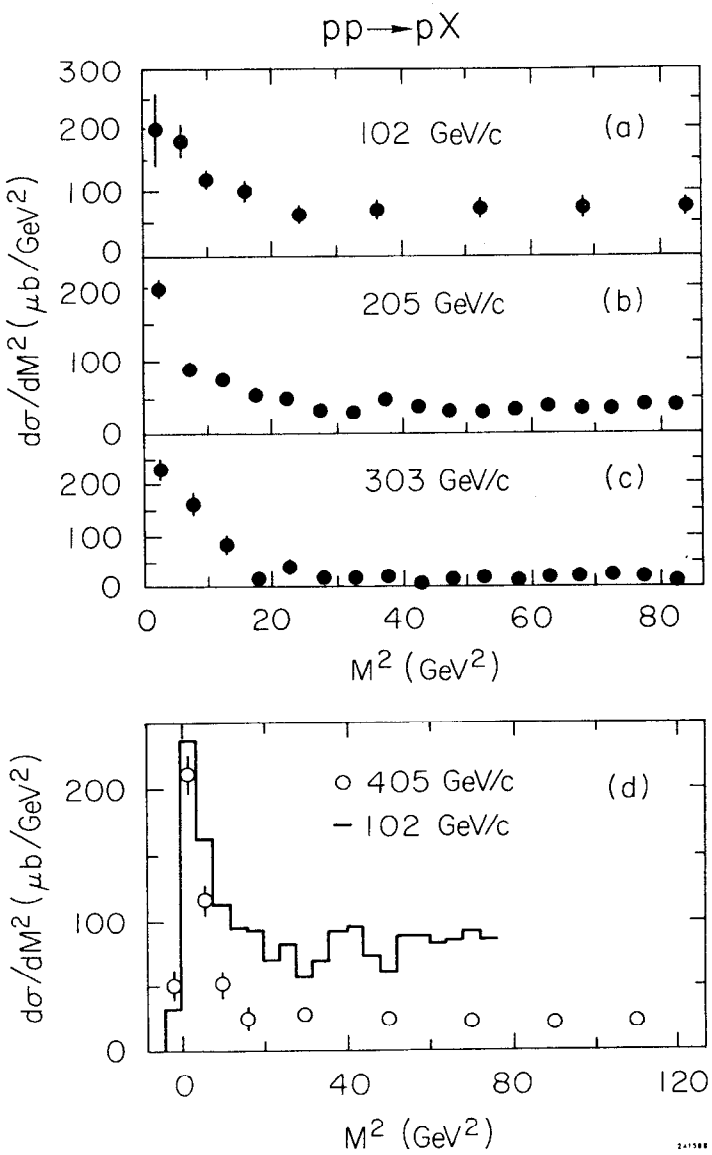

Figure 132

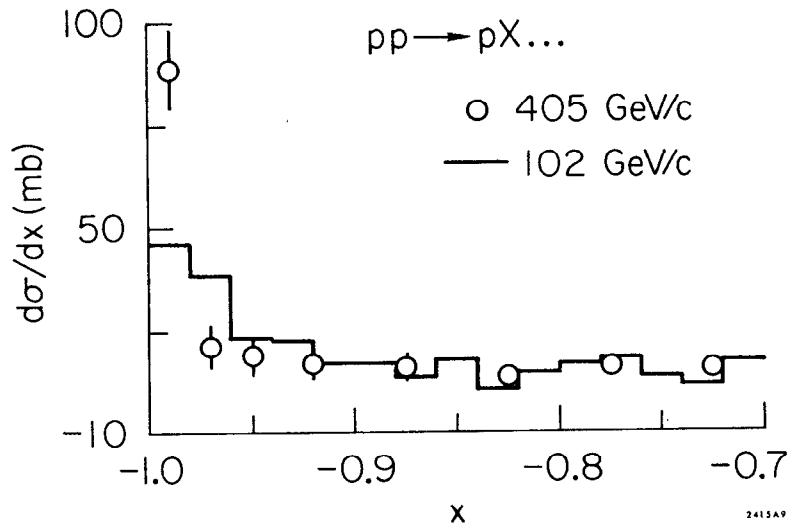

Figure 133

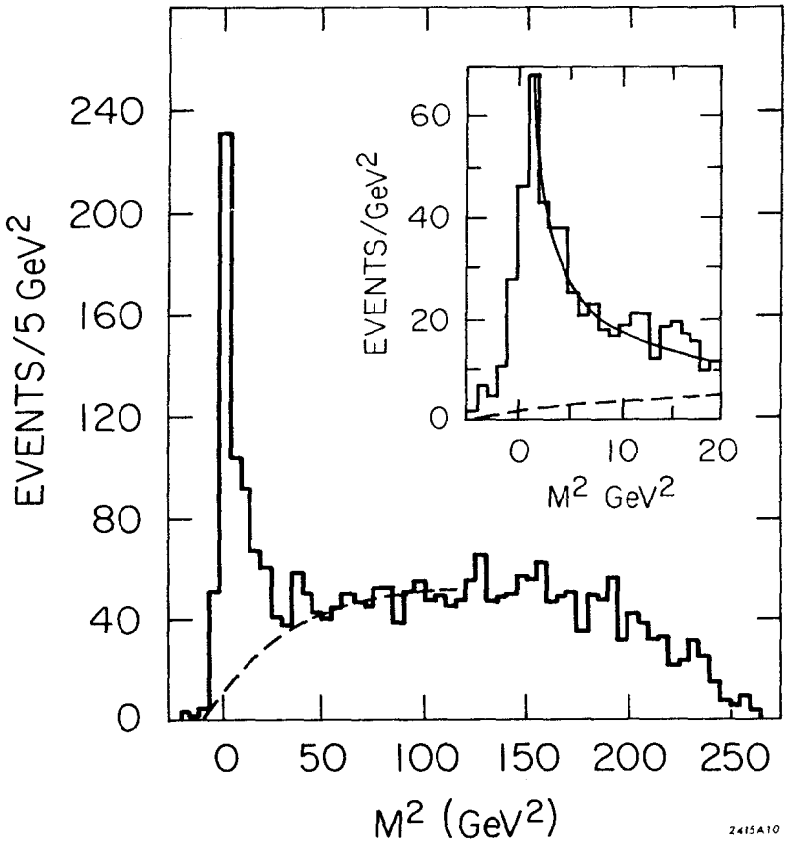

Figure 134

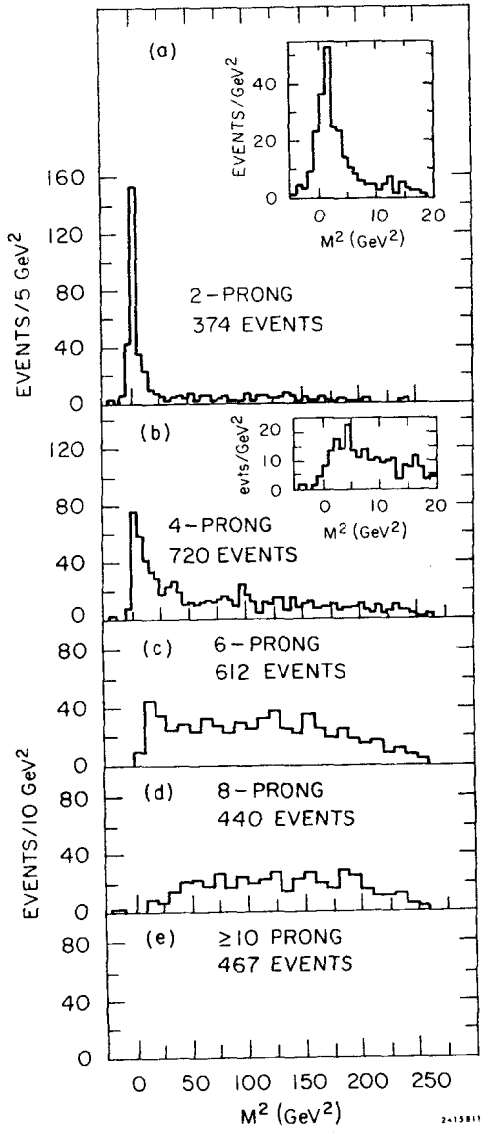

Figure 135

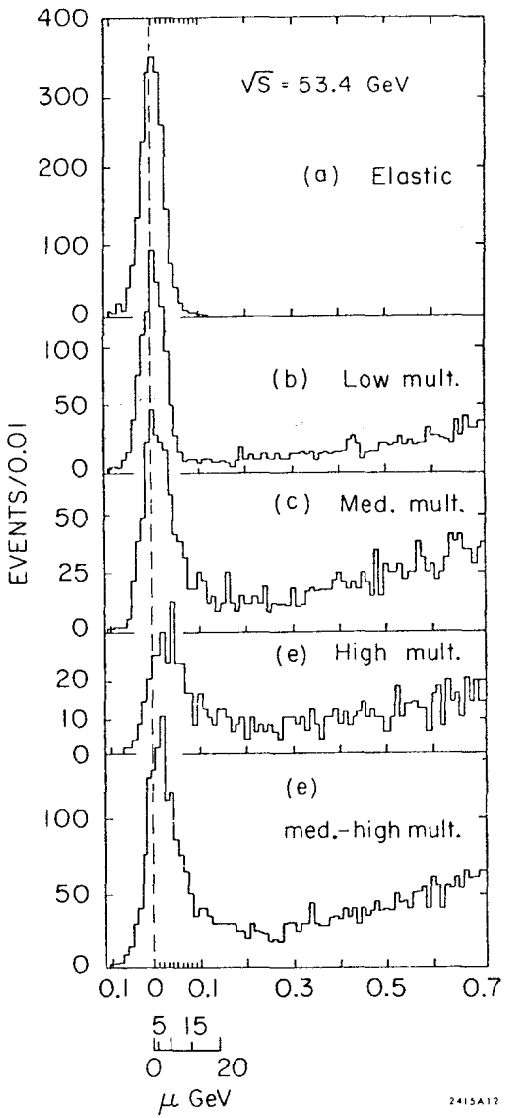

Figure 136

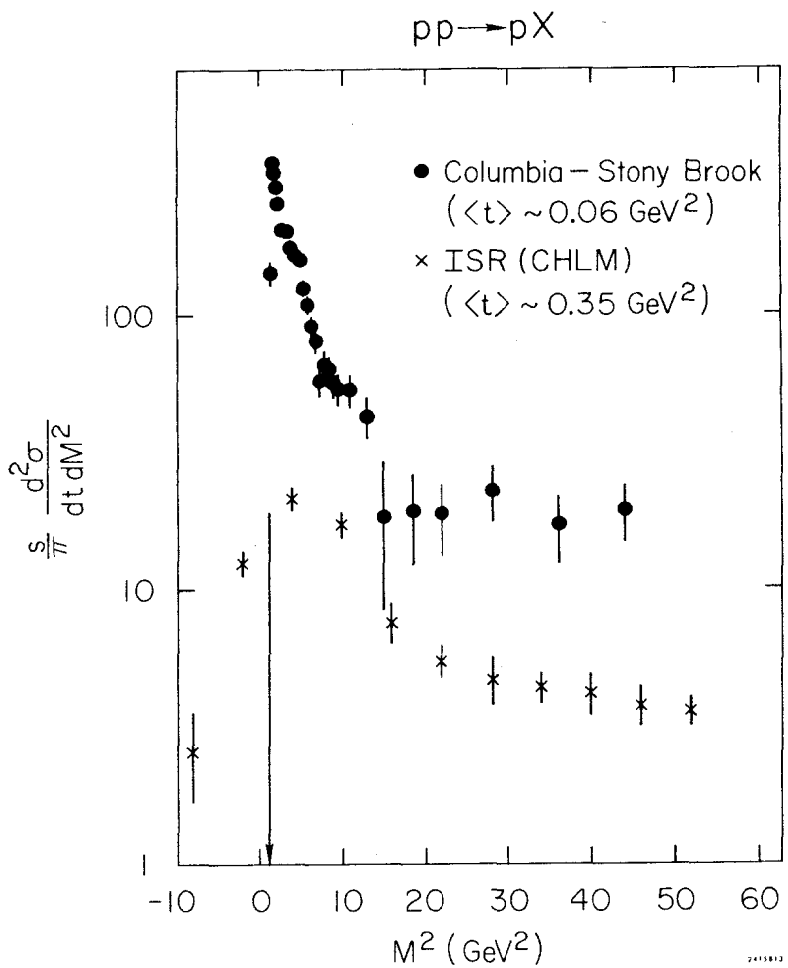

Figure 137

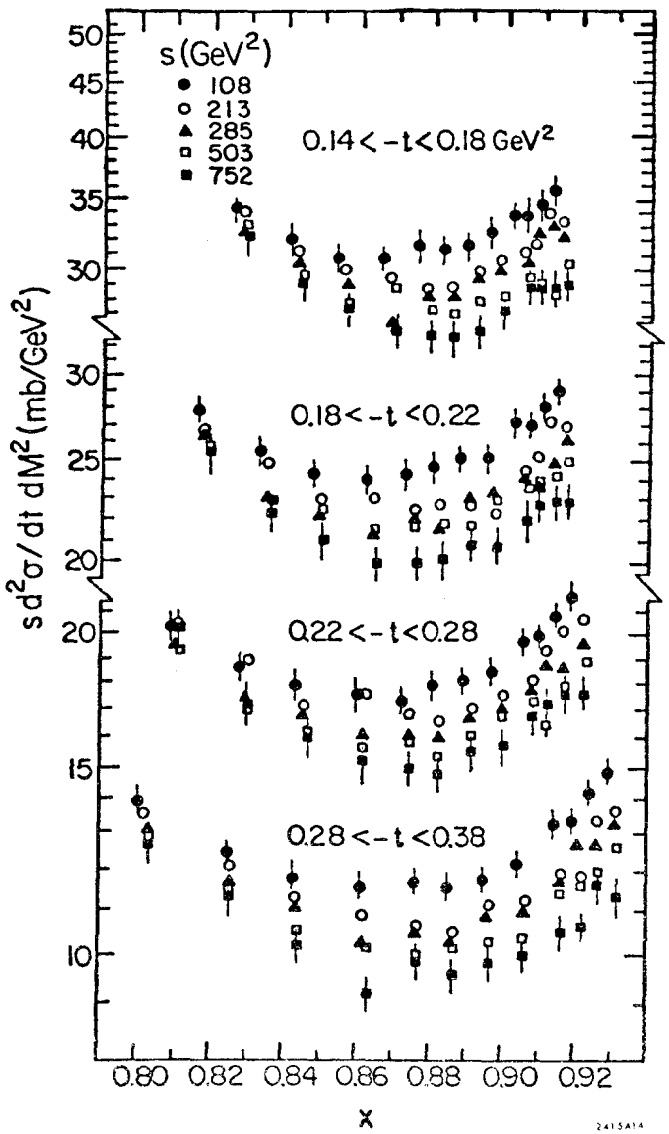

Figure 138

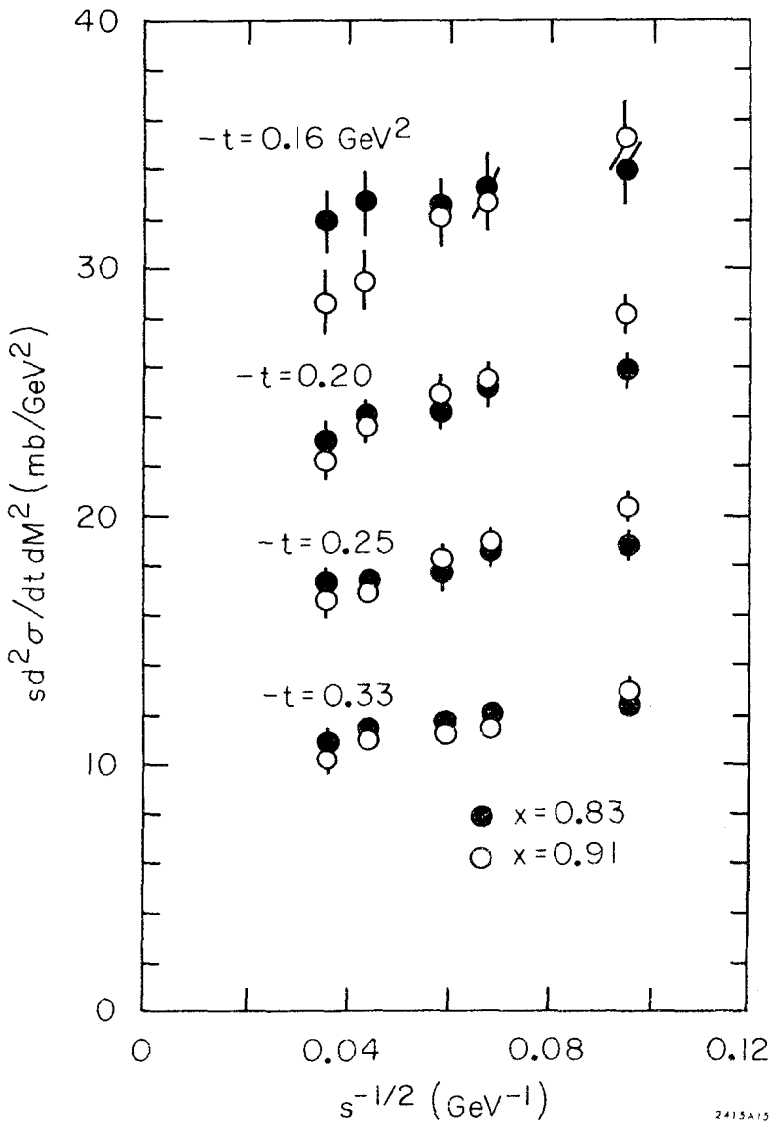

Figure 139

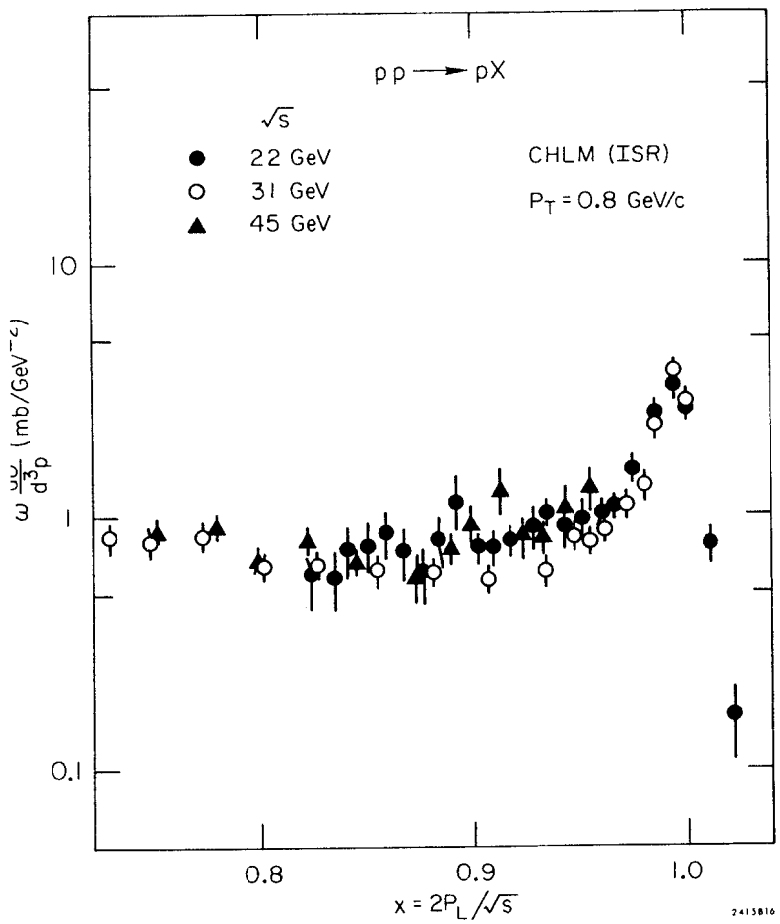

Figure 140

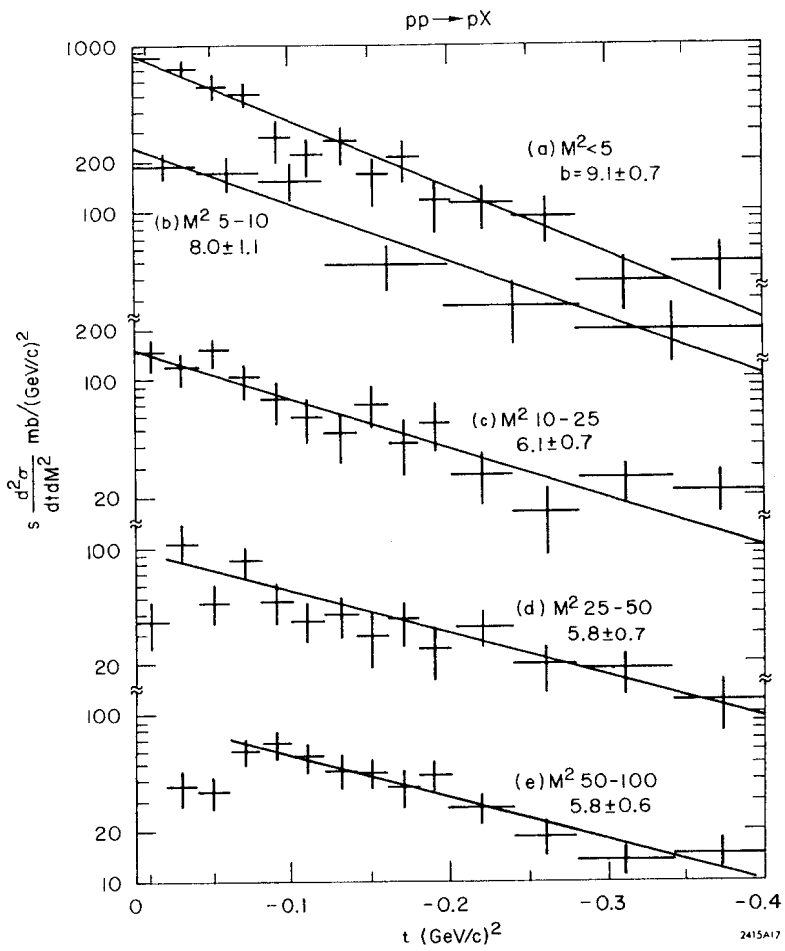

Figure 141

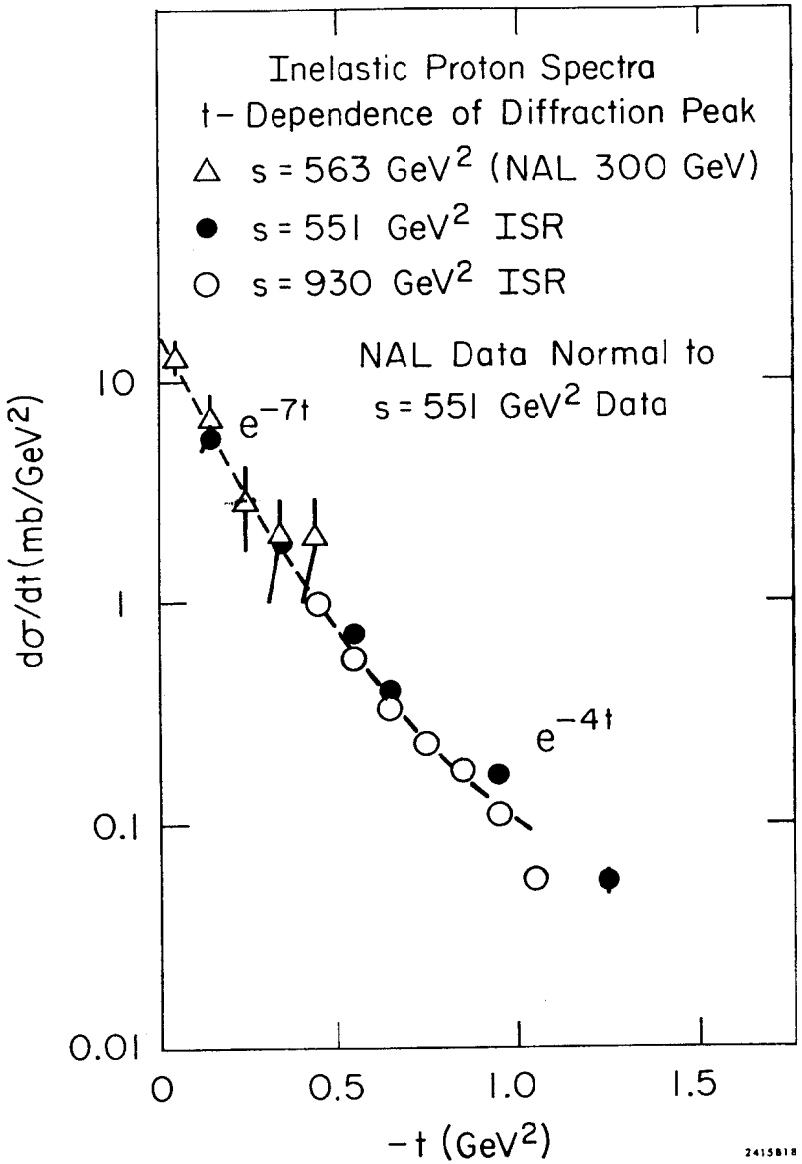

Figure 142

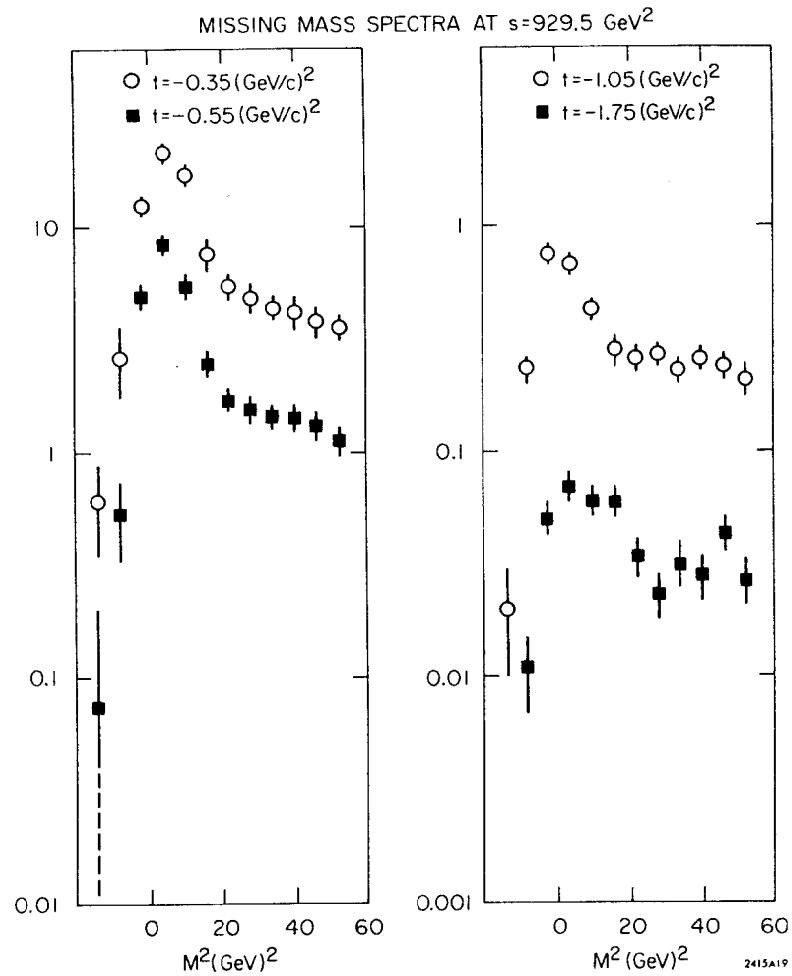

Figure 143

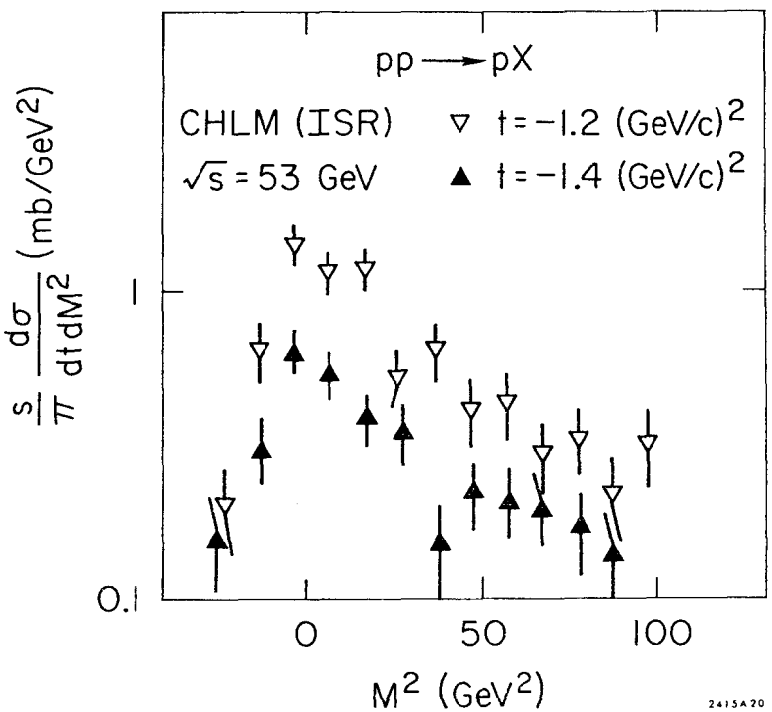

Figure 144

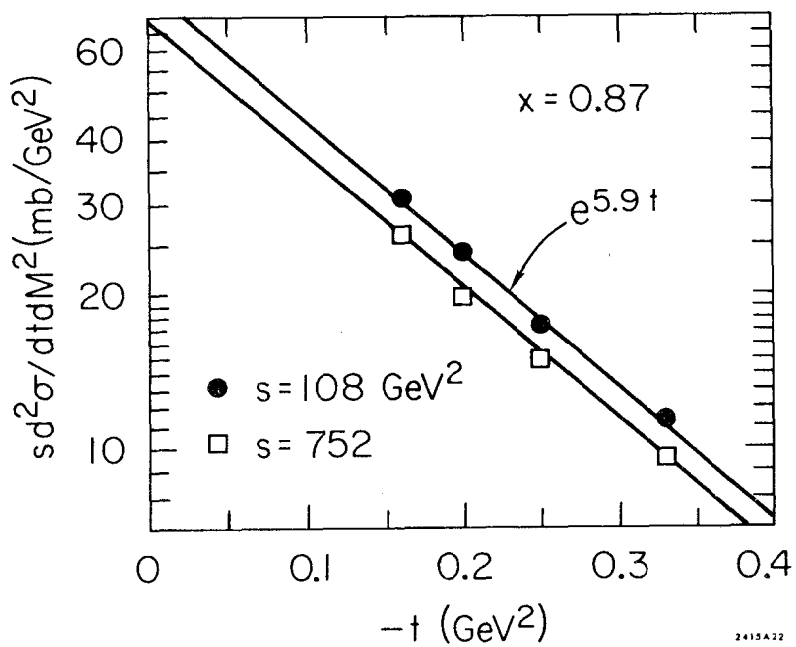

Figure 145

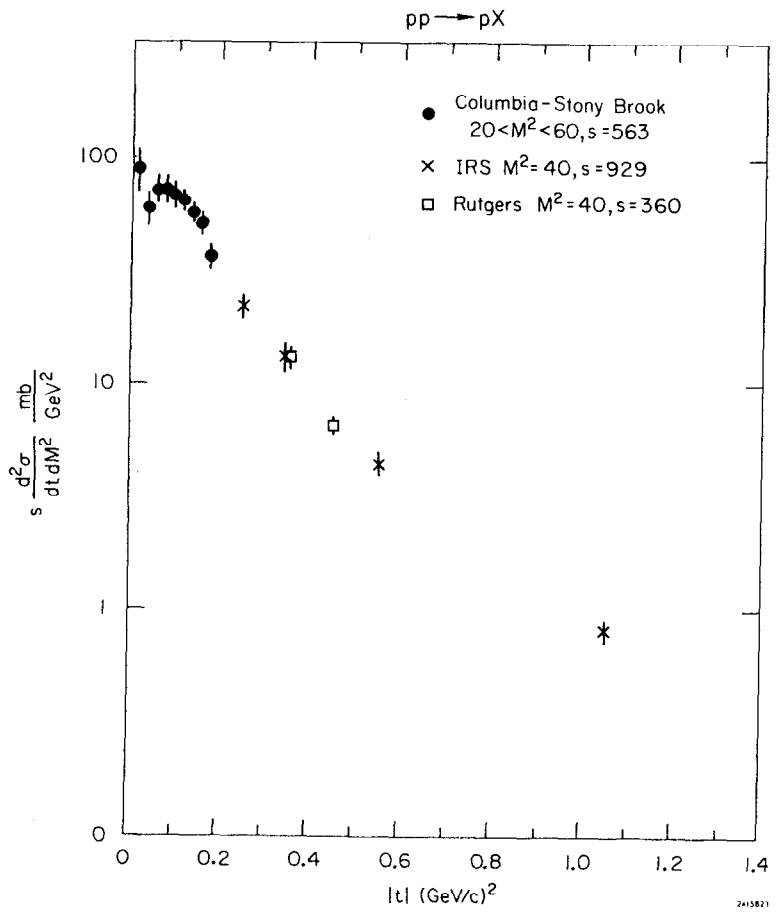

Figure 146

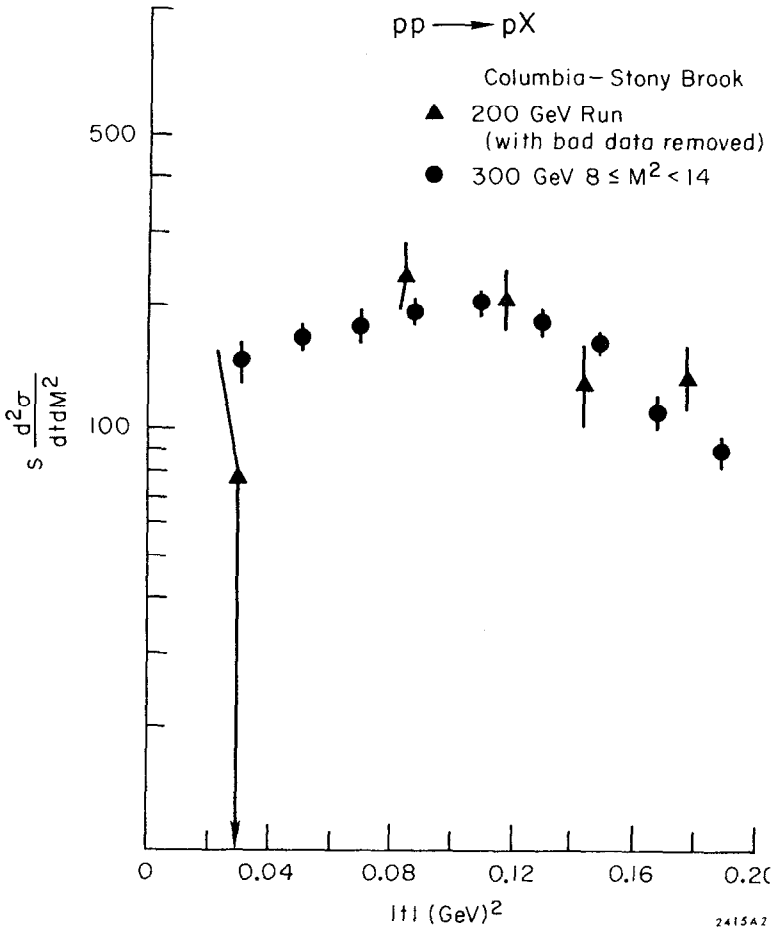

Figure 147

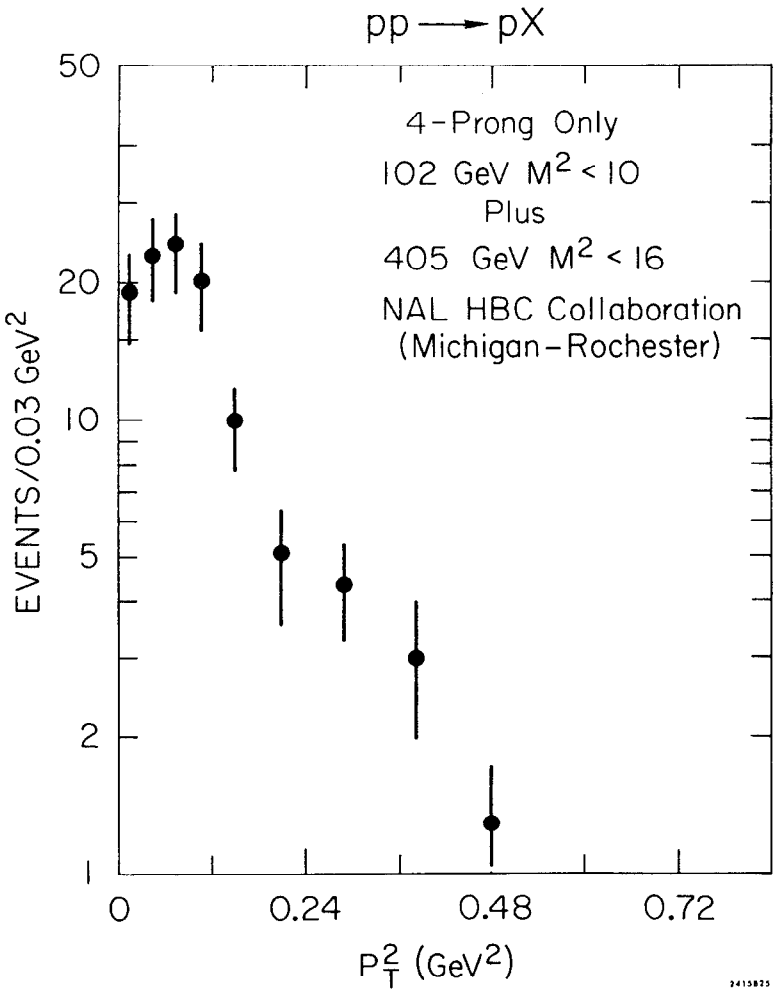

Figure 148

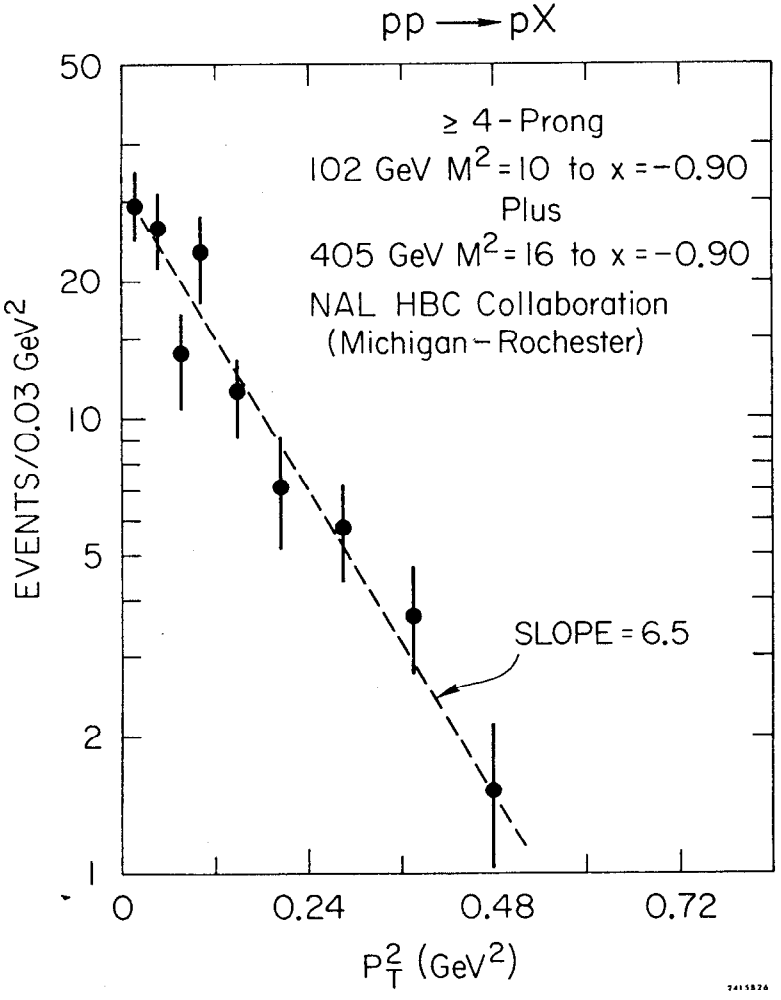

Figure 149a

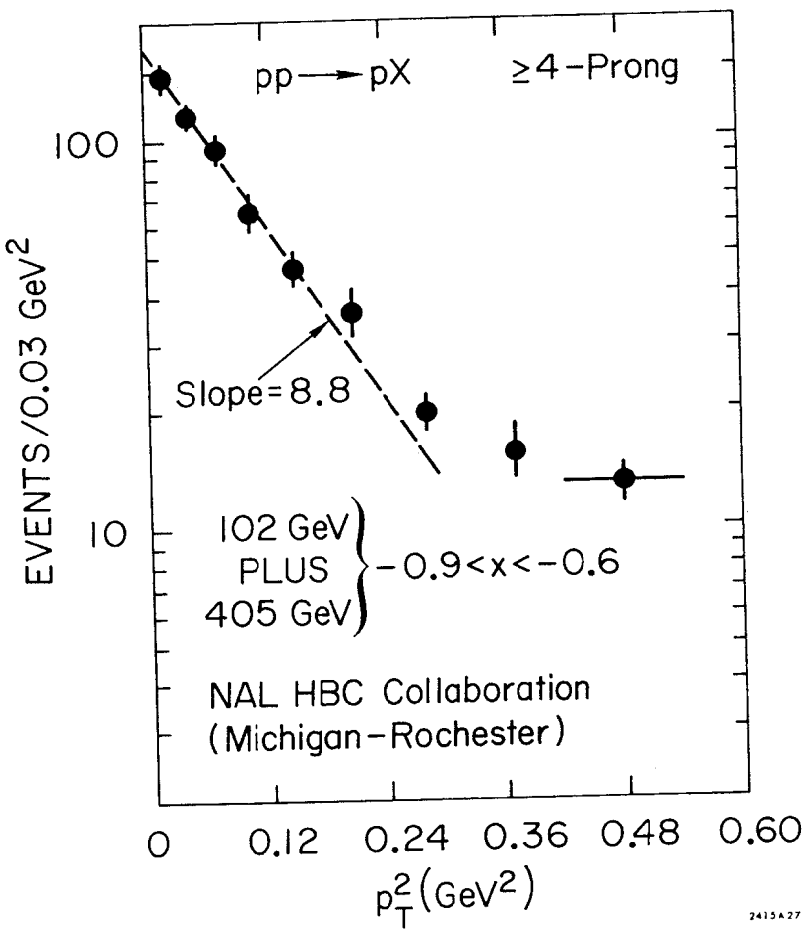

Figure 149b

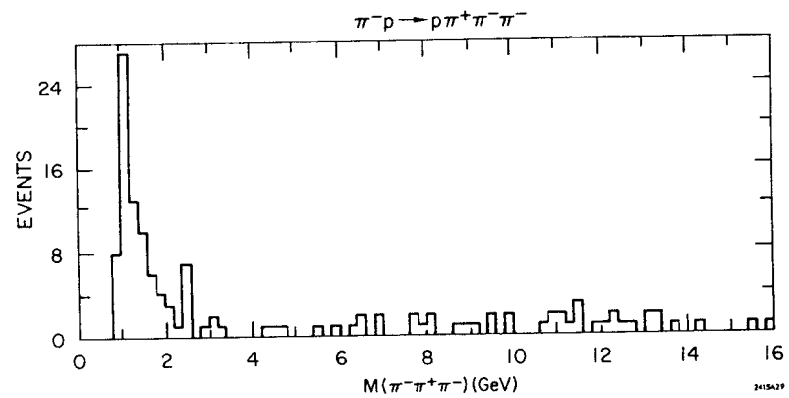

Figure 150

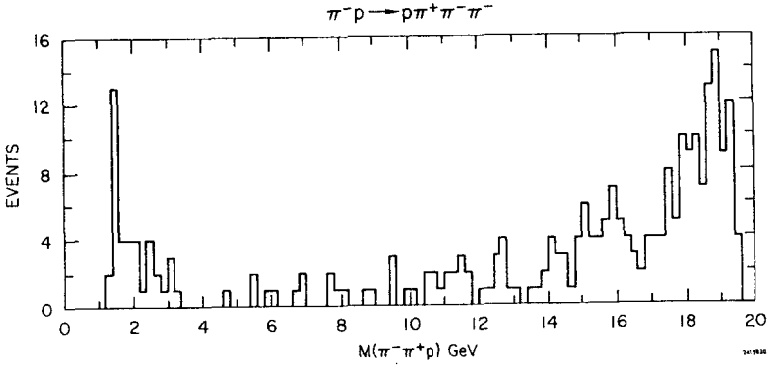

Figure 151

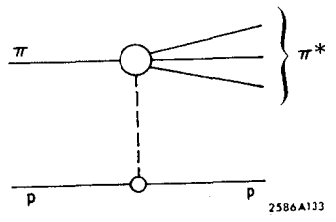

Figure 152

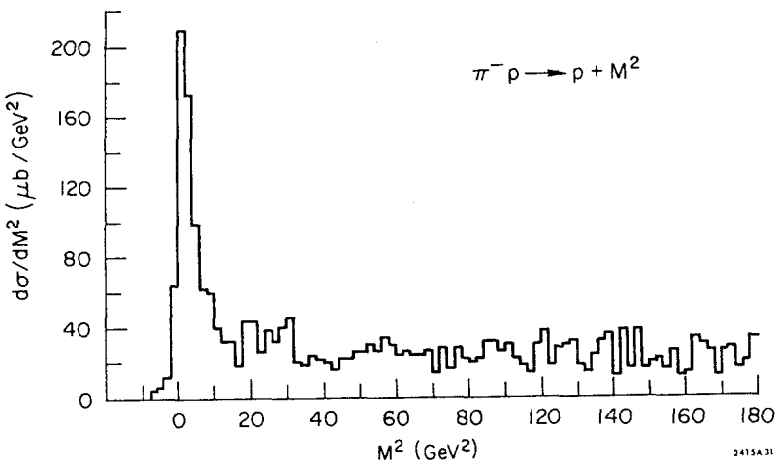

Figure 153

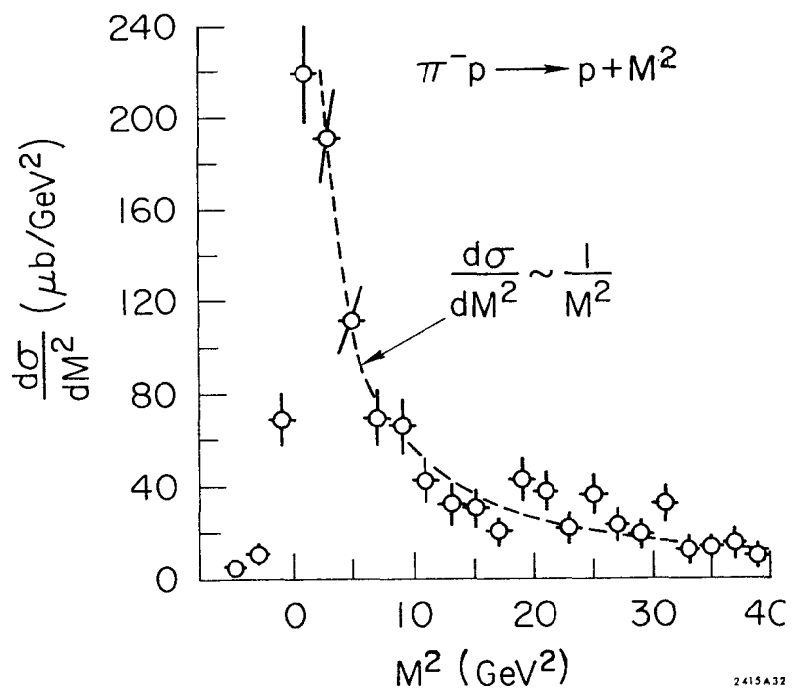

Figure 154

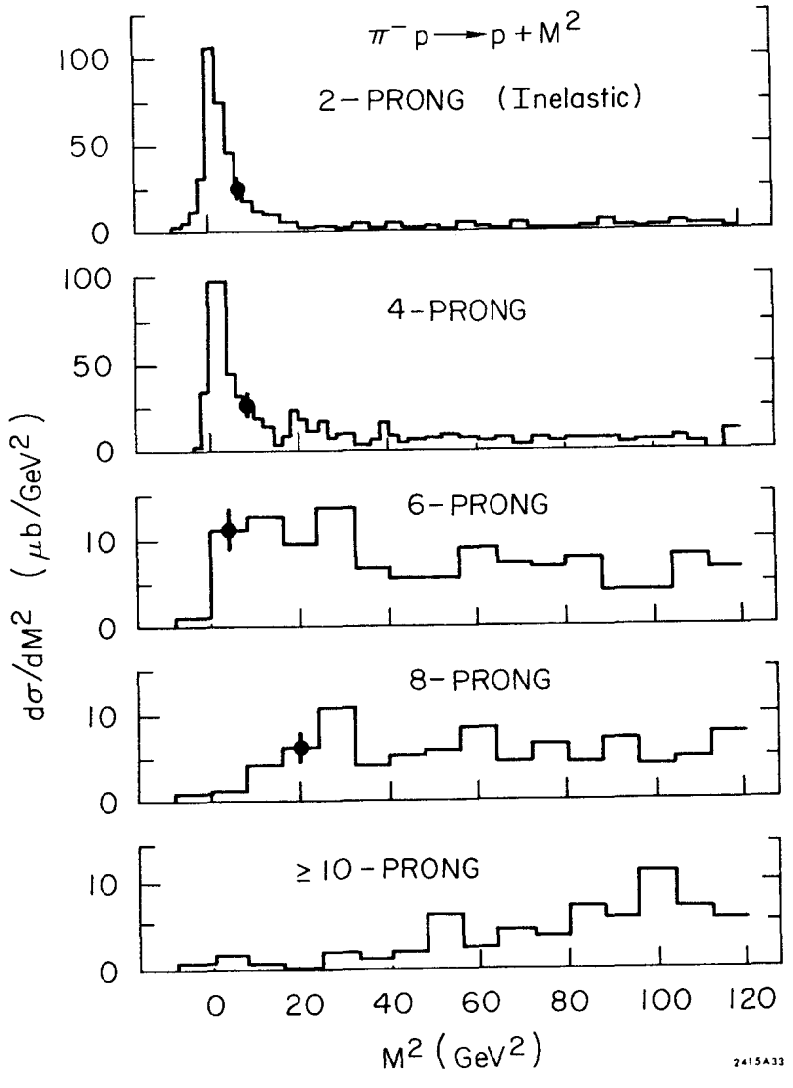

Figure 155

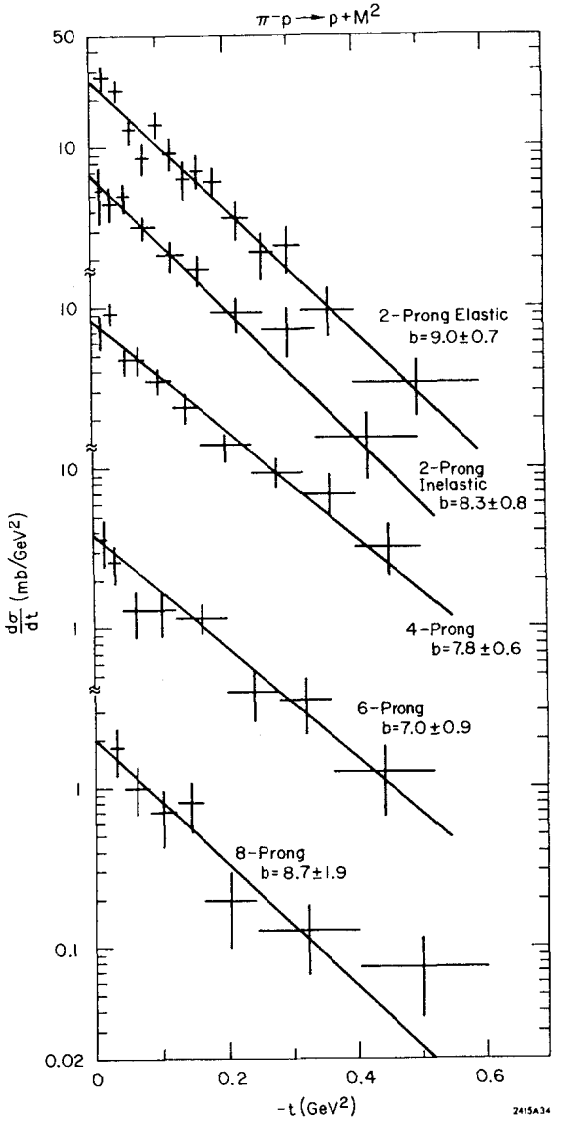

Figure 156

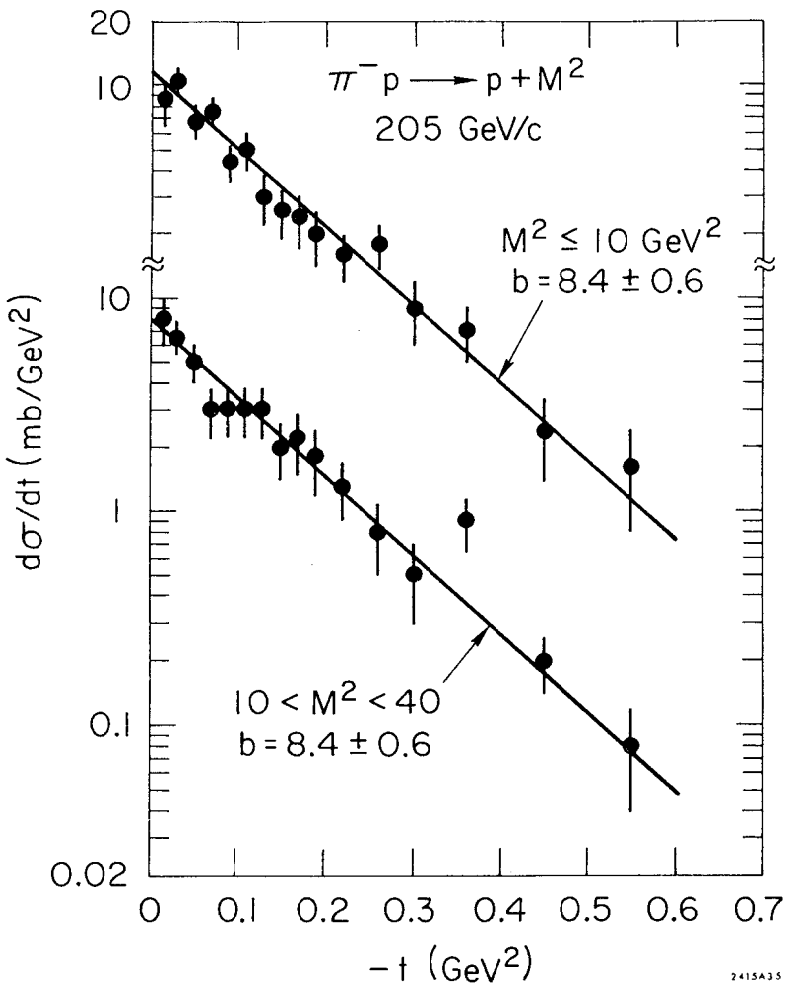

Figure 157

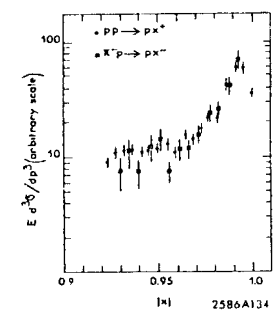

Figure 158

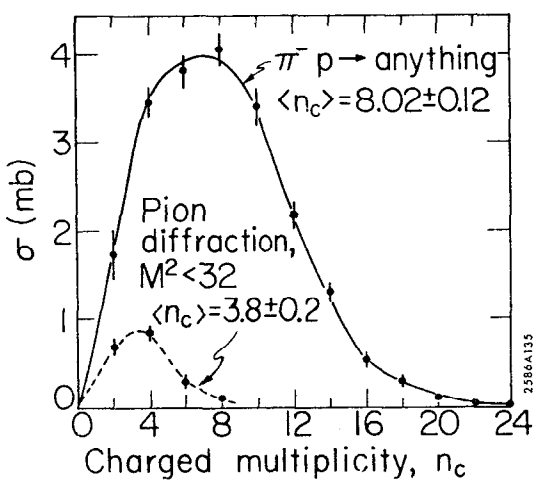

Figure 159

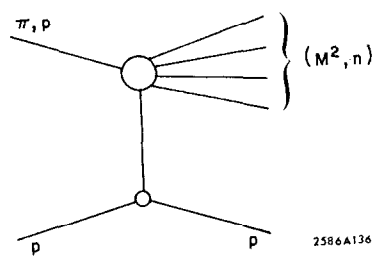

Figure 160

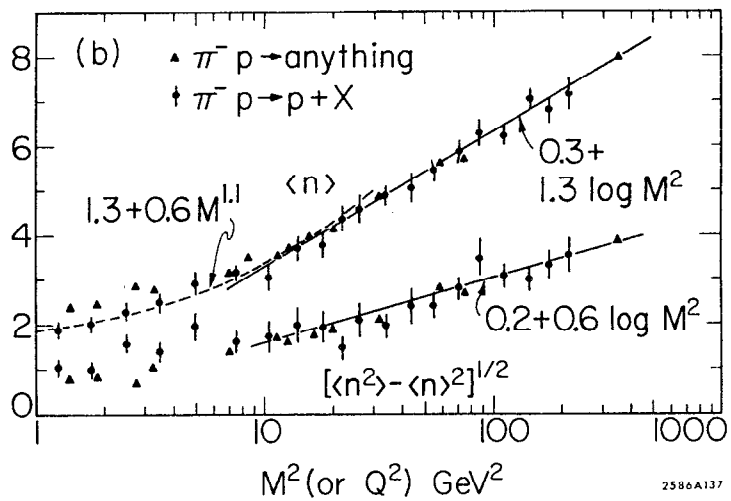

Figure 161

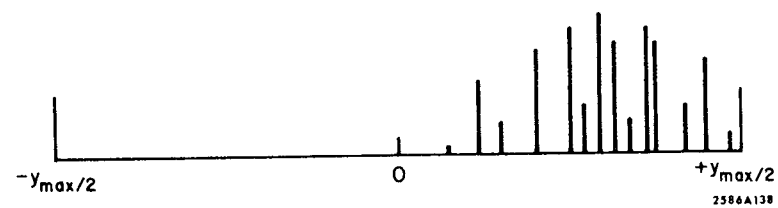

Figure 162

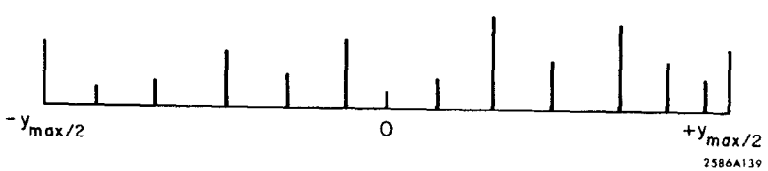

Figure 163

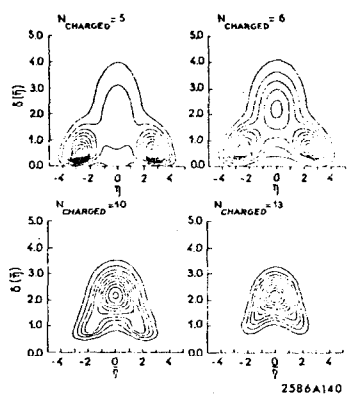

Figure 164

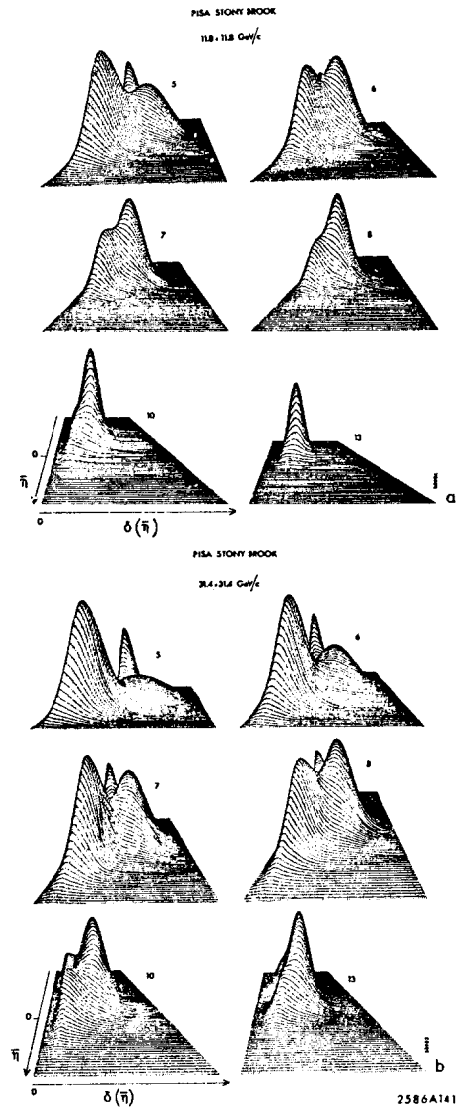

Figure 165

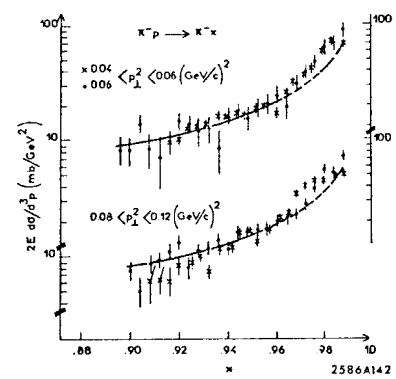

Figure 166

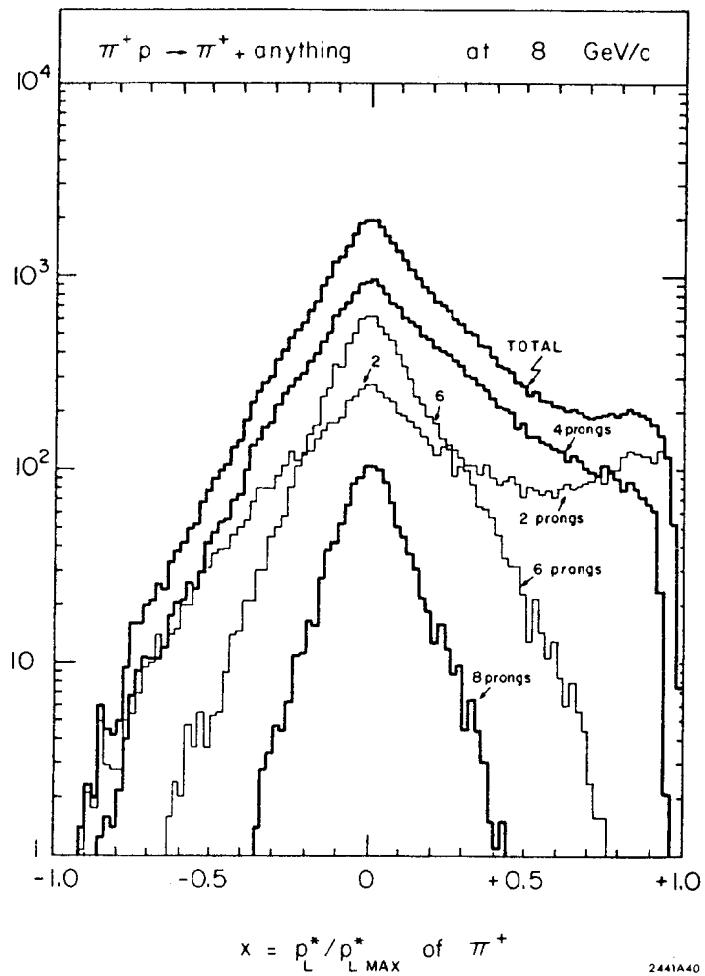

Figure 167

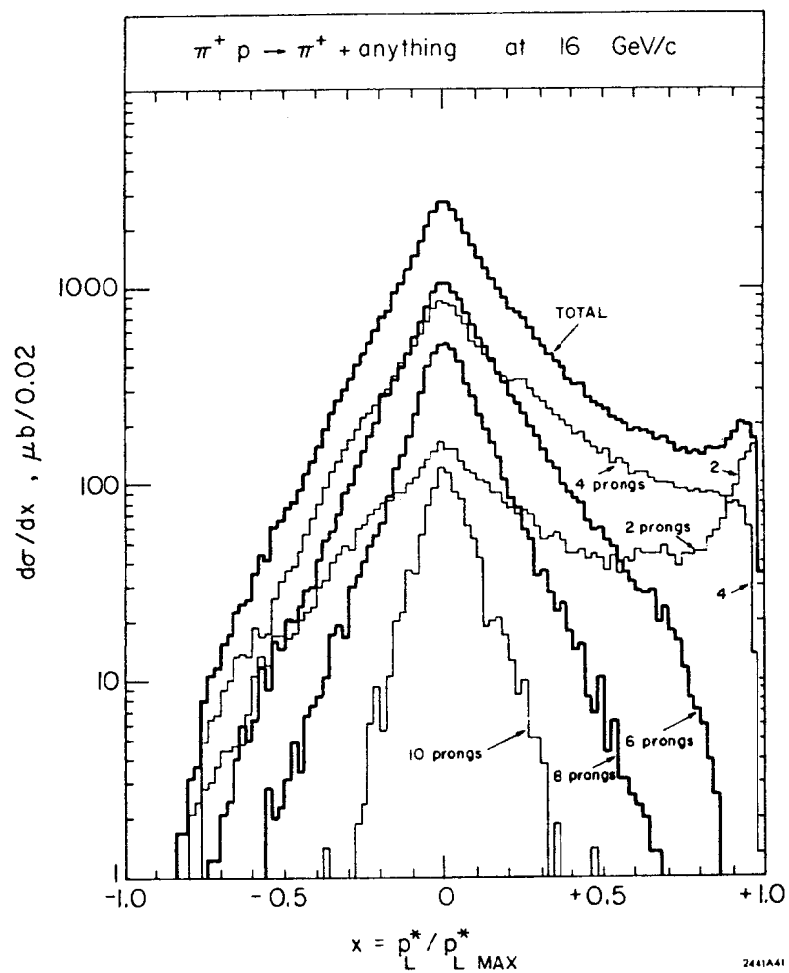

Figure 168

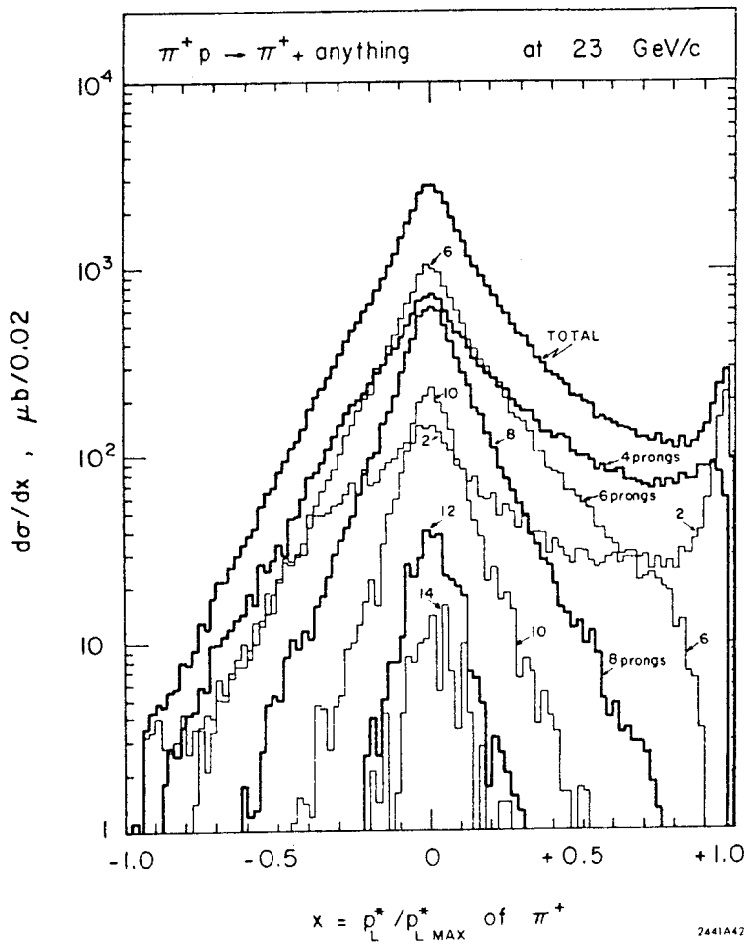

Figure 169

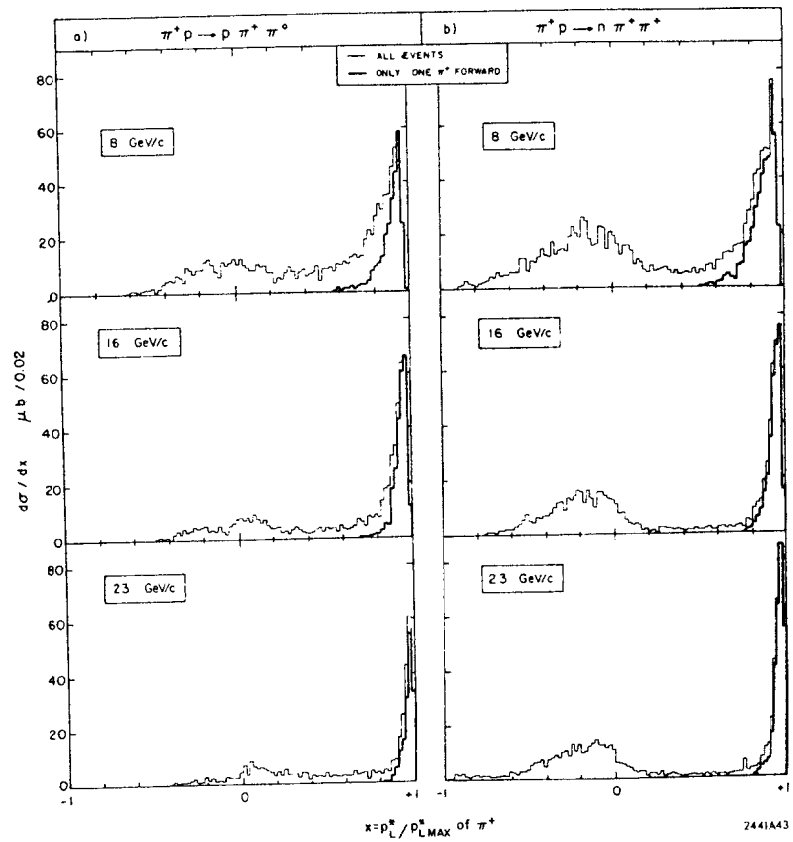

Figure 170

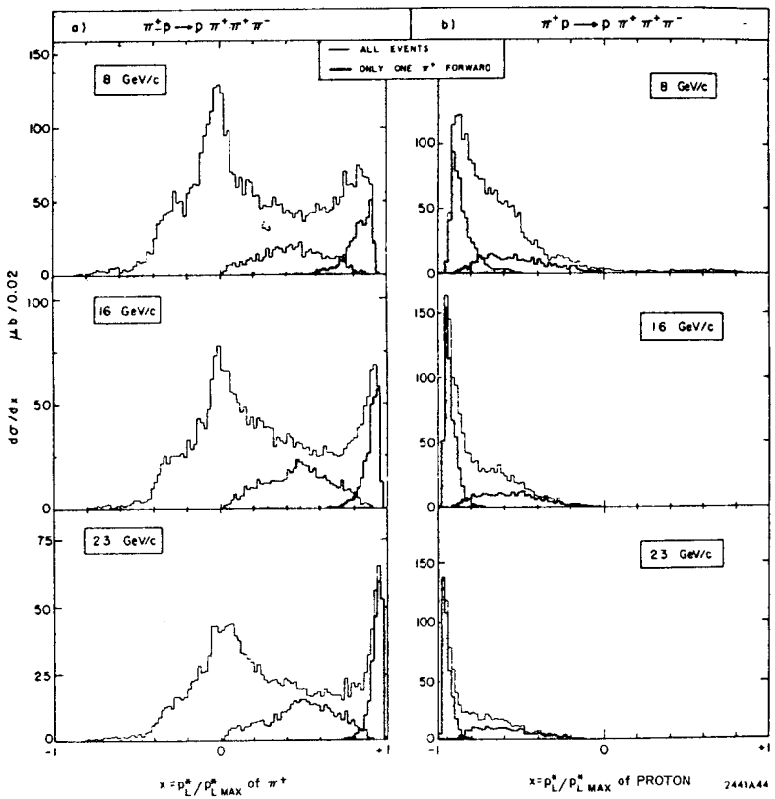

Figure 171

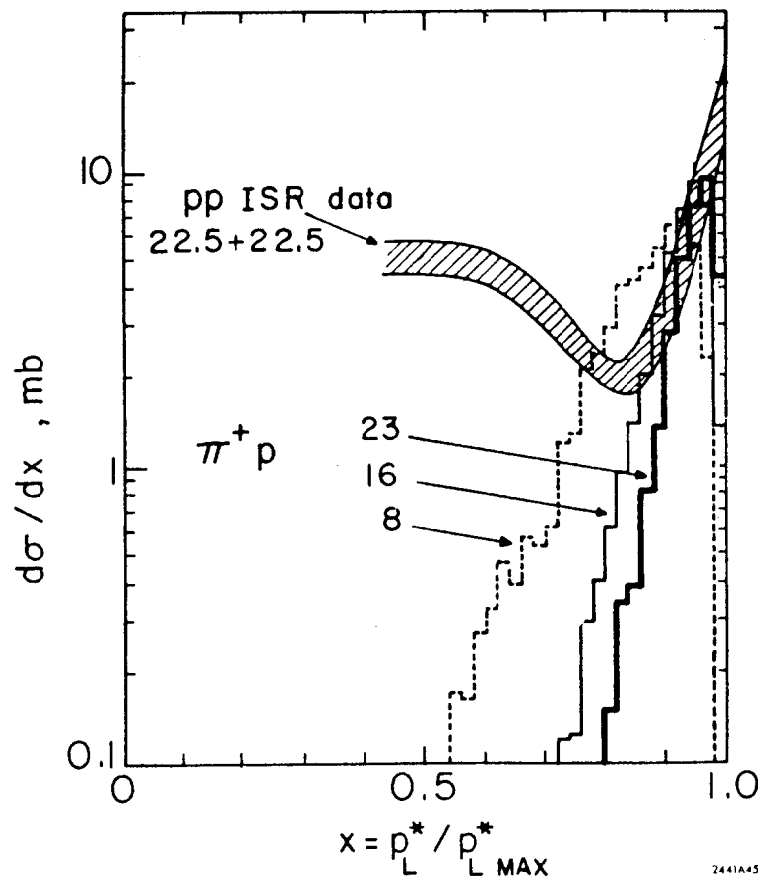

Figure 172

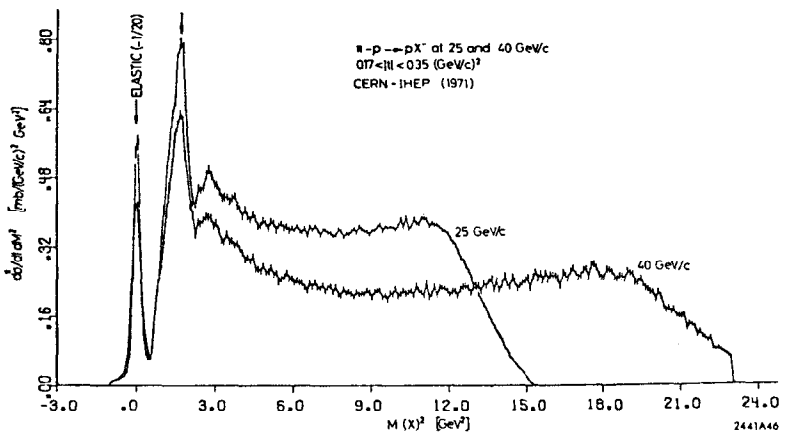

Figure 173

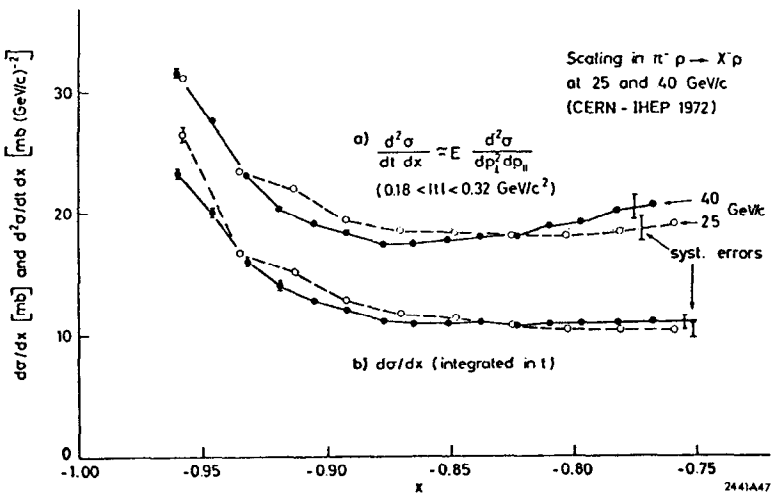

Figure 174

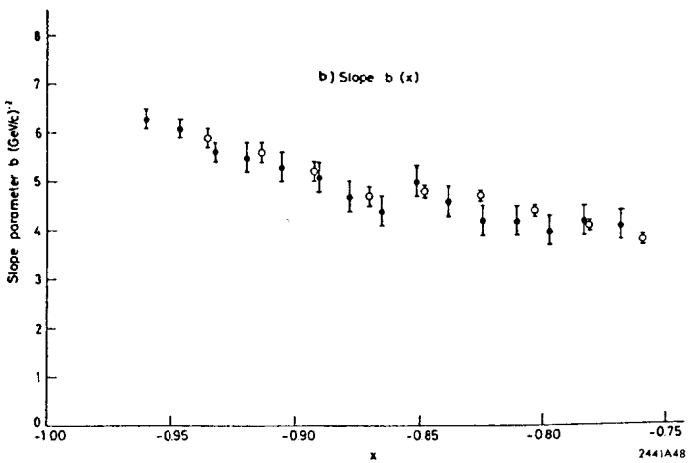

Figure 175

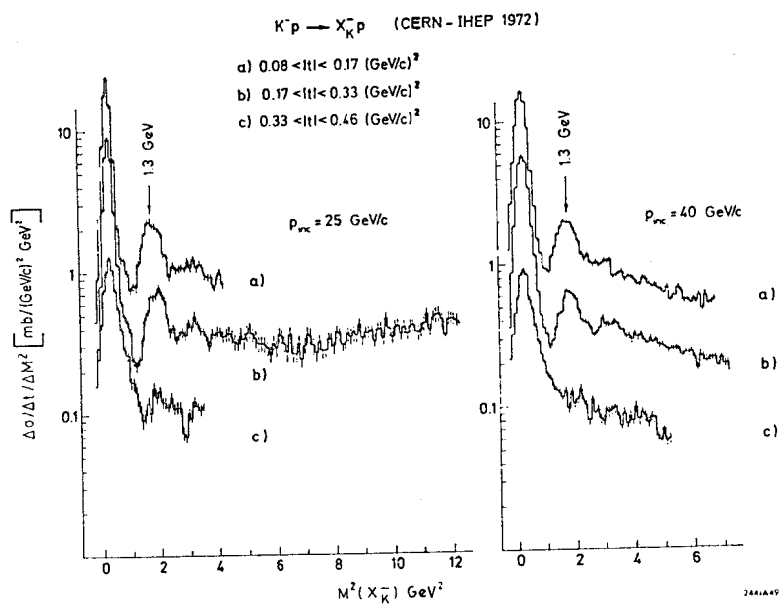

Figure 176

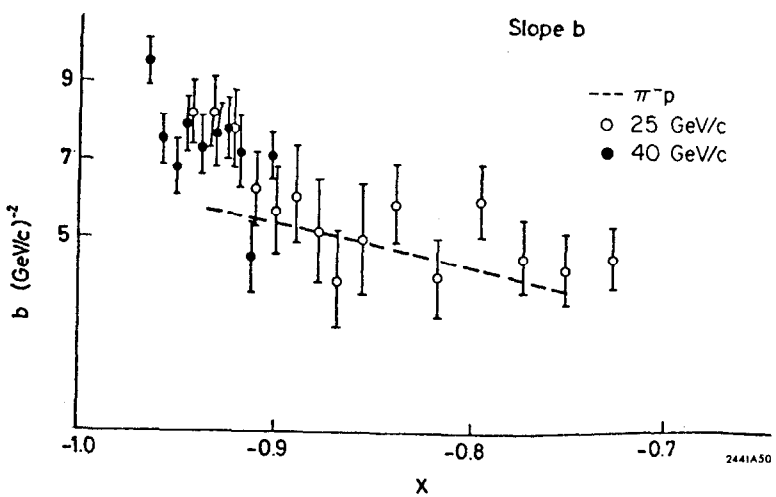

Figure 177

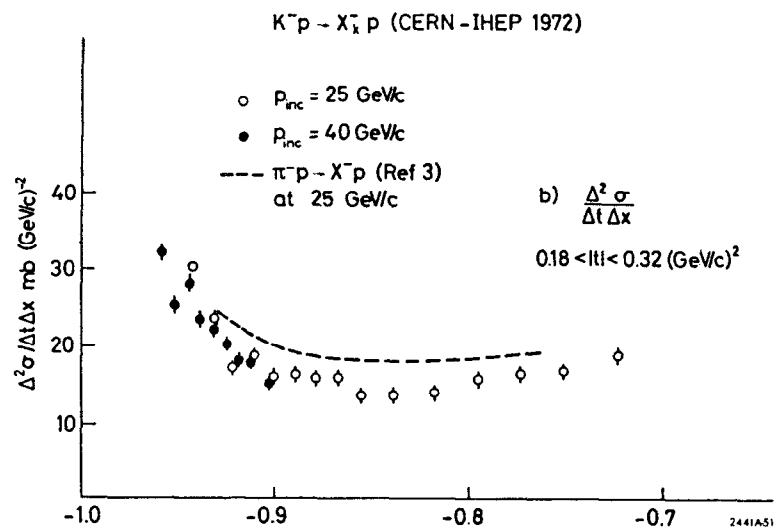

Figure 178

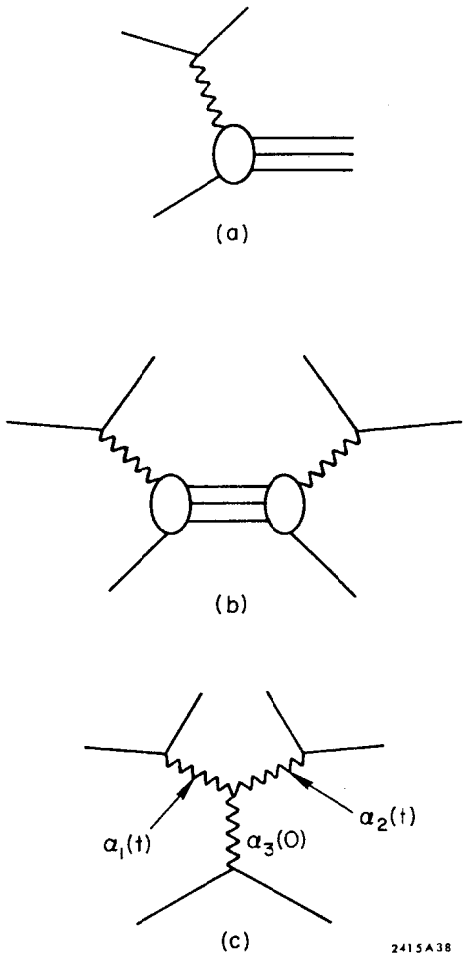

Figure 179

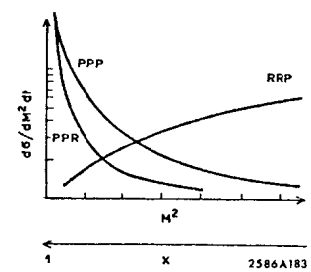

Figure 180

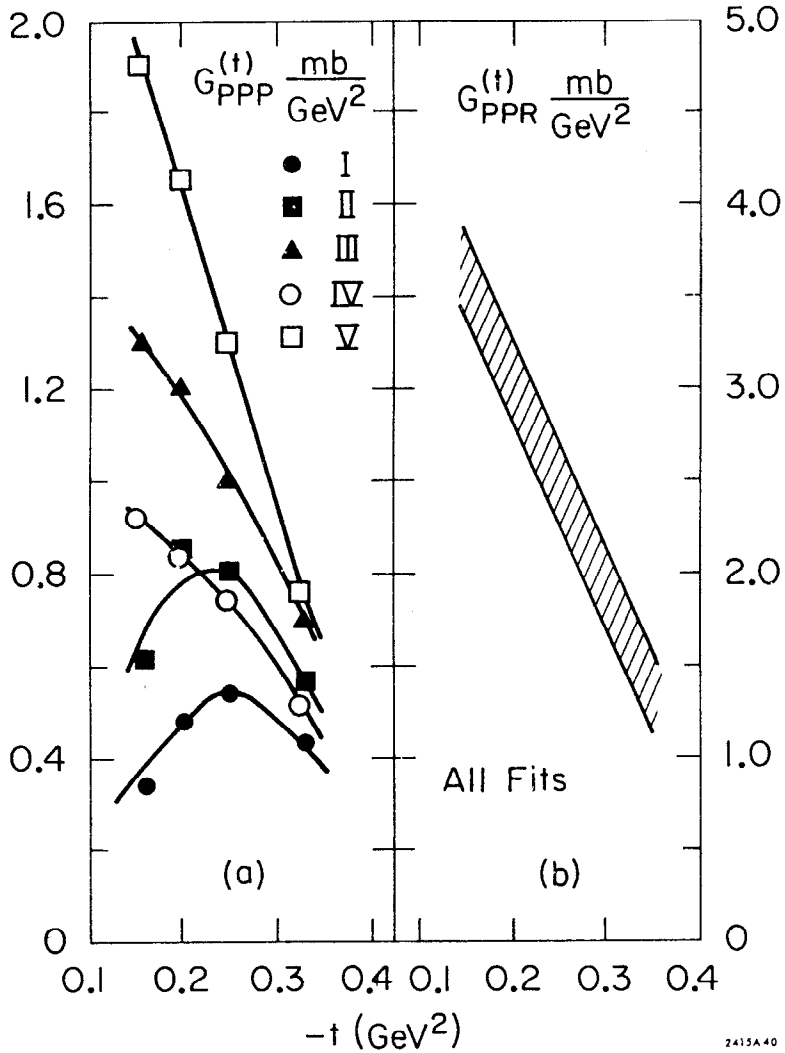

Figure 181

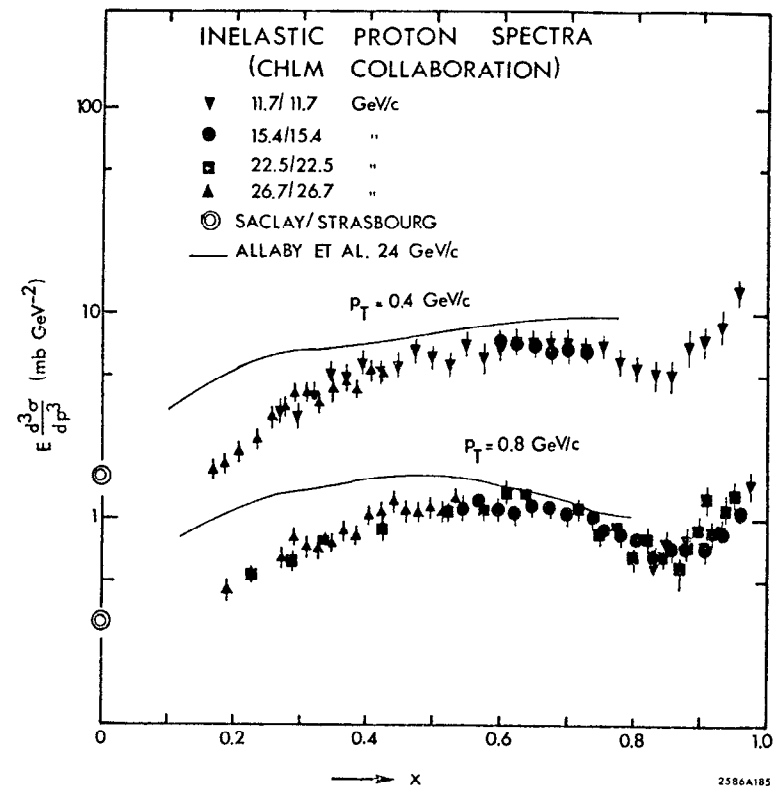

Figure 182

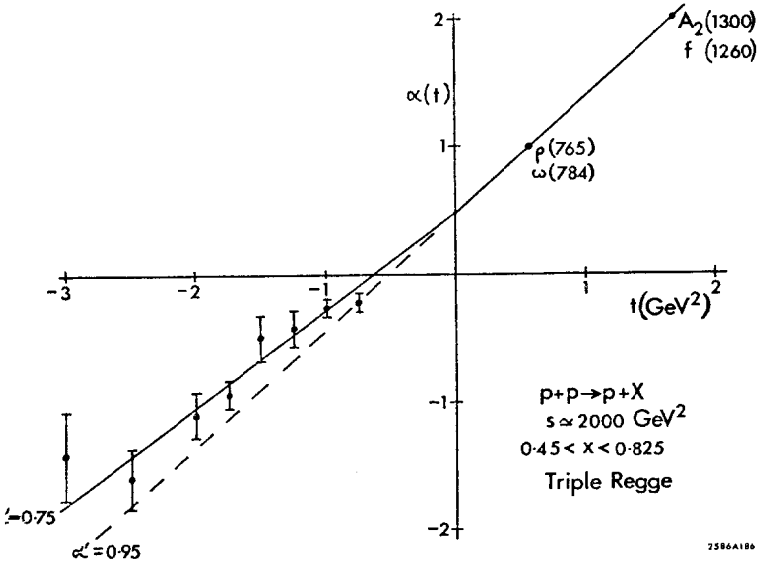

Figure 183

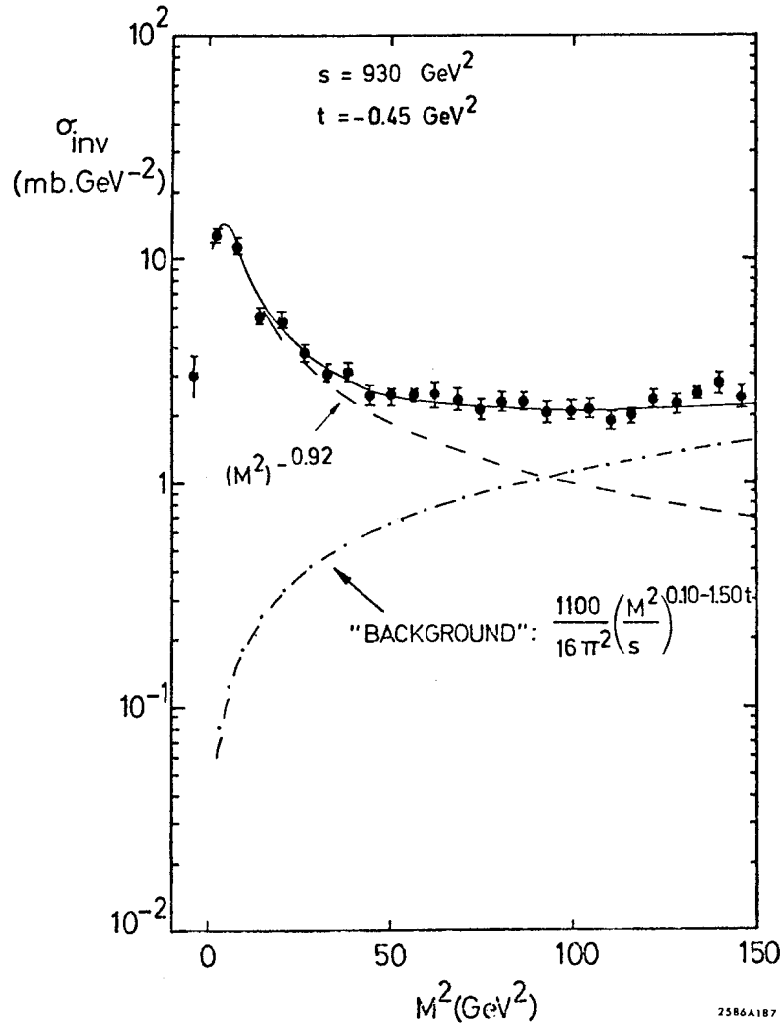

Figure 184

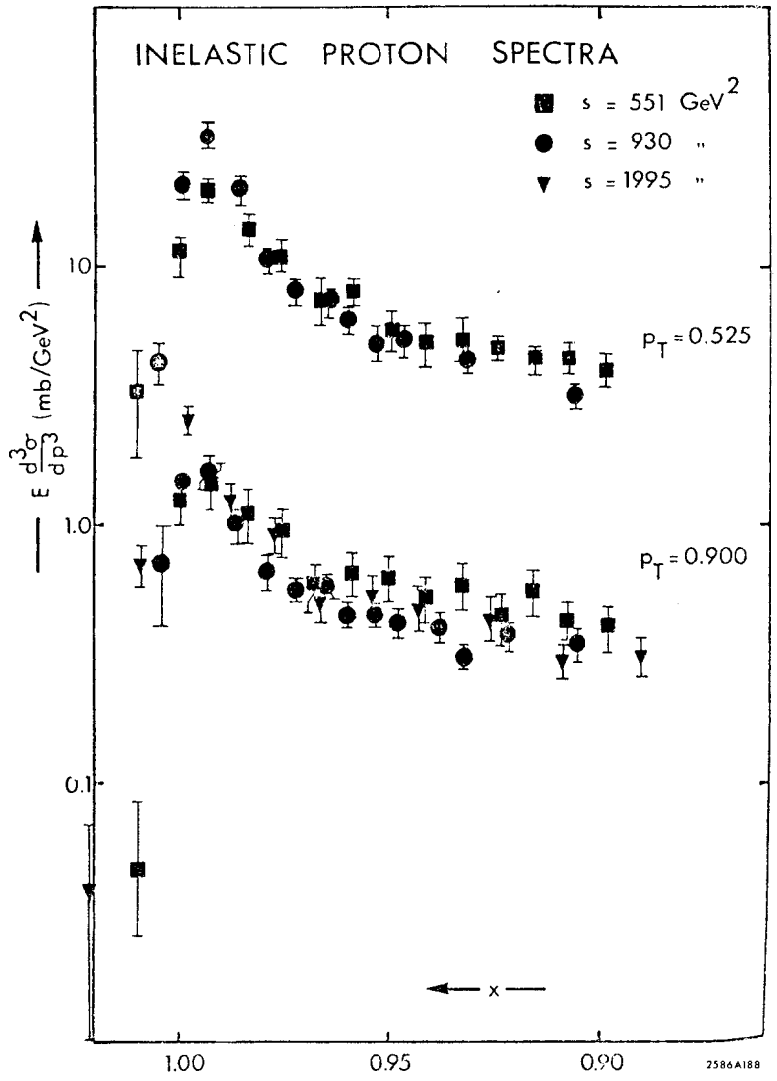

Figure 185

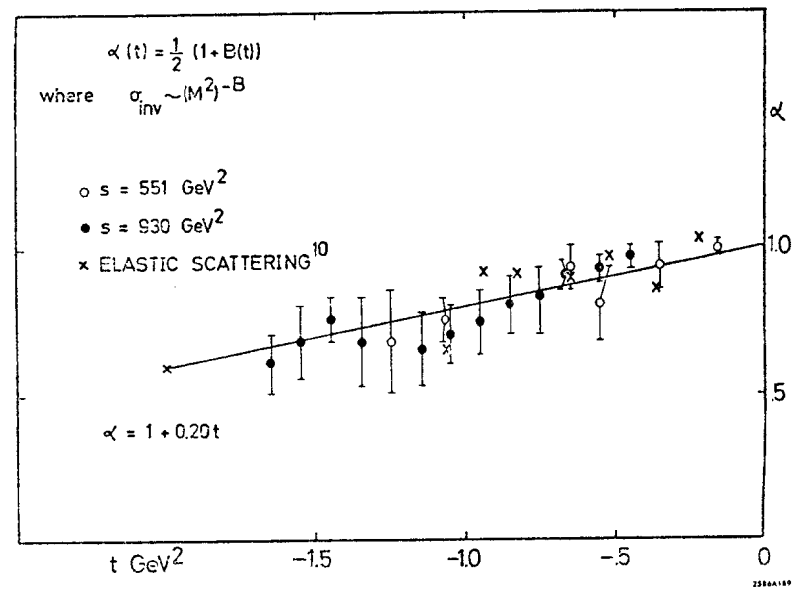

Figure 186

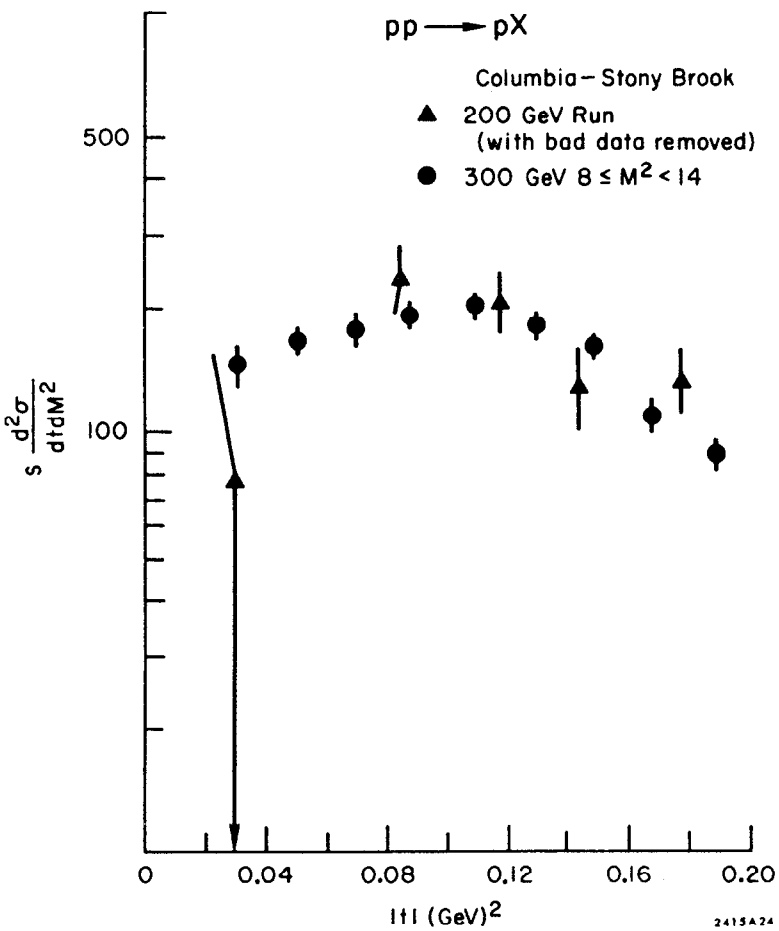

Figure 187

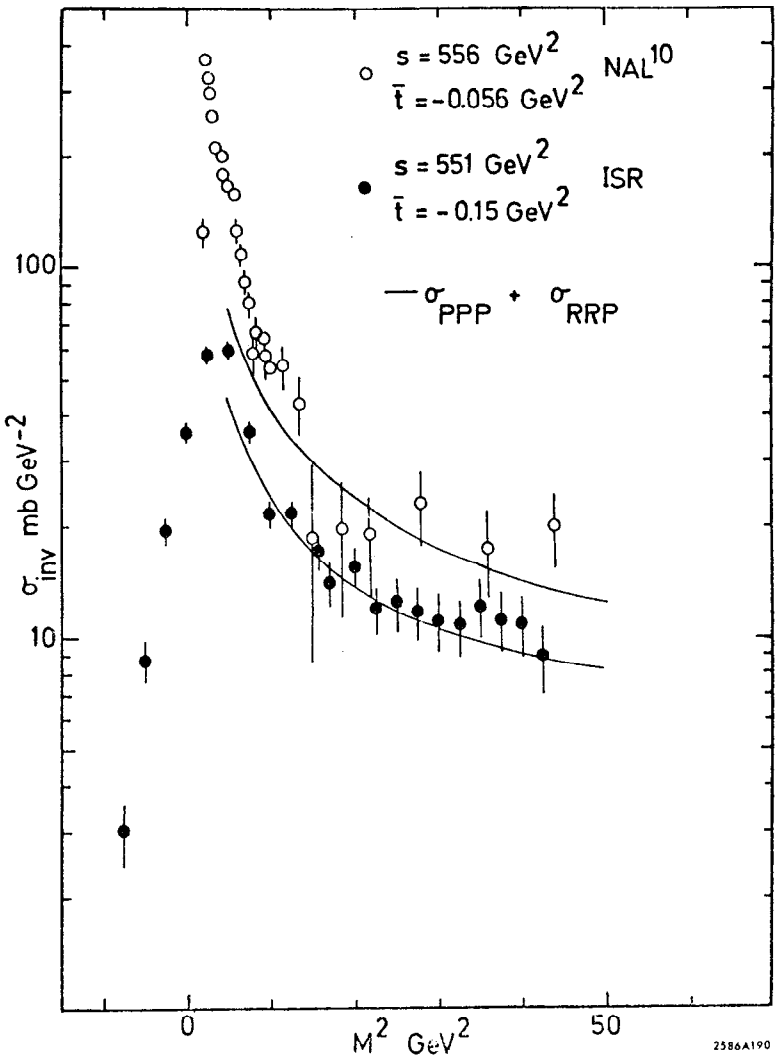

Figure 188

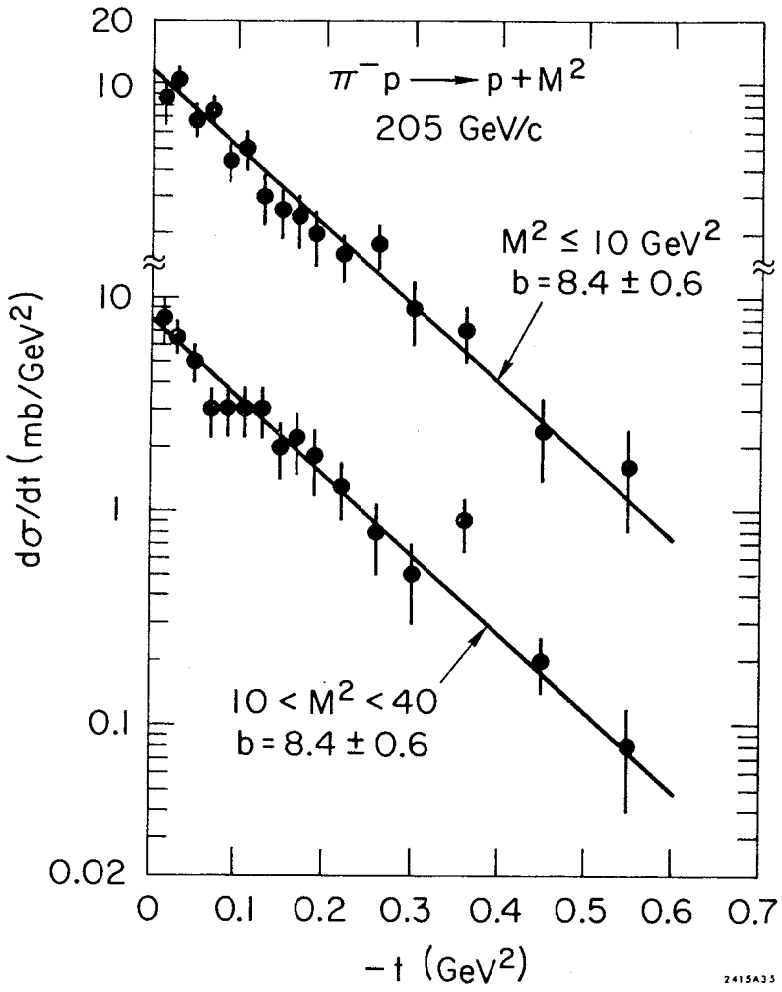

Figure 189

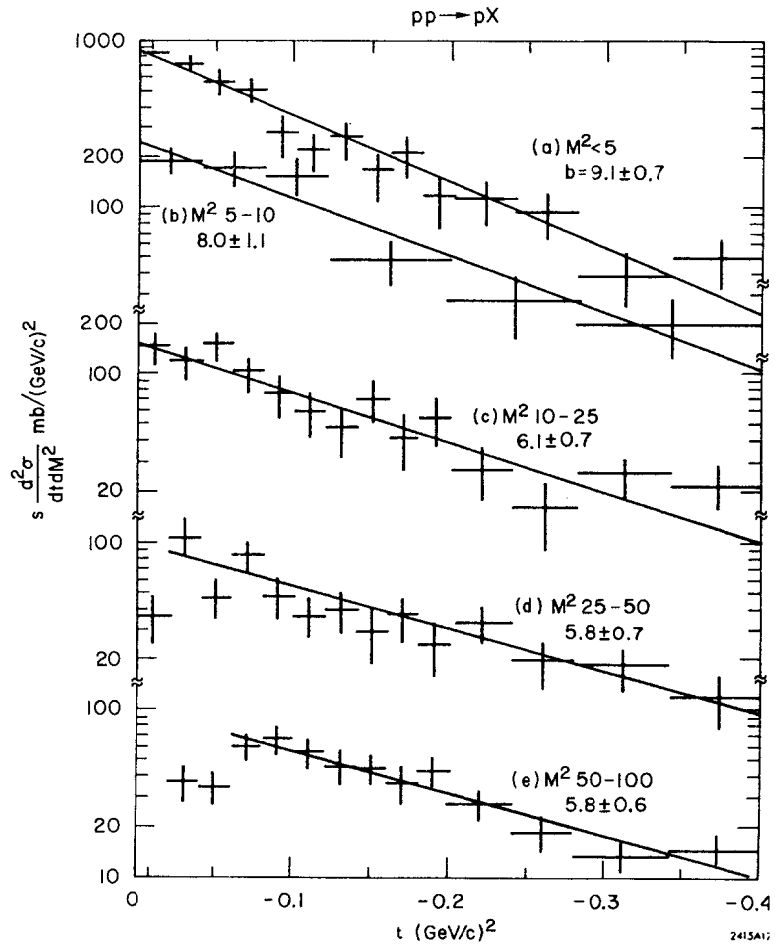

Figure 190

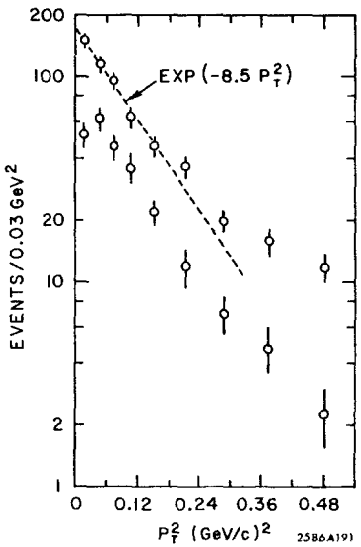

Figure 191

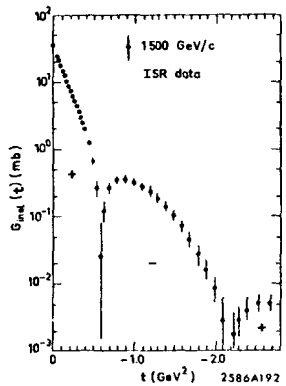

Figure 192

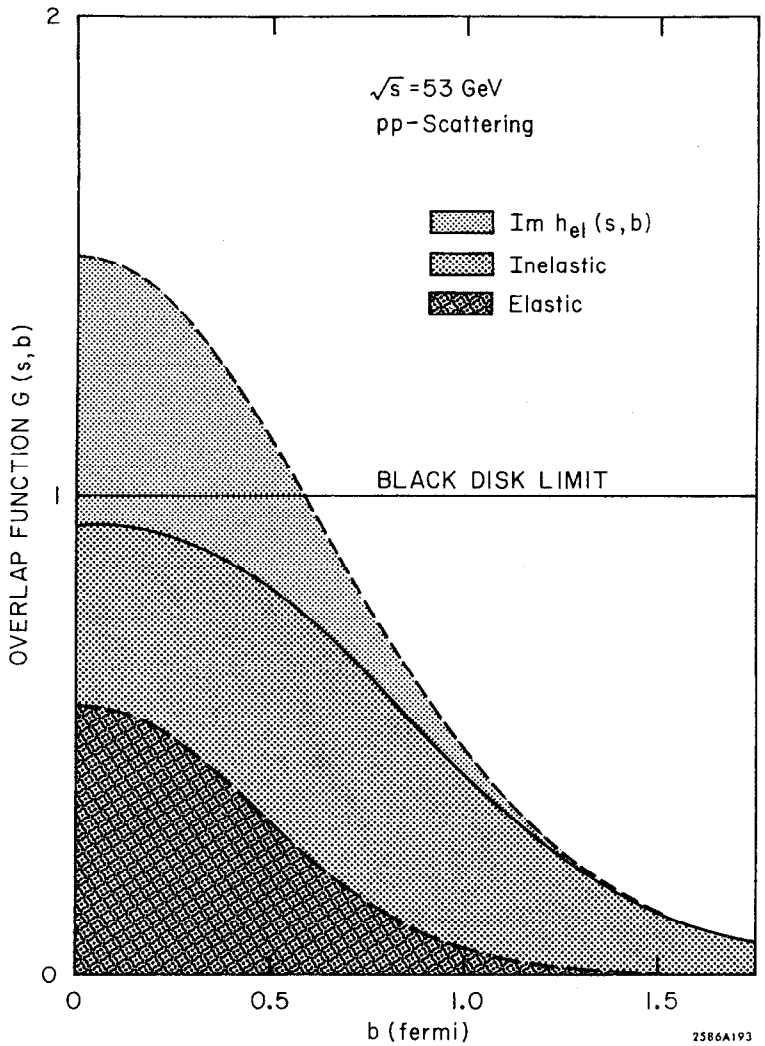

Figure 193

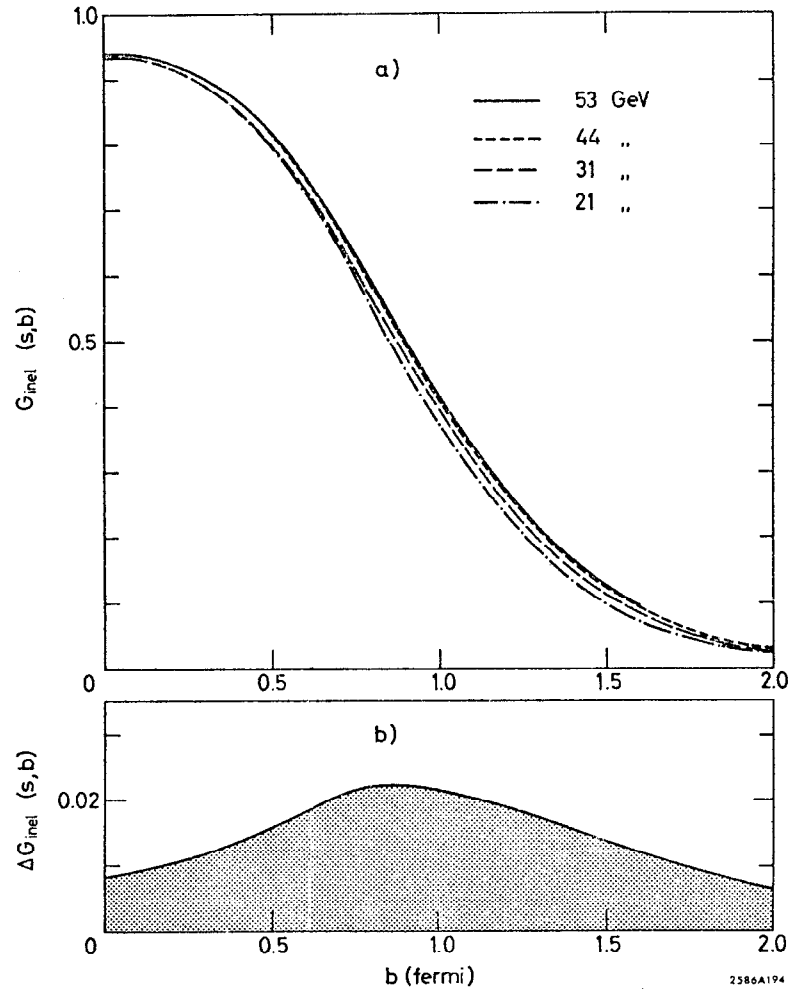

Figure 194

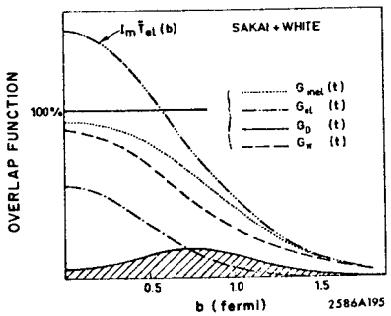

Figure 195

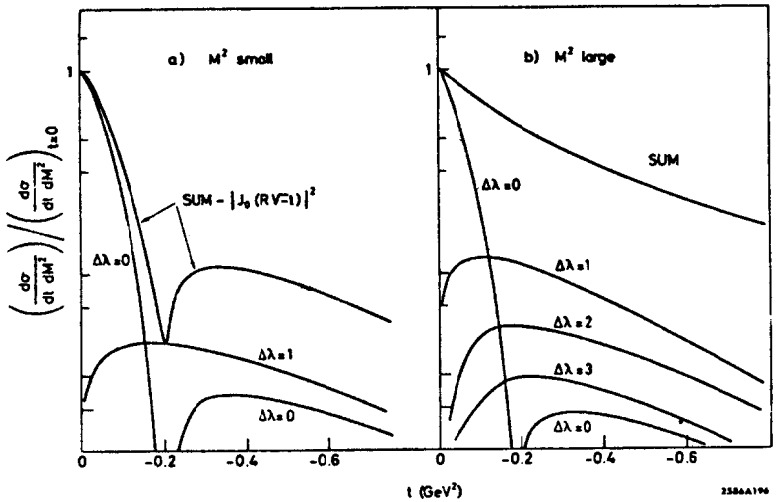

Figure 196

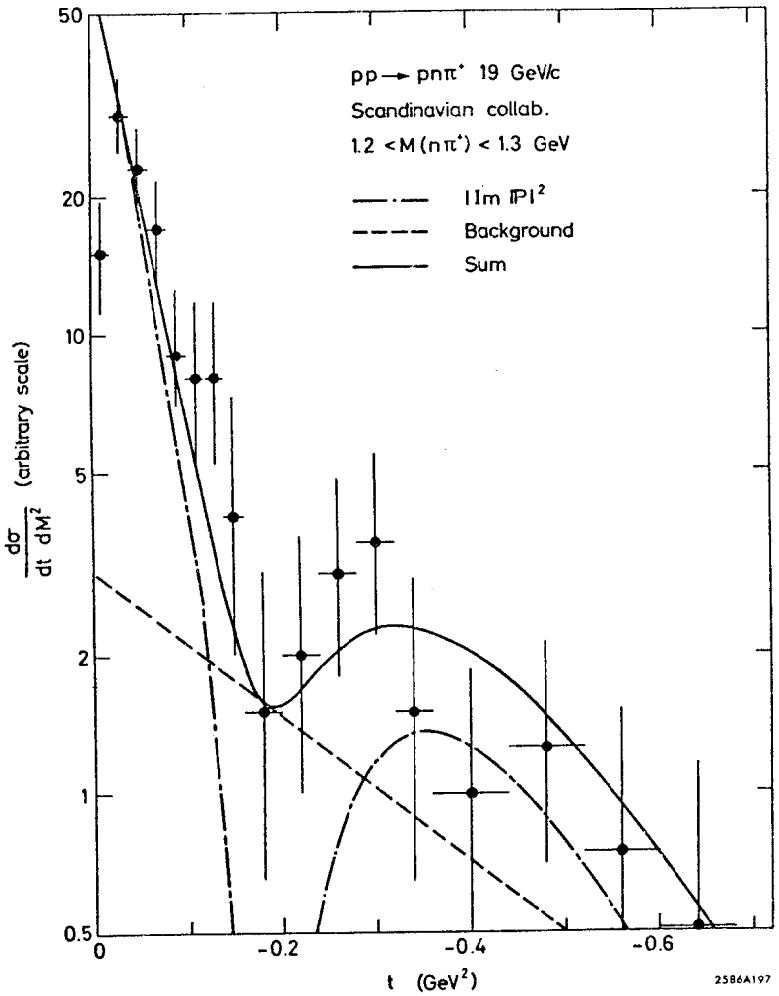

Figure 197

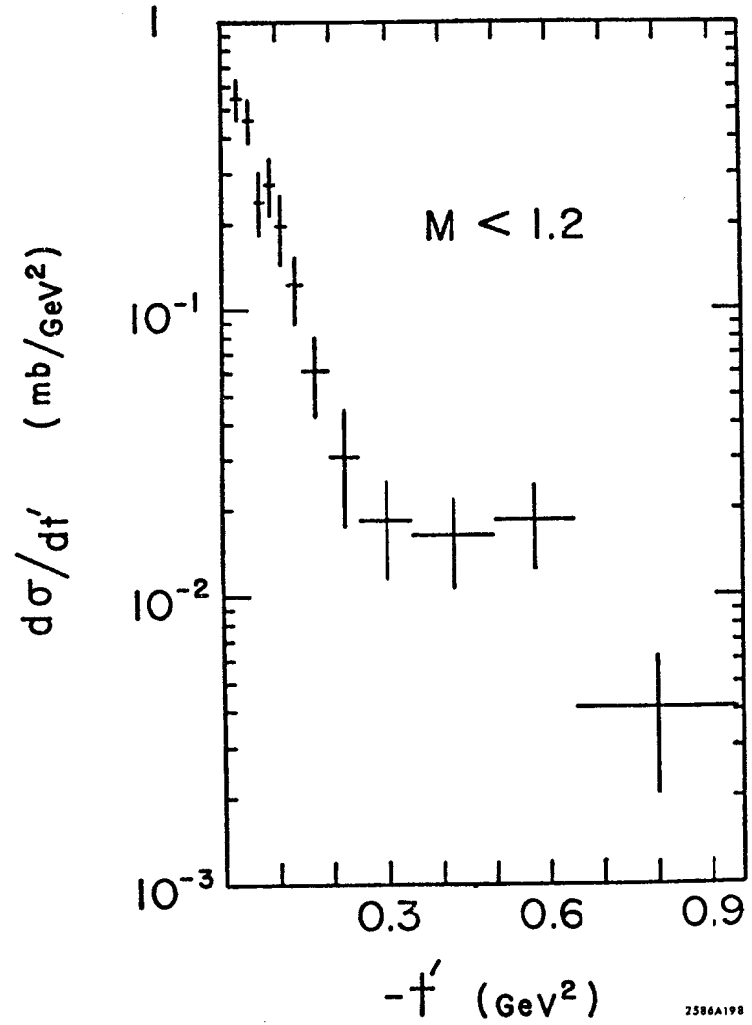

Figure 198a

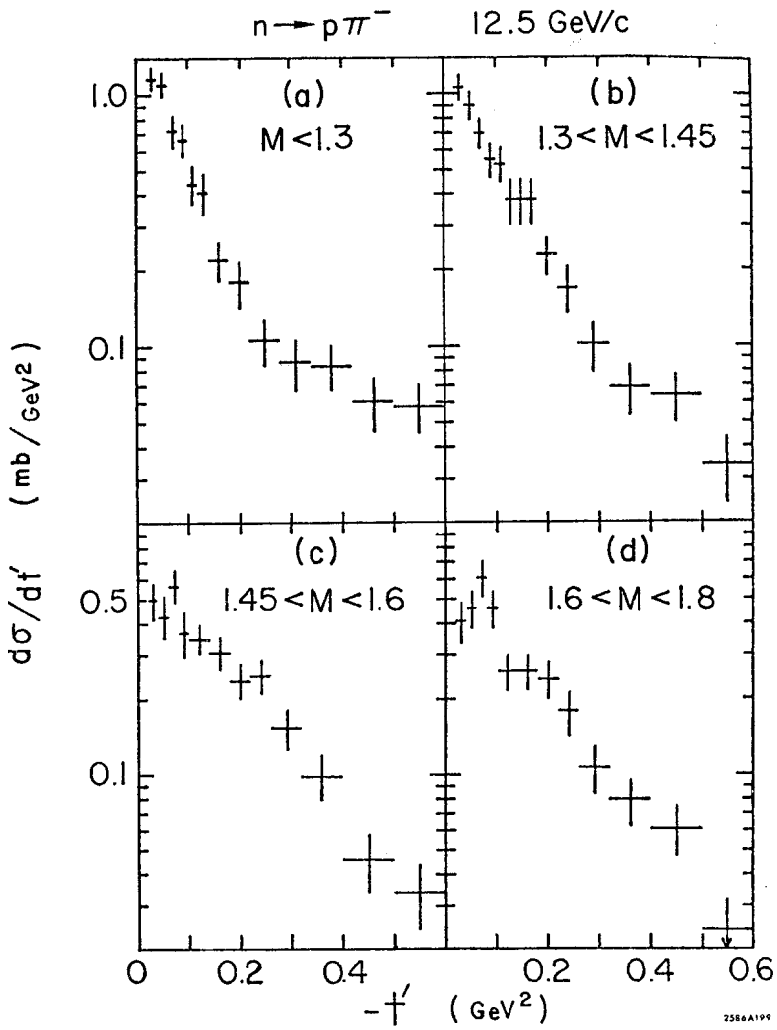

Figure 198b

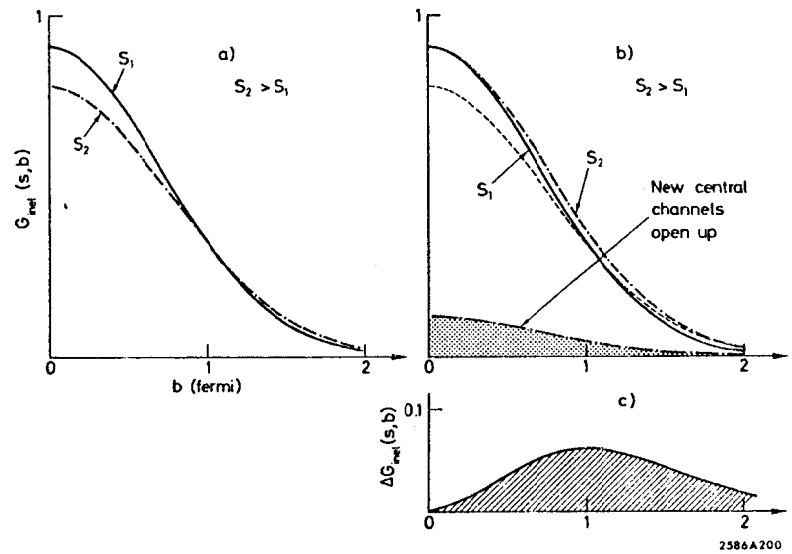

Figure 199

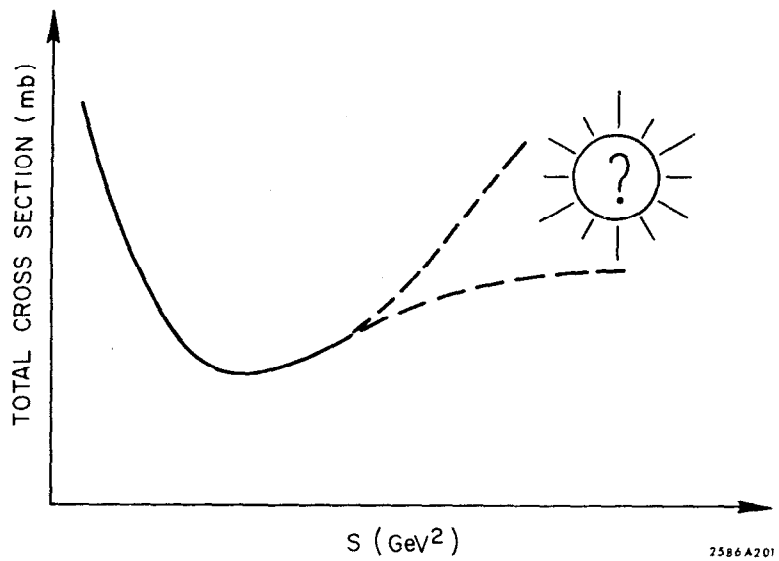

Figure 200